Particle Dynamics in Liquid-Lined Lung Airways

by Susan Jill Weekley, BSc

Thesis submitted to The University of Nottingham
for the degree of Doctor of Philosophy, February 2004

For my friends and family.

Acknowledgements

First and foremost I'd like to thank Oliver and Sarah for all their time and effort helping me to get to this point and for their unfailing patience with all my questions.

A special thank you also goes to my family for their continued support and encouragement over the years.

I'd like to thank all my friends in the department for making being at Nottingham such great fun. In particular I want to mention Rich, Andy and the rest of Captain OJ's crew, and all the postgrads who were there when I started and who have helped me out so much, especially Sarah, Catherine, Alex, John, Eleanor, Matt, Graeme, Jon and the Finn. I'd particularly like to say a big thank you to Colin for being such a splendid housemate and always being able to make me smile.

Finally, thanks must also go to EPSRC for providing the funding.

Contents

Abstract

Every time we breathe in we inhale thousands of particles, some of which may become trapped in the liquid lining of the airway wall. In this thesis we use theoretical fluid dynamics to model various aspects of the dynamics of these particles after their initial deposition on the airway wall.

In Chapter 2 we consider the behaviour of an inhaled particle trapped in an alveolar corner, modelled as a two-dimensional cylinder partially immersed in a liquid pool in the corner of a rigid-walled wedge. We balance quasi-static capillary forces acting on the particle with viscous forces, modelled using lubrication theory, acting in a small gap between the particle and the wall. The direction of particle motion is non-intuitive and we obtain predictions for the fate of a particle dependent on the wedge angle, liquid volume and the size and deposition site of the particle.

In practice, surface forces have been shown to pull particles into the airway liquid lining with sufficient force to depress underlying epithelial cells. In Chapters 3 and 4, using elastohydrodynamics, we consider the unsteady motion of a particle close to a deformable surface and the effect of wall deformation on the particle's behaviour. We model this initially as a two-dimensional cylinder moving in fluid perpendicularly and transversely close to a spring-backed plate, using simulations and asymptotic analysis based on lubrication theory. Viscous forces cause a transient overshoot of the force acting on the particle following a prescribed perpendicular displacement. Transverse motion of the particle causes the formation of a 'corner' in the wall, which is particularly sharp immediately following the particle's initial displacement. In addition we consider the extension of the model into three dimensions and examine a sphere moving close to a deformable plane in a fluid environment.

In Chapter 5 we consider the motion of a particle trapped in a mucus layer which is propelled by cilia acting within an underlying serous layer. We model

this as a cylindrical disk moving within a viscous sheet, with a uniformly-distributed body force in the lower layer representing the cilia. We predict the speed of the particle as a function of disk shape, ciliary activity and other material parameters.

Chapter 1

Introduction

During breathing we inhale many airborne particles which can become trapped in the liquid lining of the airways. Clearance mechanisms in the lungs work to remove these particles from the body, whether they be toxic and harmful to health, harmless or even beneficial. It is important to study the fate of these particles after deposition to fully understand their role in the pathogenesis of disease or in drug inhalation therapies. In this thesis we use theoretical fluid dynamics to study the dynamics of these particles after their initial deposition in the airway liquid lining of the lung.

In this chapter we review existing biological and mathematical literature relevant to the problem. We look first at the anatomy of the lung airways and the liquid lining, followed by a closer look at mucus and mucociliary transport. Next we describe the origins and effects of surface tension at a gas-liquid interface and the role of surfactants. We also consider briefly the effects of surface tension and surfactants in the lung. We then review particle deposition, retention and clearance in the lungs. Finally we consider three areas of fluid mechanics relevant to particle dynamics in airways: the migration of particles trapped at interfaces due to capillary interactions; the motion of particles near deformable interfaces (such as the airway wall); and the fluid mechanics of viscous sheets (such as the airway mucus layer).

1.1 Lung Anatomy

The main function of the lungs is to exchange gas between the outside environment and blood. Inhaled air passes along a branching network of airways which get progressively narrower and shorter, terminating in small air sacs called alveoli, of which there are about 300 million in the human lung [1]. The largest airway is called the trachea (radius $\approx$ 0.9cm), designated as generation 0. The airways bifurcate down to roughly generation 23. The first 16 generations are known as the conducting airways. Their main function is to transport air from outside to the gas-exchange region. Generations 17 to 23 are called the respiratory airways. The alveolar sacs (radius $\approx$ 0.15mm), where gas exchange takes place, are found from generation 17 onwards [1].

All lung airways are lined with a layer of fluid. In the case of the conducting airways it is believed that this is a two-phase lining (see [2] and references therein). At the base of the fluid lining are predominantly epithelial cells, the outermost cells of the airway wall. Above these cells there is an aqueous layer, known as the 'sol' phase, which surrounds epithelial cilia (see Figure 1.1). Above the sol phase is the 'gel' phase, a layer of mucus. The tips of the cilia penetrate the mucus blanket as they beat in a coordinated pattern, pushing the mucus layer towards the mouth (see §1.2 for more detail). The existence of a gel layer in the respiratory airways (generations 17 onwards) has not yet been fully established [2, 3]. Here there are no mucus-secreting cells so it is unlikely there is much mucus in the peripheral airways and the alveoli.

The alveolar sacs are not spherical; they can be described as irregular polyhedra [1]. The alveolar geometry means that pools of the fluid lining can gather in the corners of the alveolus. Clearly, the volume of air in the lung varies greatly during respiration, with the functional surface area of the alveoli (needed for gas exchange) increasing with inspiration and decreasing on expiration. However it has been suggested that these changes in alveolar vol-

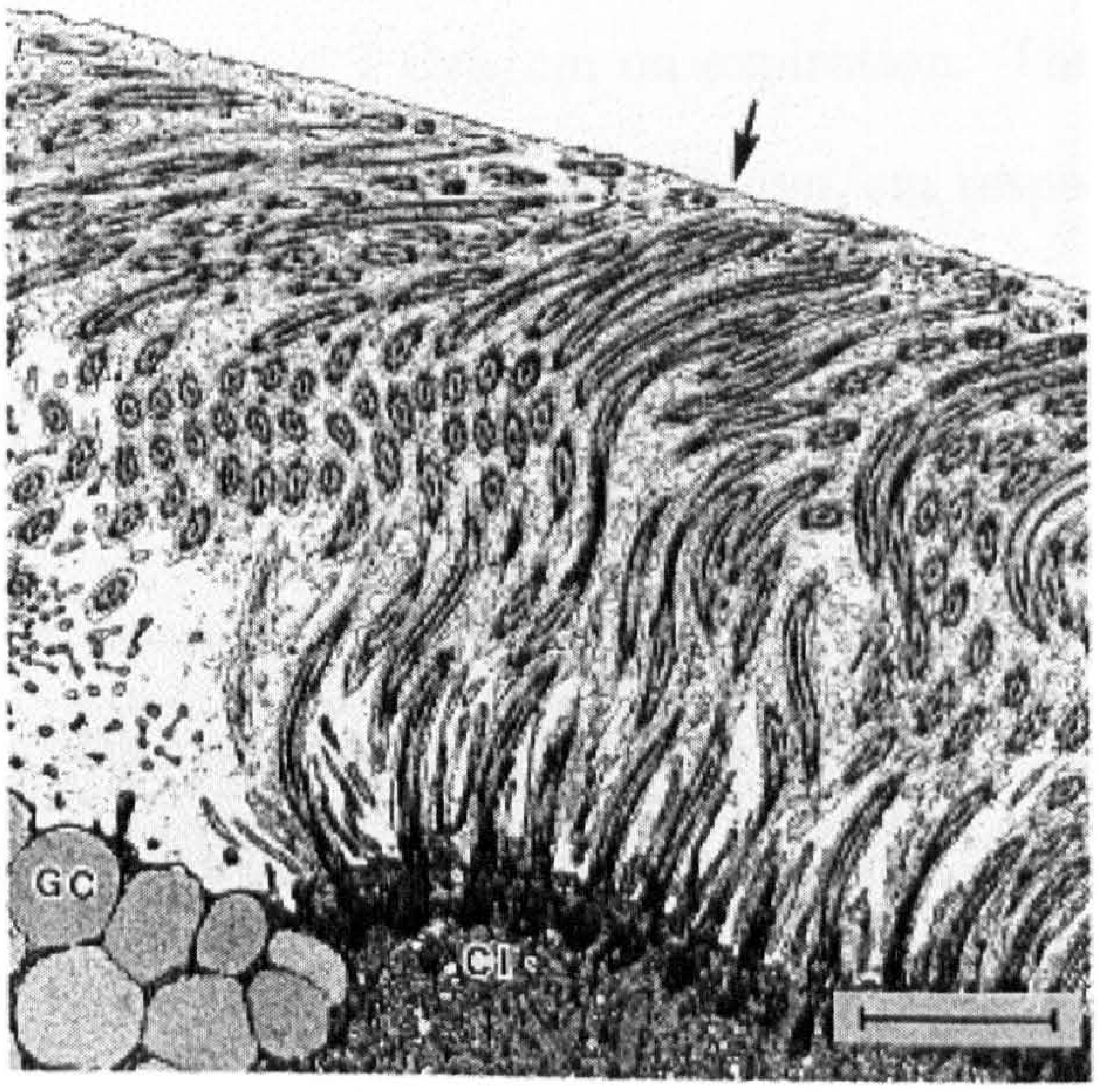

Figure 1.1: Electron micrograph of horse trachea showing the aqueous layer surrounding the cilia, from [2]. Bar=2μm. GC, Goblet cell; CI, ciliated cell.

ume are due to the recruitment/derecruitment of alveoli (re-opening of flooded alveoli) rather than significant changes in alveolar size [8].

It is extremely difficult to make accurate measurements of air pressure, surface tension and other material parameters in human lungs. There is wide variation in estimations of these parameters; for simplicity we will assume typical parameter values are as described below.

Bastacky *et al.* [4] estimated the thickness of the liquid layer in rat lungs to be 0.14 μm over the relatively flat parts of the alveolar walls and 0.89 μm at the alveolar wall junctions. The curvature of a typical undisturbed pool in an alveolar corner is approximately 0.01 μm^{-1} [1]. It is not possible to measure the alveolar air pressure directly in humans, however it has been estimated to vary between -50 cmH_2O following expiration and 50 cmH_2O following inspiration [5]. The surface tension of the alveolar liquid lining also varies with lung volume. At total lung capacity, alveolar surface tension is approximately 30 dyn/cm but this reduces to < 1 dyn/cm on expiration. The surface tensions of mucus and water are 40-50 dyn/cm and 70 dyn/cm respectively [6, 7].

1.2 Mucus and Mucociliary Transport

The purpose of the mucus layer in the airway liquid lining is to prevent dehydration of the epithelial cells and to protect the airways from external toxins by trapping inhaled particles in the mucus [9, 10]. Mucus covers most of the surface of the upper airways, though there is some debate as to whether the mucus sheet is continuous [11]. It has been shown that mucus can be secreted in response to stimulation of the epithelium so that any experimental results may be misleading; however as mucus is transported from the smaller peripheral airways into the larger airways, it seems likely that the mucus will form a continuous sheet in the larger airways simply because of the volume of mucus present [12]. Mucus is secreted from mucous glands, and occasionally goblet cells (see Figure 1.1), as droplets which coalesce and become stretched into sheets [9, 13]. In the larger airways, in the absence of disease, the mucus layer has been found to be 5-10μm thick [10, 13] (see Table 1.1 for various data on airways, mucus and cilia). The mucus sheet can be described as a non-Newtonian, viscoelastic gel as it has both viscosity (resistance to flow) and elasticity (a recoil energy in response to an applied stress). Initially the 'gel' will respond as a solid to the applied stress, followed by a viscoelastic deformation (occurring at the 'yield' stress) and then a steady flow resulting in permanent deformation [14]. Mucus viscosity decreases as the shear rate increases (*i.e.* as the applied force increases)— this is referred to as shear thinning [9]. Few rheological values for "healthy" mucus exist as it is only produced in excess in disease. However tracheal canine mucus is thought to

AIRWAYS	Generation	Trachea	1	5	15
	Diameter	1.8cm	1.22cm	0.35cm	0.066cm
	Length	12.0cm	4.76cm	1.07cm	0.20cm

MUCUS	Viscosity	20-2000P (low strain) 1-10P (high strain)
	Velocity	5-10mm/min
	Depth	5-10μm

PERICILIARY FLUID	Viscosity	0.02-0.1P
	Depth	5-500μm

CILIA	Length	5-8μm
	Beat Frequency	10-20/sec
	Spacing	0.3-0.4μm

Table 1.1: Data on airways, mucus, cilia (from [15]). Sampling, particularly in the periciliary fluid, is very difficult and all data are subject to variation.

be similar to that of humans and has been found to have viscosities of 200-2000P (Poise) at low rates of strain, reducing to 1-10P at high rates of strain (viscosity of water= 0.01P) [9].

The most important method for transport of mucus towards the pharynx, together with any trapped particles, is thought to be ciliary propulsion. As previously mentioned, cilia act in the periciliary (serous) fluid, a layer of low-viscosity fluid underlying the mucus layer. The periciliary layer acts as a lubricant allowing mucus transport and preventing dehydration in the absence of mucus, for example in the peripheral airways and alveoli [13, 16]. A reduction in periciliary fluid makes cilia beating more difficult and depletes the lubricant function, and both these effects inhibit mucociliary transport [16]. Ciliated cells form the majority of the epithelium in the trachea, principal

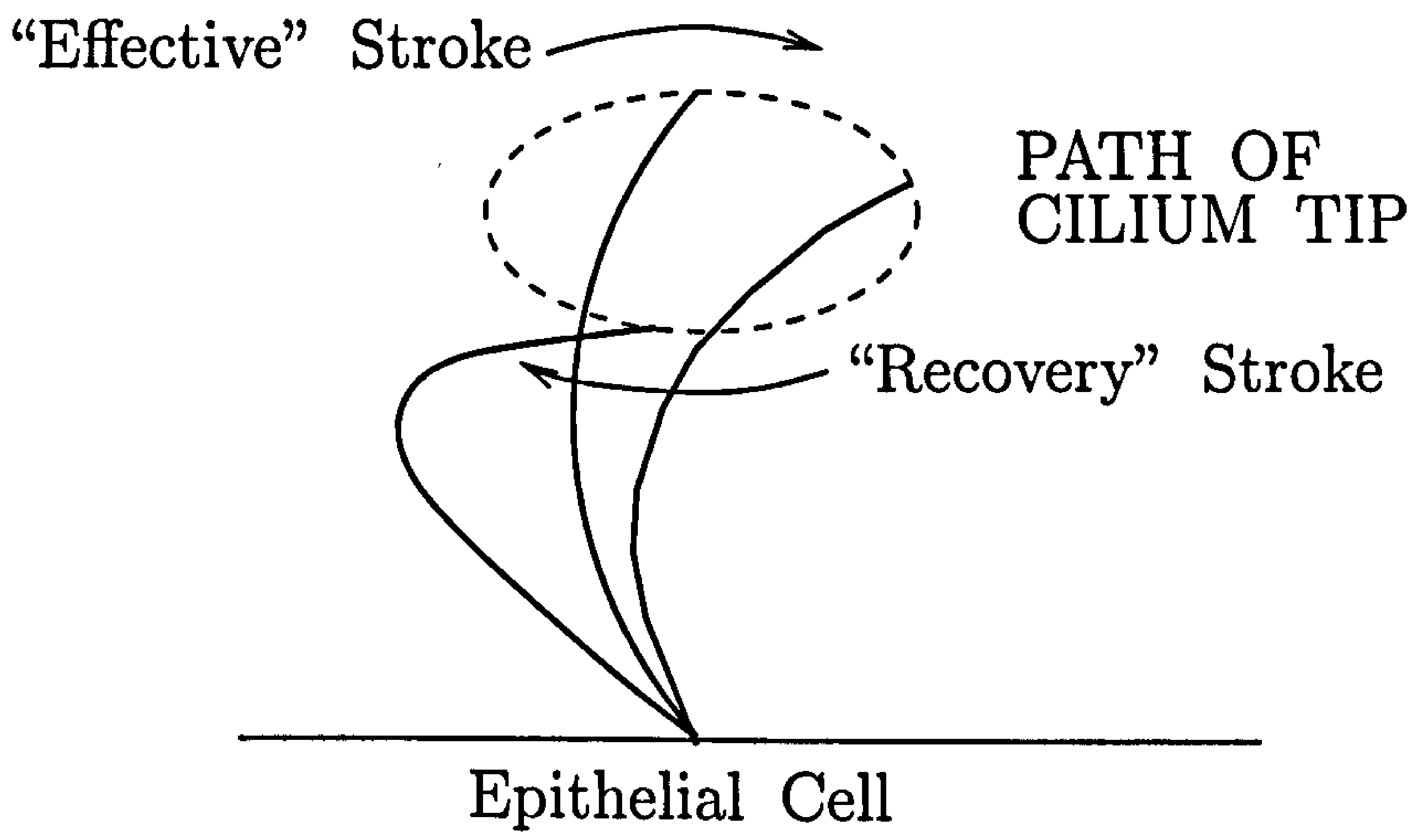

Figure 1.2: Idealised sketch of a cilium beat (from [17]). This diagram illustrates the side-view only.

bronchus and the bronchi. The length of cilia is thought to be 5-8μm (being longest in the larger airways) with a diameter of 0.2-0.3μm and spacing of approximately 0.3μm [15]. During the propulsive phase of the ciliary beat the cilium is fully extended, allowing the tip to penetrate the mucus; its motion is nearly planar in a plane perpendicular to the cell surface. In the preparatory or "recovery" phase, a bend is propagated along the cilium from base to tip so that it swings backward and to the right (relative to propulsive stroke) near to the cell surface to reach the starting position. Most mucus-propelling cilia have a rest period at the end of each propulsive stroke. During the preparatory and rest periods the cilium remains totally within the periciliary fluid and the cilium tip traces out an elliptical orbit (see Figure 1.2) [12, 17].

The movement stimulates surrounding cilia so that groups of cilia produce coordinated waves of activity [13, 18]. The ciliary beat frequency depends on the viscosity of the mucus and periciliary fluid but is thought to be about 15Hz [10, 13]. The serous layer depth has to be maintained within fairly narrow limits to allow cilia to function effectively [13]. During the non-propulsive phases the cilia provide negligible opposition to mucus flow [13]. Due to cohesion within the layer, the mucus sheet can travel at near to 'cilium tip speed'. Many estimates for the mucus velocity have been obtained by a variety of methods with the average being $\approx$ 5mm/min in the upper airways [9, 10, 11, 15, 18]. The rate of transport increases from the smaller airways to the larynx. As the viscosity of the mucus increases, or the elasticity decreases, the transport rate is reduced [14]. The periciliary fluid itself moves back and forward with the cilia so it is suggested that the net movement of the fluid is smaller than that of mucus, possibly non-existent [13]. Mathematical modelling suggests that the lower part of the serous layer at least has minimal net flow although the layer immediately below the mucus must flow at the same speed [12]. However, experiments by Knowles & Boucher [16] and Matsui *et al.* [19] suggest that the two layers move at essentially the same velocity and there is an important coupling between the layers. It is claimed that the periciliary layer is moved by frictional interaction with the mucus rather than by the cilia. In addition, they propose that the ciliary mixing of the periciliary layer may promote transfer of momentum from the mucus to the serous layer. Coupling between the sol and gel layers is an issue that we address in detail in Chapter 5.

Blake [15] considers not only the flow and shear rates of mucus due to ciliary propulsion, but also due to gravity and the stress generated by air reversal during breathing. The effects of both gravity and airflow depend on the depth and viscosity of the serous layer. Gravity becomes important if the depth increases significantly (preventing ciliary propulsion) or the viscosity (of the serous layer) decreases to near that of water. It is known that gravity can be important in diseases generating excess mucus *e.g.* asthma, cystic fibrosis, chronic bronchitis; however an increase in the serous layer depth has more effect on gravity's relevance to the flow rate. Blake claims that normal breathing may create a large enough stress to have a comparable effect to other mechanisms on mucus clearance. Airflow stresses cannot be neglected in cases of hypersecretion, *e.g.* in diseased lungs, or during high-frequency ventilation, especially in the trachea and the first few generations of the lung. Airflow patterns in the deeper lung become more complicated due to bifurcations and airway curvature as well as the unsteadiness of the flow [20]. In the extreme case of coughing, very high shear forces are created which can dislodge mucus [9, 21].

Blake [15] models the airway liquid lining as two Newtonian fluid layers of differing viscosities. However, King *et al.* [22] model the mucus layer as a viscoelastic fluid, where the effect of air motion is incorporated by prescribing the shear stress at the mucus/air interface. They model the serous layer as two sublayers with the cilia penetrating into the upper layer but not the mucus. The upper layer is propelled by the cilia, the lower has no net flow. Ross & Corrsin [17] model mucociliary pumping by representing the cilia as a constant, impermeable wall undergoing a travelling-wave motion representing ciliary beating. They assume a viscoelastic upper layer (mucus) and a viscous lower (serous) layer. They find that the mucus behaves like an elastic slab. Moderate changes in mucus viscosity seem to have little effect on mucus transport rate; however as the viscosity of the serous layer increases, or its depth decreases, the mucus transport rate decreases. They also claim that gravitational and inertial effects are negligible for "normal" cases.

The movement of cilia and mucociliary transport has also been modelled using slender body theory. Blake [20] models the ciliated airway as an infinite array of long slender bodies moving with a prescribed beat pattern. Again the fluid layers are modelled as Newtonian fluids with different viscosities. The effect on the velocity of the periciliary layer and the rate of mucus transport is calculated by finding the mean of the contributions of individual cilia. Blake [20] finds that there is little flow in the periciliary layer except close to the mucus/serous interface where shear rates are high, causing the observed high mucus flow rates.

Liron & Mochon [23] also use a 'discrete-cilia' approach. They derive a model from which time-dependent velocity profiles can be obtained and can also calculate instantaneous interaction of the cilia with the fluid. They find the velocity above the cilia sublayer is independent of time and is uniform; close to the base of the cilia variations in fluid velocity are large.

1.3 Surface Tension and Surfactants

Surface tension effects in the lung are very important in both controlling the distribution of liquid within compliant airways and promoting the 'protective' function of particle clearance (see §1.4). Here we look at the general properties of surface tension and surfactants.

The surface tension, γ, at an interface between two fluids, is the force per unit length across any line drawn on the interface acting normal to the line and tangential to the interface. The origin of surface tension is in the intermolecular cohesive forces between fluid molecules. The molecules of a liquid are subject to attractive forces from their neighbours. Molecules that are near a boundary with a gas lack this attraction on one side and are under an unbalanced force, directed away from the interface. All liquid molecules near the interface have a tendency to move inwards and this is equivalent to a tendency for the interface to contract [24]. Surface tension therefore acts to reduce the surface area of an interface.

The Young-Laplace equation relates the curvature, κ, of a liquid/gas interface to the pressure difference, Δp, across the surface. It can be written

$$\Delta p = \pm\gamma\kappa, \tag{1.1}$$

where the sign depends on the orientation of the interface [25].

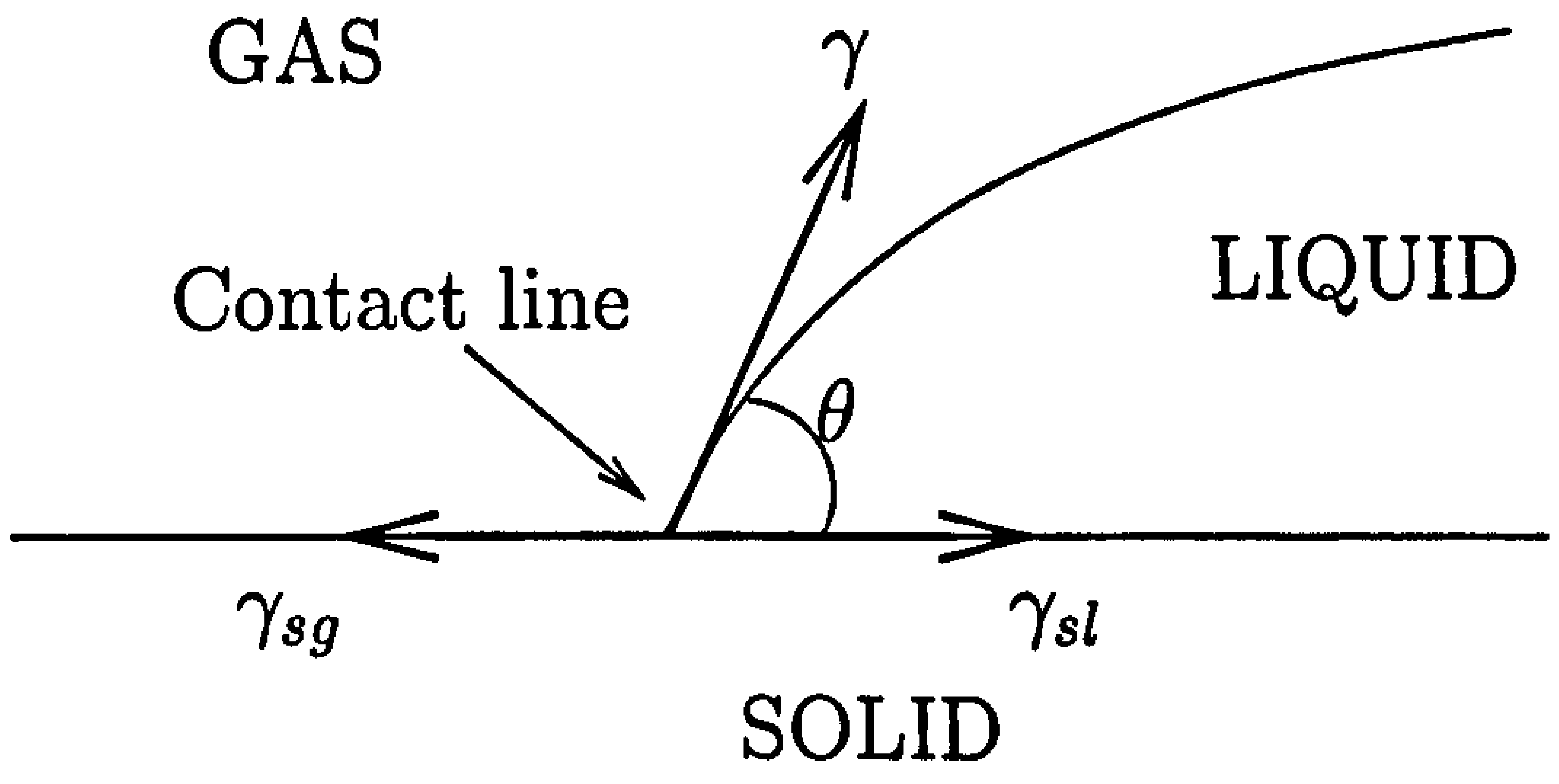

Figure 1.3: Static equilibrium of a liquid drop on a solid surface.

When a liquid drop is placed on a solid surface it may assume an equilibrium configuration with a specific static contact angle, θ, with the solid (see Figure 1.3). This contact angle is related to the surface tensions of the interfaces by Young's equation as follows. The horizontal force component associated with the liquid-gas surface tension γ has magnitude $\gamma \cos\theta$. For static equilibrium this is balanced by the remaining forces acting at the contact line. It is assumed that the surface forces can be represented by the surface tensions associated with the solid-gas and solid-liquid interfaces that act along the surface, γ_{sg} and γ_{sl} respectively. Therefore a force balance gives $\gamma \cos\theta = \gamma_{sg} - \gamma_{sl}$ [25].

Wetting is the term commonly applied to the displacement of air from a liquid or solid surface by another liquid. In the case of a liquid wetting a solid, the extent of wetting depends on the contact angle θ. If the contact angle is zero then the solid is said to be completely wetted by the liquid. If $\gamma_{sg} - \gamma_{sl} > \gamma$ the drop spreads until it is molecularly thin.

A liquid layer lining a tube can undergo a surface-tension-driven (Rayleigh) instability, commonly seen in jet breakup. Suppose we consider a small perturbation to the interface, and neglect axial curvature. In regions where the fluid thickness increases the increase in azimuthal curvature results in a local reduction in fluid pressure (see (1.1)). An increase in the axial curvature of the interface, however, leads to an increase in the local fluid pressure. If the net fluid pressure falls (which is the case for long-wave disturbances), fluid flows into these regions due to the pressure gradient, increasing the perturbation. Thus the interface becomes unstable. If there is sufficient fluid these perturbations can grow to form bridges across the tube. Therefore the azimuthal curvature has a destabilising effect on the perturbations of the interface whereas the axial curvature is stabilising. Hammond [26] investigated the surface tension-driven flow of a thin annular film of viscous fluid surrounding another within a circular cylindrical pipe. He used lubrication theory to derive and solve a nonlinear evolution equation for the interfacial disturbances and found that small axisymmetric disturbances of the interface can grow and cause the film to break up into isolated annular collars. Gauglitz & Radke [27] modified this analysis to be valid for thicker films, the ones most likely to form bridges.

The surface tension at an interface is affected by the presence of surfactants. Typical aqueous surfactants are organic compounds with a hydrophobic tail and a hydrophilic head. When these come into contact with a clean liquid-air interface they form a monolayer at the surface, with the hydrophilic heads reducing the net inward attraction on liquid molecules near the interface. Surfactant therefore lowers the surface tension of the interface [25]. There is a critical concentration of surfactant after which any additional surfactant molecules cluster to form micelles in the bulk liquid and have no further effect on surface tension. At surfactant concentrations below the critical micelle concentration, the interfacial surface tension is a decreasing function of the surface concentration of surfactant. Therefore a nonuniform distribution of surfactant on a clean liquid-air interface generates gradients in surface tension. These gradients drive a flow from regions of low tension to regions of high tension causing the surfactant to spread to areas of low concentration. These surface tension-driven flows are known as Marangoni flows (see *e.g.* [28, 29, 30]).

Since the presence of surfactant lowers the surface tension and reduces the contact angle, another effect of surfactant is to promote wetting [25, 31]. Surfactant adsorption can also alter the mobility of the interface. Lower surface tensions develop in regions where the surface flow converges and surfactant accumulates. A Marangoni flow then develops towards the regions of higher surface tension retarding the surface flow and immobilising the interface [32]. Thus surfactants can hinder the Rayleigh instability of a liquid-lined tube.

We now consider how surface tension and surfactants influence lung mechanics and physiology.

1.4 Surface Tension Effects in the Lung

The air-liquid interface in the lung has a large surface area (approximately $140\mathrm{m}^2$) and very high curvature (since alveoli are approximately $300\mu\mathrm{m}$ in diameter). Therefore surface tension effects are very significant (see the Young-Laplace equation (1.1)). For example, surface tension contributes to lung compliance (the volume change per unit pressure change). If the surface tension of the air-liquid interface in the lungs is high, the lungs are stiffer and more difficult to inflate [33]. Surface tension also controls the distribution and balance of the liquid lining in the lung, for example causing the formation of the fluid pools in the alveolar corners. Furthermore if the surface tension is high and the fluid pressure of the airway lining is less than that of the surrounding interstitial fluid, this can lead to oedema, where fluid floods the airway.

Another effect of surface tension in the lung which has received a lot of attention is that of airway closure (see [10] and references therein). Airway closure occurs when the liquid lining of an airway undergoes a Rayleigh instability, causing the formation of liquid bridges provided there is sufficient fluid available. These liquid bridges can close off small airways, most often at the end of expiration where airways diameters are small. Since airways are deformable they can also buckle and collapse due to the reduced fluid pressure if the surface tension of the interface is high enough, this is known as compliant collapse [34]. Halpern & Grotberg [34] extended the analysis of Hammond [26] and Gauglitz & Radke [27] to consider a thin film coating the inside of an elastic tube. They found a critical film thickness, ϵ_c, which depends on the properties of the fluid and the wall, above which unstable disturbances grow and liquid bridges are formed. This critical thickness decreases with increasing surface tension or wall compliance. Airway closure is more rapid with increasing film thickness, surface tension and wall flexibility.

On inhalation airways can reopen as airways expand [35]. The reopening of closed airways has been modelled by considering the motion of a semi-infinite bubble blown into a fluid-filled elastic-walled channel [36, 37]. The channel walls are modelled as membranes under longitudinal tension and supported by external springs. The bubble pressure must exceed a critical value to allow the bubble front to propagate steadily and reopen the collapsed airway. The opening of airways occluded by liquid bridges is likely to be abrupt as the bridge ruptures and the walls snap open. These ruptures may cause the crackling noises in the lung heard using a stethoscope [10].

Lung surfactant is manufactured by Type II alveolar epithelial cells and spreads throughout the lung via Marangoni flows. The presence of surfactant in the lungs is very important as it decreases the surface tension of the air-liquid interface, thereby increasing lung compliance, preventing oedema and reducing the risk of airway closure.

Otis *et al.* [38] consider a computational model of airway closure by liquid bridging during expiration. They include both surfactant effects and the effects of a reduction in tube dimensions with time, as would occur on expiration.

They find that the presence of surfactant has two effects: firstly, to reduce the overall surface tension as the lung volume decreases leading to a lower lung volume at which bridging occurs; secondly, axial variations in surfactant concentration cause surface tension gradients that stabilise perturbations of the liquid layer, therefore again retarding, possibly eliminating, bridging. In addition the overall reduction in surface tension reduces the negative pressure in the fluid and may therefore prevent airway compliant collapse. Halpern & Grotberg [39] similarly investigated the effect of surfactant on airway closure. They found the presence of surfactant increases ϵ_c by as much as 60% and closure time can be five times larger.

Pulmonary surfactant is formed late in foetal development and so premature babies are often born with a deficiency of surfactant. This can cause respiratory distress syndrome. This is usually treated by surfactant replacement therapy (SRT) where surfactant is artificially delivered to reduce the high surface tension in the lungs.

Surface tension and surfactant have another important effect in the lungs, on the fate of inhaled particles. In the next section, we consider what happens to particles after inhalation.

1.5 Particle Deposition and Retention

Many inhaled particles become trapped in the airway liquid lining (see Figure 1.4). Some of these particles are toxic, *e.g.* smoke, bacteria etc., but also an increasing number of drugs are delivered by aerosol. Therefore the fate of these particles after deposition is important for predicting their therapeutic or pathogenic potential. To understand the effect these particles can have on health we need to consider mechanisms of particle deposition, retention and, in particular, clearance from the lungs [2].

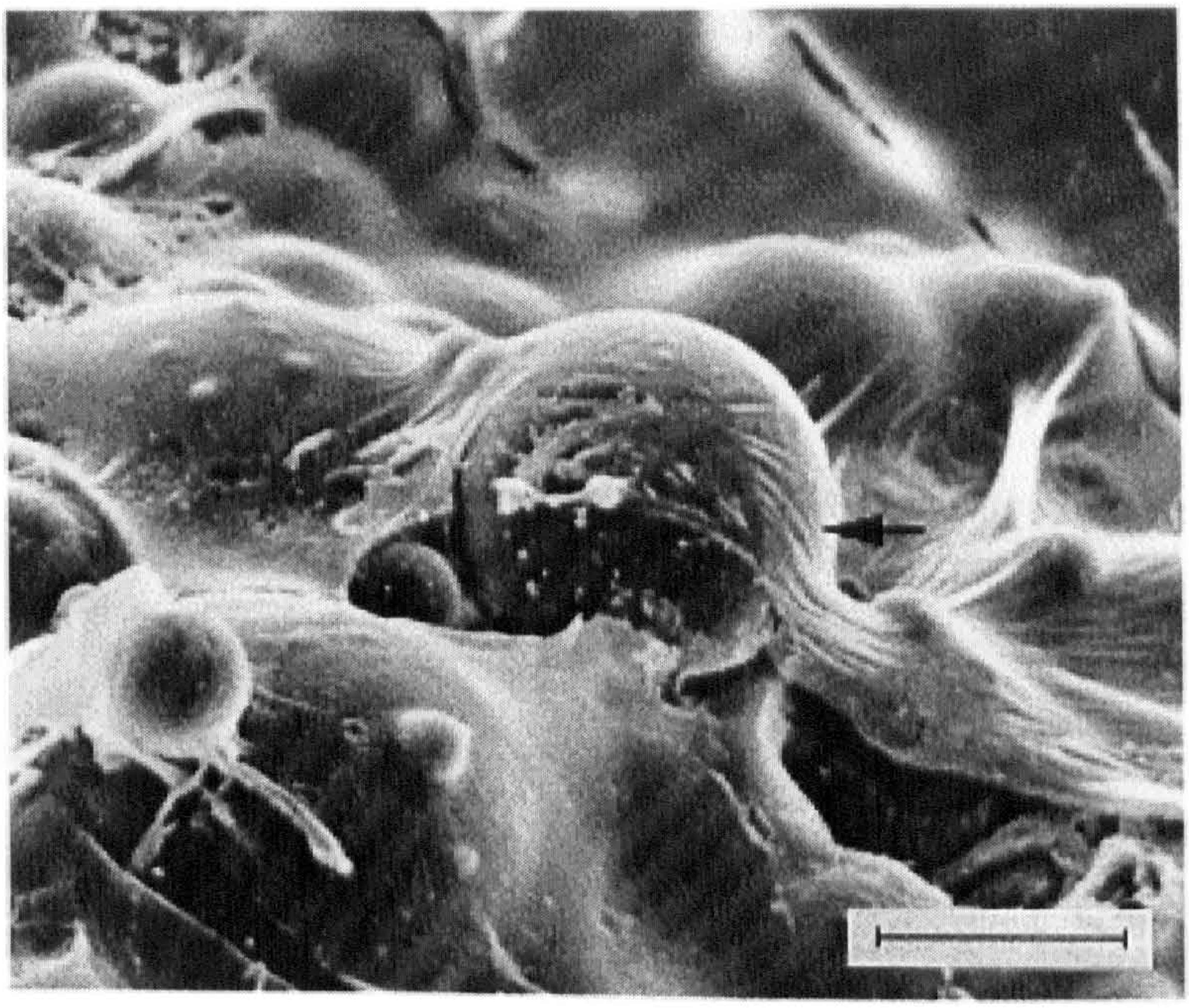

Figure 1.4: Electron micrograph of particles in the mucus layer in a guinea pig trachea, from [2]. Bar=20μm.

There are three main methods of particle deposition. The first is inertial impaction. This occurs when particles are being carried in an airstream and the airstream suddenly changes direction, for example at a bifurcation or in the nose and mouth. The particles' momentum can cause them to continue in their original direction for a short time and deposit on the airway wall. Particles can also be deposited by gravitational settlement. Both these methods depend on the size and density of the particle. The third method of deposition is by diffusion. Particles are bombarded by gas molecules in the inhaled air. They acquire a random (Brownian) motion and can therefore deposit on the airway walls. In general the largest particles are deposited by inertial impaction in the nose, mouth and upper airways. The very smallest particles, which have a high coefficient of diffusion, are also filtered out in the upper airways. Particles between these extremes are able to penetrate to the periphery of the lung. The size of particles that deposit in the alveoli is between 1 and 5 μm, with the majority having a size between 2 and 3 μm. Particles of approximately 0.5μm penetrate to the alveoli during inhalation but remain airborne and are carried out of the lungs on exhalation [40].

Thompson [41] discusses the possibilities of targeting drug delivery to specific regions of the lung, increasing the efficiency and effectiveness of the drug. Current asthma drug delivery, for example, is not very efficient in depositing medication specifically in the peripheral airways of the lung where it is required [41]. Factors such as lung morphology, ventilatory parameters, and the characteristics of the inhaled particles can influence deposition sites and therefore it may be that airborne pharmaceuticals can be selectively targeted to prescribed regions [42].

Deposited particles are retained in the fluid lining by surface forces acting at the air-liquid interface (see §1.3). These forces determine the extent of the particles' displacement towards the epithelium and hence whether they come into contact with the epithelial cells or cells of the defence system such as macrophages, which inhabit the fluid lining [43, 44]. Schürch *et al.* provide evidence, using light microscopy, that surface forces can displace particles through the fluid lining to such an extent that the underlying epithelial cells become indented, which may inhibit particle clearance (see Figure 1.5). It has been found that the presence of a surfactant film promotes the displacement of deposited particles towards the epithelium [2, 6, 45] and Schürch *et al.* claim that the increased displacement of the particles is due to the reduction in surface tension of the interface resulting from the presence of surfactant [2, 45]. However, it is likely that the presence of surfactant also plays an important role in promoting wetting of the particles. In addition smaller particles are wetted to a greater extent than larger ones regardless of the thickness of the fluid layer [6, 45]. It has been postulated that this dependence on particle size

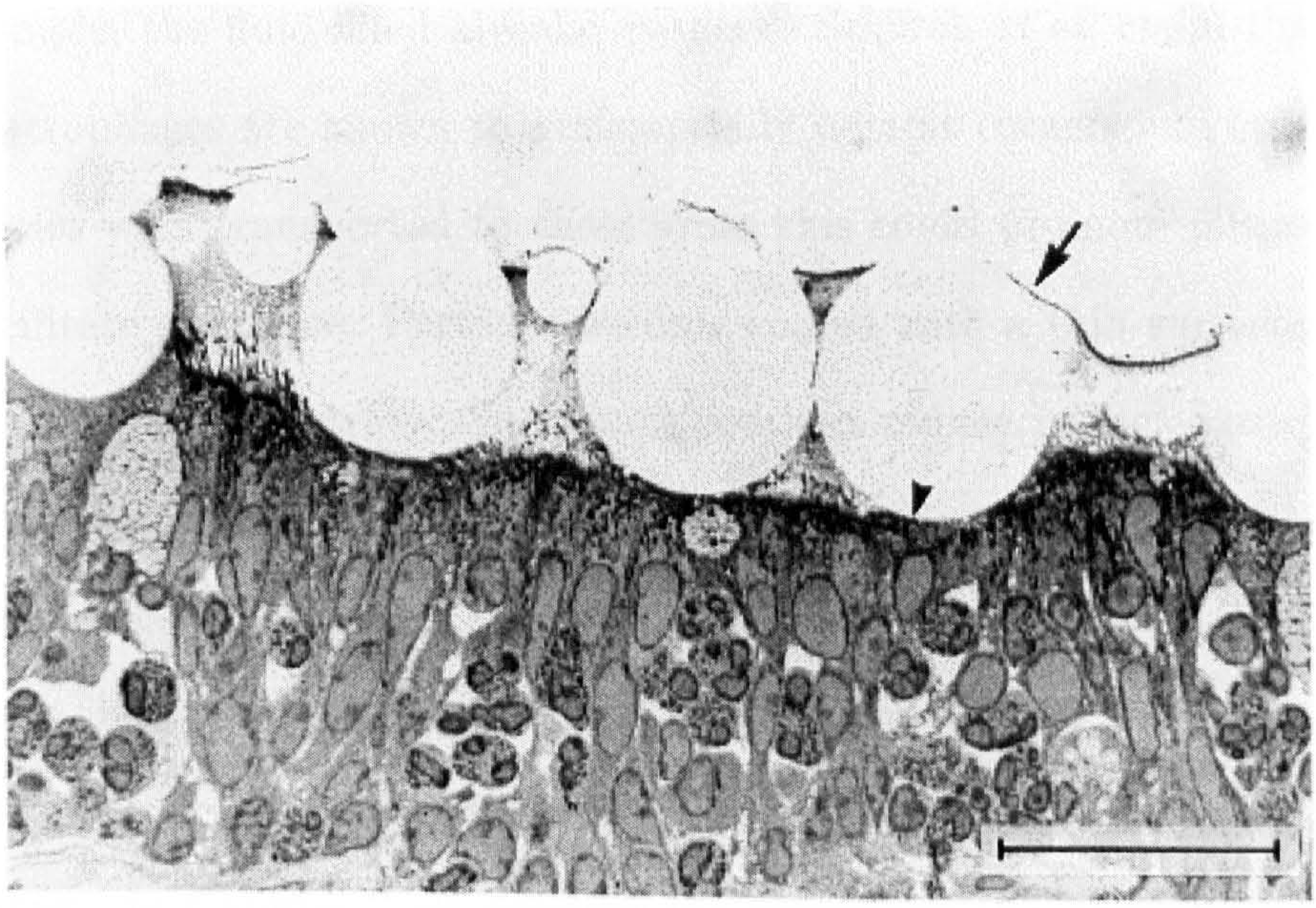

Figure 1.5: Displaced particles indenting epithelial cells as a result of surface forces, from [2]. Bar=30μm

may be a result of line tension [6].

Particles deposited in the conducting airways can be cleared rapidly from the lungs by the mucociliary escalator. A particle that lands in the mucus layer is swept along with the mucus as it is pushed towards the mouth by the cilia, and is then removed by coughing or swallowing. Particles are generally cleared by this mechanism within 24 hours. In the gas-exchange region, clearance may take months and is due to phagocytosis by free cells, such as macrophages [2, 43, 44, 6]. Owing to their prolonged retention time, inhaled particles that have deposited in the small airways and alveoli may have a greater effect on health. Schürch *et al.* [45] claim that, if particles do not remain floating in the surfactant film, they cannot be transported into the conducting airways by Marangoni flows. They suggest that particles deposited in alveoli will instead be moved by capillary action or pressure gradients in the serous layer towards places with greater amounts of the subphase material, for example, the fluid-filled alveolar corners. Schürch *et al.* claim that alveolar macrophages are known to preferentially inhabit corners and crevices so if particles were transported to these areas this could promote phagocytosis and facilitate clearance. Particles become coated with a thin surfactant film as they enter the substrate. Surfactant coatings reduce particle toxicity and promote phagocytosis by opsonization, where proteins in the film "label" the particle for destruction [45, 7].

In this thesis, motivated by these observations [2, 6, 45, 7], we examine three key features of particle dynamics in the lung using mathematical modelling techniques. In Chapter 2 we consider the behaviour of a partially immersed particle in a liquid pool in an alveolar corner. In Chapters 3 and 4 we consider the perpendicular and transverse motion of a particle close to a deformable airway wall. In Chapter 5 we consider the motion of a particle trapped in a cilia-propelled mucus sheet. In §1.6–§1.8 we review existing models related to these problems.

1.6 Particle interactions at interfaces

There is an extensive literature on the interactions between particles and fluid interfaces. In this section we begin by reviewing the static equilibrium shapes of fluid interfaces in relation to cylinders, spheres and plane walls. We then review studies of interactions of particles both floating at horizontal fluid interfaces and confined in thin liquid films.

The effect of surface tension on fluid interfaces is well known: many of the classical problems and solutions are reviewed by Princen [46]. The shapes of interfaces with one finite radius of curvature (*i.e.* cylindrical interfaces) are relatively simple as Laplace's equation (1.1) can be integrated analytically. Examples of this include the formation of a meniscus against a plane wall or

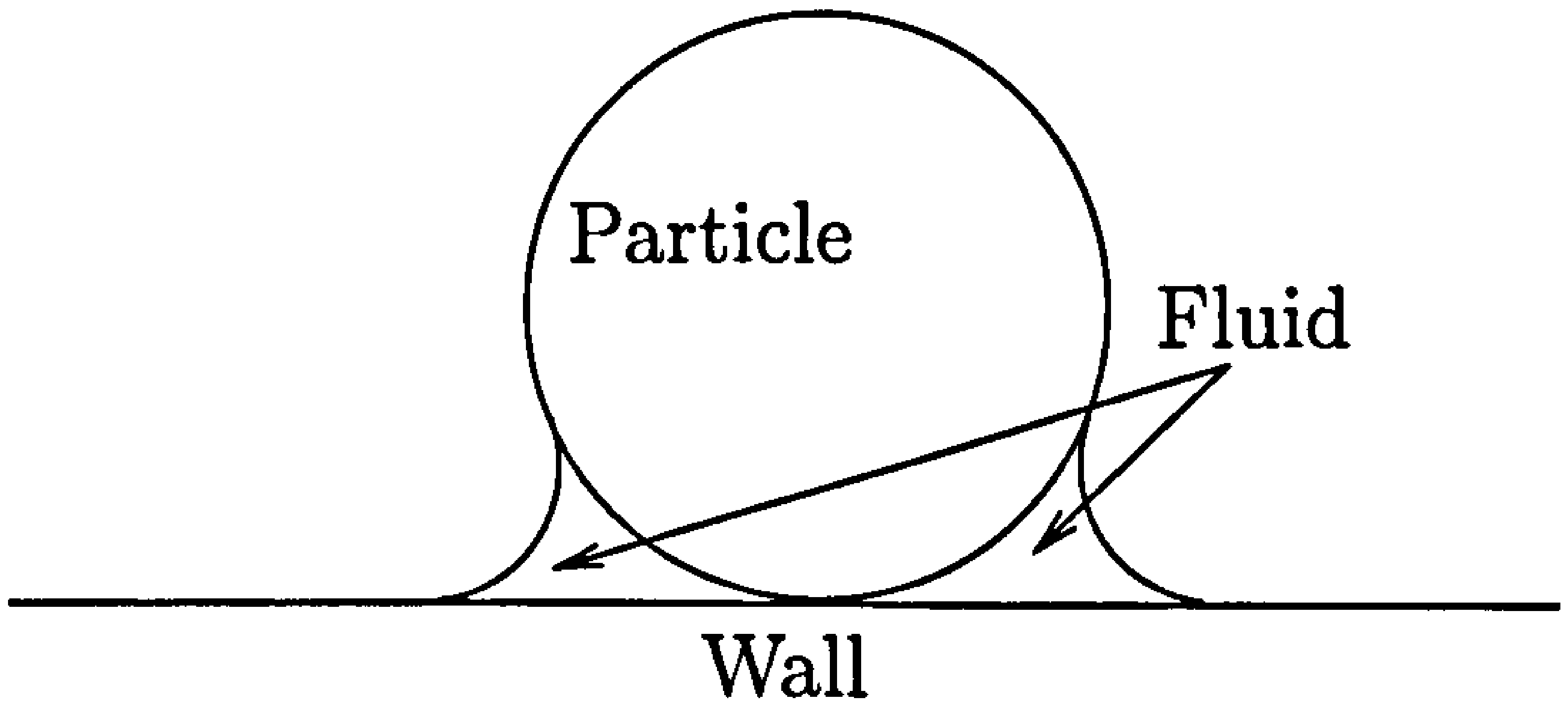

Figure 1.6: Sketch of a solid particle in contact with a solid wall, showing the presence of fluid at the contact point.

between two vertical plane walls. Princen also considers interfaces with axial symmetry such as the capillary rise of liquid observed in a thin tube.

Princen considers the capillary forces between solid particles and solid interfaces where a small quantity of liquid is present at the point or area of contact (see Figure 1.6). For the case of a cylinder or a sphere in contact with a flat plate, the presence of the liquid increases the existing downwards force on the particle due, say, to gravitational effects. The increase in force is due to surface tension acting at the contact points and the negative pressure in the trapped fluid. As the amount of fluid decreases the adhesive force increases; in the cylindrical case the force tends to infinity, in the spherical case the force tends to a finite limiting value.

Princen [46] considers solid particles floating at horizontal fluid interfaces. A particle will either take up an equilibrium position at the interface or sink, depending on the size of the particle, the densities of the particle and the fluid, the interfacial tension and the contact angle at the fluid/air/solid boundary. Rapacchietta *et al.* [47] study the position of cylindrical and spherical particles at fluid interfaces using a thermodynamic approach which is shown to agree with the free-body force analysis.

It is well known that similar floating particles experience an attractive force and will cluster together. Allain & Cloitre [48] perform a force analysis of the capillary interaction between two horizontal cylinders at a liquid/air interface. These capillary forces can create an attractive force between the cylinders causing the formation of aggregates. The lateral capillary forces that create this particle motion are caused by deformations to the otherwise flat surface due to the presence of particles at the interface. In the case of similar floating particles the meniscus deforms in such a way that the gravitational potential energy of the two particles decreases as they approach each other and hence the origin of the force is the weight and buoyancy of the particle. Kralchevsky & Nagayama [49] extend this to non-floating particles motivated by the finding that small particles (where the weight is too small to have an effect on the interface) which are trapped in liquid films also attract and form clusters. In this case the origin of the force between the particles is driven by the wetting properties of the particle, such as the contact angle. In these two cases, which we denote ‘flotation’ and ‘immersion’ respectively, the force has similar dependency on separation distance but very different dependencies on particle radius and surface tension.

Figure 1.7 shows the origin of the force between two particles partially immersed in a liquid film. There is a net force acting on each particle due to surface tension, σ, acting at the contact lines, L_1, L_2, and the pressure distribution in the liquid and in the air. If the contact lines were horizontal the force distributions would be symmetrical and there would be no net capillary force. However the deformations to the interface, created by the presence of the particles, overlap and cause the contact lines to be slightly inclined, resulting in a non-zero net transverse force.

In both flotation and immersion cases, the capillary force can be either attractive or repulsive. There is an attractive force between two similar particles in both flotation and immersion cases (see Figure 1.8(a),(b)). There is a

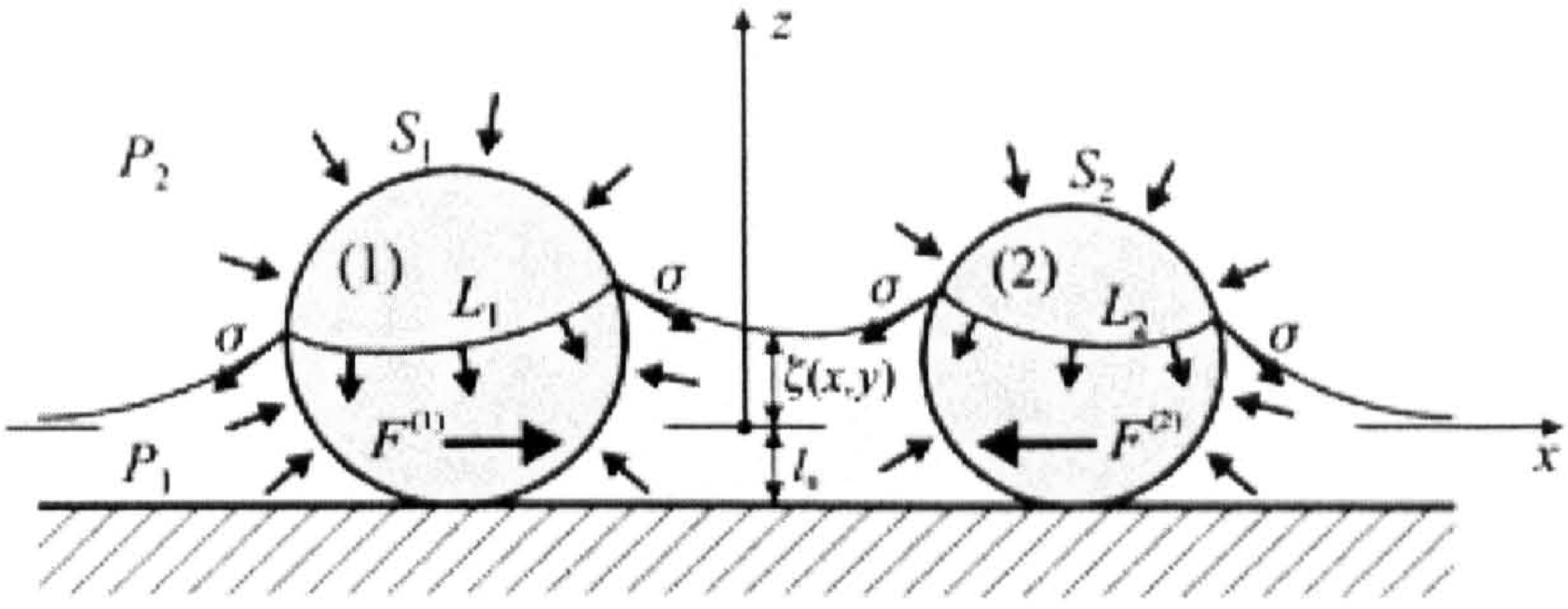

Figure 1.7: Origin of the capillary force between two particles partially immersed in a liquid film, from [49].

repulsion force between a heavy and a light particle in the flotation case, and between a hydrophilic and a hydrophobic particle in the immersion case (see Figure 1.8(c),(d)). Forces between floating particles can disappear when they become small (radii $< 5\mu$m) as the particle's weight is negligible. However, since deformations for the immersion case are due to wetting properties, a net lateral force can exist even for very small particles (see Figure 1.8(e),(f)).

Kralchevsky & Nagayama [49] use these interactions to predict the capillary force between a floating particle and a nearby vertical planar wall, where the contact angle at the wall is 90°. The shape of the meniscus would be the same if the wall, situated at a distance s from the particle, was replaced by an identical (with regards to size, weight, wetting properties) particle at a distance $2s$. Two such particles will always attract each other, so therefore the lateral capillary force will attract the floating particle to the wall.

In Chapter 2 we combine some of these ideas to consider the capillary force on a particle and its resulting motion in a liquid-lined, rigid-walled wedge.

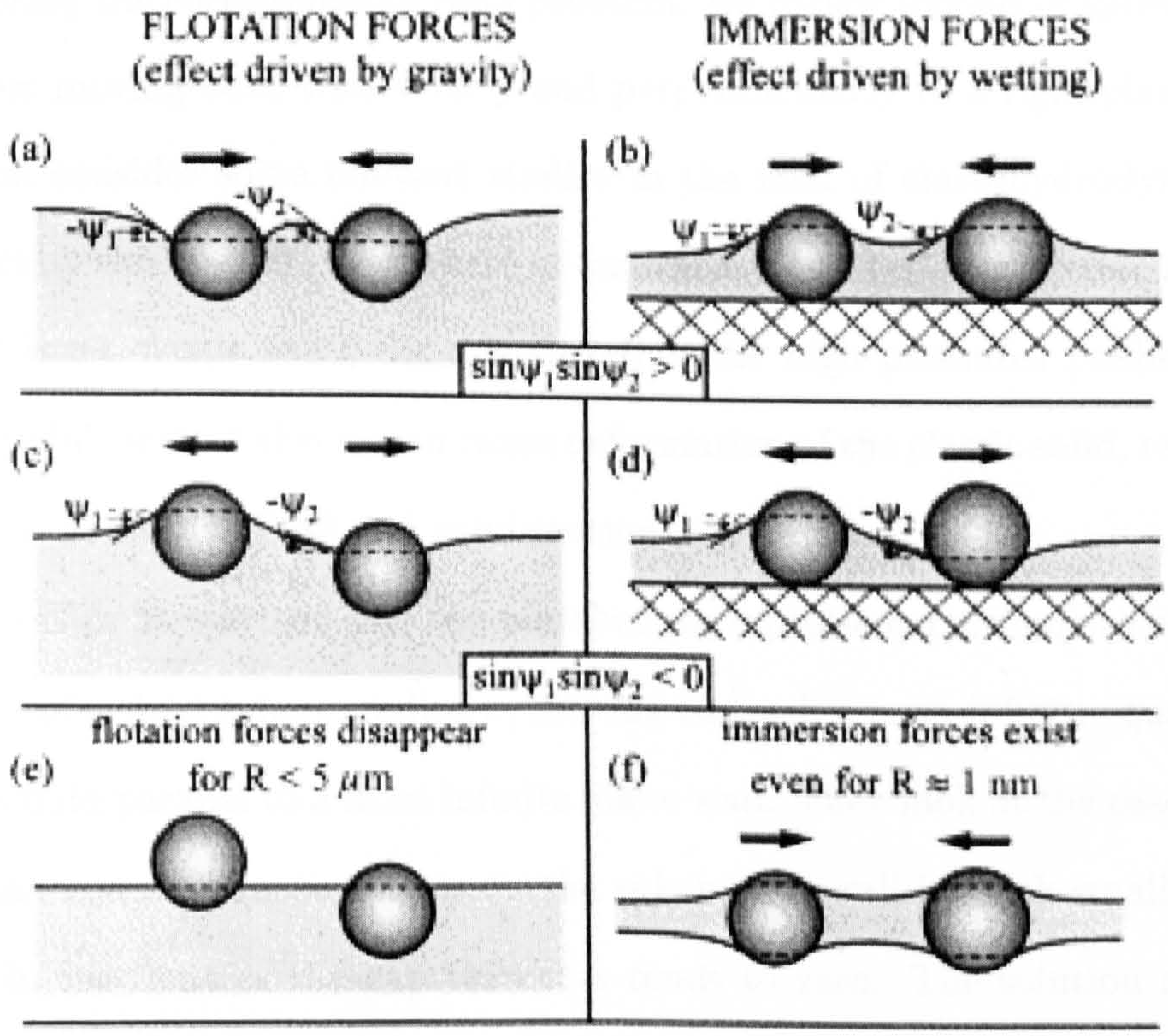

Figure 1.8: (a) attraction between two similar floating particles; (b) attraction between two similar particles in a liquid film; (c) repulsion between a light and a heavy floating particle; (d) repulsion between a hydrophilic and a hydrophobic particle in a liquid film; (e) no interaction between small floating particles; (f) interaction between small particles confined in a liquid film, from [49].

1.7 Particles in proximity to deformable interfaces

In Chapters 3 and 4 we consider the effects of the deformable airway wall on a particle moving in proximity to the wall. In this section we begin by considering the corresponding rigid problem: we review models of spheres and cylinders moving both transversely and perpendicularly to a rigid plane wall. We then consider some relevant studies in the field of elastohydrodynamics. Specifically we consider cases where at least one of two surfaces in close relative motion is an elastic solid. In this situation the high pressures predicted by standard lubrication theory can cause deformation of the elastic solid, resulting in a model in which fluid and solid motions are coupled.

O'Neill & Stewartson [50] use matched asymptotic expansions to consider the case of a rigid sphere, radius a, moving through a semi-infinite, quiescent, viscous fluid parallel to a fixed infinite plane wall. They look at the case where the minimum clearance ϵa between the sphere and wall is much smaller than a, *i.e.* in the limit as the gap thickness tends to zero. The solution requires matching an 'inner' solution, where velocity gradients are large and lubrication theory can be applied, to an 'outer' solution where it can be assumed that the sphere touches the wall. They find that the forces and torques acting on the sphere and plane take the form $\alpha_1 \log \epsilon + \alpha_2 + \alpha_3 \epsilon \log \epsilon + O(\epsilon)$ where α_i are known constants.

Goldman *et al.* [51] solve this problem independently deriving asymptotic solutions of the Stokes equations and their results for the hydrodynamic forces and torques acting on the sphere and the wall agree with [50]. In addition they combine the translational and rotational results to consider a sphere rolling down an inclined plane. They show that the sphere will effectively 'slip' as it rolls and that it cannot be in actual physical contact with the wall. In practice, however, surface roughness may have a major effect on particle motion.

In a subsequent paper Goldman *et al.* [52] consider a neutrally buoyant sphere moving parallel to a plane wall under the influence of a simple shear flow. Using bipolar coordinates they derive an exact solution of Stokes' equations for the translational and rotational sphere velocities, valid for all ratios of sphere radius to distance from wall. They consider two asymptotic solutions: the sphere very close to the wall, using lubrication theory; the sphere far from the wall, using a 'method-of-reflections' approximation.

We also consider the related problem of the steady motion of a solid sphere perpendicular to a fixed plane wall bounded by a semi-infinite viscous fluid. Brenner [53] uses bipolar coordinates to find exact solutions in two cases: (*i*) the plane is rigid and the fluid does not slip over the surface; and (*ii*) the plane is a free surface where tangential stresses vanish (neglecting deformation of the plane). Cox & Brenner [54] extend this analysis in the limit where the gap thickness tends to zero. Using singular perturbation techniques they expand the exact bipolar coordinate expression for the force on the sphere found by Brenner [53]. They also develop a perturbation solution of the governing equations, with the inclusion of inertial effects, for general axisymmetric particles in the limit of small gap widths.

Jeffrey & Onishi [55] consider the case of an infinite cylinder translating parallel to a plane wall at zero Reynolds number. They find that the torque on a purely translating cylinder is zero, and similarly for a non-translating rotating particle the force is zero, which is surprising when compared with the spherical case where the force and torque are both non-zero. A simplified explanation for this is illustrated in Figure 1.9. Suppose a cylinder is moving parallel to a plane wall in the positive x direction. A clockwise torque is created on the cylinder due to the flow through the gap. However, as the gap is small, fluid will be drawn away from the gap both in front of and behind

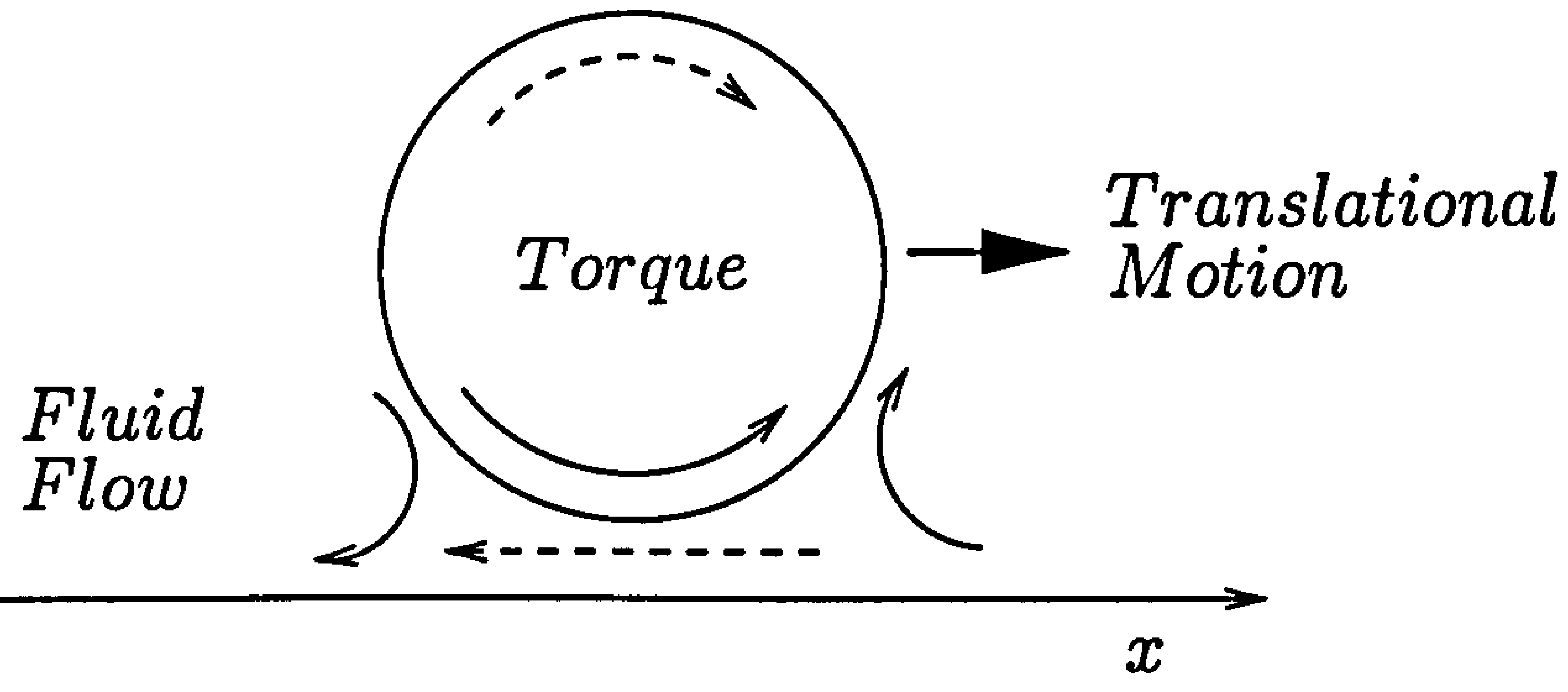

Figure 1.9: Sketch of the torque balance on a cylinder translating close to a plane wall. Arrows show the directions of fluid flow and corresponding resultant torques.

the cylinder creating an anticlockwise torque. For cylinders, the two torques balance exactly.

We now review some studies of elastohydrodynamic lubrication theory where we have a coupling between fluid dynamics and elastic solid mechanics, as will occur in our model of a rigid particle close to an elastic wall. Initially we discuss a paper by Lighthill [56] modelling rigid pellets in elastic tubes. We then consider deformable roll-coating problems where the stress distribution in lubricating fluids causes the roll covers to deform. We also examine the collision of elastic spheres in a viscous fluid, which has a similar coupling between the pressure distribution and the surface deformation, although, in this case, the surfaces move perpendicularly to each other.

Lighthill [56] models the motion of tightly fitting deformable pellets being forced along viscous-fluid-filled elastic tubes by pressure gradients. This model was motivated by the movement of red blood cells in narrow capillaries but has greater relevance to relatively stiff white blood cells in capillaries or to kidney stones lodged in the ureter. Elastic deformation occurs when the pellet radius is larger than the tube radius; when the pellet radius is smaller the tube may still be distended, depending on the thickness of the lubricating film and other material parameters. It is assumed that deformation varies linearly with local pressure. The problem becomes a differential equation dependent on a parameter L which is then solved numerically for particular values of L and asymptotically for large and small L. For large L, which corresponds to large deformations of the tube, Lighthill shows that the solution requires matching between six different asymptotic regions of behaviour. Lighthill also notices a 'necking' or narrowing of the gap (between the pellet and the tube) behind the pellet as it is forced along the tube. (There is a well-known error in [56]. In balancing the pressure difference in the tube with the viscous resistance to the pellet's motion, Lighthill neglects to include the effect of fluid pressure acting on the tilted surface of the pellet; see [56], equation (12)).

In industrial roll-coating problems, fluid is drawn into the narrow gap between two rotating rolls and fluid pressures can cause deformation of the compliant layers on the surface of each roll. This change to the gap geometry then alters the velocity and pressure fields. To describe this problem requires an elastohydrodynamic model which couples fluid dynamics with solid mechanics [57]. The thickness of the coated film emerging from the 'nip' between the cylinders depends on the balance between the hydrodynamic forces exerted by the fluid and the elastic forces arising from the deformation of the roll covers [58]. As the fluid leaves the nip the film splits, coating both rollers and forming a meniscus. Models of this behaviour generally apply the lubrication approximation in the gap and choose a suitable boundary condition for the film-split meniscus, such as the (empirical) Reynolds condition which sets pressure and pressure gradient to zero [59].

Coyle [60] develops a one-dimensional, elastohydrodynamic model of forward roll coating with deformable rolls. There are two approaches to the model: choosing to set the load or choosing to set the gap thickness between the rolls. This model uses a linearly elastic (Hookean) springs approximation for the elastic wall which assumes the local deformation to be directly proportional to the local fluid pressure. Coyle calculates the surface deformation, pressure distribution, fluid flow rate and the 'roll-separating' force in both the small and large deflection limits. The model is insensitive to the choice of downstream pressure boundary condition except in the small-deflection limit where the Reynolds condition seems to be more accurate than the submerged condition (where the rollers are submerged in an infinite fluid), although the Reynolds condition does not allow the pressure to be negative. The difference caused by the use of different boundary conditions decreases rapidly as roll deformation increases. Coyle sees a necking of the gap between the two rolls similar to that noted by Lighthill [56].

Carvalho & Scriven [57] confirm and extend Coyle's analysis to consider the difference between the 1D linearly elastic model and a 1D nonlinear elastic model which better describes the response of rubber to deformation. They also consider the roll deformation and pressure relation using a plane strain approximation which accounts for the Poisson ratio of rubber. This model takes the local displacement to be a function of the whole pressure distribution, not just the local pressure; they model the deformable layer as an elastic half-space. The flow rate predictions for the three models differ by less than 10%, suggesting that Coyle's 1D model, although simpler, actually predicts the overall behaviour reasonably well.

Gostling *et al.* [61] consider the more industrially relevant case of incompressible deformable layers and show that the 1D linear springs model cannot model the elastic deformation effectively in this case. Unlike Carvalho & Scriven [57], Gostling *et al.* consider the effect of finite layer thickness and suggest that layer thickness and elasticity may have similar effects on the fluid pressure and flow rate. Once again, constrictions in the gap thickness, similar to those found by Lighthill [56], also arise in these models of deformable roll coating.

Davis *et al.* [62] consider the elastohydrodynamic collision of two spheres, accounting for both elastic deformation and viscous fluid forces. A thin fluid layer between the spheres prevents direct contact, but depending on the speed of the sphere, a large pressure may build up in the gap and cause deformation. As one sphere moves towards the other through a very viscous fluid, its kinetic energy is dissipated in the fluid causing the particle's speed to decrease with its approach. Strong viscous dissipation leads to no deformation or rebound. At the other extreme, if there is negligible fluid resistance, most of the kinetic energy of the particle is converted to elastic strain energy as the contact area deforms and is restored as the particle rebounds. Davis *et al.* consider cases between these extremes and look at the conditions needed for rebound to occur. As in Carvalho & Scriven [57], the elastic deformation is modelled using a boundary integral coupled to lubrication theory. This requires integrating the surface-stress distribution multiplied by a suitable Green Function over the area of deformation.

The gap between the two surfaces may become as small as a few nanometres; in a subsequent paper Serayssol & Davis [63] consider the effect that interparticle surface forces may have on the collision and rebound process. Interparticle forces are weak compared to viscous forces so spheres initially behave as found in [62]. However, when the spheres come to rest at an equilibrium distance the interparticle forces may have an effect.

In many applications, surface roughness may have more of an effect on this type of particle motion than interparticle forces. Zhao *et al.* [64] consider the motion of a sphere down a rough plane in a viscous fluid. The translational velocity of the sphere decreases upon contact with an artificial 'asperity' on the plane whereas the rotational velocity generally increases.

Finally in this section, we consider some models where the interaction between the deformable ‘particle’ (or in this case, cell or drop) and a rigid wall is studied by modelling the particle as a membrane enclosing a fluid volume. Although these models are less directly relevant to our problem than the previous elastohydrodynamic models, it will be seen that we find draining and peeling behaviour similar to these results.

Hodges & Jensen [65] consider the problem of a two-dimensional cell interacting with a plane adhesive surface. The cell is modelled as an extensible membrane under tension containing fluid of a constant volume. Assuming rapid binding kinetics, they use lubrication theory to model the flow in the thin film between the particle and the wall. First they model sedimentation of the cell as adhesive forces pull the cell normally onto the wall. Initially a small segment is pulled rapidly onto the wall causing fluid to be displaced sideways and the centre of the membrane to be briefly lifted upwards. Subsequently the cell is pulled down and the bound region lengthens, trapping a thin layer of fluid between the particle and the wall. Some of this fluid then drains out slowly and the cell reaches an equilibrium state. Hodges & Jensen also consider the case of a bound cell being removed from the wall by a point force applied to the top of the cell; this situation is dominated by a quasi-steady peeling motion. The model is extended to consider a cell tank-treading over an adhesive wall in an external shear flow, spreading at the leading edge and peeling behind the particle. At low speeds the relation between rolling speed and shear rate is linear and independent of the viscosity of the surrounding fluid; at higher speeds it is nonlinear and viscosity-dependent.

Hodges *et al.* [66] also consider the similar problem of the steady sedimentation under gravity of a viscous drop along an inclined plane. The drop is suspended in a viscous liquid and is supported by a thin liquid film. They look for expressions for the shape, film thickness and drop speed as functions of three parameters: the angle of the plane to the horizontal, the viscosity ratio and the ratio of buoyancy to capillary forces. This problem is related to models of a rigid sphere moving through viscous fluid close to a plane wall [50, 51]. The model combines a capillary-statics approximation for the drop shape away from the wall, lubrication theory in the thin film region and a combination of lubrication theory and a half-plane boundary-integral method for the drop interior. Lubrication force, coupled to deformation of the base of the drop, induce a lift force on the drop; we compute analogous forces with a different deformation model in Chapter 4 below.

A related model, though with very different applications, is that of pulling a large object from a sandy seabed, where the seabed is assumed porous but rigid [67]. It is known that the initial increase of the gap between the object and the 'sand' is slow until a critical 'breakout' time when the object breaks free suddenly. With a porous seabed, fluid is withdrawn from the underlying solid as the object is lifted, reducing suction in the gap and reducing the breakout time. Mei *et al.* [67] show that soil elasticity is not essential to breakout and they also consider the case of a wedge-shaped gap between the object and the seabed. Using lubrication theory and assuming a thin boundary layer in the porous solid, it is shown that pulling at one edge (with a wedge-shaped gap) is much more effective than pulling at the centre. Initially the increase in the gap thickness is due to the upwards flux from the seabed, and breakout occurs when the horizontal flux becomes the dominant part of the fluid flux into the gap. Breakout is quicker for wedged shaped gaps and also porosity reduces breakout time. This model explores the effect of wall porosity on an object moving perpendicularly away from the wall through fluid. The airway wall is porous and, in practice, fluid will be drawn through the wall to the liquid lining in response to particle motion, so that some of the physical principles described in [67] may be relevant; however in this thesis we assume the airway is impermeable.

1.8 Viscous sheet flow

In Chapter 5 we consider the motion of a deposited particle trapped in a lung mucus layer. In this section, therefore, we review mathematical modelling of viscous sheets.

Van de Fliert *et al.* [68] study pressure-driven flow of a thin sheet of viscous fluid. For non-negligible curvature, they use asymptotic expansions to simplify the Navier-Stokes equations to derive a 'viscous shell theory' model, assuming a balance between the external forces and the viscous stresses in the fluid. They consider a variety of special cases: planar and nearly planar sheets, axisymmetric sheets and general cylindrical sheets.

Howell [69] reviews the existing theory of inertia-free two-dimensional viscous sheets. This predicts behaviour for three aspects of thin sheet theory: buckling under compression, straightening under tension (from an initially curved state) and stretching under tension. Howell extends this to include inertial effects and develops a model for the evolution of the viscous sheet centre-line. This model is shown to be ill-posed when under compression and requires a correction to the scaling dependent on the Reynolds number and the aspect ratio of the sheet. This two-dimensional theory is extended to consider models for three-dimensional sheets, in particular the case of a nearly flat, thin, inertia-free viscous sheet between two free surfaces, which has applications to the modelling of mucus flow below.

Ribe [70] also develops a 'viscous shell theory' model for the deformation of thin viscous sheets of arbitrary shape subject to arbitrary loading. For flow in a shallow (nearly planar) sheet with constant thickness loaded by an harmonic normal stress, two types of deformation can occur: 'inextensional' (bending) and 'membrane' (stretching). The three-dimensional equations for flow in the sheet are reduced to a set of two-dimensional equations, describing the velocity of sheet midsurface, valid in both limits. Ribe also derives kinematic evolution equations for the sheet shape and thickness.

Also of interest in the modelling of viscous sheets is the literature related to the spreading of liquids. Di Pietro & Cox [71] consider the spreading of a very viscous liquid (*e.g.* oil) on a quiescent water surface. They look first at the 'gravity-viscous' spreading model, where the boundary-layer drag between the oil and the water is important. It is shown that the model is invalid in the limit of substrate viscosity tending to zero (*i.e.* negligible drag). They develop a different model for drag-free spreading and also a general theory including both limits as special cases. Matar *et al.* [72] consider surfactant transport on a viscous film (modelling mucus) overlying a less viscous layer (modelling the serous layer)— a situation likely to occur in the lung airways. The model includes the effect of Van der Waals forces which can cause thin films to rupture; in lungs this can (in principle) create pools of stranded surfactant and prevent spreading. In surfactant replacement therapy (SRT), for example, this may seriously endanger the health of the patient. Matar *et al.* develop evolution equations for the total height of the fluid (both layers), the mucus (viscous) layer depth, the surfactant distribution and the mucus velocity. Similarity solutions are found for both negligible and significant Van der Waals effects.

Of particular interest to the modelling of lung airways is the behaviour of objects trapped within viscous sheets. This is relevant to the situation of inhaled and deposited particles. Stone & Ajdari [73] consider the translation of a disk-shaped object in a thin viscous surface film overlying a fluid of finite depth. The friction coefficient on the disk is found for a range of the two dimensionless parameters: the sublayer thickness ratio H/R (where H is the sublayer depth and R is the object radius), and the ratio of the sublayer (μ) to membrane (μ_m) viscosities, $\Lambda = \mu R/\mu_m h$, where h is the thickness of the surface film. The drag on the disk is predicted based on the different ordering of the lengthscales occurring in the problem. Stone & Ajdari also retrieve the existing approximations for the hydrodynamic force acting on a disk in various limits of the two parameters. For $\Lambda \ll 1$ (high membrane viscosity) and large sublayers the results agree with the earlier analysis of Saffman [74] and the subsequent improved asymptotic expansion by Hughes *et al.* [75]. In the limit of thin sublayers the model retrieves the work of Evans & Sackmann [76] who considered the additional resistance produced by a rigid planar boundary, modelled using a linear velocity-dependent drag relation. They derive the equations of motion for the flow in the surface film (or membrane) for the steady translation and rotation of the disk and find that the drag coefficients acting on the disk depend on the particle size; this agrees with Hughes [75] for a membrane bounded by semi-infinite liquid domains. Stone & Adjari [73] show that the Evans-Sackmann formula for the hydrodynamic force is valid provided $(H/R)\Lambda < 1$, *i.e.* sublayers need not be particularly thin.

Fischer [77] considers the similar problem of the drag on a needle moving in a surface film overlying a fluid of depth H. Both edge-on motion (in the direction of the tip) and broadside-on motion (perpendicular to the tip) are considered. A new scaling regime for the needle drag, compared to the drag on a circular disk ([73, 74, 75]), arises when the ratio between the surface viscosity and the subphase viscosity is smaller than the needle length.

In Chapter 5 we consider a particle deposited in a lung mucus layer modelled as an object trapped within a mucus sheet. This situation is highly relevant to the studies reviewed in this section.

1.9 Motivation and Thesis Structure

In this thesis we use theoretical fluid dynamics to model various aspects of the dynamics of particles deposited in the liquid-lining of lung airways. We consider three model problems inspired by existing studies of deposited particles.

It has been suggested that particles deposited in the alveoli will be transported by capillary action and pressure gradients in the substrate towards areas with greater amounts of substrate material such as an alveolar corner [45]. In Chapter 2 we consider the motion of a particle partially immersed in a fluid-filled, rigid-walled corner. We aim to predict the speed and direction of the particle's motion within the wedge resulting from competing surface tension and viscous forces.

It has been shown that surface forces can displace a deposited particle into the fluid layer with sufficient force to indent the underlying epithelial cells [45]. In Chapters 3 and 4 we consider the perpendicular and transverse motion of a particle relative to a deformable wall. We aim to find the effect of wall deformability on the force acting on the particle.

In the larger airways, particles can become trapped in the mucus layer and be transported towards the pharynx with the mucus by propulsive cilia in the underlying serous layer [18]. In Chapter 5 we consider the motion of a trapped particle within a cilia-propelled mucus sheet. We aim to find how the speed of the particle, relative to the surrounding mucus, depends on various material parameters, such as the extent of the particle's protrusion into the serous layer and the particle's effect on local ciliary function.

Chapter 2

Motion of a partially immersed particle in a rigid-walled corner

In this chapter we consider the behaviour of an inhaled particle after deposition in an alveolar corner, motivated by the suggestion that particles are transported by capillary action and pressure gradients towards fluid-filled alveolar corners [45]. We model this as a two-dimensional cylinder partially immersed in a liquid-lined rigid-walled wedge. In §2.1 we determine the static distribution of liquid when the cylinder is fixed relative to the wedge wall. In §2.2 we consider the dynamic particle motion in the wedge due to competing viscous and capillary effects. In the dynamic problem we assume there is a small gap between the particle and the wall, thickness ϵ, where viscous forces dominate. We show that, at leading order in ϵ, the problem reduces to the static case of §2.1.

There is a great deal of existing literature relevant to this problem, considering particles both floating at interfaces and trapped in thin fluid films [46, 49]. For example, it has been shown that a cylinder partially immersed in a liquid film on a flat surface is subject to capillary forces and also that the presence of an additional particle may create a non-zero net horizontal force. Here we consider the new problem of a cylinder trapped in a fluid-filled wedge.

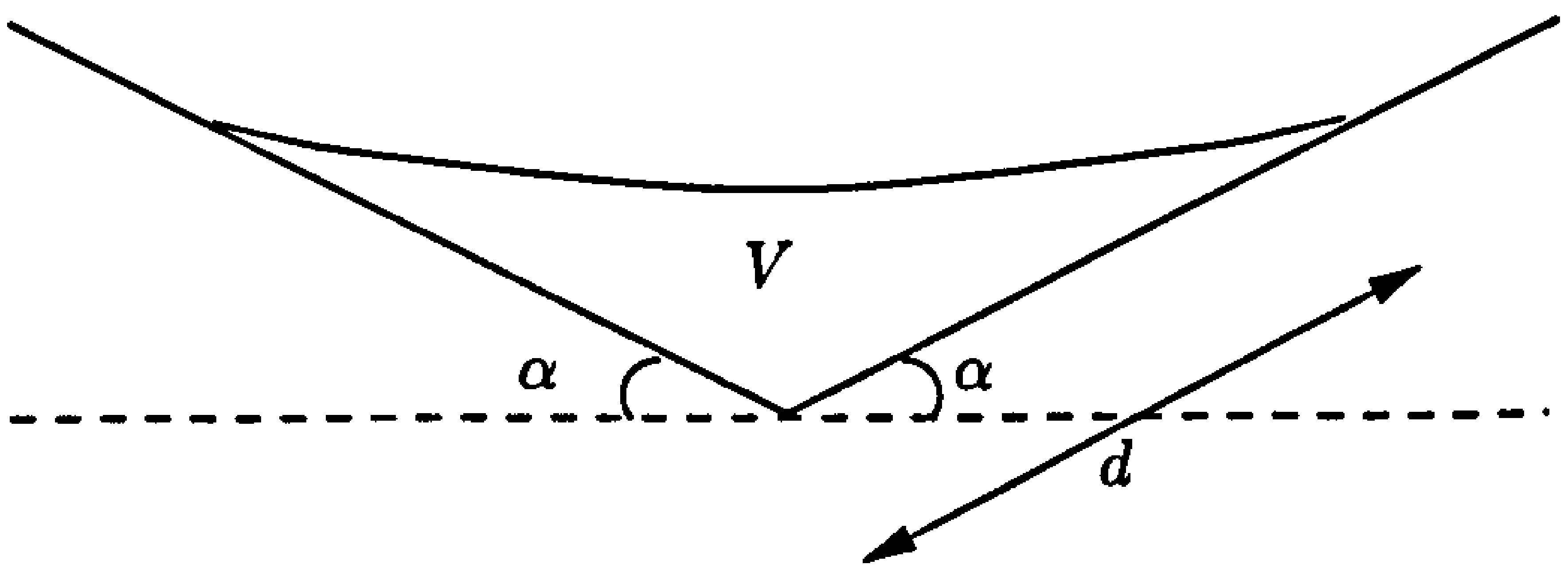

Figure 2.1: Two-dimensional wedge containing fluid volume V

We then extend this to consider the dynamic motion of the particle resulting from the capillary forces.

2.1 The Static Problem

The alveolar corner is modelled as a two-dimensional wedge, with internal angle $\pi - 2\alpha$, containing total fluid volume V per unit length (see Figure 2.1). The length of wall initially covered by the fluid, d, is given by

$$d^2 = \frac{V \tan\alpha}{1 - (\alpha/\tan\alpha)}. \tag{2.1}$$

In this static model we want to determine the forces on a partially immersed cylinder of radius a fixed in this fluid (see Figure 2.2(b)). The Bond number (the ratio of gravitational effects to surface tension effects) in an airway is small and so we assume there is no gravitational force acting on the particle. Therefore the forces on the particle are due to surface tension acting at the contact line and sub-zero capillary pressure in the fluid (taking atmospheric pressure to be zero). We want to find the direction of the net force on the particle due to these capillary effects. We assume the fluid interface meets the particle and walls with zero contact angles. We assume that when the particle is deposited it is pulled down rapidly through the fluid by the surface forces to make contact with the wedge wall a distance d_2 say, from the wedge vertex,

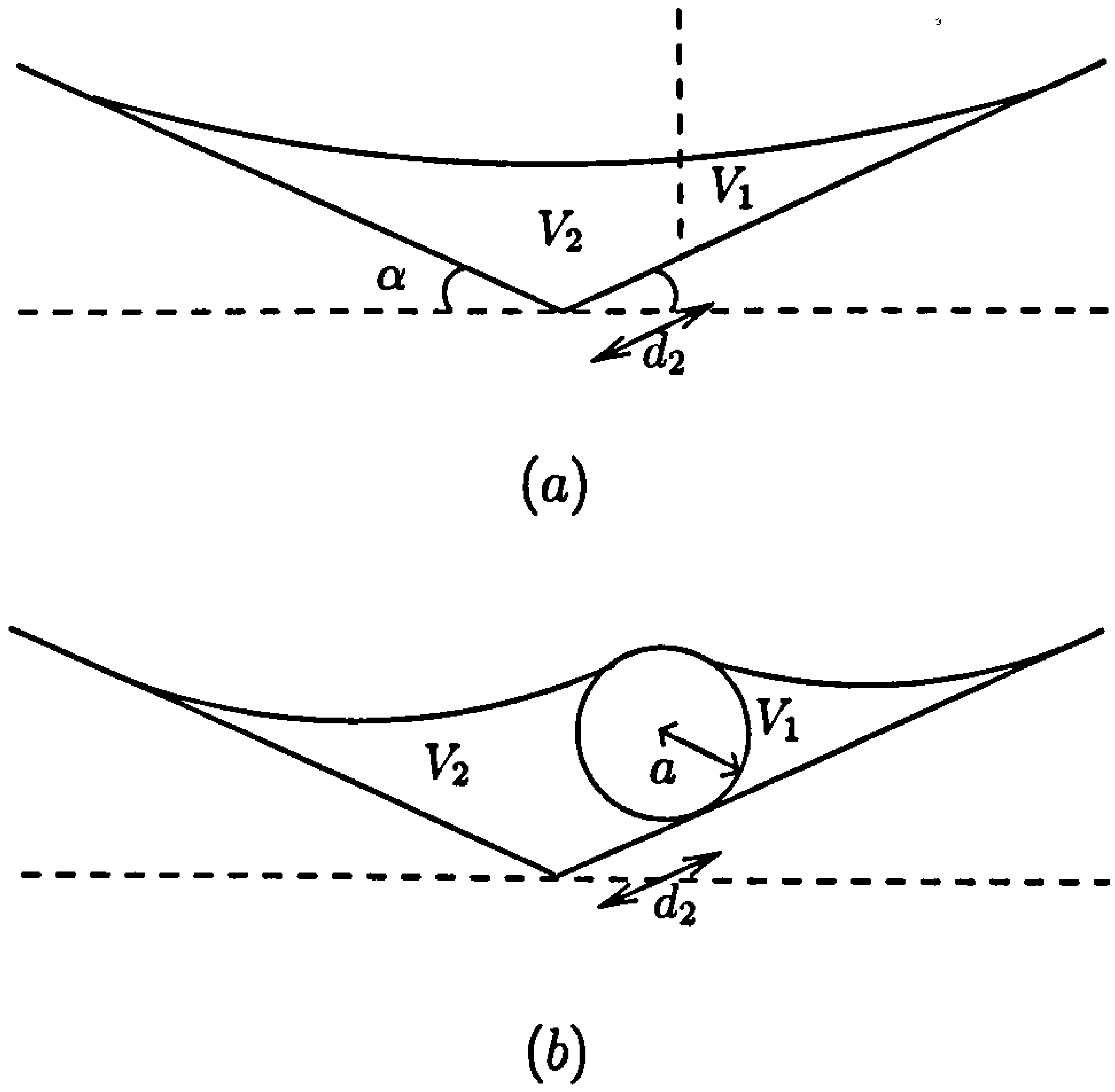

(a)

(b)

Figure 2.2: (a) Fluid is cut vertically at d_2, (b) Particle is fixed on the wedge wall at d_2

where $0 \leq d_2 \leq d$ (Fig 2.2(a)). We arbitrarily divide the fluid vertically into separate volumes V_1, V_2 (see Figure 2.2), given by

$$V_1 = \frac{V}{2}\frac{(d-d_2)^2}{d^2}, \qquad V_2 = V - \frac{V}{2}\frac{(d-d_2)^2}{d^2}, \tag{2.2}$$

and assume the partitioned fluid comes to equilibrium either side of the particle.

Before we investigate the forces on the particle we need to look at the shape of the interface. To fully describe the state of the fluid we need three variables for each volume of fluid: the length of the wall covered by fluid d_1, d_3; the angles to the vertical subtended at the centre of the cylinder by the contact point θ_1, θ_2; and the radii of curvature of the fluid/air interface R_1, R_2 (see Figure 2.3). Since this is a static problem the fluid is in equilibrium and so the Young-Laplace condition (1.1) at the interface tells us that the curvature is constant and hence the fluid/air interfaces are arcs of circles.

By geometry, given parameters a, V, α, d_2, we obtain six equations in these

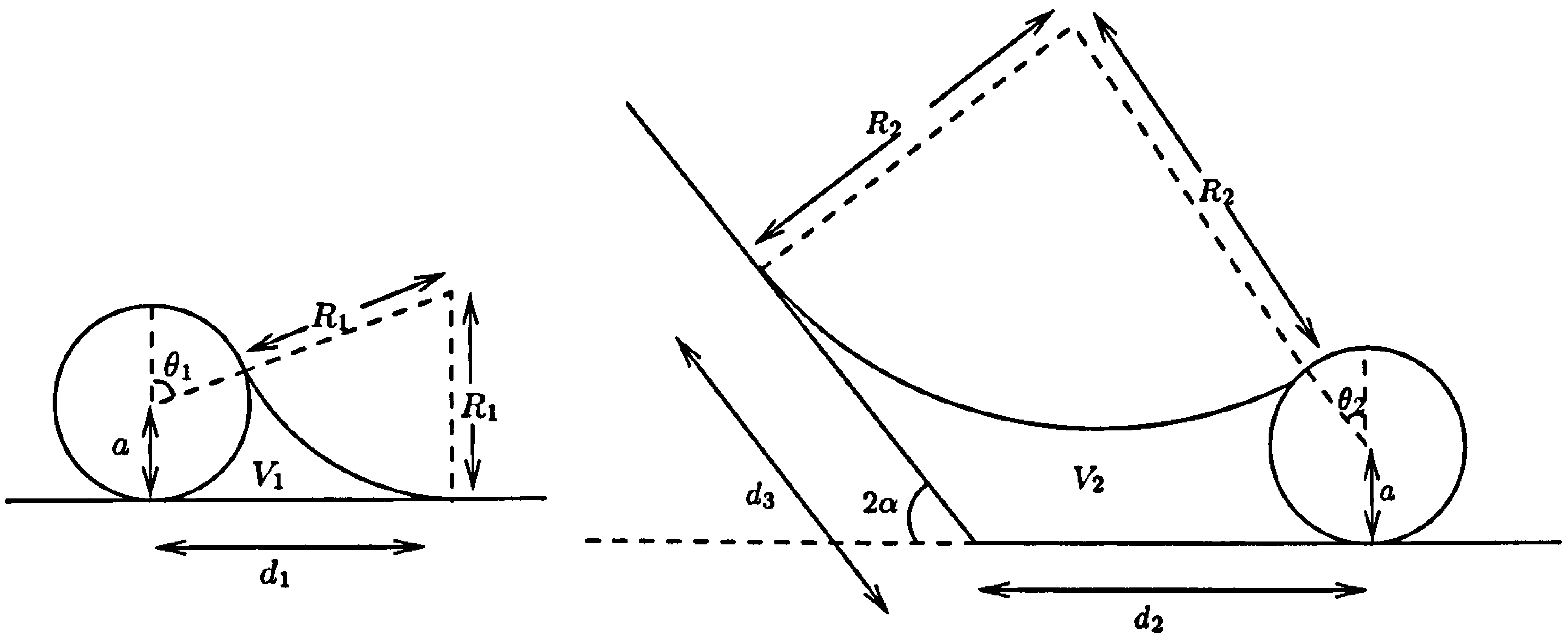

(a) (b)

Figure 2.3: (*a*) Diagram showing the interface when the volume V_1 meets the particle and the wall. (*b*) Diagram showing the interface for the volume V_2.

six unknowns:

$$
\begin{aligned}
& d_1 = (R_1 + a)\sin\theta_1, \\
& R_1 = a\frac{(1+\cos\theta_1)}{(1-\cos\theta_1)}, \\
& \frac{a^2}{2}(\pi - \theta_1) + V_1 + \frac{R_1^2\theta_1}{2} = \frac{d_1^2}{2\tan\theta_1} + ad_1, \\
& d_2 = R_2\sin2\alpha + (R_2 + a)\sin\theta_2 - d_3\cos2\alpha, \\
& (R_2 + a)\cos\theta_2 + a = R_2\cos2\alpha + d_3\sin2\alpha, \\
& 2V_2 = (R_2 + a)\cos\theta_2\left(\frac{d_3}{\cos2\alpha} + d_2 + a\tan\theta_2\right) - d_3^2\tan2\alpha \\
& \qquad\qquad - R_2^2(2\alpha + \theta_2) + a\left(\frac{d_3}{\cos2\alpha} + d_2 - a(\pi - \theta_2)\right).
\end{aligned}
$$

Nondimensionalising using the lengthscale a gives the modified variables $\hat{V}_1 = V_1/a^2$, $\hat{R}_1 = R_1/a$, $\hat{d}_1 = d_1/a$, $\hat{V}_2 = V_2/a^2$, $\hat{R}_2 = R_2/a$, $\hat{d}_3 = d_3/a$, $\hat{d}_2 = d_2/a$. Dropping hats for simplicity, we obtain

$$d_1 = (R_1 + 1)\sin\theta_1, \tag{2.4a}$$

$$R_1 = \frac{(1+\cos\theta_1)}{(1-\cos\theta_1)}, \tag{2.4b}$$

$$\frac{1}{2}(\pi-\theta_1)+V_1+\frac{R_1^2\theta_1}{2}=\frac{d_1^2}{2\mathrm{tan}\theta_1}+d_1, \tag{2.4c}$$

$$d_2=R_2\mathrm{sin}2\alpha+(R_2+1)\mathrm{sin}\theta_2-d_3\mathrm{cos}2\alpha, \tag{2.4d}$$

$$(R_2+1)\mathrm{cos}\theta_2+1=R_2\mathrm{cos}2\alpha+d_3\mathrm{sin}2\alpha, \tag{2.4e}$$

$$\begin{aligned} 2V_2 = (R_2+1)\cos\theta_2\left(\frac{d_3}{\cos 2\alpha}+d_2+\tan\theta_2\right)-d_3^2\tan 2\alpha \\ -R_2^2(2\alpha+\theta_2)+\left(\frac{d_3}{\cos 2\alpha}+d_2-\pi-\theta_2\right), \end{aligned} \tag{2.4f}$$

with dimensionless parameters V_1, V_2, d_2, α. Given (2.1, 2.2), the problem is parameterised by α and V alone.

We can find θ_1, d_1, R_1 in terms of V_1 by eliminating R_1 and d_1 in (2.4b, 2.4c) and solving for θ_1 numerically. These results are shown in Figure 2.4. As the volume V_1 increases the contact line moves towards the top of the particle, the interface becomes flatter and the length of wall covered by fluid, d_2, increases as expected.

The description of the fluid behaviour for the volume V_2 is more complicated as the relevant equations (2.4e, 2.4f) involve three parameters V_2, α, d_2. For the purposes of comparison, Figure 2.5 shows results for varying V_2 given $\alpha=\frac{\pi}{8}$ and $d_2=5$. Again, as the fluid volume increases, the contact line moves higher up the particle, the interface flattens and more of the wall is covered by fluid.

Figure 2.6 illustrates the interface shape for (*a*) $\alpha=0.426$, (*b*) α close to 0 where the wedge angle is shallow and (*c*) α closer to $\pi/2$. The latter is less relevant to alveolar corners but it demonstrates that the model holds for larger values of α.

We now consider the forces acting on the cylinder and determine if the net force on the particle is towards the corner of the wedge or towards the nearest contact line. The net force per unit length F acting on the particle parallel to

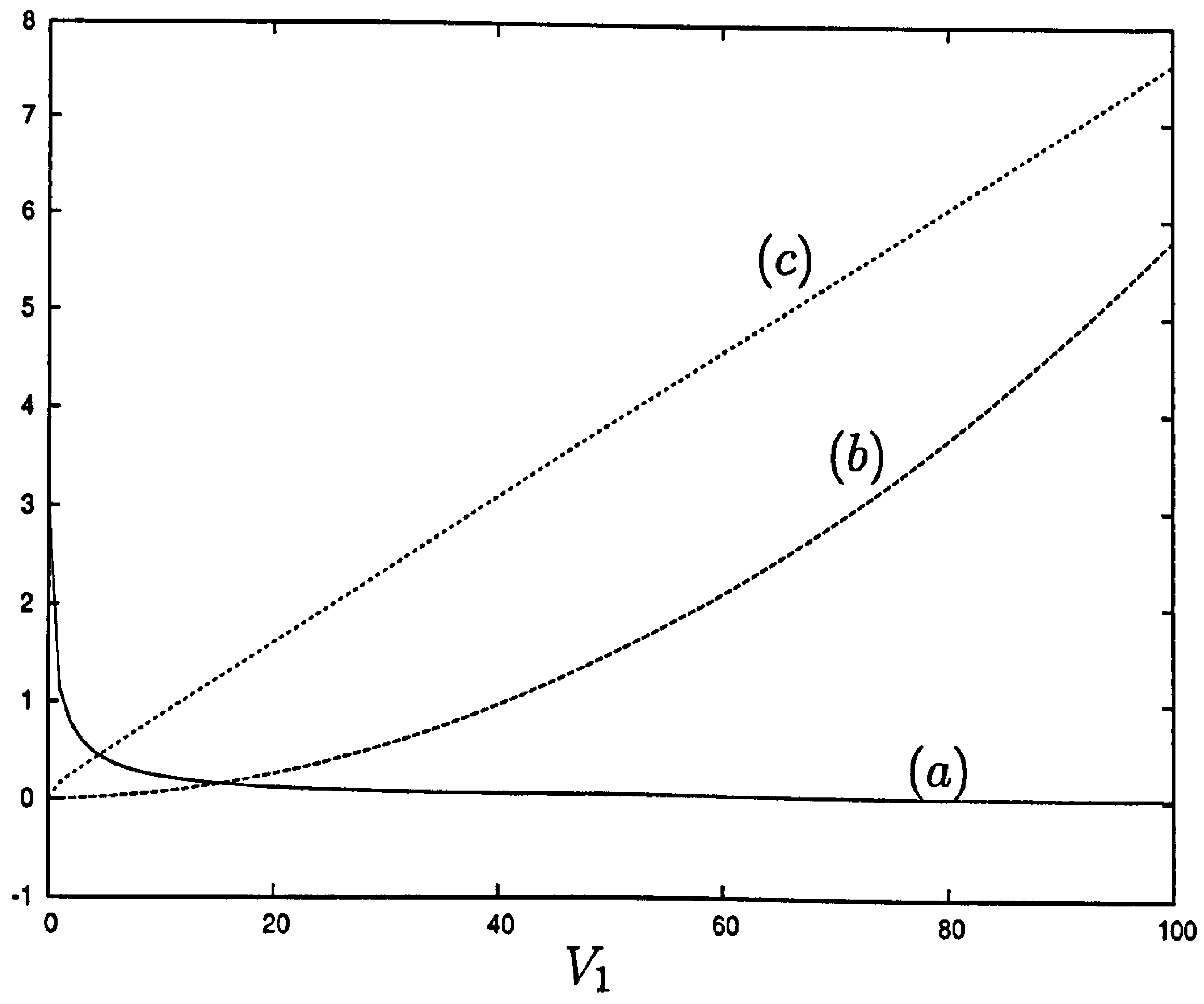

Figure 2.4: The effect of varying the parameter V_1 on (*a*) the contact point θ_1, (*b*) the scaled curvature of the interface $R_1/1000$, (*c*) the scaled distance the fluid covers along the wall $d_1/20$

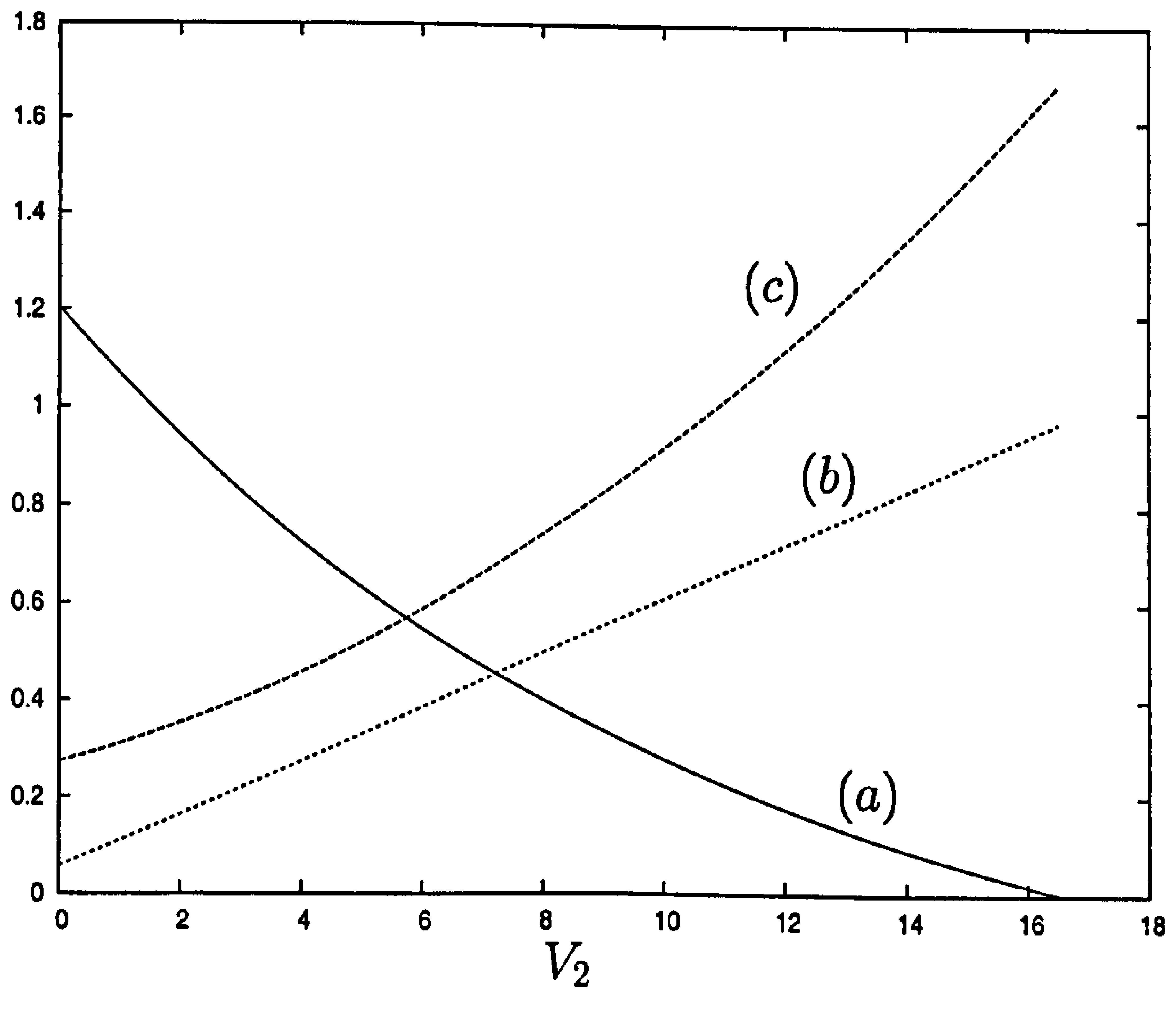

Figure 2.5: The effect of varying the parameter V_2 on (a) the contact point θ_2, (b) the scaled distance the fluid covers along the wall $d_3/10$, (c) the scaled curvature of the interface $R_2/10$, for $\alpha = \pi/8$, $d_2 = 5$.

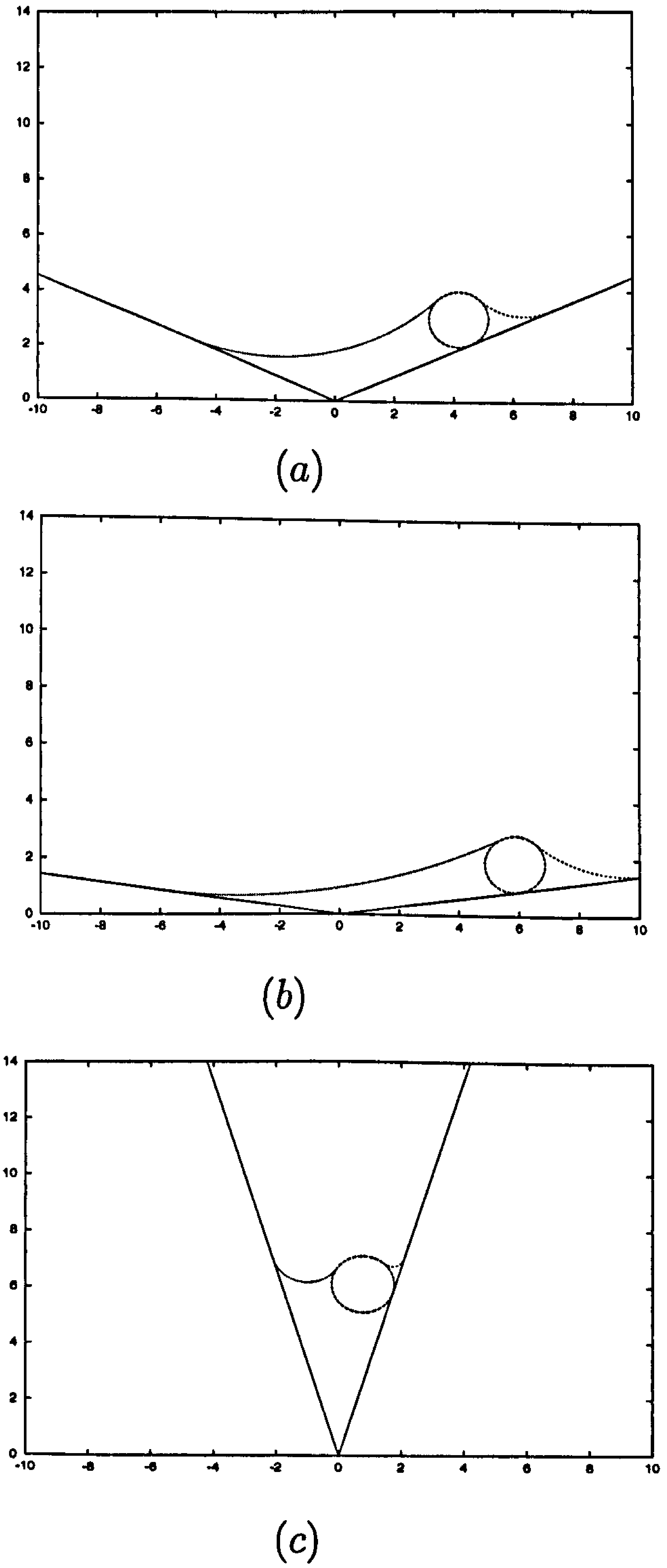

(a)

(b)

(c)

Figure 2.6: (*a*) V=10, α=0.426, d_2=5.03 (*b*) V=10, α=0.142, d_2=6.06 (*c*) V=10, α=1.279, d_2=6.04

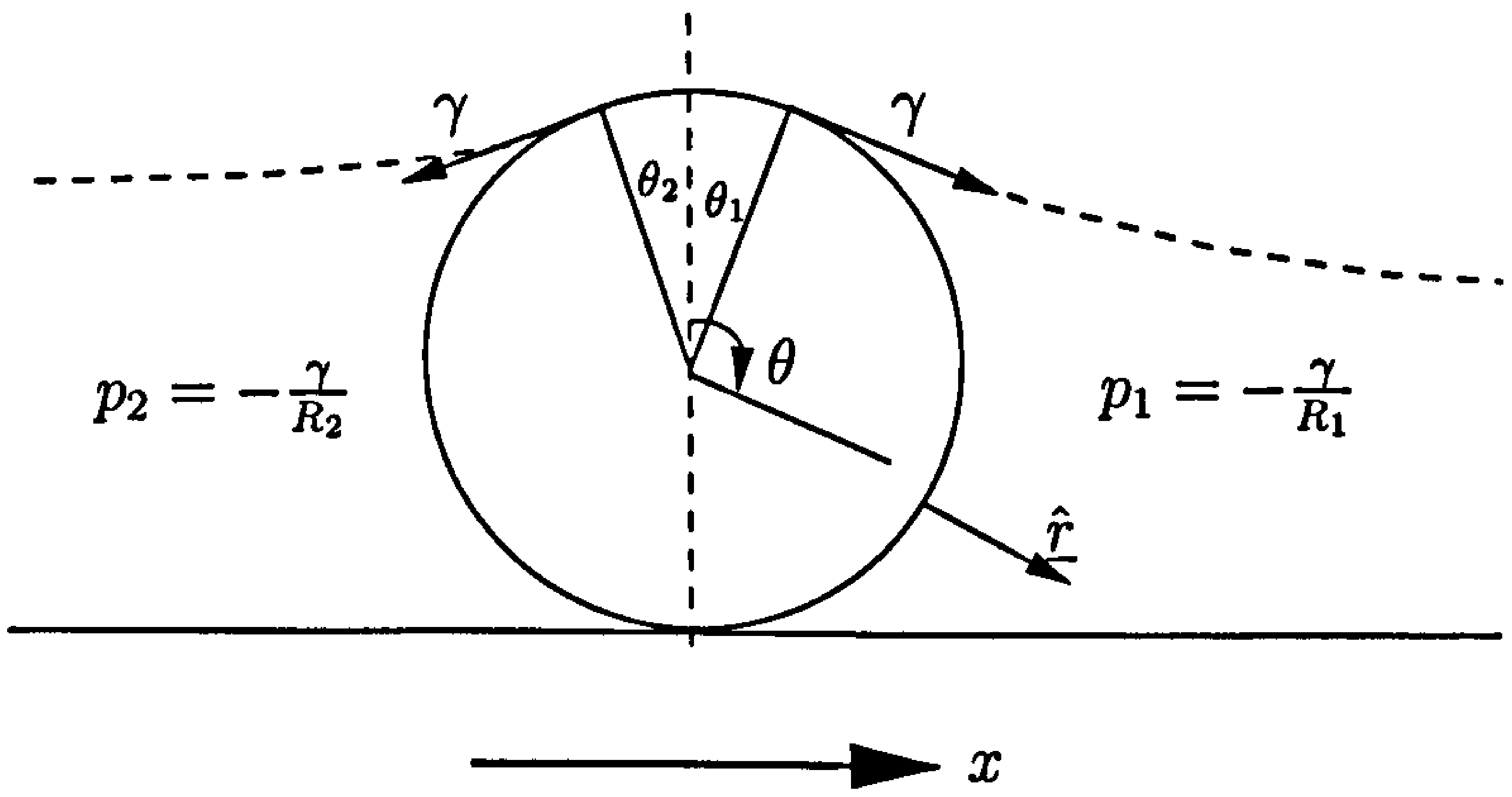

Figure 2.7: Force acting on the particle

the wedge wall (measured in the x direction (see Figure 2.7)) is

$$\frac{F}{\gamma} = \cos\theta_1 - \cos\theta_2 + \frac{(1+\cos\theta_1)}{R_1} - \frac{(1+\cos\theta_2)}{R_2}. \tag{2.5}$$

The first two terms on the right-hand side of (2.5) are due to surface tension γ acting at the contact lines; the second two are due to capillary pressures in the fluid. We now look at how the force on the particle varies with the position of the particle on the wall.

Figure 2.8 shows the force for $V = 5$. Each line on the graph represents a different value of α with α increasing from close to 0 to close to $\pi/2$. Consider the line AB, which corresponds to $\alpha = 1.1366$. The point A gives the value of d_2 for which the particle becomes submerged ($\theta_1 = -\theta_2$). The point B is the other extreme where the particle is at the contact line ($d_1 = 0$). Where $F > 0 (< 0)$ the particle experiences a force away from (towards) the corner. Therefore for low α the force is always towards the corner, but for sufficiently large α (in this example) there is an equilibrium position for the particle where the net force on it will be zero. We seek to determine the values of V and α for which an equilibrium position exists.

Figure 2.9 shows (V, α)-parameter space. In regions A or D there is no equilibrium position for the particle, and the force is always negative, towards

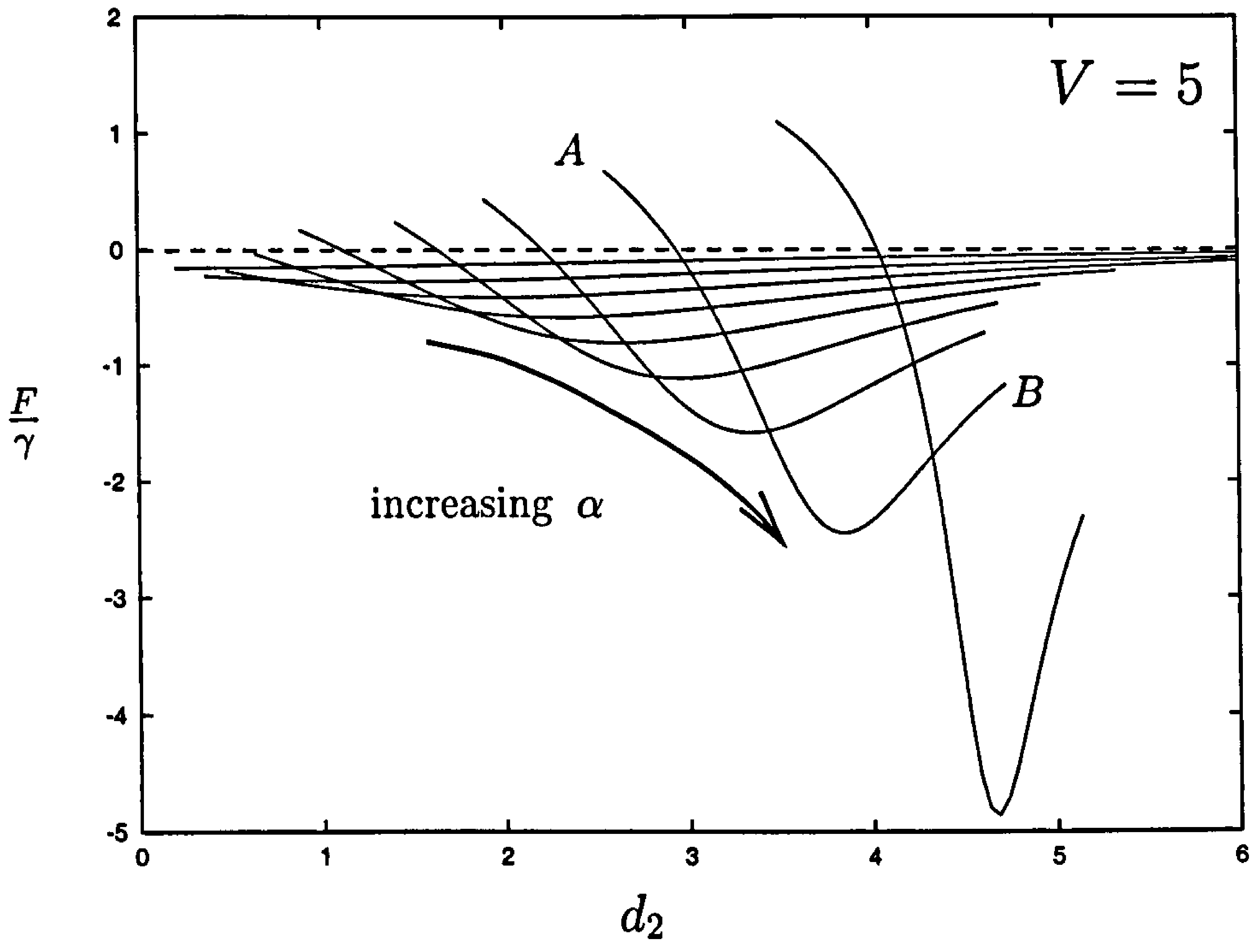

Figure 2.8: Net force on the particle varying with d_2 for $0 < \alpha < \pi/2$ where $V = 5$. The line AB corresponds to $\alpha = 1.1366$.

the corner (and the force-distance curve is as shown in Figure 2.9(a)). In regions B or C there is an equilibrium position. In region B the force-distance graph shows there is an equilibrium position, where particles placed to the left of this point on the wall will be under a negative force and those placed to the right will be under a positive force (see Figure 2.9(b)). Therefore, subject to the assumptions of this model, this equilibrium is unstable. In region C the force is positive on particles to the left of the equilibrium position and negative on those to the right, implying this equilibrium is stable (see Figure 2.9(c)).

For each (α, V) there is a minimum value of d_2 for which a solution exists (see Figure 2.8, point A). A particle placed at this point is either in the corner of the wedge or is just submerged in the fluid. For values of d_2 lower than this minimum the model is invalid. We can work out geometrically which situation exists for a given (α, V) since if $\theta_2 \leq -\theta_1$ the particle is submerged and if

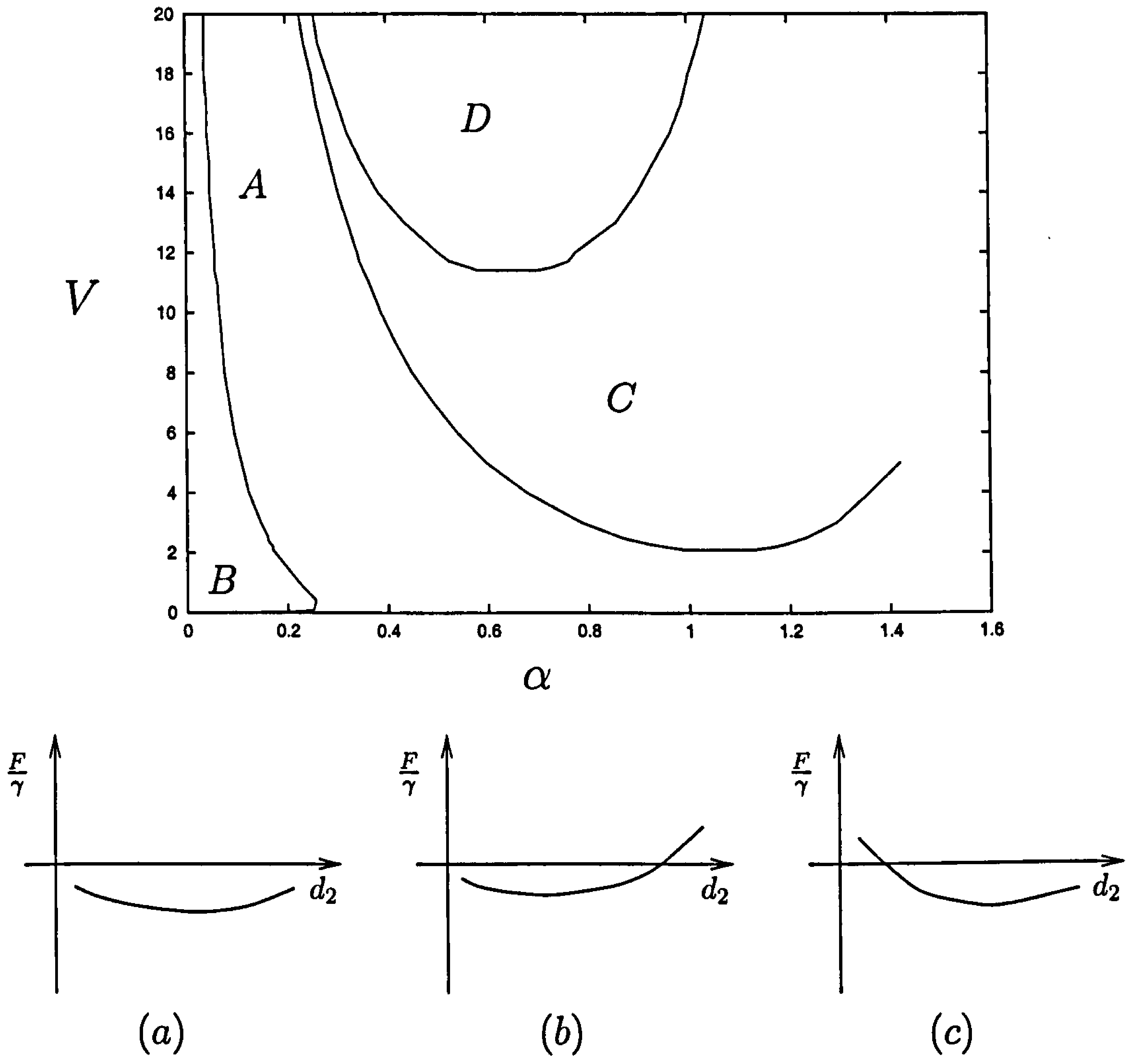

Figure 2.9: V,α parameter space with corresponding typical force-distance graphs. (a) corresponds with Regions A and D. (b) & (c) correspond with Regions B and C respectively and illustrate the existence of equilibria in these regions.

$d_2 \leq \tan\alpha$ the particle is in the corner of the wedge. Figure 2.10 illustrates these behaviours.

Figure 2.11 shows this division of the (α, V)-parameter space (solid line) overlaid on the regions of equilibria shown in Figure 2.9 (dotted lines). In region (a), below the solid line, the particle is in the corner at minimum d_2; in region (b) the particle is submerged at minimum d_2.

Since we are considering a static problem we cannot predict exactly what will happen to the particle once it moves. However these results do suggest the following dynamics: in Region A (see Figure 2.9) a particle placed anywhere on the wall will move into the corner of the wedge; in Region D a particle will move towards the corner but become submerged before it reaches the corner; in Region B a particle will move into the corner or move to the contact point, depending on its initial position; in Region C a particle will move towards a stable equilibrium, wherever it is placed on the wall.

2.1.1 Large Volumes

Finally, it is interesting to look at what happens for larger values of V. Figure 2.12(a) shows sideways force against particle position for $V = 2000$ taking 100 equally-spaced steps in α, where $10^{-3} \leq \alpha \leq 1.430$. Figure 2.12($a$) shows that equilibrium positions do still exist for some values of α. Figure 2.12(b) shows the case for $V = 5000$. We can see that for higher values of α the force is always negative. We can check whether this is also true for small α by taking 1000 steps in α and plotting the first few curves (see Figure 2.12(c)). For the values of α considered, the force on the particle is always negative, regardless of d_2. This implies that regions B and C on Figure 2.9 have disappeared at $V = 5000$. These results imply that for large V, for any value of α, all particles will move towards the corner of the wedge. For small α, particles can land almost anywhere on the wedge wall; for large α, particles have only a small

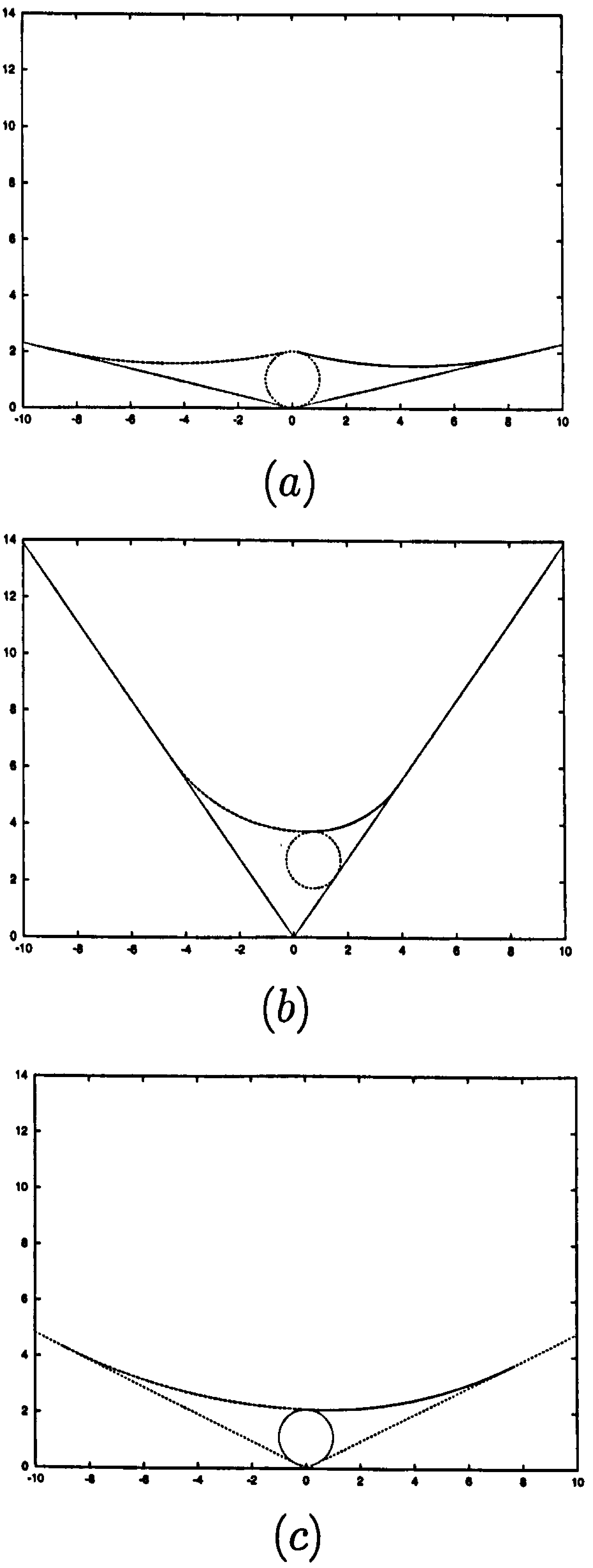

Figure 2.10: (a) Particle in corner of wedge, $V = 9$, $\alpha = 0.227$, $d_2 = 0.2412$, (b) Particle submerged, $V = 9$, $\alpha = 0.947$, $d_2 = 2.6417$, (c) Particle submerged and in corner, $V = 9$, $\alpha = 0.4499$, $d_2 = 0.4858$

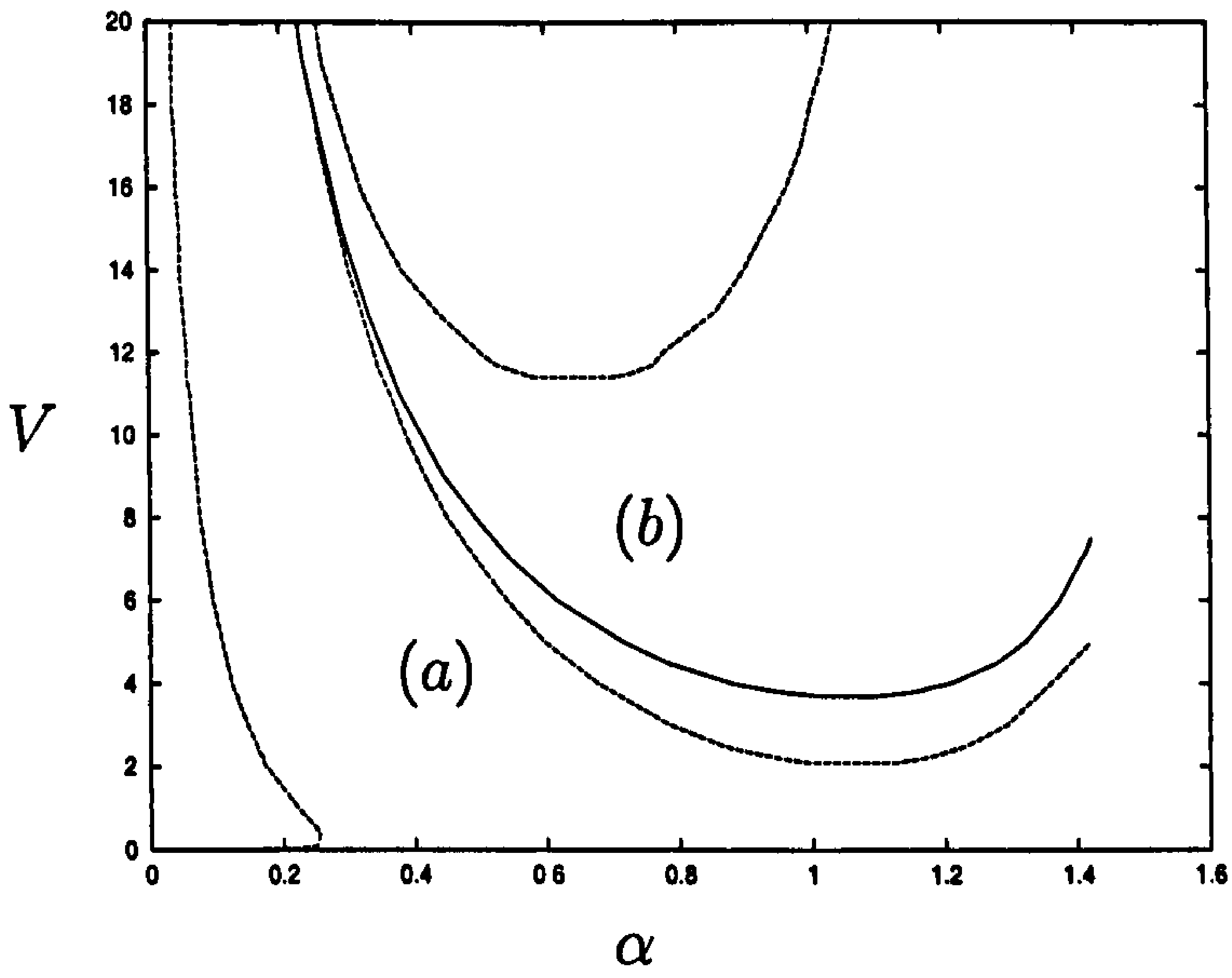

Figure 2.11: V,α parameter space showing the physical situation at minimum d_2, overlaid on the regions of equilibria (dashed lines).

range of d_2 where the particle can land (see Figure 2.12(*b*)). For particles landing outside this range the model is invalid.

In §2.2 below we look at the movement of the particle through the fluid and so we will also need to know the force on a particle normal to the wedge wall. This normal force towards the wall is given by

$$\frac{F_2}{\gamma} = \sin\theta_1 + \sin\theta_2 + \frac{\sin\theta_1}{R_1} + \frac{\sin\theta_2}{R_2}. \tag{2.6}$$

In this section we have calculated the direction of initial motion of the particle; however as soon as the particle moves the static model breaks down. This raises many questions: for example, do the fluid volumes V_1 and V_2 remain constant as the particle moves, and does the force-distance curve change as the particle moves from its initial location? In §2.2 we consider the dynamic behaviour of the deposited particle, and address these questions.

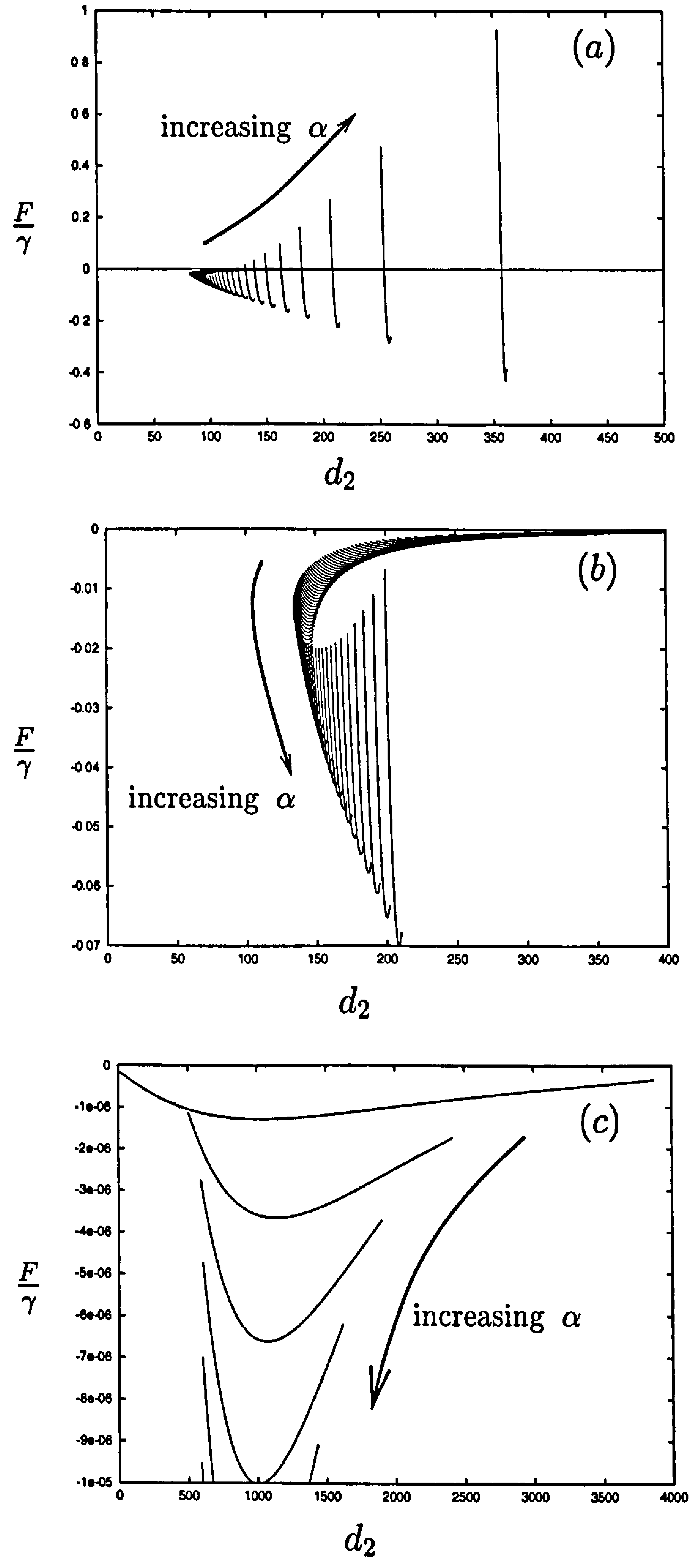

Figure 2.12: Parallel force against particle position for $10^{-3} \leq \alpha \leq 1.430$ with (*a*) $V = 2000$, (*b*) $V = 5000$. Graph (*c*) shows position against force for small values of α when $V = 5000$.

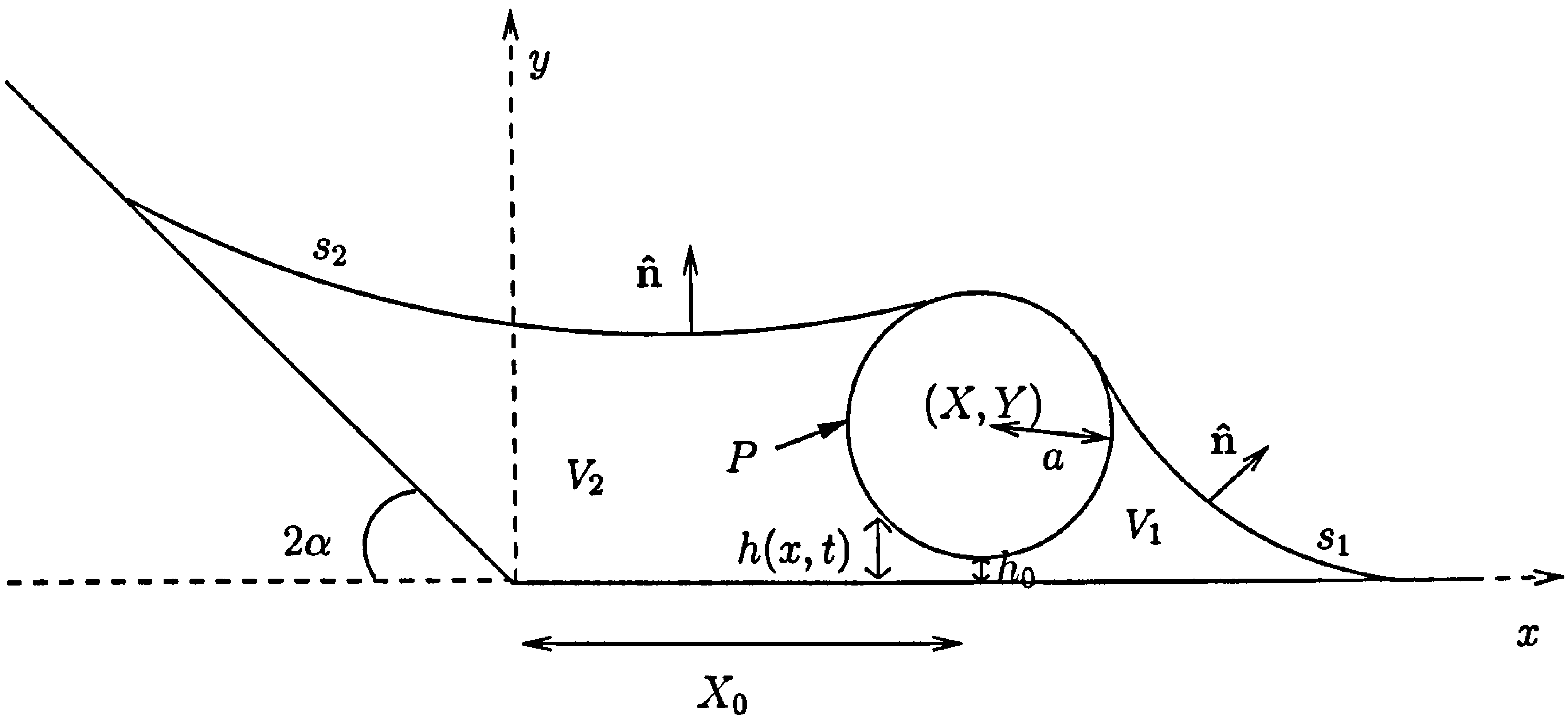

Figure 2.13: Particle after initial deposition in liquid-lined wedge

2.2 The Dynamic Problem

The aim of the dynamic problem is to model the unsteady behaviour of the particle after initial deposition in the fluid-filled alveolar corner. As in the static problem we assume that the particle is pulled down rapidly by the surface forces into the fluid, in this case leaving a small gap between the particle and the wall. We aim to find the 'sliding speed', the particle speed parallel to the wedge wall, and the 'squeezing speed', the speed normal to the wall, and hence to find the trajectory of the particle through the fluid. The fluid/particle interface is denoted P, and the height of P above the wedge wall is given by $h(x,t)$. The centre of the particle is given by $(X(t), Y(t))$ where $Y(t) = a + h(X,t)$. The model parameters are: α, the wedge angle; a, the particle radius; V, the total fluid volume; h_0, the initial gap thickness; and $X_0 = X(0)$, the initial horizontal position of the particle (see Figure 2.13). The fluid/air interfaces are denoted s_1, s_2 with outward-pointing unit normal $\hat{\mathbf{n}}$.

We assume the Reynolds number is low and so the inertia of both the fluid and the particle are negligible compared to viscous effects. Therefore we can assume there is zero net force acting on the particle. We know there is a force on the particle due to surface tension effects and this causes the particle to move. This capillary force is balanced by a viscous drag on the particle. The torque on a cylinder translating close to a rigid wall is zero [55], as surface tension force and viscous force exert no net torque. We therefore assume no rotation of the particle. As before the Bond number is small and so gravitational effects are neglected. We want to exploit the fact that the gap thickness is small compared to the particle radius, so we define a small parameter,

$$\epsilon = \frac{h_0}{a} \ll 1.$$

We will show that the problem requires a matching between capillary statics in the outer regions and lubrication theory in the gap. We will show that at leading order in ϵ, the flow in the fluid and the gap between the cylinder and the wall are negligible and the problem reduces to the static case, as previously considered in §2.1. The capillary forces calculated in §2.1 are balanced by strong viscous forces in the gap, modelled using lubrication theory.

In this problem the flow is governed by the Stokes equations,

$$0 = -\nabla p + \mu \nabla^2 \mathbf{u}, \tag{2.7}$$

$$\nabla \cdot \mathbf{u} = 0, \tag{2.8}$$

where $\mathbf{u}$ is the fluid velocity, μ is the fluid viscosity and p is the fluid pressure. These governing equations are subject to the following conditions: no-slip on wedge walls,

$$\begin{aligned} \mathbf{u} = 0 \quad \text{on} \qquad & y = 0,\ x > 0, \\ & y = -x \tan 2\alpha,\ x < 0; \end{aligned} \tag{2.9}$$

no-slip on the moving particle,

$$\mathbf{u} = \mathbf{U} \ \text{ on } \ P, \ \text{ where } \mathbf{U} = (\dot{X}, \dot{Y}); \tag{2.10}$$

the stress condition at the fluid/air interfaces,

$$\sigma \cdot \hat{\mathrm{n}} = -p\hat{\mathrm{n}} + \mu(\nabla \mathrm{u} + \nabla \mathrm{u}^T) \cdot \hat{\mathrm{n}} = \gamma\kappa\hat{\mathrm{n}} \text{ on } s_1, s_2, \tag{2.11}$$

where κ is the interfacial curvature; conservation of total fluid volume,

$$\int_{\text{fluid}} dV = V = \text{constant}; \tag{2.12}$$

the integrated form of the continuity equation (2.8) together with the kinematic boundary condition at the interfaces, $v = h_t + uh_x$ implying

$$h_t + Q_x = 0, \tag{2.13}$$

where $Q = \int_0^h u \, dy$ is the flux of fluid; zero net force on the particle,

$$\mathrm{F} = 0; \tag{2.14}$$

and zero contact angles where the fluid interfaces meet the walls and the particle.

2.2.1 Scaling Arguments

In the outer fluid (excluding the gap region) the typical lengthscale is a, the particle radius. Since gravity is neglected in the model and the capillary number, $\mu U/\gamma$, is assumed small (implying viscous forces are small relative to surface tension) the pressure in the fluid is constant to leading order. From the Young-Laplace (2.11) $p = \gamma\kappa$. Therefore the force per unit length on the particle due to the capillary pressure is of magnitude γ. Since we have zero net force on the particle, the force per unit length due to viscous stresses in the gap region must also be $O(\gamma)$.

Figure 2.14 shows the various lengthscales of the gap region, with the gap length denoted L. In the gap region viscous effects are important and we can use lubrication theory. In this region, where the particle is close to the wedge wall, the curvature of the particle is h_{xx}. Therefore

$$\frac{1}{a} \sim h_{xx} \quad \Longrightarrow \quad L \sim (ah)^{1/2}.$$

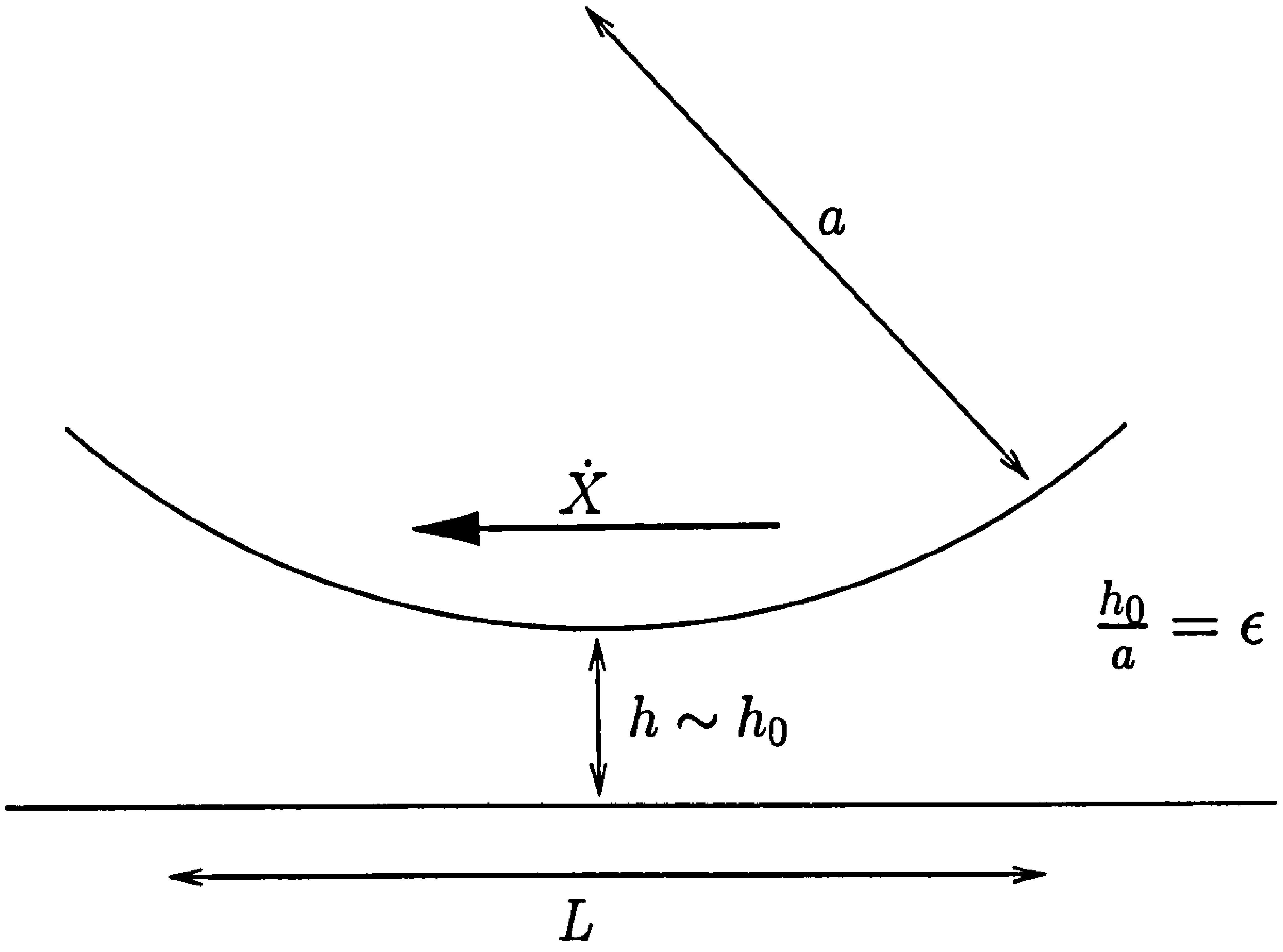

Figure 2.14: Lengthscales in the gap region

From the incompressibility condition, $u_x + v_y = 0$, we obtain

$$v \sim \frac{uh}{L}.$$

This implies that, in the gap, horizontal fluid velocities dominate vertical velocities.

Squeezing (Vertical Particle Motion)

The vertical motion of the particle, v, is given by

$$v \sim \dot{h},$$

implying $u \sim L\dot{h}/h$, and in the gap, using lubrication theory,

$$p_x \sim \mu u_{yy}, \tag{2.15}$$

representing a balance between the pressure gradient and the shear stress. This gives

$$p \sim \frac{\mu \dot{h} a}{h^2}.$$

Since we are looking at the force due to the squeezing motion, the vertical component of the stress vector, $\hat{\mathbf{y}} \cdot \sigma \cdot \hat{\mathbf{n}}$, is dominated by the pressure component. Therefore the force balance gives

$$\gamma \sim \frac{\mu \dot{h} a}{h^2}(ah)^{\frac{1}{2}},$$

since the pressure acting over the gap region must provide a force of $O(\gamma)$. Using the above arguments we obtain the scale of the squeezing pressure,

$$p_q \sim \frac{\gamma}{a}\left(\frac{a}{h}\right)^{\frac{1}{2}},$$

and the squeezing speed,

$$\dot{h} \sim \frac{\gamma}{\mu}\left(\frac{h}{a}\right)^{\frac{3}{2}} \sim \frac{h}{T_q},$$

with timescale,

$$T_q \sim \frac{\mu a}{\gamma}\left(\frac{a}{h}\right)^{\frac{1}{2}}.$$

Sliding (Horizontal Particle Motion)

Horizontal motion of the particle is given by

$$u \sim \dot{X},$$

and as in (2.15) we have a balance between the pressure gradient and viscous effects leading to

$$p \sim \frac{\mu \dot{X}}{h^2}(ah)^{\frac{1}{2}}.$$

The outward pointing unit normal is

$$\frac{(h_x, 1)}{(1 + h_x^2)^{\frac{1}{2}}},$$

and so $\hat{\mathbf{x}} \cdot \sigma \cdot \hat{\mathbf{n}}$ has two dominant components. The pressure component is

$$-p\hat{\mathbf{x}} \cdot \mathbf{I} \cdot \hat{\mathbf{n}} \sim -p h_x \sim \frac{\mu \dot{X}}{h^2}(ah)^{\frac{1}{2}} \frac{h}{(ah)^{\frac{1}{2}}} \sim \frac{\mu \dot{X}}{h}.$$

The viscous drag component is

$$\hat{\mathbf{x}} \cdot \mu(\nabla \mathbf{u} + (\nabla \mathbf{u})^T) \cdot \hat{\mathbf{n}} \sim \mu u_y \sim \frac{\mu \dot{X}}{h},$$

and the force balance is

$$\gamma \sim \frac{\mu \dot{X}}{h}(ah)^{\frac{1}{2}}.$$

These arguments imply that the pressure generated by sliding has magnitude,

$$p_s \sim \frac{\gamma}{a}\left(\frac{a}{h}\right),$$

and the sliding speed has magnitude,

$$\dot{X} \sim \frac{\gamma}{\mu}\left(\frac{h}{a}\right)^{\frac{1}{2}} \sim \frac{a}{T_s},$$

with timescale (the time for the particle to move one radius),

$$T_s \sim \frac{\mu a}{\gamma}\left(\frac{a}{h}\right)^{\frac{1}{2}}.$$

So the sliding and squeezing motion of the particle occur over the same timescale but at different speeds, and so will arise at different orders in our asymptotic expansion below. In the next section we show that pressure-driven drainage through the gap can be neglected.

Drainage

The fluid pressures in the volumes V_1 and V_2 are different in general and therefore there may be a small pressure-driven flow through the gap between the particle and the wall. We can show using a scaling argument that this drainage can be neglected, and that the fluid volumes may be taken to be constant. In the gap region, we have $p_x \sim \mu u_{yy}$. Taking u_D to be the draining velocity, and since $p \sim \gamma/a$, we obtain

$$u_D \sim \frac{\gamma}{\mu}\left(\frac{h}{a}\right)^{\frac{3}{2}},$$

which is a factor of ϵ smaller than $\dot{X}$. We also know that the flux through the gap balances the change in fluid volume, *i.e.* $uh \sim \dot{V}_1$, which gives the draining timescale

$$T_D \sim \left(\frac{\mu a}{\gamma}\right)\left(\frac{a}{h}\right)^{\frac{5}{2}},$$

which is $O(\epsilon^{-2})$ longer than T_s or T_q. Therefore the effects due to drainage are much slower than those due to the squeezing or sliding motion of the particle. Therefore on the sliding and squeezing timescale, since ϵ is small, negligible fluid flows through the gap to change V_1 and V_2, and we can assume that drainage due to the pressure difference is negligible.

2.2.2 Nondimensionalisation

From the previous scalings we nondimensionalise lengths on a, pressures on γ/a, speeds on $\gamma\epsilon^{1/2}/\mu$, times on $a\mu/\gamma\epsilon^{1/2}$ and obtain the dimensionless governing equations for the fluid

$$0 = -\nabla p + \epsilon^{\frac{1}{2}}\nabla^2\mathbf{u}, \quad \nabla\cdot\mathbf{u} = 0, \tag{2.16}$$

and the stress condition at the interface,

$$-p\hat{\mathbf{n}} + \epsilon^{\frac{1}{2}}(\nabla\mathbf{u} + \nabla\mathbf{u}^T)\cdot\hat{\mathbf{n}} = \kappa\hat{\mathbf{n}} \text{ on } s_1, s_2, \tag{2.17}$$

plus equations (2.8, 2.9, 2.10, 2.12, 2.13, 2.14) which are unchanged.

2.2.3 Outer Problem

We now expand p and $\mathbf{u}$ in powers of $\epsilon^{\frac{1}{2}}$,

$$p = p_0 + \epsilon^{\frac{1}{2}}p_1 + \cdots$$

$$\mathbf{u} = \mathbf{u}_0 + \epsilon^{\frac{1}{2}}\mathbf{u}_1 + \cdots$$

and consider the leading order problem. The governing equations give

$$0 = -\nabla p_0, \quad -p_0 = \kappa_0 \text{ on } s_1, s_2.$$

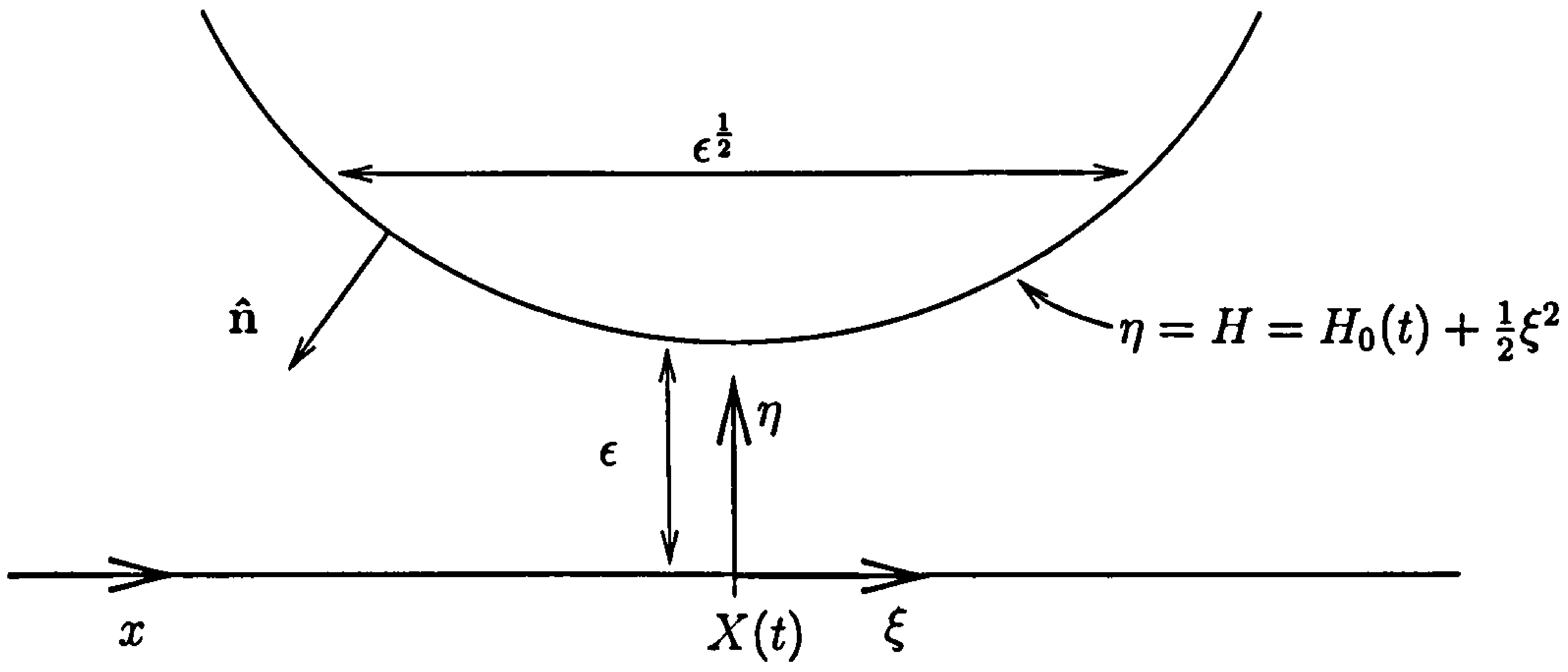

Figure 2.15: Rescaling in the inner gap region

This implies that the flow in the fluid and the gap between the particle and the wall are negligible at leading order, since the gap is order ϵ. Therefore the leading-order problem describes the static case, see §2.1, and we can find the capillary force parallel to the wall, F_p, and the capillary force normal to the wall, F_n, in terms of V_1, V_2, α and X as previously shown. However there must be a small gap between the particle and the wall since the flow and pressures in the gap create a force balancing these capillary forces.

2.2.4 Inner Problem

To understand the dynamics of the gap region we need to rescale the variables. The gap thickness is $O(\epsilon)$ and so the lengthscale of the lubrication region is now $O(\epsilon^{\frac{1}{2}})$. We define new coordinates ξ, η with origin at $(X(t), 0)$ (see Figure 2.15). The variables are rescaled as follows:

$$x = X(t) + \epsilon^{\frac{1}{2}}\xi,$$

$$y = \epsilon\eta, \quad h(x,t) = \epsilon H(\xi, t),$$

$$u = \tilde{u},$$

$$v = \epsilon^{\frac{1}{2}}\tilde{v},$$

$$p = \frac{\tilde{p}}{\epsilon},$$
$$Q = \int_0^h u\,dy = \epsilon\tilde{Q}.$$

From the previous scaling arguments we know that the largest pressure in the gap is p_s which had magnitude $(\gamma/a)(a/h)$, whereas the pressure in the outer fluid had magnitude γ/a. Therefore we take the pressure in the gap to be $O(\epsilon^{-1})$. The height of the bottom of the particle above the wall is now given by $H(0,t) = H_0(t)$ and so the vertical particle speed will be denoted $\dot{H}_0$ and the horizontal speed by $\dot{X}$.

The governing equations for the inner problem are therefore

$$0 = -\frac{\tilde{p}_\xi}{\epsilon^{\frac{3}{2}}} + \left(\frac{\tilde{u}_{\eta\eta}}{\epsilon^{\frac{3}{2}}} + \frac{\tilde{u}_{\xi\xi}}{\epsilon^{\frac{1}{2}}}\right), \tag{2.19a}$$

$$0 = -\frac{\tilde{p}_\eta}{\epsilon^2} + \left(\frac{\tilde{v}_{\eta\eta}}{\epsilon} + \tilde{v}_{\xi\xi}\right), \tag{2.19b}$$

$$\tilde{u}_\xi + \tilde{v}_\eta = 0, \tag{2.19c}$$

$$\tilde{u} = \tilde{v} = 0 \text{ on } \eta = 0, \tag{2.19d}$$

$$\tilde{u} = \dot{X} \text{ on } \eta = H, \tag{2.19e}$$

$$\tilde{v} = \epsilon^{\frac{1}{2}} H_t + (\tilde{u} - \dot{X})H_\xi \text{ on } \eta = H, \tag{2.19f}$$

$$\tilde{Q}_\xi - \dot{X}H_\xi + \epsilon^{\frac{1}{2}} H_t = 0 \text{ on } \eta = H. \tag{2.19g}$$

The x-component of the force on the particle due to viscous stresses in the gap must balance the parallel capillary force, $-F_p$, and the y component must balance the normal capillary force, F_n (since F_n is taken in the negative y direction), so that the condition of zero net force on the particle may be satisfied. Therefore we seek

$$\hat{\mathbf{x}} \cdot \int \sigma \cdot \hat{\mathbf{n}}\, dS = -F_p,$$
$$\hat{\mathbf{y}} \cdot \int \sigma \cdot \hat{\mathbf{n}}\, dS = F_n,$$

where the integrals are evaluated on $\eta = H$, and dS is a small length of the line $\eta = H$. In order to rescale the stress condition we need to find $\hat{\mathbf{n}}$, the outward pointing unit normal to $\eta = H$. In scaled variables the normal is

$$\hat{\mathbf{n}} = \frac{\epsilon^{\frac{1}{2}} H_\xi \hat{\mathbf{x}} - \hat{\mathbf{y}}}{(1 + \epsilon H_\xi^2)^{\frac{1}{2}}} = (n_x, n_y).$$

The rescaled stress vector therefore looks like

$$-\frac{\tilde{p}}{\epsilon}\begin{pmatrix} n_x \\ n_y \end{pmatrix} + \epsilon^{\frac{1}{2}} \begin{pmatrix} \frac{2}{\epsilon^{\frac{1}{2}}}\tilde{u}_\xi & \frac{1}{\epsilon}\tilde{u}_\eta + \tilde{v}_\xi \\ \frac{1}{\epsilon}\tilde{u}_\eta + \tilde{v}_\xi & \frac{2}{\epsilon^{\frac{1}{2}}}\tilde{v}_\eta \end{pmatrix} \begin{pmatrix} n_x \\ n_y \end{pmatrix}.$$

Thus

$$\begin{aligned}
\hat{\mathbf{x}} \cdot \boldsymbol{\sigma} \cdot \hat{\mathbf{n}} = \quad & -\frac{\tilde{p}}{\epsilon} n_x + \epsilon^{\frac{1}{2}} \left(\frac{2}{\epsilon^{\frac{1}{2}}} \tilde{u}_\xi n_x + \left(\frac{1}{\epsilon} \tilde{u}_\eta + \tilde{v}_\xi \right) n_y \right) \\
= \quad & \frac{-\tilde{p} H_\xi}{\epsilon^{\frac{1}{2}} (1 + \epsilon H_\xi^2)^{\frac{1}{2}}} + \epsilon^{\frac{1}{2}} \left(\frac{2 H_\xi \tilde{u}_\xi}{(1 + \epsilon H_\xi^2)^{\frac{1}{2}}} - \frac{1}{\epsilon} \frac{\tilde{u}_\eta}{(1 + \epsilon H_\xi^2)^{\frac{1}{2}}} - \frac{\tilde{v}_\xi}{(1 + \epsilon H_\xi^2)^{\frac{1}{2}}} \right)
\end{aligned}$$

and

$$\begin{aligned}
\hat{\mathbf{y}} \cdot \boldsymbol{\sigma} \cdot \hat{\mathbf{n}} = \quad & -\frac{\tilde{p}}{\epsilon} n_y + \epsilon^{\frac{1}{2}} \left(\left(\frac{1}{\epsilon} \tilde{u}_\eta + \tilde{v}_\xi \right) n_x + \frac{2}{\epsilon^{\frac{1}{2}}} \tilde{v}_\eta n_y \right) \\
= \quad & \frac{\tilde{p}}{\epsilon (1 + \epsilon H_\xi^2)^{\frac{1}{2}}} \\
& + \epsilon^{\frac{1}{2}} \left(+ \frac{1}{\epsilon^{\frac{1}{2}}} \frac{H_\xi \tilde{u}_\eta}{(1 + \epsilon H_\xi^2)^{\frac{1}{2}}} + \frac{\epsilon^{\frac{1}{2}} H_\xi \tilde{v}_\xi}{(1 + \epsilon H_\xi^2)^{\frac{1}{2}}} - \frac{2 \tilde{v}_\eta}{\epsilon^{\frac{1}{2}} (1 + \epsilon H_\xi^2)^{\frac{1}{2}}} \right).
\end{aligned}$$

We know that $dS^2 = dx^2 + dy^2$ so in scaled variables we have $dS = \epsilon^{\frac{1}{2}} d\xi (1 + \epsilon H_\xi^2)^{\frac{1}{2}}$. Therefore the force balance integrals are

$$\int \hat{\mathbf{x}} \cdot \sigma \cdot \hat{\mathbf{n}} \, dS = \int_{-\infty}^{\infty} (-\tilde{p} H_\xi + 2\epsilon H_\xi \tilde{u}_\xi - \tilde{u}_\eta - \epsilon \tilde{v}_\xi) d\xi = -F_p \tag{2.20}$$

$$\int \hat{\mathbf{y}} \cdot \sigma \cdot \hat{\mathbf{n}} \, dS = \int_{-\infty}^{\infty} (\frac{\tilde{p}}{\epsilon^{\frac{1}{2}}} + \tilde{u}_\eta H_\xi \epsilon^{\frac{1}{2}} + \epsilon^{\frac{3}{2}} \tilde{v}_\xi H_\xi + 2\epsilon^{\frac{1}{2}} \tilde{v}_\eta) d\xi = F_n \tag{2.21}$$

As before we expand the variables,

$$\begin{aligned}
\tilde{u} &= \tilde{u}_0 + \epsilon^{\frac{1}{2}} \tilde{u}_1 + O(\epsilon) \\
\tilde{v} &= \tilde{v}_0 + \epsilon^{\frac{1}{2}} \tilde{v}_1 + O(\epsilon) \\
\tilde{p} &= \tilde{p}_0 + \epsilon^{\frac{1}{2}} \tilde{p}_1 + O(\epsilon) \\
\tilde{Q} &= \tilde{Q}_0 + \epsilon^{\frac{1}{2}} \tilde{Q}_1 + O(\epsilon)
\end{aligned}$$

and compare orders of $\epsilon^{\frac{1}{2}}$. Firstly however we require an extra condition on the volume V, formally checking the scaling arguments above.

2.2.5 Volume Condition

Since there is no flux through the contact lines, any change in the fluid volume V_1 (or V_2) is due to flux through the gap between the particle and the wall. As a result of this we can obtain the following conditions (for derivation of these, see Appendix A):

$$\dot{V}_1 = Q|_X - \dot{X}h|_X, \tag{2.22}$$

$$\dot{V}_2 = -Q|_X + \dot{X}h|_X. \tag{2.23}$$

Hence $\dot{V}_1 + \dot{V}_2 = 0$ as required by the constant fluid volume condition.

To apply these conditions to the inner problem we have to rescale the variables. Let

$$V_1 = V_{10} + \epsilon^{\frac{1}{2}} V_{11} + \epsilon V_{12} + \epsilon^{\frac{3}{2}} V_{13} + O(\epsilon^2),$$

and compare orders of $\epsilon^{\frac{1}{2}}$. We obtain

$$\dot{V}_{10} = \dot{V}_{11} = 0, \tag{2.24}$$

$$\dot{V}_{12} = \tilde{Q}_0|_X - \dot{X}H|_X, \tag{2.25}$$

$$\dot{V}_{13} = \tilde{Q}_1|_X. \tag{2.26}$$

From equation (2.24) we can see that at leading order and $O(\epsilon^{1/2})$ the rate of change of volume is zero. This means pressure-driven flow is negligible (as anticipated) and that at leading order we can assume there is no flow through the gap and V_1, V_2 are constant.

2.2.6 Leading Order: Sliding Motion

Looking at the leading order terms in the governing equations and the force balance integrals we obtain

$$\begin{aligned}
&0 = -\tilde{p}_{0\xi} + \tilde{u}_{0\eta\eta},\\
&0 = -\tilde{p}_{0\eta},\\
&\tilde{u}_{0\xi} + \tilde{v}_{0\eta} = 0,\\
&\tilde{u}_0 = \tilde{v}_0 = 0 \quad \text{on} \quad \eta = 0,\\
&\tilde{u}_0 = \dot{X} \quad \text{on} \quad \eta = H,\\
&\tilde{v}_0 = 0 \quad \text{on} \quad \eta = H,\\
&\tilde{Q}_{0\xi} - \dot{X} H_\xi = 0,\\
&\int_{-\infty}^{\infty} (-\tilde{p}_0 H_\xi - \tilde{u}_{0\eta}) \, d\xi = -F_p, \qquad (2.27)\\
&\int_{-\infty}^{\infty} \tilde{p}_0 d\xi = 0. \qquad (2.28)
\end{aligned}$$

We see that the leading order problem describes the sliding motion. From the governing equations we obtain $\tilde{p}_0 = \tilde{p}_0(\xi)$ and $\tilde{Q}_0 - \dot{X}H = f(t)$, where f is an arbitrary function. We can solve to get equations for the fluid speed and the flux,

$$\tilde{u}_0 = \frac{\eta \dot{X}}{H} - \frac{\tilde{p}_{0\xi}\eta}{2}(H - \eta) \qquad (2.29)$$

$$\tilde{Q}_0 = \int_0^H \tilde{u}_0 \, d\eta = \frac{\dot{X}H}{2} - \frac{\tilde{p}_{0\xi}H^3}{12} = \dot{X}H + f(t) \qquad (2.30)$$

From §2.2.5 we know at $\xi = 0$, $\tilde{Q}_0 = \dot{V}_{12} + \dot{X}H$ and therefore $f(t) = \dot{V}_{12}$, leading to

$$\frac{-\tilde{p}_{0\xi}H^3}{12} = \dot{V}_{12} + \frac{\dot{X}H}{2}.$$

We rearrange this to find

$$\tilde{p}_0 = -12 \int_{-\infty}^{\xi} \left(\frac{\dot{V}_{12}}{H^3} + \frac{\dot{X}}{2H^2} \right) d\xi.$$

Using the boundary condition $\tilde{p}_0 \longrightarrow 0$, $\xi \longrightarrow \pm\infty$, and rearranging we obtain

$$\dot{V}_{12} = -\frac{\dot{X}}{2}\frac{\int_{-\infty}^{\infty} H^{-2}\, d\xi}{\int_{-\infty}^{\infty} H^{-3}\, d\xi} = -\frac{2}{3}\dot{X}H_0.$$

Therefore

$$\tilde{p}_0 = \frac{8\dot{X}\xi}{(2H_0+\xi^2)^2}.$$

Equation (2.28) is satisfied and, using (2.29), (2.27) becomes

$$F_p = \frac{2\sqrt{2}\pi\dot{X}}{H_0^{\frac{1}{2}}}. \tag{2.31}$$

2.2.7 Next Order ($O(\epsilon^{\frac{1}{2}})$): Squeezing Motion

Looking at the $O(\epsilon^{\frac{1}{2}})$ terms in the governing equations and the force balance integrals we obtain

$$\begin{aligned}
&0 = -\tilde{p}_{1\xi} + \tilde{u}_{1\eta\eta},\\
&0 = -\tilde{p}_{1\eta},\\
&\tilde{u}_{1\xi} + \tilde{v}_{1\eta} = 0,\\
&\tilde{u}_1 = \tilde{v}_1 = 0 \quad \text{on} \quad \eta = 0,\\
&\tilde{u}_1 = 0 \quad \text{on} \quad \eta = H,\\
&\tilde{v}_1 = H_t \quad \text{on} \quad \eta = H,\\
&\tilde{Q}_{1\xi} + H_t = 0,\\
&\int_{-\infty}^{\infty} (-\tilde{p}_1 H_\xi - \tilde{u}_{1\eta})\, d\xi = 0, && (2.32)\\
&\int_{-\infty}^{\infty} \tilde{p}_1 d\xi = F_n. && (2.33)
\end{aligned}$$

This problem describes the squeezing motion. We obtain $\tilde{p}_1 = \tilde{p}_1(\xi)$ and $\tilde{Q}_1 = g(t) - \dot{H}_0\xi$, where $g(t)$ is an arbitrary function. Solving for the fluid speed and the flux gives

$$\tilde{u}_1 = -\frac{\tilde{p}_{1\xi}\eta}{2}(H-\eta), \tag{2.34}$$

$$\tilde{Q}_1 = \int_0^H \tilde{u}_1\, d\eta = -\frac{\tilde{p}_{1\xi}H^3}{12} = g(t) - \dot{H}_0\xi. \tag{2.35}$$

From §2.2.5 we have $\tilde{Q}_1 = \dot{V}_{13}$ at $\xi = 0$, and so $g(t) = \dot{V}_{13}$. So we have

$$-\frac{\tilde{p}_{1\xi} H^3}{12} = \dot{V}_{13} - \dot{H}_0 \xi.$$

If we apply $\tilde{p}_1 \longrightarrow 0$, $\xi \longrightarrow \pm\infty$ as before, we obtain $\dot{V}_{13} = 0$ and hence

$$\tilde{p}_1 = 12 \int_{-\infty}^{\xi} \frac{\dot{H}_0 \xi}{H^3} \, d\xi = \frac{-24 \dot{H}_0}{(2H_0 + \xi^2)^2}.$$

Using (2.34), equation (2.32) is satisfied and (2.33) becomes

$$F_n = -\frac{3\sqrt{2}\pi \dot{H}_0}{H_0^{\frac{3}{2}}}. \tag{2.36}$$

Now, for given values of the wedge angle, the fluid volumes, and the initial position of the particle, we have two differential equations for the sliding and the squeezing speed of the particle relative to the wall,

$$\dot{X} = \frac{F_p H_0^{\frac{1}{2}}}{2\sqrt{2}\pi} \tag{2.37}$$

$$\dot{H}_0 = -\frac{F_n H_0^{\frac{3}{2}}}{3\sqrt{2}\pi}. \tag{2.38}$$

2.2.8 Numerical Simulations

We solved (2.37, 2.38) numerically using NAG routines D02PVF and D02PCF which integrate using Runge-Kutta methods with an adaptive timestep. Given values for the parameters V, total fluid volume, α, wedge angle, and X_0, initial position of the particle in the x direction, we can find X, H_0 at time t. Due to the rescaling $H_0(0) = 1$. From §2.2.5 we know that V_1 and V_2 change by $O(\epsilon)$ during the motion of the particle, so we assume V_1, V_2 to be constant and dependent on X_0, α and V. At each timestep we calculate F_p and F_n for the current value of X as in §2.1 using

$$F_p = \cos\theta_1 - \cos\theta_2 + \frac{(1+\cos\theta_1)}{R_1} - \frac{(1+\cos\theta_2)}{R_2},$$

$$F_n = \sin\theta_1 + \sin\theta_2 + \frac{\sin\theta_1}{R_1} + \frac{\sin\theta_2}{R_2}.$$

Figure 2.16 shows the solutions for the case $V = 10$, $\alpha = \pi/6$, $X_0 = 4$. From graph (*a*) we see that the particle moves towards the corner of the wedge at a decreasing speed until it reaches its equilibrium position $X \approx 1.671$ (where $F_p = 0$), shown by a dotted line on the graph. Similarly graph (*b*) shows that the particle is pulled quickly into the wall but slows down before it gets there. Graph (*c*) illustrates the shape of the trajectory that the particle travels through the fluid, moving towards the equilibrium position, $X \approx 1.671$, again shown by the dotted line.

For given V, α, each initial deposition site has a different corresponding equilibrium point. This is because we have assumed that the fluid is divided vertically into two fixed volumes, V_1 and V_2, at the deposition point. We showed in §2.2.5 that drainage through the gap, *i.e.* rate of change of volume of V_1 (or V_2) is order ϵ and hence we have assumed it to be negligible. Therefore since the values of V_1 and V_2 are marginally different for each initial position, the equilibrium point X_{eq} is dependent on the initial conditions and will vary by a small amount for each V and α. In reality, over long timescales, the two volumes will adjust and we anticipate that there will be a unique equilibrium point for each V and α.

In §2.1 we found there were four regions of the (V, α) parameter space corresponding to different predicted particle behaviours (Figure 2.9). For each region we take a pair of values for V, α and perform the simulation for a range of initial positions, X_0.

For the region-A example we take $V = 6$, $\alpha = \pi/8$ and for region D we take $V = 14$, $\alpha = \pi/5$. In the static problem we found that the initial force on a particle in either region is always negative (see Figure 2.17). In the region A example the upper limit for X_0 is 6.917 (where particle is at the contact line) and the lower limit is $X_0 = 0.414$ (where the particle is in the corner). For the region D example the upper limit is $X_0 = 8.674$ and the lower is $X_0 = 2.355$

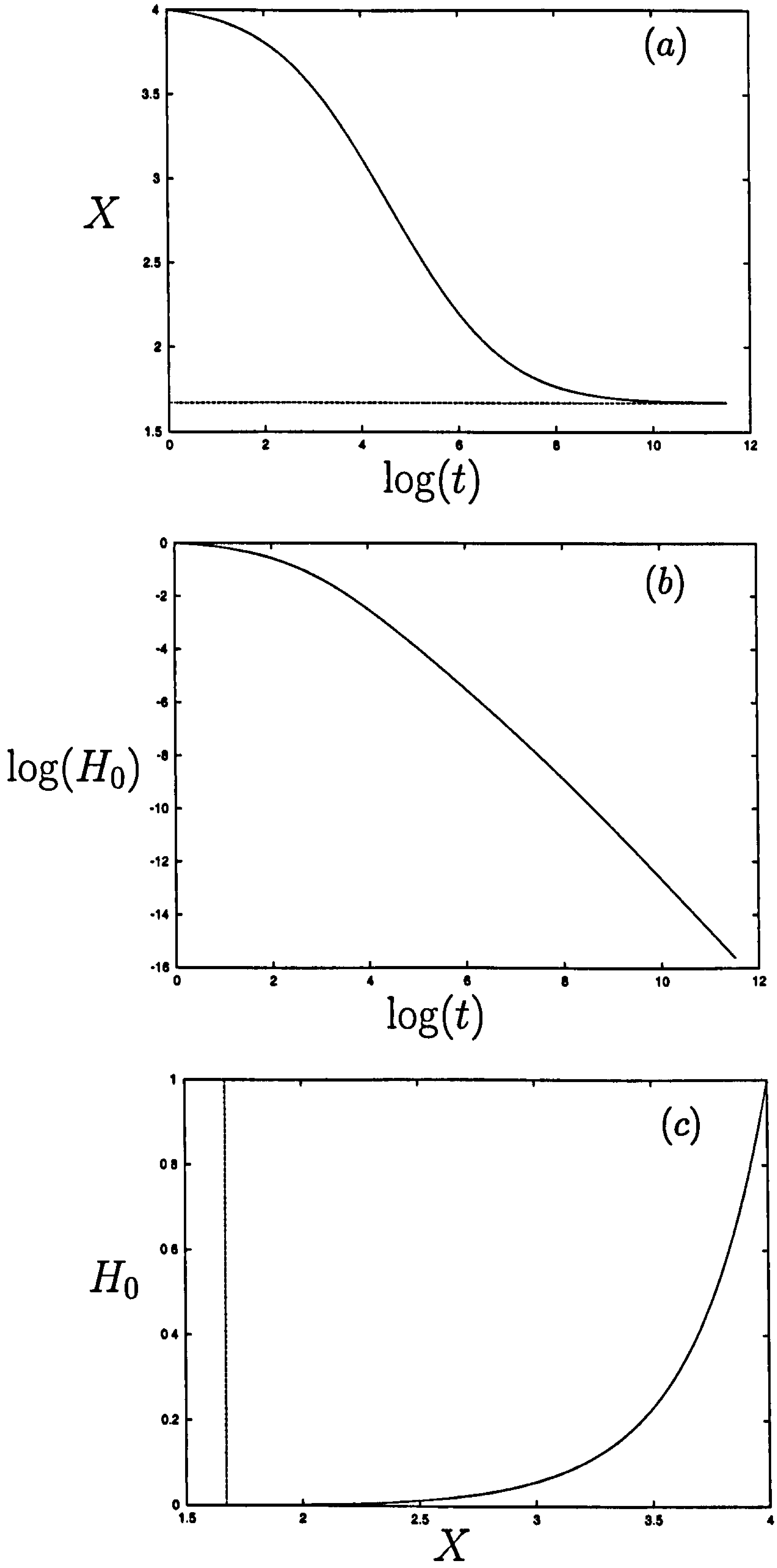

Figure 2.16: Movement of the particle for the case $V = 10$, $\alpha = \pi/6$, $X_0 = 4$ (*a*) horizontal position against $\log(t)$, (*b*) $\log(H_0)$ against $\log(t)$, (*c*) horizontal position against vertical position (relative to the wedge wall).

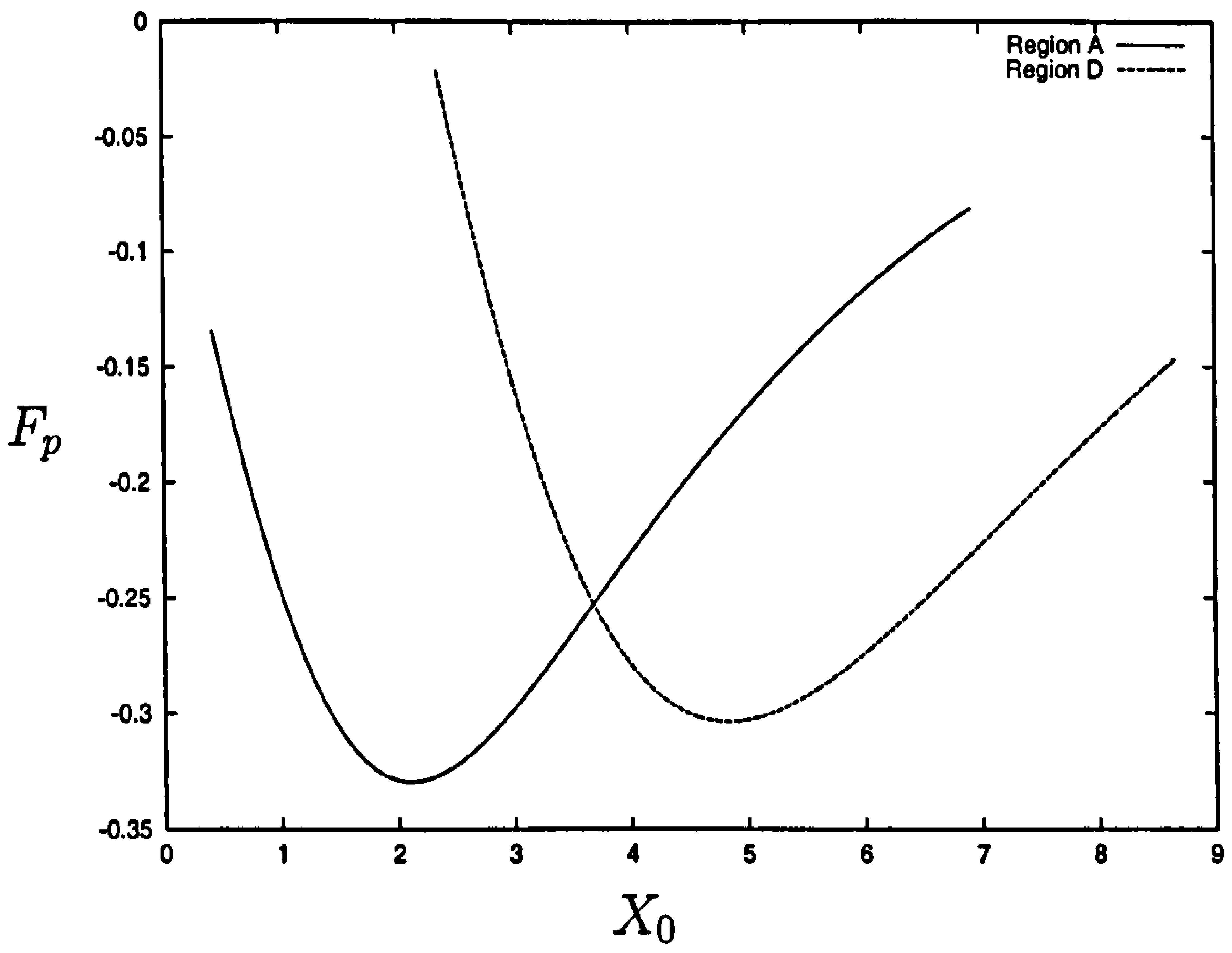

Figure 2.17: Initial parallel force against initial position for a particle in region A and a particle in region D.

(where the particle is initially submerged). Once the particle has moved from its initial position, however, the force-distance profile may change.

Figures 2.18(a),(b) show the region A and region D cases respectively up to $t = 10^5$. From Figure 2.18(a) we can see that the particle moves towards the corner but its speed decreases as time increases. For small values of X_0 the particle moves into the corner and remains there. Figure 2.18(b) shows similar behaviour except the simulation stops for small X_0 due to submersion of the particle. Since F_p depends on V_1, V_2 for each X_0 there turns out to be a corresponding equilibrium point towards which the particle appears to move, where $F_p = 0$. The range of X_{eq} for these values of X_0 is marked on the side of the graphs. For some X_0, the particles reach this equilibrium point relatively quickly, for example on Figure 2.18(b) particles initially at $X_0 = 3$ and $X_0 = 3.5$ reach their equilibrium points of $X_{eq} = 2.421$ and $X_{eq} = 2.513$ respectively and remain there. From the static problem we predicted that in regions A and D there would be no equilibrium. We see now that the results from the static case are misleading. Since there is no motion, the static problem tells us only about the initial behaviour of the particle. In regions A and D the force is always negative and the particle will always move towards the corner, but once in motion the static model breaks down and the particle moves to an equilibrium predicted by the dynamic model.

For the region-B example we take $V = 2$ and $\alpha = \pi/30$. The upper limit is $X_0 = 7.581$ and the lower limit is $X_0 = 0.105$ (where the particle is in the corner). The static problem predicts that for $X_0 > 5.297$ the particle initially moves towards the contact line and for $X_0 < 5.297$ the particle initially moves towards the corner (see Figure 2.19).

Figure 2.20 shows what happens for a range of X_0. For $X_0 > 5.297$ the particles do move towards the contact line but at a very slow speed. For $X_0 < 5.297$ particles move towards the corner and for X_0 sufficiently small they move into the corner and remain there, see for example the case $X_0 = 1$ in Figure 2.20. Again we can calculate each particle's equilibrium point, marked on Figure 2.20 and we find that a particle will always move in the opposite direction to its equilibrium along the wedge wall.

For region C we take $V = 10$ and $\alpha = \pi/6$. The upper limit is $X_0 = 7.875$ and the lower is $X_0 = 1.107$ (where the particle is initially submerged). The static problem predicts that the particle moves to a stable equilibrium point for all allowable values of X_0 (see Figure 2.21). From Figure 2.22 we see that the particles follow this behaviour. For particles with X_0 small we can see that they move to their respective equilibrium positions quickly, for example $X_0 \leq 4$ in Figure 2.22. If $X_0 = 1.18$ the particle will remain stationary (in the horizontal direction).

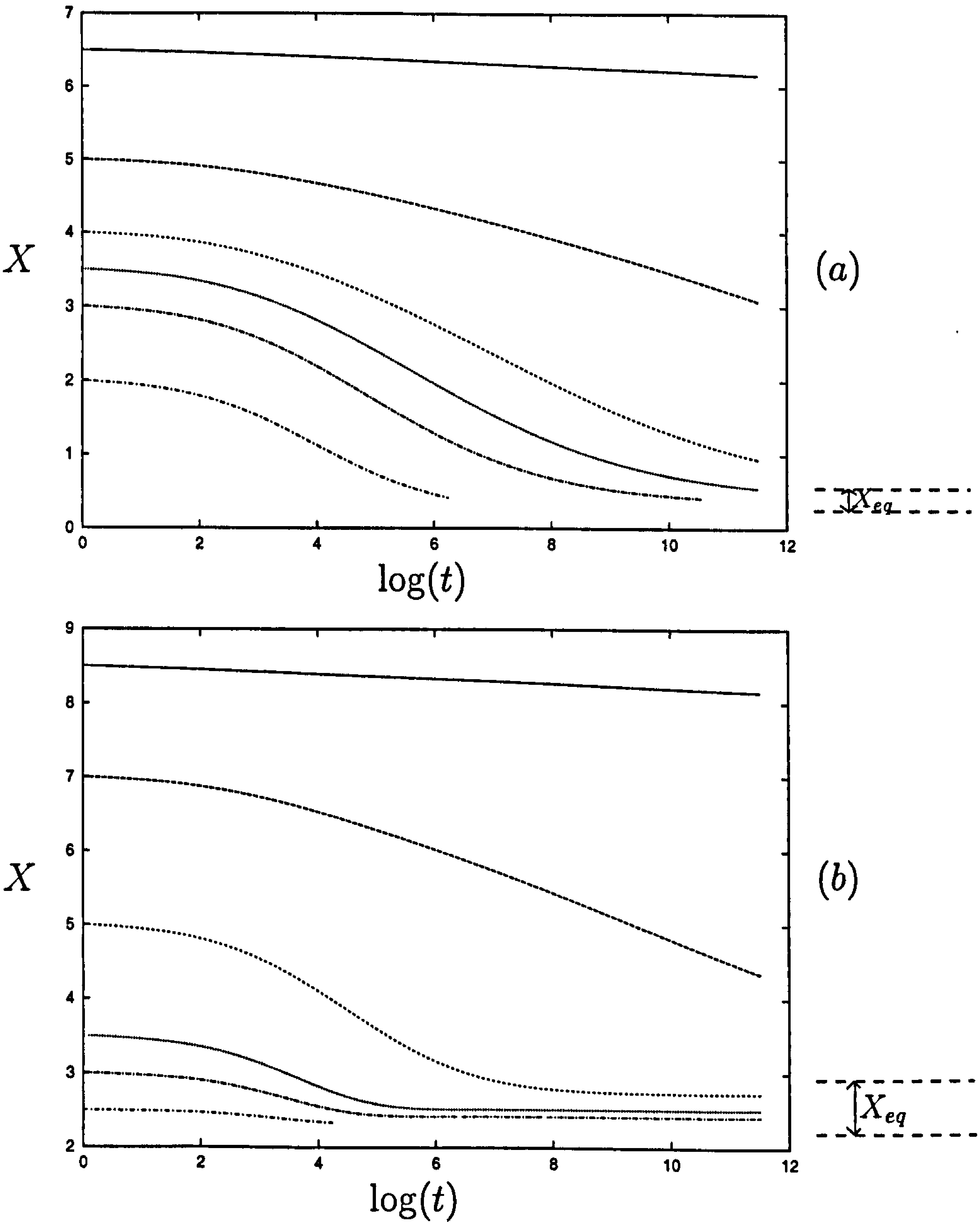

Figure 2.18: (*a*) X varying against $\log t$ with $V = 6$, $\alpha = \pi/8$ (region A) for a range of X_0. Each X_0 has a corresponding equilibrium point, X_{eq}, in the range marked. (*b*) X varying against $\log t$ with $V = 14$, $\alpha = \pi/5$ (region D) for a range of X_0.

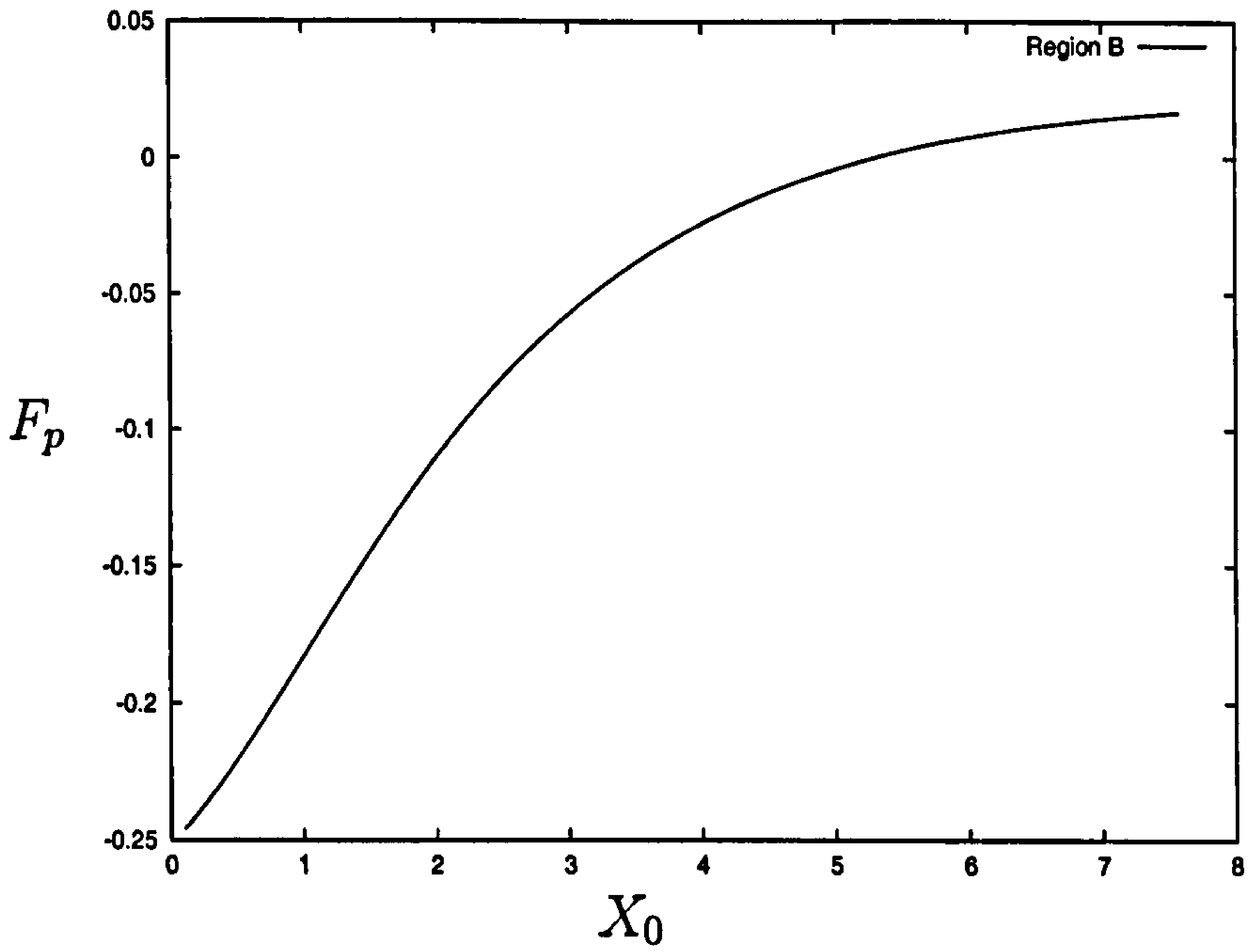

Figure 2.19: Initial parallel force against initial position for a particle in region B.

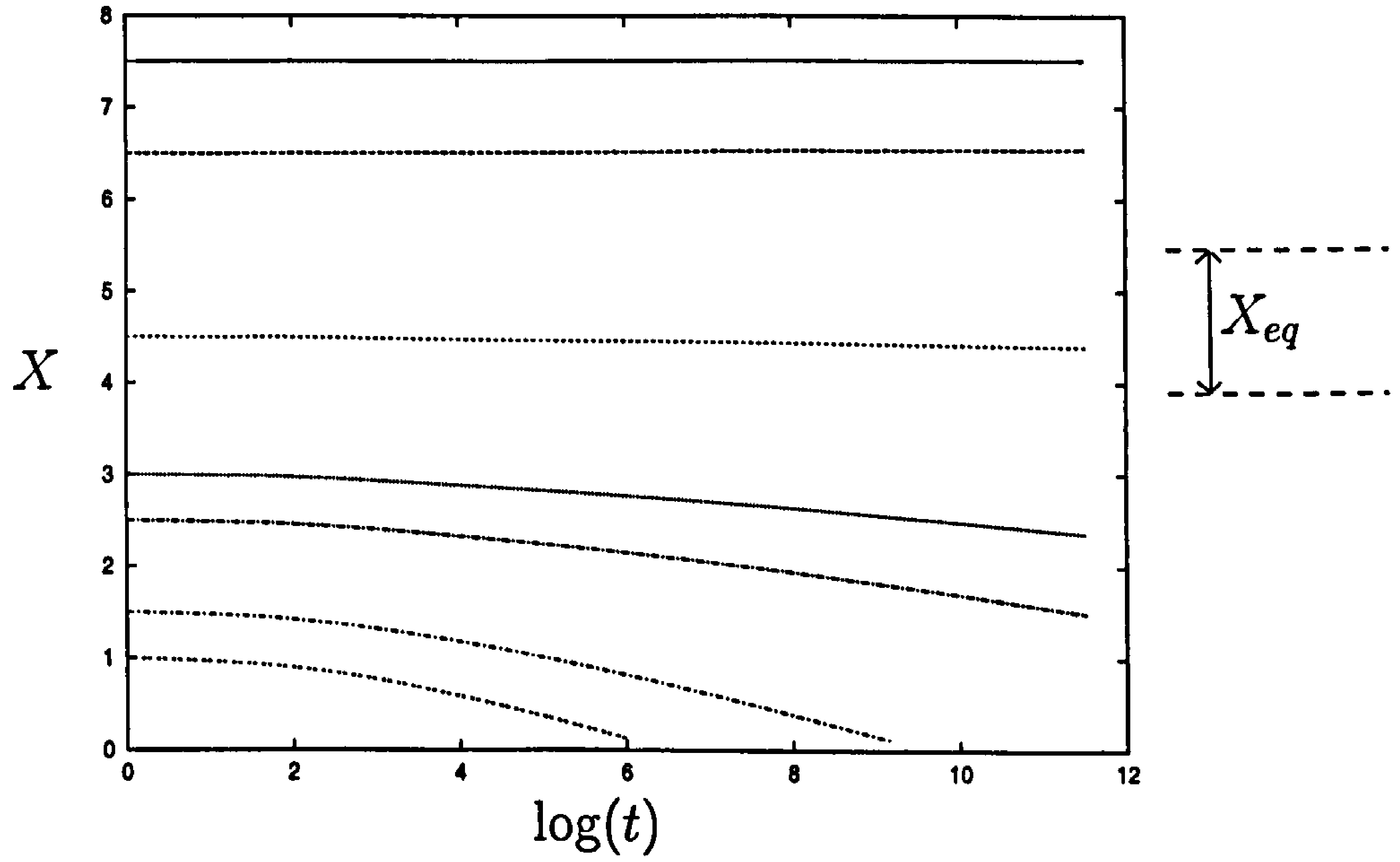

Figure 2.20: X varying against $\log t$ with $V = 2$, $\alpha = \pi/30$ (region B) for a range of X_0.

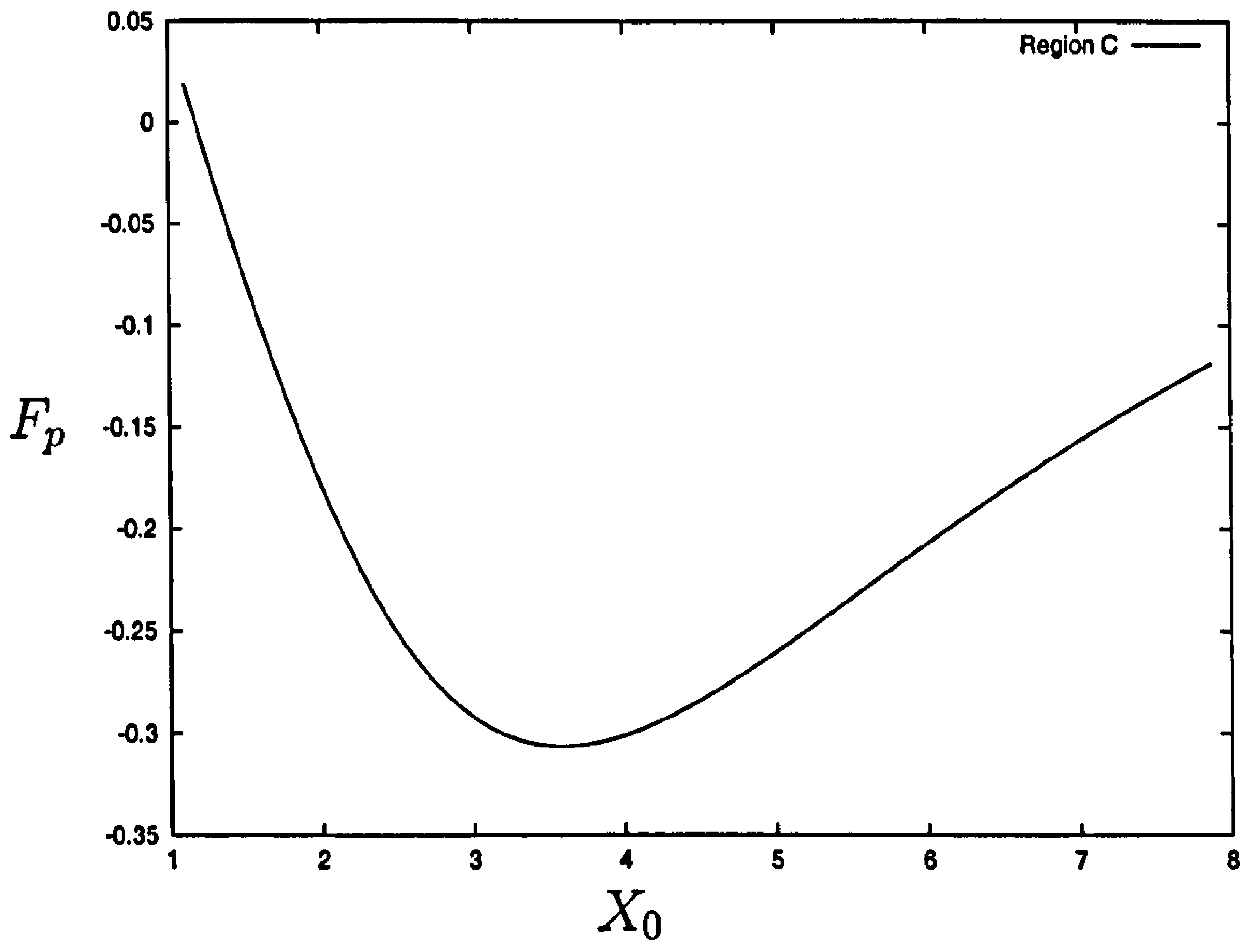

Figure 2.21: Initial parallel force against initial position for a particle in region C.

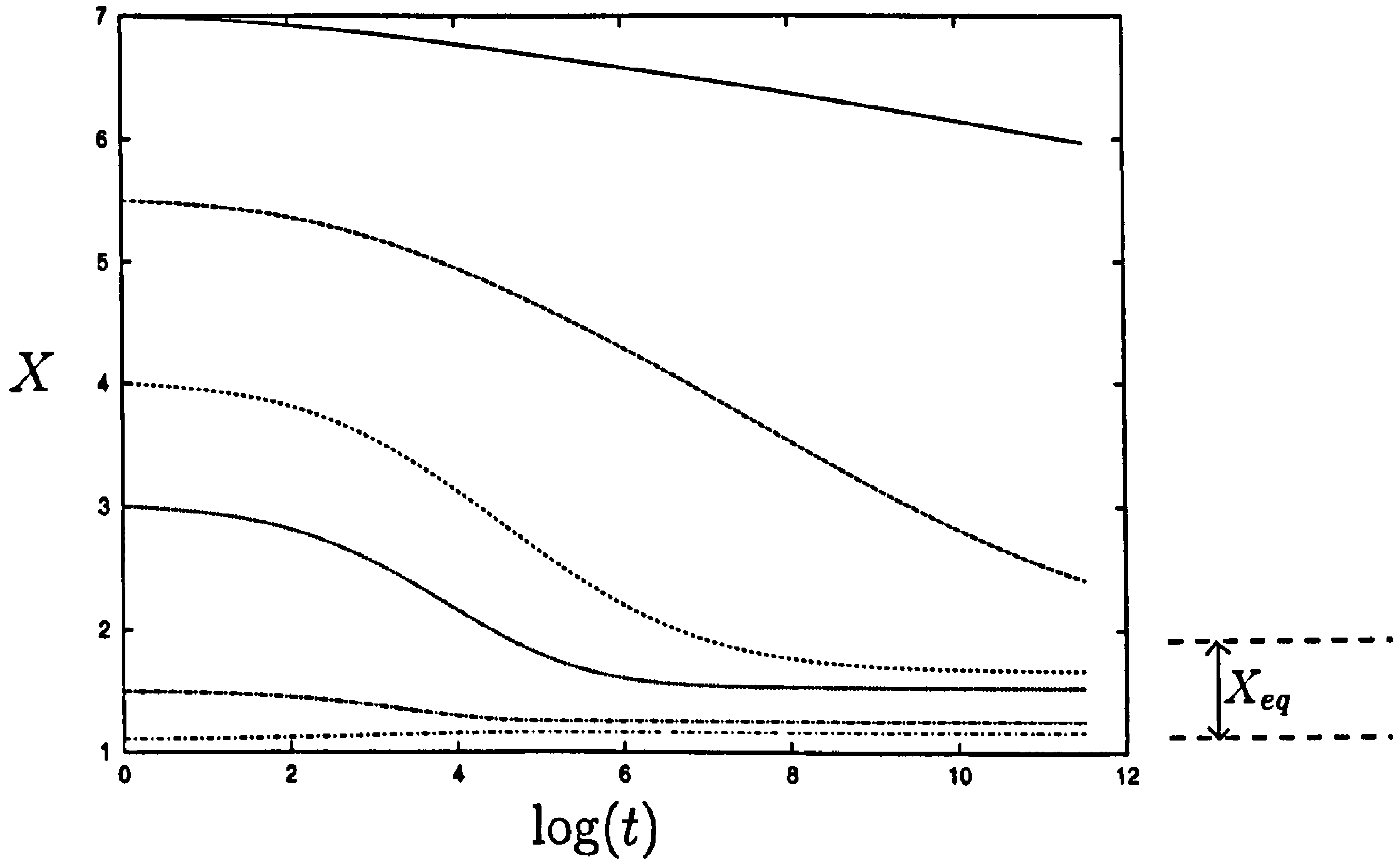

Figure 2.22: X varying against $\log t$ with $V = 10$, $\alpha = \pi/6$ (region C) for a range of X_0.

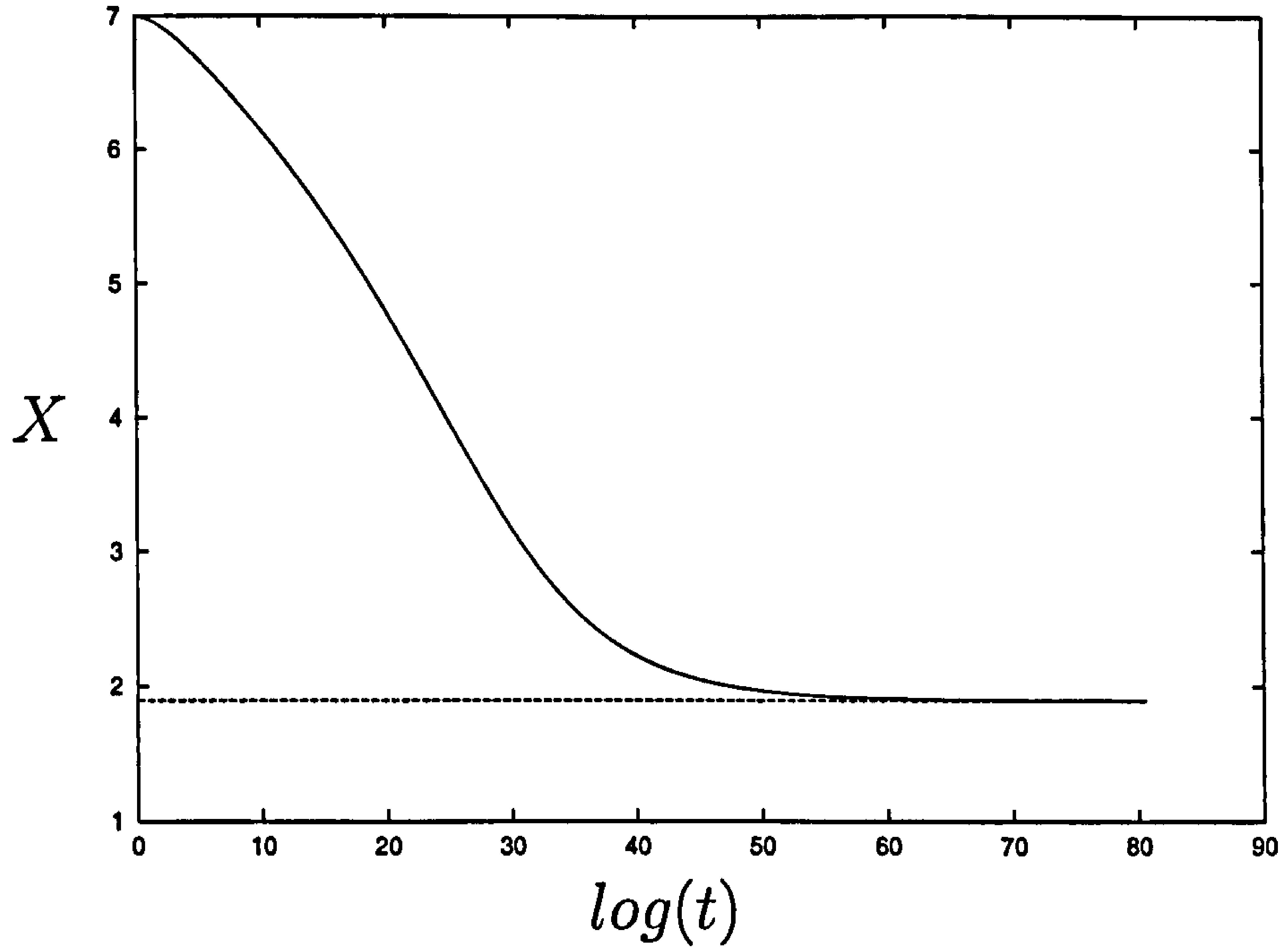

Figure 2.23: X against $\log(t)$ for $V = 10$, $\alpha = \pi/6$, $X_0 = 7$ with t up to 10^{35} showing the particle moving to its equilibrium $X_{eq} = 1.895$ (dashed line).

The previous simulations were run for t up to 10^5. We would like to know if all particles shown in this example move to a stationary position at long times regardless of X_0. We look at the case $V = 10$, $\alpha = \pi/6$, $X_0 = 7$ (region C) as shown on Figure 2.22. Figure 2.23 illustrates the particle behaviour up to $t = 10^{35}$. We see that at long time the particle with $X_0 = 7$ reaches its equilibrium position $X_{eq} = 1.895$. Similar runs confirm that particles with the previous sets of parameter values (see Figures 2.18, 2.20, 2.22) all move to their equilibrium position, to the contact line, to the corner or become submerged at sufficiently long time.

From the scaling arguments in §2.2.1 we know that the timescale for sliding and squeezing motion is $\mu a^{3/2}/\gamma h^{1/2}$. For typical parameter values observed in airways, this is of the order of 10^{-5}. Therefore we see that although the behaviour observed in Figures 2.18,2.20,2.22 will occur in approximately one second, the time taken for all the particles to reach their final position is approximately 10^{30} seconds, which is clearly unrealistic.

2.2.9 Analysis

We now look at the differential equations (2.37), (2.38) analytically. We can expand $F_p(X)$ and $F_n(X)$ as Taylor series about a point $X = X_p$. If $F_p(X_p) \neq 0$ then $F_p(X) \approx F_p(X_p)$, $F_n(X) \approx F_n(X_p)$ and we can integrate (2.38) to get

$$H_0^{\frac{1}{2}} \approx \frac{6\sqrt{2}\pi}{F_n(X_p)t + C_1}, \tag{2.39}$$

where C_1 is an undefined constant. Equation (2.37) then integrates to give

$$X \approx X_p + \frac{3F_p(X_p)}{F_n(X_p)} \ln(F_n(X_p)t + C_1) + C_2, \tag{2.40}$$

where C_2 is also constant. This approximate solution for X near X_p where $X_p \neq X_{eq}$ shows that the particle's transverse motion is slow on the sliding and squeezing timescale.

If $F_p(X_p) = 0$, *i.e.* if $X_p = X_{eq}$, the particle's equilibrium point, then $F_p(X) \approx (X - X_{eq})F_p'(X_{eq})$, $F_n(X) \approx F_n(X_{eq})$, and (2.37) becomes

$$\frac{d}{dt}(X - X_{eq}) = \frac{3F_p'(X_{eq})}{F_n(X_{eq})t + C_1}(X - X_{eq}).$$

Letting $z = X - X_{eq}$ and integrating with respect to z, we obtain

$$X = X_{eq} + C_3(F_n(X_{eq})t + C_1)^k, \tag{2.41}$$

where C_3 is a constant and $k = 3F_p'(X_{eq})/F_n(X_{eq})$.

We can check these predictions against the numerical simulations. We take again the case $X_0 = 7$ in region C, and let $X_p = 4$. We can calculate $F_p(X_p)$, $F_n(X_p)$ and at large times we can neglect C_1 giving the analytic solution about $X = 4$ to be $X = 4 - 0.169\ln(4.855t) + C_2$. For this case $X_{eq} = 1.895$ and so near the equilibrium we have $X = 1.895 + C_3(4.235t)^{-0.3227}$, again neglecting C_1 at large times. Figure 2.24 shows good agreement between the analytic

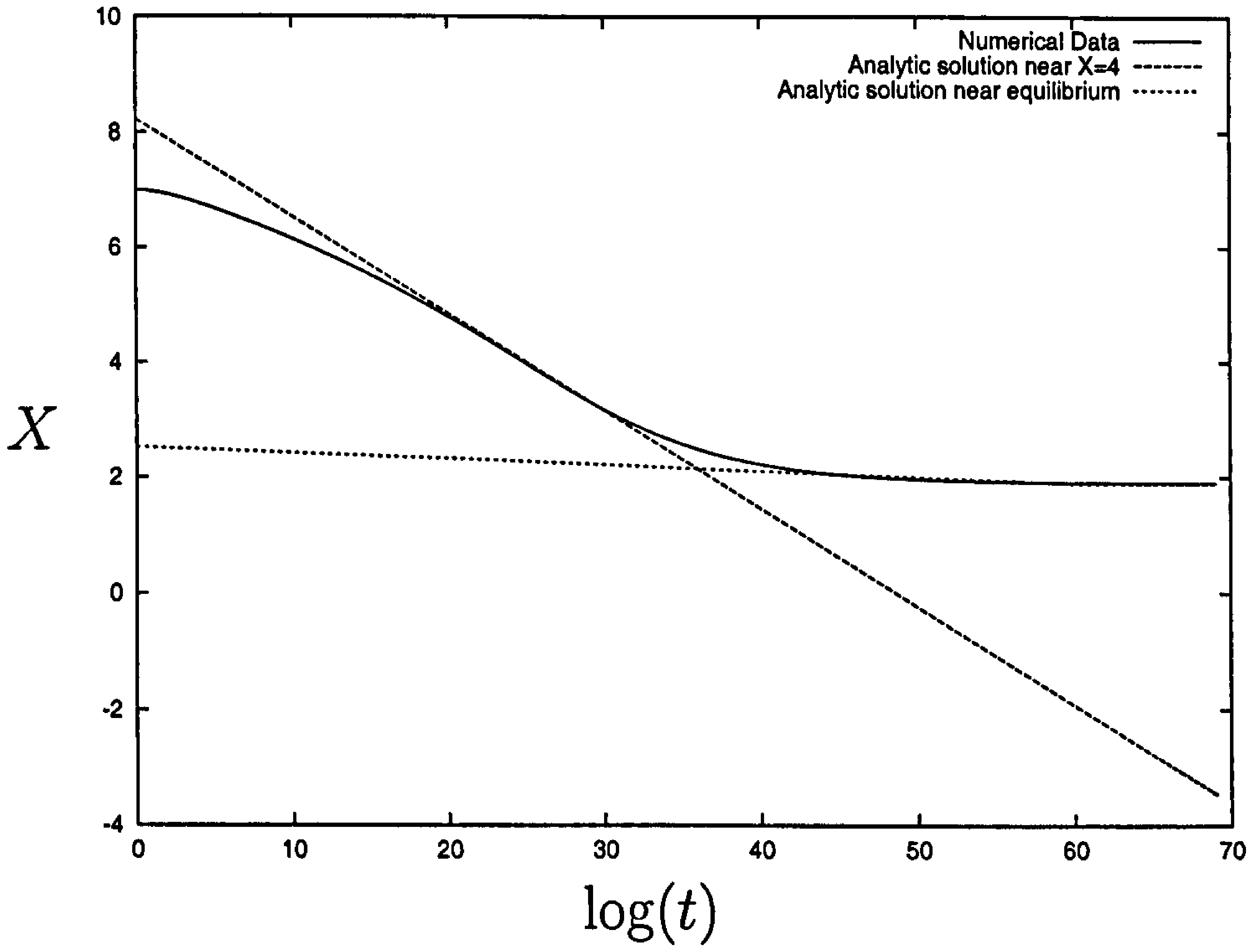

Figure 2.24: X against $\log(t)$ showing agreement between analytic solutions (2.40, 2.41) and numerical simulation.

solutions (2.40, 2.41), taking $C_2 = 4.5$ and $C_3 = 1$, and the data obtained from the numerical simulation.

In summary, simulations suggest the following pattern of behaviour. Particles in region A of the (V, α)-parameter space (Figure 2.25) will move slowly towards the corner and either reach an equilibrium position or move into the corner and remain there. Particles in region D have similar behaviour but will become submerged before they can reach the corner. In region C all particles move to an equilibrium position, with the direction of movement dependent on initial position. Particles in region B will move into the corner or to the contact line, again depending on their initial position.

To understand better the dynamics suggested by simulations we consider the effect of varying V for physically realistic values of α. For given values of

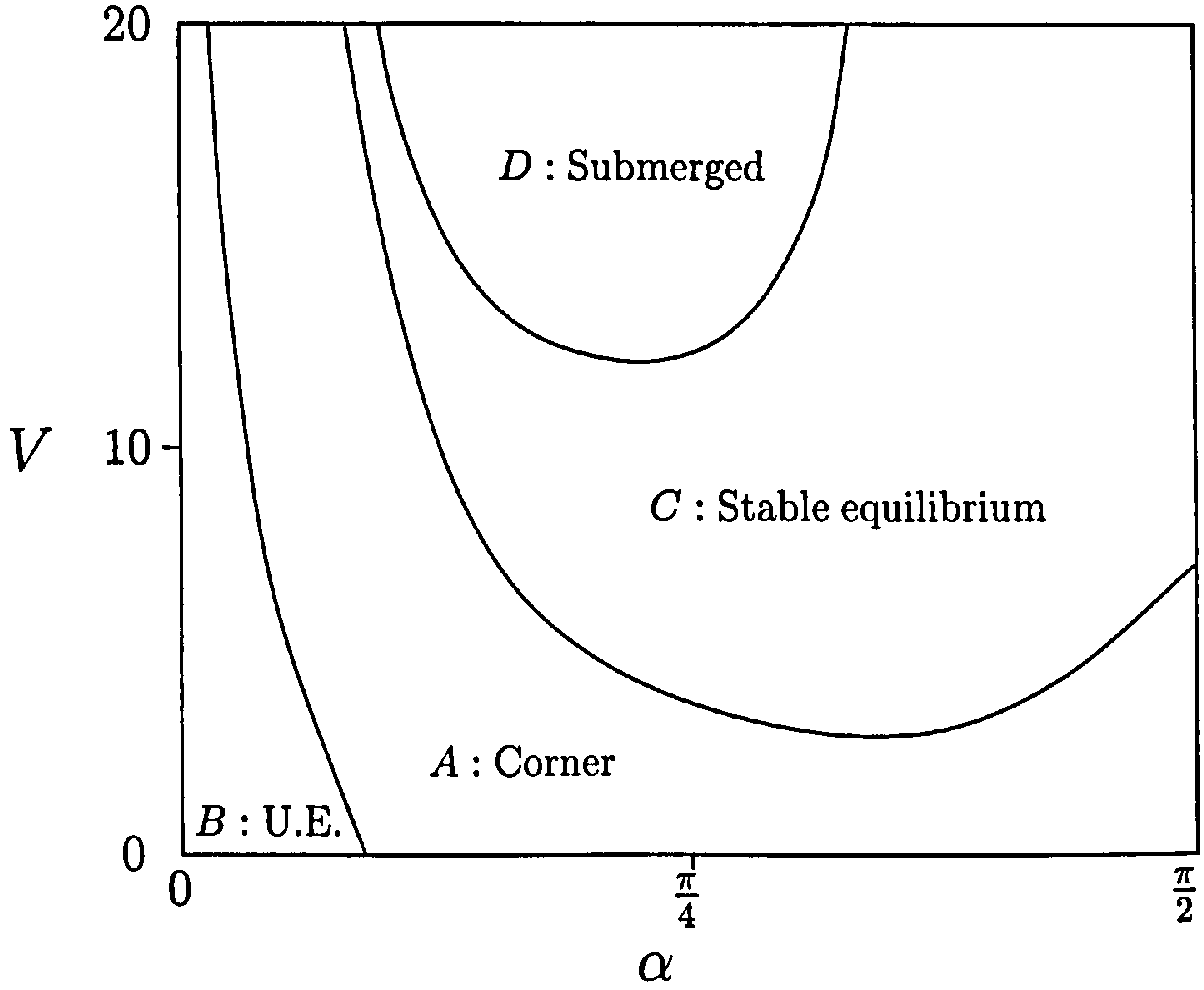

Figure 2.25: Schematic of the V, α parameter space showing the four regions (from Figure 2.9). In Region B an unstable equilibrium position exists and particles will move towards the corner or towards the contact line. In Region C particles move towards a stable equilibrium position. In Regions A and D particles move towards a stable equilibrium position but will either reach the corner (Region A) or become submerged (Region D) first and the model will break down.

α, V there is a short range of X values where a particle's equilibrium position, X_{eq}, will lie; the exact value of X_{eq} depends on the particle's initial deposition site. As V increases the typical equilibrium position for a particle is positioned further away from the corner. For an alveolar corner, we assume that α will typically lie in the range $\pi/8 < \alpha < \pi/4$ [78]. Therefore for small V, Region A behaviour is valid (see Figure 2.25). In Region A a typical equilibrium position (if it exists) will be close to the corner. Therefore all particles will essentially move into the corner. As V increases, Region C behaviour becomes valid. In Region C, X_{eq} will be further away from the corner. Particles can be deposited either side of this point and all particles will move to the equilibrium. For large V (for this range of α) Region D behaviour is valid. In Region D the typical equilibrium position (if it exists) is situated further still from the corner, however particles deposited to the left of this point will be submerged due to the large volume of fluid in the wedge (at which point the model becomes invalid). Therefore all particles will move in the direction of the corner towards X_{eq}. If an equilibrium position does not exist particles move in the direction of the corner but become submerged.

2.3 Summary and Conclusions

In this chapter we consider the behaviour of an inhaled particle after deposition in an alveolar corner. We model this in two dimensions by studying a cylinder partially immersed in a fluid-filled wedge.

Initially we consider the static problem of the cylinder fixed relative to the wedge wall. We calculate the magnitude and direction of the initial net force acting on the particle due to capillary effects. The static model shows a range of particle behaviour is possible, depending on V, the fluid volume, and α, the wedge angle. For some cases there exists an equilibrium position for the particle where the net force is zero; the model suggests that the equilibrium can be stable or unstable dependent on the parameters. There is no simple description of how the particle will move.

In the dynamic problem we consider the unsteady motion of the particle after deposition. Unlike the static model we assume there is a small gap between the particle and the wedge wall. We find the transverse and perpendicular speed of the particle relative to the wall, and hence the trajectory of the particle through the fluid, by matching the force due to capillary effects with a viscous drag in the gap region. We find that the problem requires asymptotic matching between capillary statics in the outer regions and lubrication theory in the gap. We obtain two differential equations for the 'sliding' and 'squeezing' speeds of the particle which we solve numerically to find the position of the particle as a function of time. Given V, α and the particle's initial position we can predict whether the particle will move to the corner of the wedge, move towards the corner but become submerged, move to the contact line, or reach a stable equilibrium position. We show that theoretically all particles will reach their predicted positions but only at biologically unrealistic times.

Therefore, dependent on the alveolar geometry and the size and deposition site of the particle we can, in principle, predict the direction of motion. For some values the model suggests that a particle moves into the corner of the alveolus which may facilitate particle clearance, as macrophages are known to preferentially inhabit alveolar corners [45]. However the drift forces are weak and may not move particles far in practice. If there is excess fluid in the lung and V is large, the model shows that particles are likely to become submerged as is expected.

From §2.2.1 we see that the particle sliding speed is of magnitude $\gamma\epsilon^{1/2}/\mu$ and the squeezing speed is of magnitude $\gamma\epsilon^{3/2}/\mu$. Therefore the speed of the particle motion, and potentially particle clearance, will increase as surface tension increases or fluid viscosity decreases. However, in reality, physical effects that we have neglected would need to be included before any realistic therapeutic predictions could be made.

The most obvious limitation of the model is two-dimensionality. The effect of modelling in three dimensions may be very significant to the predictions as the volume of fluid will no longer be divided into separate regions and forces will act upon a sphere from all directions. In this model we have assumed a perfectly circular particle; it would be interesting, for a more realistic model, to consider the effect of particle surface roughness and even different particle shapes. In particular, particle roughness will likely cause the gap between the particle and the wall to be larger and the pressure-driven drainage flux through the gap to be non-negligible. In addition, many types of particles are inhaled into the lungs and as well as varying in size and shape, different materials may have different wetting properties. In this model we have predicted particle behaviour over a short timescale (approximately one second). For this model to realistically apply to particle clearance in the lungs we need to consider longer timescales and therefore look at the effect of respiration on the model predictions. For example, we have assumed that alveolar surface tension is constant; however measurements show that typical values vary from approximately 0 to 30 dyn/cm during the respiratory cycle [7]. Similarly, we have assumed alveolar air pressure to be fixed, but in reality the pressure changes significantly during breathing [5]. In addition, it may also be necessary to consider the effect of moving wedge walls. Wei *et al.* [79] consider the flow, in the presence of surfactants, in a viscous fluid layer lying on a planar membrane which undergoes cyclic stretching, mimicking breathing motions. They find that a very small, steady flow is induced by the stretching motion; such flows would obviously affect particles immersed in the liquid layer. Another obvious limitation of this model is the assumption of rigid walls. Airway walls are not rigid and may become indented by trapped particles. The deformability of the wall may have a significant effect on the motion of a particle in close proximity to the wall; in Chapters 3 and 4 we consider this problem in detail.

Chapter 3

The perpendicular motion of a particle relative to a deformable wall

In the previous chapter we assumed the wedge wall was rigid. In practice, however, at the alveolar level surface forces appear to pull the particles into the fluid lining with sufficient force to depress the underlying capillaries and epithelial cells [45]. The airway wall deformation may have a significant effect on the motion of the particle over the wall's surface and hence an effect upon the ultimate fate of the particle within the lung. To understand this issue in more depth, in this chapter we consider a particle moving perpendicular to an elastic wall which is modelled initially as a spring-backed plate. Transverse motion is considered in the following chapter. These are fundamental problems in elastohydrodynamics and will have applications beyond the lung.

Existing models have considered the force on a two-dimensional cylinder and a three-dimensional sphere moving perpendicular and parallel to a nearby rigid planar wall [50, 51, 53, 54, 55]. Here we extend this to look at motion near a deformable wall and consider the effect of deformability on the hydrodynamic

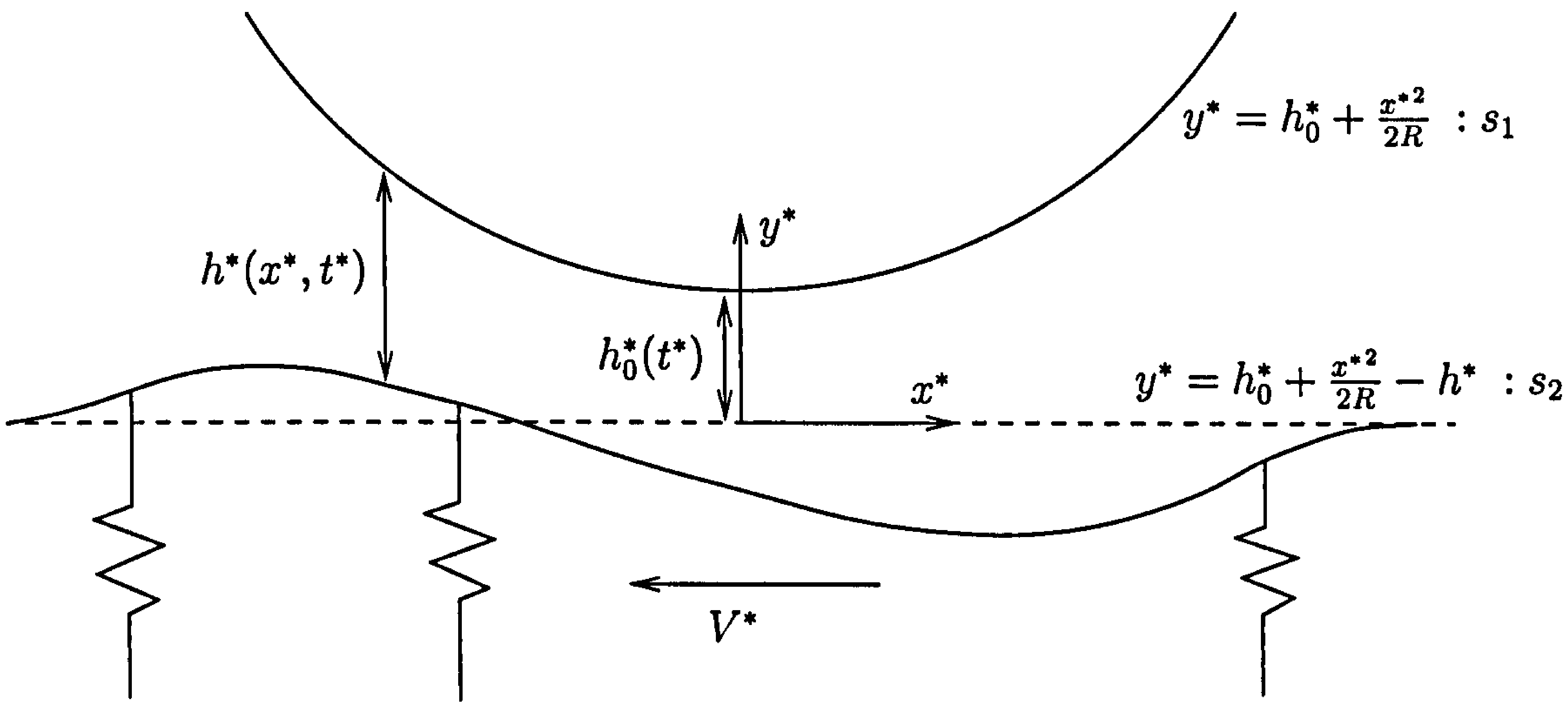

Figure 3.1: Particle depressing the underlying epithelial cells.

force acting on the particle. In the two-dimensional problem we will show that the model produces results similar to those found in studies of industrial roll coating flows with deformable roll covers and studies of deformable pellets moving through tubes [56, 57, 60].

In §3.1 we set up the model and derive the governing equations for both perpendicular and transverse motion of the particle. Firstly, we consider motion perpendicular to the wall where the displacement of the particle is prescribed (both pushing into the wall, §3.2, and pulling off the wall, §3.3). In §3.4 we again consider perpendicular motion but prescribe the force acting on the particle instead of the displacement. As before we examine both pushing (§3.4.1) and pulling (§3.4.2). We will consider transverse displacement of the particle in Chapter 4.

3.1 Model Formulation

Again we consider a two-dimensional geometry with the particle modelled as a cylinder (see Figure 3.1). We look at a small region close to the wall where

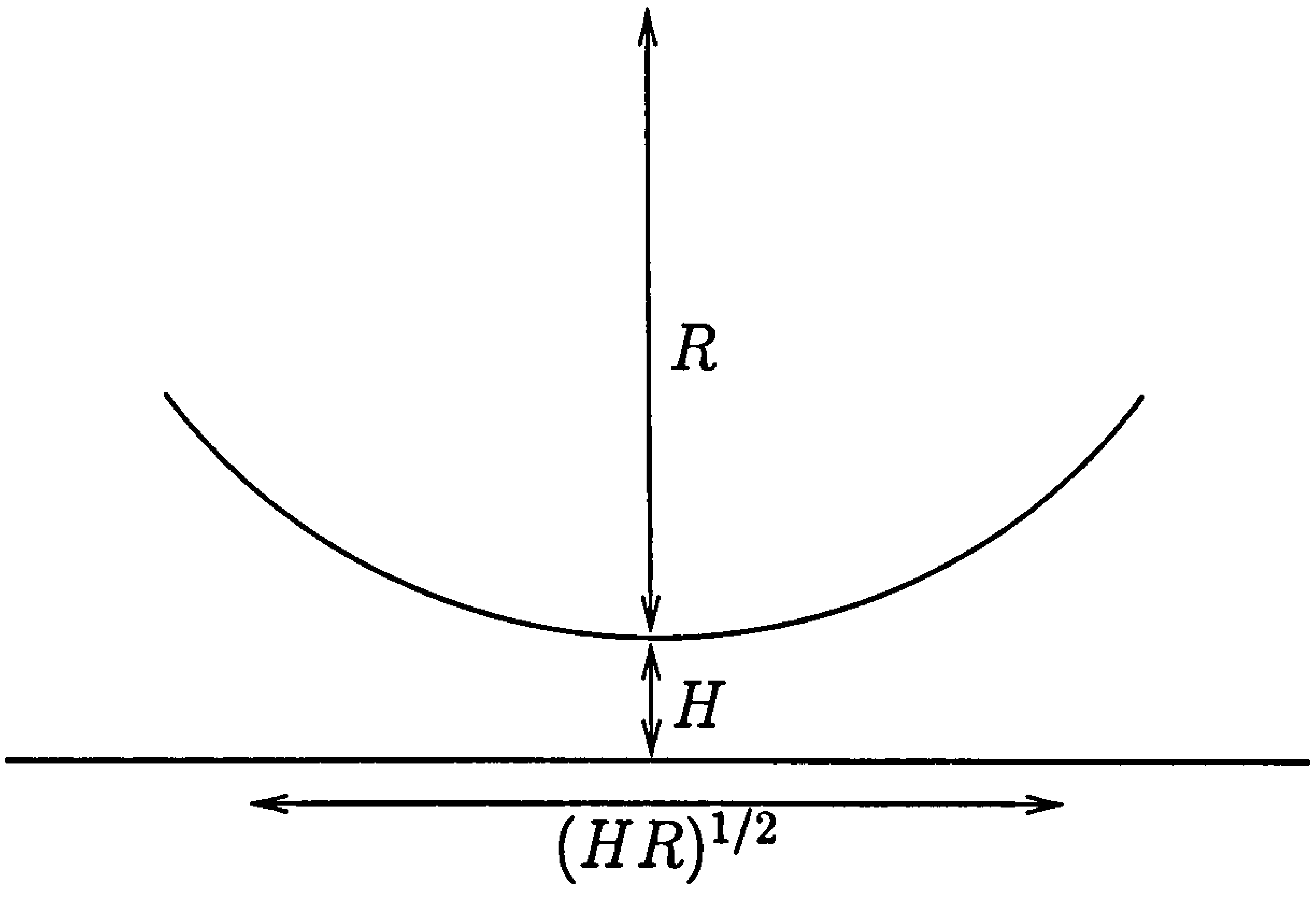

Figure 3.2: Scalings in the gap region

the particle surface, s_1, is given by $y^* = h_0^*(t^*) + x^{*2}/2R$, where $h_0^*(t^*)$ is the vertical displacement from $y^* = 0$ at $x^* = 0$ and R is the radius of the particle. The thin film thickness is denoted $h^*(x^*, t^*)$ and therefore the wall, s_2, is given by $y^* = h_0^*(t^*) + x^{*2}/2R - h^*(x^*, t^*)$. We assume the cylinder moves at speed V^* with respect to the wall in the positive x^* direction. We work in the frame of the cylinder, so that the wall moves with speed $-V^*$. (In this chapter we consider perpendicular motion and so $V^* = 0$. In Chapter 4 we will consider transverse motion and let $V^* \neq 0$.)

As before we exploit the fact that the gap thickness is much smaller than the radius of the particle, *i.e.* $H \ll R$, where H is a typical gap thickness. As in §2.2.1 the lengthscale of the lubrication region is taken to be $(HR)^{1/2}$ (see Figure 3.2). Let (u^*,v^*) be the velocity of the fluid, p^* be the fluid pressure and μ be the fluid viscosity.

Using lubrication theory in the gap we have the governing equations,

$$0 = -p^*_{x^*} + \mu u^*_{y^*y^*}, \tag{3.1}$$

$$0 = -p^*_{y^*}, \tag{3.2}$$

$$0 = u^*_{x^*} + v^*_{y^*}, \tag{3.3}$$

with the following boundary conditions: no-slip on the particle and wall,

$$u^* = 0 \text{ on } s_1, \tag{3.4}$$

$$u^* = -V^* \text{ on } s_2, \tag{3.5}$$

and no-penetration on the particle and wall,

$$v^* = h^*_{0t^*} \text{ on } s_1, \tag{3.6}$$

$$v^* = h^*_{0t^*} - h^*_{t^*} + V^*\left(h^*_{x^*} - \frac{x^*}{R}\right) \text{ on } s_2. \tag{3.7}$$

The integrated form of the continuity equation (3.3) gives

$$h^*_{t^*} + Q^*_{x^*} = 0, \text{ where } Q^* = \int_{s_2}^{s_1} u^*\, dy^*. \tag{3.8}$$

The pressure in the fluid due to the elasticity of the wall is assumed to be a linear function of the wall displacement,

$$p^* = -\kappa(h^*_0 + \frac{x^{*2}}{2R} - h^*), \tag{3.9}$$

where κ is an effective spring stiffness. This assumption is used in similar problems such as roll coating flows with compliant roll covers, see §1.7. Coyle [60], for example, uses a one-dimensional constrained column model (CCM) to model the deformation of a compliant layer in which the local fluid pressure is assumed to be directly proportional to the deformation. The validity of this simple Hookean springs model as a simple description of an elastic half-space was confirmed by Carvalho & Scriven [57]. Gostling *et al.* [61], however, show that Hookean spring models cannot model the deformation effectively when the layer is incompressible. They also consider the effects of layer thickness on the model. If we assume that the airway wall behaves as a compressible half-space, Carvalho & Scriven's results allow us to assume a linear springs model in a first approximation. We know little about how epithelial cells behave in reality so we have chosen to use the simplest model. In addition, using a simple model allows analysis that gives important insights into mechanisms that would be less obvious with more complex wall models.

3.1.1 Nondimensionalisation and scaling

The continuity equation (3.3) gives $u^* \sim v^*(HR)^{1/2}/H$ where $v^* \sim H_t$. The balance between pressure gradient and viscous terms in (3.1) therefore gives $p^* \sim \mu H_t R/H^2$. We know also from (3.9) that $p^* \sim \kappa H$ and therefore we obtain $H_t \sim \kappa H^3/\mu R$. Using these scaling arguments we nondimensionalise by letting $x^* = (HR)^{1/2}x$, $y^* = Hy$, $u^* = (\kappa H^{5/2}/\mu R^{1/2})u$, $v^* = (\kappa H^3/\mu R)v$, $p^* = \kappa H p$, $h^* = Hh$, $h_0^* = Hh_0$, $t^* = (\mu R/\kappa H^2)t$, $V^* = (\kappa H^{5/2}/\mu R^{1/2})V$.

The governing equations are therefore, in dimensionless variables,

$$p_x = u_{yy}, \tag{3.10}$$

$$p_y = 0, \tag{3.11}$$

$$u_x + v_y = 0, \tag{3.12}$$

subject to

$$u = 0 \quad \text{on} \quad y = s_1, \tag{3.13}$$

$$u = -V \quad \text{on} \quad y = s_2, \tag{3.14}$$

$$v = h_{0t} \quad \text{on} \quad y = s_1, \tag{3.15}$$

$$v = h_{0t} - h_t + V(h_x - x) \quad \text{on} \quad y = s_2, \tag{3.16}$$

with

$$h_t + Q_x = 0, \quad Q = \int_{s_2}^{s_1} u \, dy, \tag{3.17}$$

and

$$p = -h_0 - \frac{x^2}{2} + h. \tag{3.18}$$

3.1.2 Evolution equation

We solve equation (3.10) using the boundary conditions (3.13, 3.14) to obtain u. We then obtain

$$Q = -\frac{1}{12}(p_x h^3 + 6Vh). \tag{3.19}$$

Using $p_x = -x + h_x$ and substituting into equation (3.17) we obtain the evolution equation for $h(x,t)$,

$$h_t + \left[\frac{h^3}{12}(x - h_x)\right]_x - \frac{V}{2}h_x = 0, \tag{3.20}$$

which is subject to the boundary condition

$$h \longrightarrow h_0 + \frac{1}{2}x^2 \text{ as } x \longrightarrow \pm\infty. \tag{3.21}$$

which assumes the pressure is zero in the far field. We assume that initially the wall is undeformed, *i.e.* $h(x,0) = h_0 + x^2/2$.

3.1.3 Force on the cylinder

The force, $\mathbf{F}^*$, on the particle is given by

$$\mathbf{F}^* = \int_{S^*} \boldsymbol{\sigma}^* \cdot \hat{\mathbf{n}}\, dS^*,$$

where $\boldsymbol{\sigma}^*$ is the stress vector, $\hat{\mathbf{n}} = (n_x, n_y)$ is the outward pointing unit normal to the cylinder and S^* is the surface of the cylinder. The stress vector is given by

$$\boldsymbol{\sigma}^* \cdot \hat{\mathbf{n}} = -p^*\hat{\mathbf{n}} + \mu(\nabla^*\mathbf{u}^* + \nabla^*\mathbf{u}^{*T}) \cdot \hat{\mathbf{n}}.$$

We nondimensionalise pressures on κH, lengths on H, speeds on $\kappa H^3/\mu R$ and then scaling in the gap we let $x = (1/\epsilon^{1/2})\tilde{x}$, $u = (1/\epsilon^{1/2})\tilde{u}$, where $\epsilon = H/R \ll$

1. Dropping tildes, the stress vector becomes

$$\boldsymbol{\sigma}\cdot\hat{\mathbf{n}} = -p\begin{pmatrix} n_x \\ n_y \end{pmatrix} + \epsilon\begin{pmatrix} 2u_x & \frac{u_y}{\epsilon^{1/2}} + \epsilon^{1/2}v_x \\ \frac{u_y}{\epsilon^{1/2}} + \epsilon^{1/2}v_x & 2v_y \end{pmatrix}\begin{pmatrix} n_x \\ n_y \end{pmatrix}. \tag{3.22}$$

The outward pointing unit normal to the cylinder is

$$\hat{\mathbf{n}} = (n_x, n_y) = \frac{\epsilon^{1/2}x\hat{\mathbf{x}} - \hat{\mathbf{y}}}{(1+\epsilon x^2)^{1/2}}. \tag{3.23}$$

The $\hat{\mathbf{x}}$ and $\hat{\mathbf{y}}$ components of the stress vector are therefore

$$\hat{\mathbf{x}}\cdot\boldsymbol{\sigma}\cdot\hat{\mathbf{n}} = \frac{1}{(1+\epsilon x^2)^{1/2}}\left(-p\epsilon^{1/2}x + 2\epsilon^{3/2}u_x x - \epsilon^{1/2}u_y - \epsilon^{3/2}v_x\right), \tag{3.24}$$

$$\hat{\mathbf{y}}\cdot\boldsymbol{\sigma}\cdot\hat{\mathbf{n}} = \frac{1}{(1+\epsilon x^2)^{1/2}}\left(p + \epsilon u_y x + \epsilon^2 v_x x - 2\epsilon v_y\right). \tag{3.25}$$

We know that, in dimensional variables, $dS^{*2} = dx^{*2} + dy^{*2}$, where $S^* = HS$, so we obtain

$$dS = \epsilon^{-1/2}(1+\epsilon x^2)^{1/2}dx. \tag{3.26}$$

Therefore the force $\mathbf{F} = (F_x, F_y)$ is given by

$$F_x = \int_{-\infty}^{\infty}\left(-px + 2\epsilon u_x x - u_y - \epsilon v_x\right)dx, \tag{3.27}$$

$$F_y = \int_{-\infty}^{\infty}\left(\frac{p}{\epsilon^{1/2}} + \epsilon^{1/2}u_y x + \epsilon^{3/2}v_x x - 2\epsilon^{1/2}v_y\right)dx. \tag{3.28}$$

At leading order we obtain

$$F_x = \int_{-\infty}^{\infty}\left(-px - u_y\right)\,dx. \tag{3.29}$$

Using the solution for u obtained in §3.1.2 we find

$$u_y = (h_x - x)y + \frac{V}{h} - \frac{(h_x - x)}{2h}(2hh_0 + hx^2 - h^2). \tag{3.30}$$

Since we are calculating the force on the particle, $y = h_0 + x^2/2$, we obtain

$$F_x = \int_{-\infty}^{\infty}\left(-\frac{hx}{2} + h_0 x + \frac{x^3}{2} - \frac{V}{h} - \frac{hh_x}{2}\right)dx. \tag{3.31}$$

From (3.28) we obtain

$$\tilde{F}_y = \epsilon^{1/2}F_y = \int_{-\infty}^{\infty}\left(h - h_0 - \frac{x^2}{2}\right)dx, \tag{3.32}$$

neglecting smaller terms.

3.1.4 Torque on the cylinder

The (dimensionless) torque, T, on the cylinder (scaled on κH^2) is given by

$$T = \int_S \hat{\mathbf{t}} \cdot \sigma \cdot \hat{\mathbf{n}} \, dS,$$

where the unit tangent to the cylinder, $\hat{\mathbf{t}}$, is given by

$$\hat{\mathbf{t}} = (t_x, t_y) = \frac{\hat{\mathbf{x}} + \epsilon^{1/2} x \hat{\mathbf{y}}}{(1+\epsilon x^2)^{1/2}}.$$

Using (3.22) and (3.26) we obtain

$$T = \int_{-\infty}^{\infty} \frac{1}{(1+\epsilon x^2)^{1/2}} \left(2\epsilon u_x x + (u_y + \epsilon v_x)(\epsilon x^2 - 1) - 2\epsilon v_y x \right) \, dx, \qquad (3.33)$$

and so to leading order we have

$$T = -\int_{-\infty}^{\infty} u_y \, dx. \qquad (3.34)$$

Using (3.30) and $y = h_0 + x^2/2$, since we are calculating the torque on the cylinder, we obtain

$$T = \int_{-\infty}^{\infty} \left(-\frac{V}{h} - \frac{h h_x}{2} + \frac{h x}{2} \right) \, dx. \qquad (3.35)$$

In the case of purely perpendicular motion ($V = 0$) the torque acting on the cylinder is zero due to symmetry. In the case of transverse particle motion if we prescribe the displacement we choose also to prescribe no rotation of the particle and compute the necessary torque to sustain this motion.

3.2 Perpendicular Motion:

Prescribed Displacement- Pushing

We look first at purely perpendicular motion, *i.e.* $V = 0$. In this case the gap thickness, h, is symmetrical, *i.e.* $h_x = 0$ at $x = 0$. In this section, and the following section, we prescribe the displacement of the particle, h_0, and

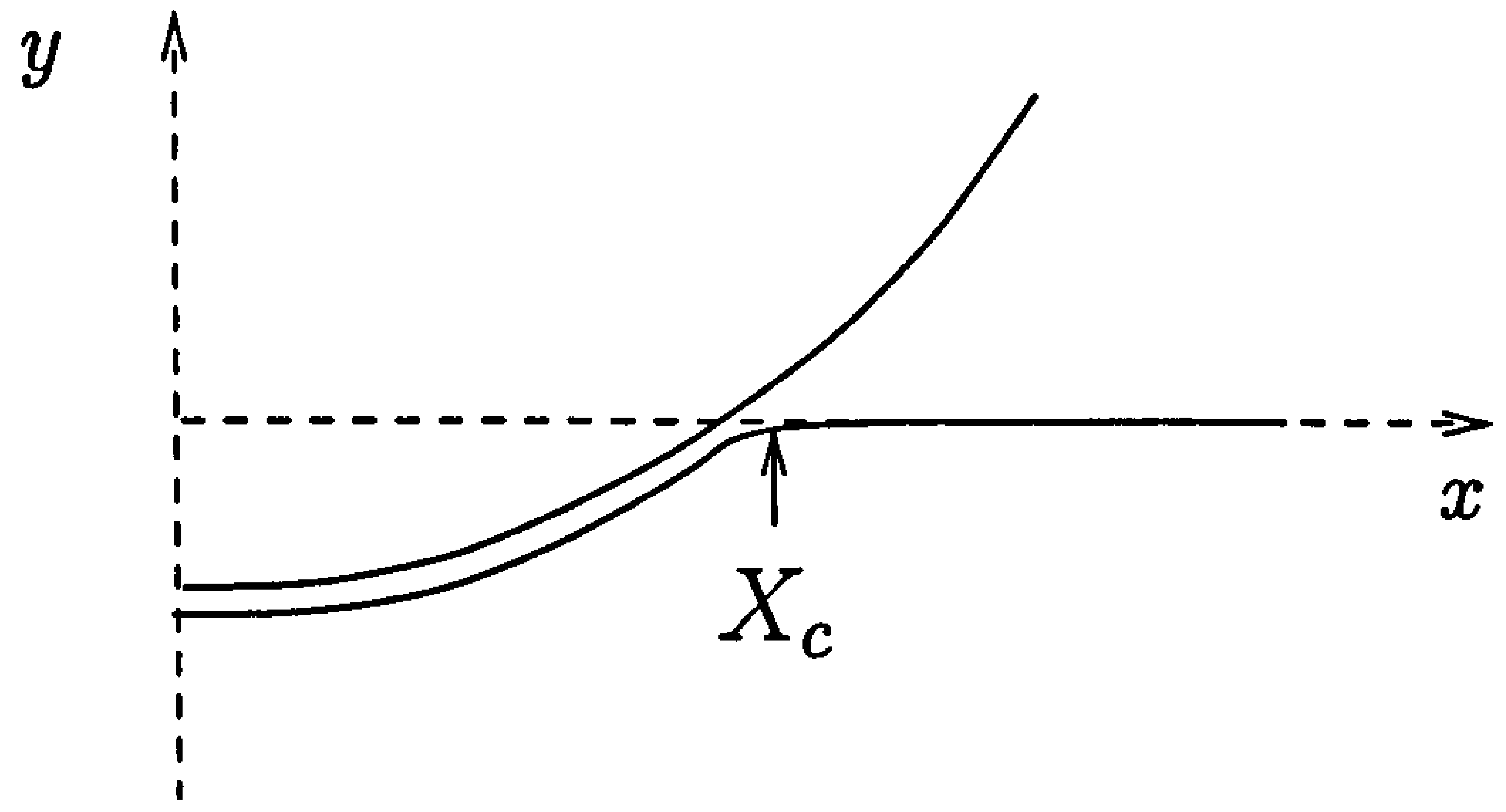

Figure 3.3: Schematic of the shape of the wall (at $t \gg t_{final}$) showing the corner position X_c.

compute the force. In §3.4 we consider the opposite case where we prescribe the force, F, and compute the resulting displacement.

We prescribe the initial position of the particle above the wall $h_0(0)$, and the displacement of the particle with time $h_0(t)$, *i.e.* the particle is pushed down to a given position at a given speed and then remains at that point. The initial condition for the gap thickness, h, is therefore $h = h_0(0) + x^2/2$. The displacement of the particle is given by

$$\begin{aligned} h_0(t) &= h_0(0) - \frac{1}{2}\left(h_0(0) + \frac{X_c^2}{2}\right)\left(1 - \cos\left(\frac{t\pi}{t_{final}}\right)\right), \quad 0 \le t \le t_{final}, && (3.36) \\ &= -\frac{X_c^2}{2}, \quad t > t_{final}. && (3.37) \end{aligned}$$

where X_c is the final position of the corner of the deformed wall (see Figure 3.3). As $t \to \infty$, X_c is the value of x at which $h \to 0$ and $h \to h_0 + x^2/2$. We assume that the wall is always ultimately indented, *i.e.* $X_c^2 > 0$.

Numerical Method

We use finite difference methods (NAG routine D02NBF) to integrate the evolution equation (3.20) over the region $[0, L]$, applying $h = h_0 + x^2/2$ at $x = L$. The following simulations used 1001 meshpoints with $L = 10$ and

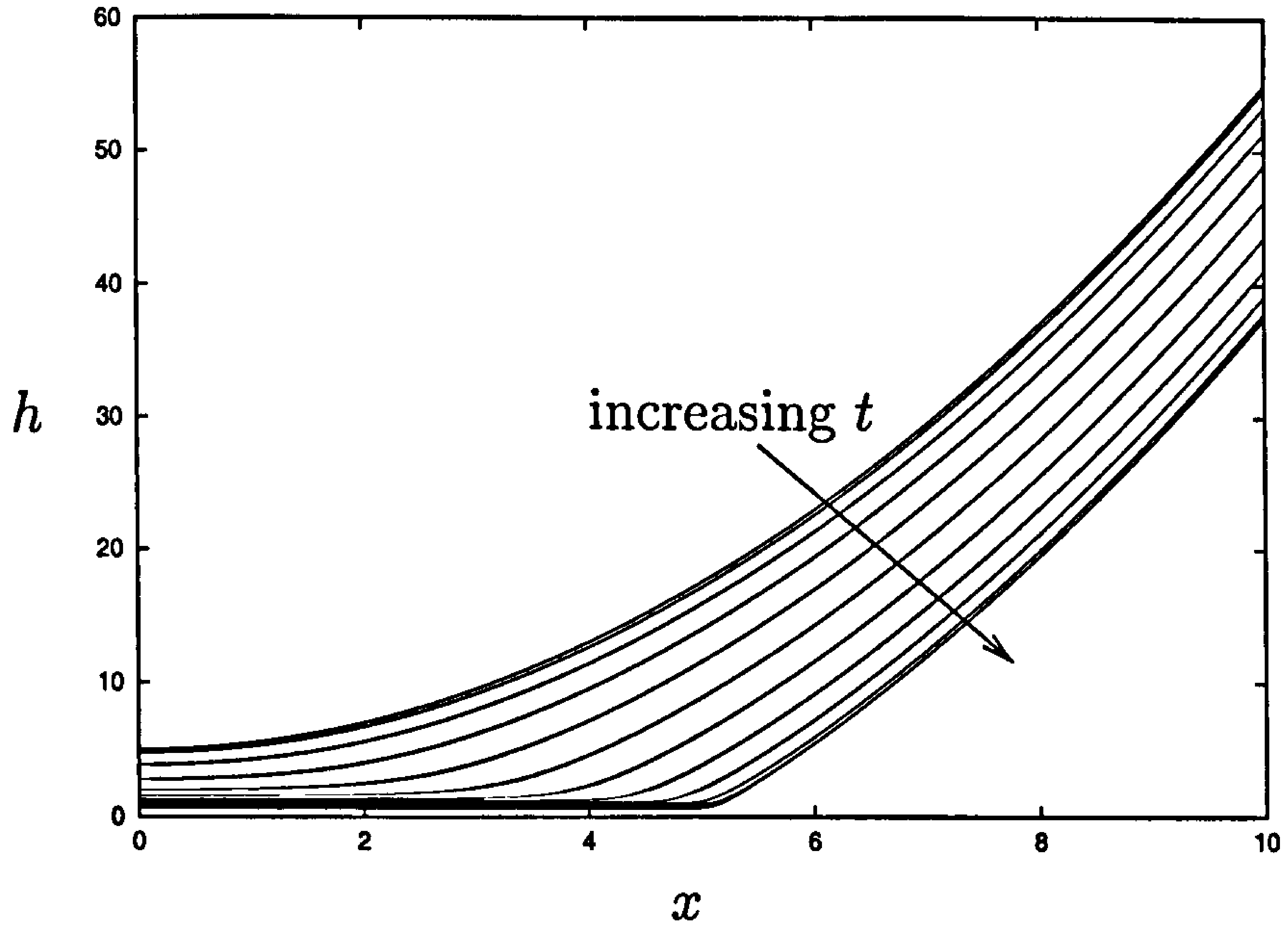

Figure 3.4: Gap thickness, $h(x,t)$, as t increases from $t = 10^{-5}$ to $t = 18$ in unit intervals, where $t_{final} = 10$ and $X_c = 5$.

$h_0(0) = 5$. The accuracy of the results was checked by varying the number of meshpoints and the domain length and by checking conservation of the fluid volume. To do the latter, we integrated $h(x,t)$ over the domain at each time interval to calculate the fluid volume, and compared this to the flux, calculated at $x = L$, integrated with respect to t at each time interval.

Simulations

As a first case we take $X_c = 5$ and $t_{final} = 10$. Figure 3.4 shows how the gap thickness, h, between the particle and the wall varies as t increases. As $t \to \infty$, the gap thickness tends to zero for $0 \leq x \leq X_c$, while $h \approx h_0 + x^2/2$ for $X_c < x < L$.

We can also look at how the force, $\hat{F}_y = \tilde{F}_y/2$, depends on the vertical speed of the particle. Figure 3.5 shows $\hat{F}_y(t)$, for various values of t_{final}. When the particle is pushed down rapidly (*e.g.* $t_{final} = 2$) the force increases quickly to a

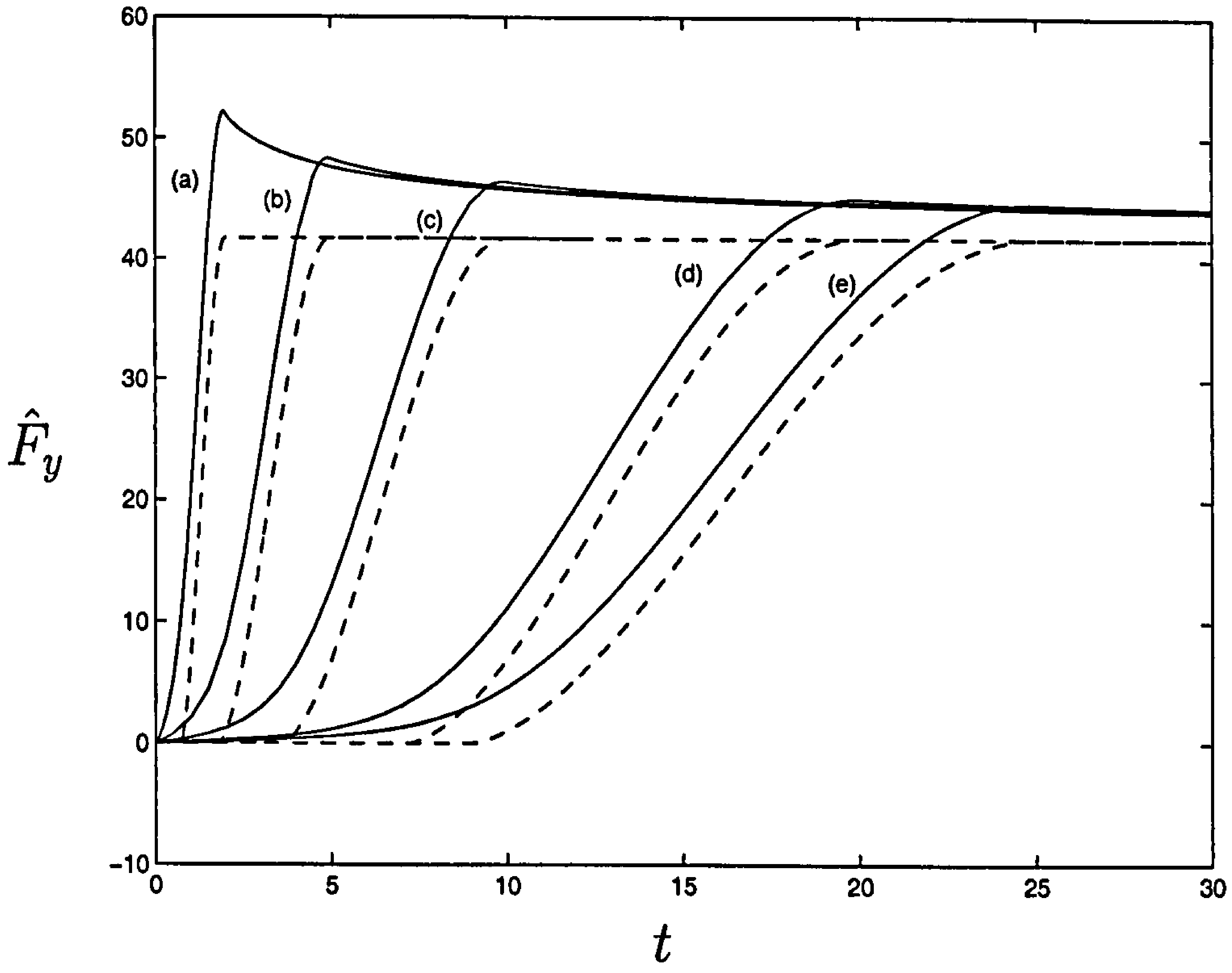

Figure 3.5: Force varying with time where (a) $t_{final} = 2$, (b) $t_{final} = 5$, (c) $t_{final} = 10$, (d) $t_{final} = 20$, (e) $t_{final} = 25$. Dashed lines show the corresponding equilibrium curves.

peak near $t = t_{final}$. The force then decreases towards its constant value as the wall relaxes, squeezing out fluid trapped between the particle and wall. When the particle is pushed down more slowly (*e.g.* $t_{final} = 25$) the wall relaxes whilst the particle is still moving, resulting in a smaller overshoot of the force. The dotted lines in Figure 3.5 show the corresponding equilibrium curves for each value of t_{final} (*i.e.* the force that would be exerted on the particle by the wall in the absence of fluid), *i.e.* $h = 0$ for $0 \leq x \leq X_c$ and $h = h_0 + x^2/2$ for $X_c < x < \infty$ in (3.32). Simulations show that the presence of the fluid film has a pronounced effect on the force even for large t_{final}.

We now consider various asymptotic limits of the problem. In §3.2.1 we examine the problem at short times, for both large and small values of t_{final}, and derive approximations for the force at short times. In §3.2.2 we consider long-time behaviour of the gap thickness and the force, which involves an asymptotic matching between three regions exhibiting different behaviour.

3.2.1 Asymptotic Analysis: Short times $t \ll t_{final}$

(i) Large t_{final}

At short times the deformation of the wall is very small, so we let $h = h_0 + x^2/2 + \hat{h}$, where $\hat{h}$ is a small perturbation from the undeformed state. Since t_{final} is large we assume the behaviour is quasi-steady and so we take $d\hat{h}/dt$ to be negligible. Linearising, (3.20) becomes

$$h_{0t} = \frac{1}{12}\left[\left(h_0 + \frac{1}{2}x^2\right)^3 \hat{h}_x\right]_x .$$

Integrating, taking $\hat{h}_x = 0$ at $x = 0$, we obtain

$$\frac{\hat{h}_x}{12}\left(h_0 + \frac{1}{2}x^2\right)^3 = h_{0t}x,$$

which is the equation describing squeezing motion towards a rigid wall (see §2.2.7). Integrating with respect to x, with $\hat{h} \to 0$ as $x \to \infty$, we get an expression for $\hat{h}$ and therefore we obtain

$$\hat{F}_y(t) = \int_0^\infty \hat{h}\, dx = \int_0^\infty \frac{-24h_{0_t}}{(2h_0 + x^2)^2}\, dx = -\frac{3\sqrt{2}\pi h_{0_t}}{2h_0^{3/2}}. \tag{3.38}$$

This agrees with (2.36), the normal force on a particle close to a rigid wall. Equation (3.38) is a factor of 1/2 smaller since we consider only half the lubrication region in this model due to symmetry. Since we prescribe the displacement of the particle we know $h_0(t)$ and $h_{0_t}(t)$. Figure 3.6 shows the analytical solution for $\hat{F}_y$ (dashed line) compared with the numerical simulation (solid line) at short times for the case $t_{final} = 100$. We find the perturbation analysis fits well for large t_{final} because as the particle is pushed down slowly the fluid deforms the wall only slightly. As the particle gets close to the wall (approx $t = t_{final}/3$) and deformations become larger the analysis breaks down.

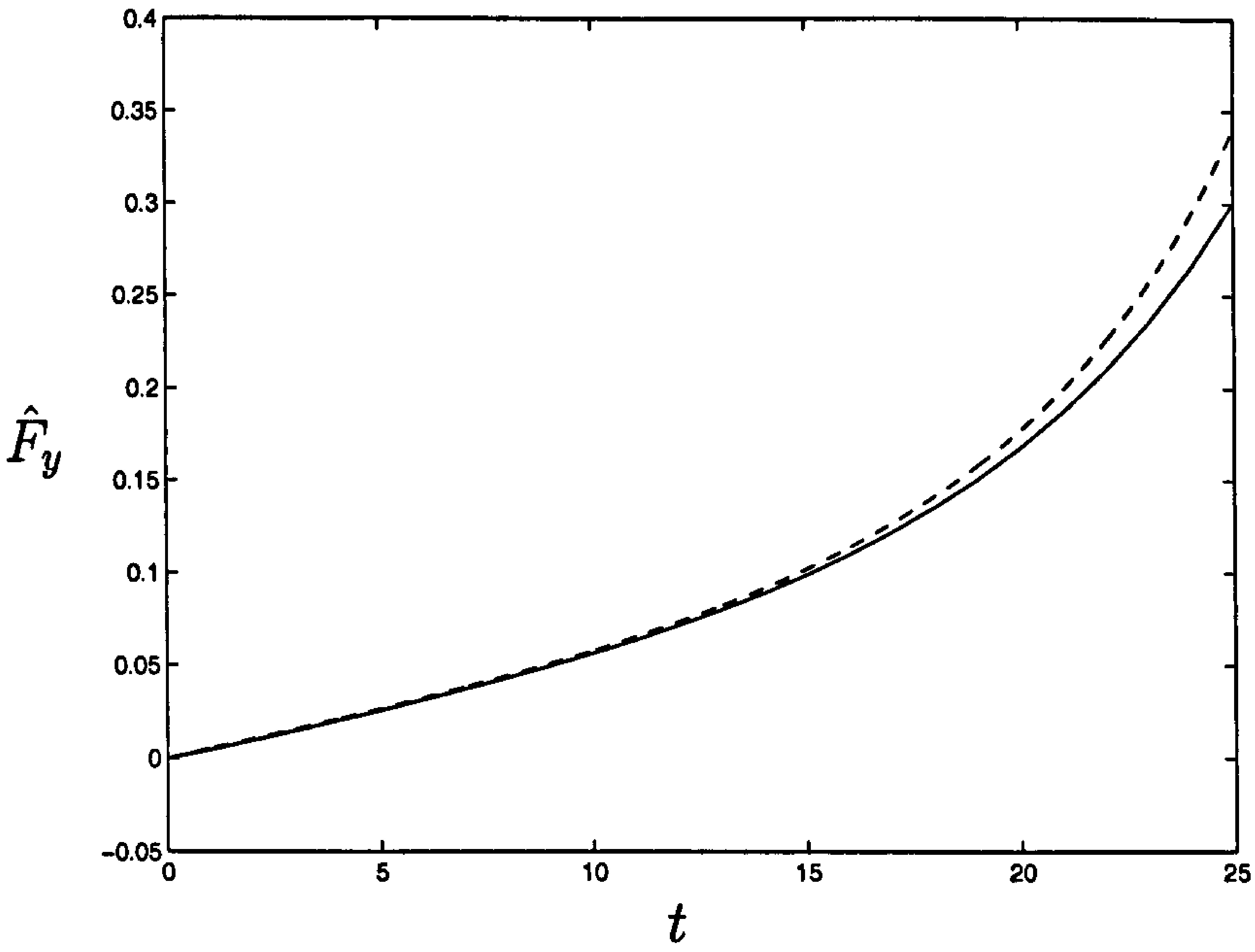

Figure 3.6: Analytical solution for $\hat{F}_y$ (3.38) (dashed line) compared with the numerical simulation (solid line) for the case $t_{final} = 100$.

(ii) Small t_{final}

For small t_{final} the above analysis is invalid because small deformations are unsteady and $\hat{h}_t \neq 0$. Simulations suggest that the speed of the particle motion allows no fluid to be squeezed out of the narrowest part of the gap whilst the particle is moving, causing fluid between the particle and the wall to be "frozen" at short times. The force on the particle reaches a peak near $t = t_{final}$ (see Figure 3.5) and the subsequent drop when the particle is stationary corresponds to the wall relaxation squeezing out trapped fluid. This peak and drop becomes more pronounced as the value of t_{final} gets smaller.

For $t \ll t_{final}$, $h_0 \approx h_0(0) - Ct^2/2$, from (3.36), where C is a known constant. Since deformations from the initial configuration are small, in the far field we have $h \sim x^2$. The evolution equation (3.20) then gives $Ct \sim (x^6 p_x)_x$ and hence $p \sim Ct/x^4$. Within the frozen region $h(x,t) \approx h(x,0) = h_0(0)+x^2/2$

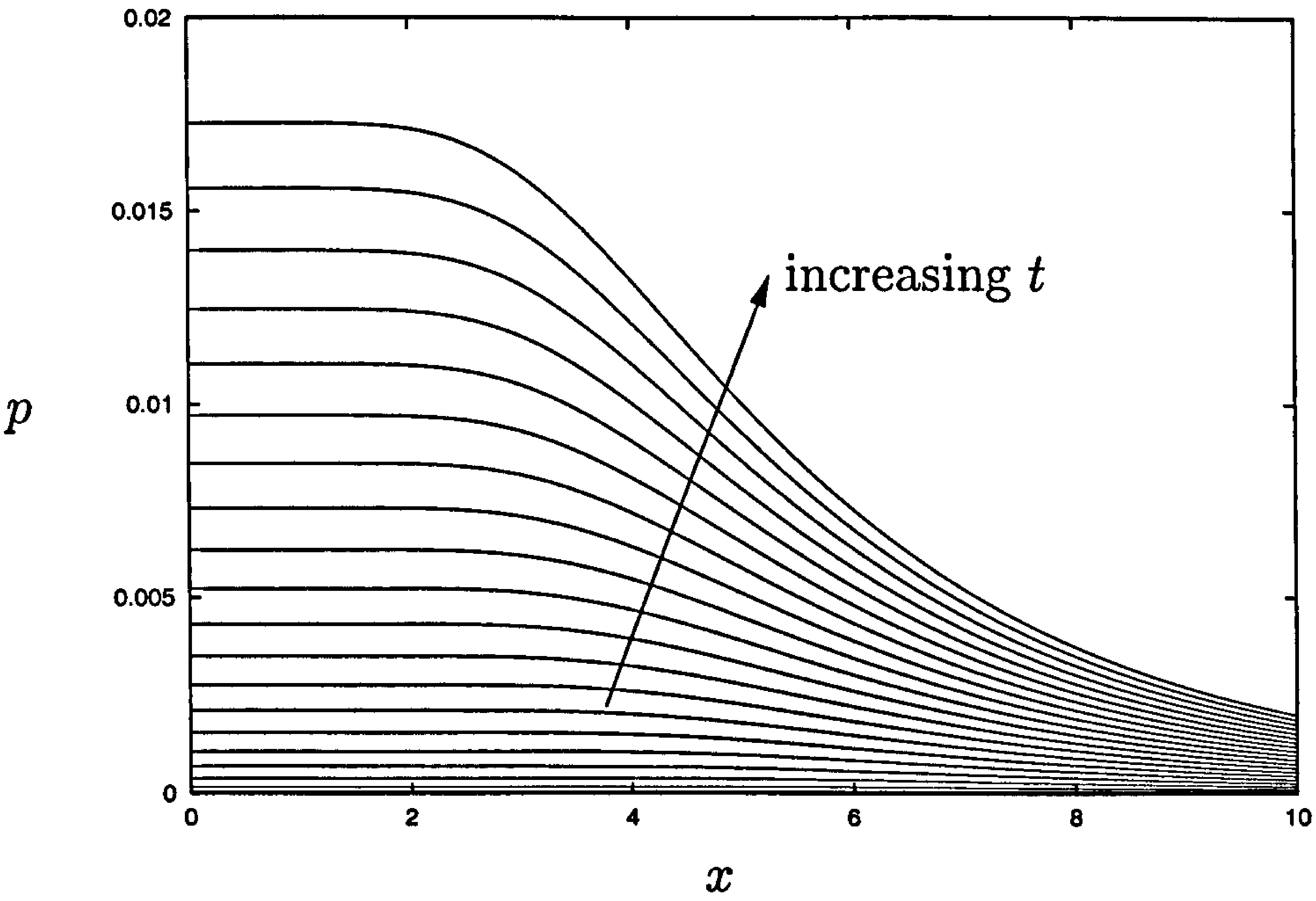

Figure 3.7: Pressure in the fluid as time increases from $t = 10^{-5}$ to $t = 0.02$ in uniform intervals when $t_{final} = 1$.

and hence from (3.18) $p \sim Ct^2/2$. Matching this pressure with the pressure in the outer region, we find a lengthscale for the frozen region is $x \sim t^{-1/4}$. This is illustrated by Figure 3.7 which shows the pressure in the fluid at short times when $t_{final} = 1$. We see that, as time increases, there is a decreasing region of uniform pressure centred at the origin corresponding to a decreasing amount of trapped fluid.

We let $\zeta = t^{1/4}x$ and $h = h_0(0) + x^2/2 + t^2 H(\zeta)$, since changes in h are due to the forced displacement of the particle which is given by $h_0 \approx h_0(0) - Ct^2/2$. Therefore at short times, for small t_{final}, equation (3.32) gives

$$\begin{aligned}\hat{F}_y &= \frac{\tilde{F}_y}{2} = \int_0^\infty \left(h_0(0) + \frac{x^2}{2} + t^2 H - \frac{x^2}{2} - h_0(0) + \frac{Ct^2}{2}\right) \frac{d\zeta}{t^{\frac{1}{4}}} \\ &= t^{\frac{7}{4}} \int_0^\infty \left(H + \frac{C}{2}\right) d\zeta = At^{\frac{7}{4}}, \qquad (3.39)\end{aligned}$$

where A is a constant. Analytical work to determine $H(\zeta)$ (and hence A) is shown below.

With the above scalings, the evolution equation (3.20) becomes

$$2tH + \frac{t\zeta H_\zeta}{4} + \frac{1}{12}\left[\left(5 + \frac{\zeta^2}{2t^{1/2}} + t^2 H\right)^3 \left(-H_\zeta t^{5/2}\right)\right]_\zeta = 0, \qquad (3.40)$$

and comparing the $O(1)$ terms, since t is small, we obtain

$$2H + \frac{\zeta H_\zeta}{4} = \frac{1}{96}\left(\zeta^6 H_\zeta\right)_\zeta. \qquad (3.41)$$

The condition that pressure is zero in the far field, (3.21), becomes

$$p \approx t^2 H + \frac{Ct^2}{2} \longrightarrow 0 \quad \text{as } \zeta \longrightarrow \infty, \qquad (3.42)$$

and so (3.41) is subject to the boundary condition

$$H \longrightarrow -\frac{C}{2} \quad \text{as } \zeta \longrightarrow \infty. \qquad (3.43)$$

We consider solutions of (3.41) as $\zeta \to 0$. Using a WKB approximation we let

$$H = e^{s_0(\zeta)+s_1(\zeta)+\dots}, \quad \text{with } |s_0| \gg |s_1| \gg \dots,$$

and hence (3.41) becomes

$$2 + \frac{\zeta}{4}(s_0' + s_1' + \dots) = \frac{1}{96}\left[6\zeta^5(s_0' + s_1' + \dots) + \zeta^6(s_0'^2 + s_0'' + \dots)\right]. \qquad (3.44)$$

Dominant balance arguments give $2 + \zeta s_0'/4 = 0$ or $\zeta s_0'/4 = \zeta^6 s_0'^2/96$. The former results in a solution $H \approx \zeta^{-8}$ which blows up as $\zeta \to 0$. Therefore we consider

$$\frac{\zeta s_0'}{4} = \frac{\zeta^6 s_0'^2}{96}.$$

This can be rearranged to give

$$s_0'(\zeta^5 s_0' - 24) = 0,$$

and so $s_0 = A_0$ (where A_0 is a constant) or $s_0' = 24/\zeta^5$. We therefore obtain

$$H = C_0 e^{-6/\zeta^4}. \qquad (3.45)$$

We can also consider the behaviour of H as $\zeta \to \infty$. We let $H = -C/2 + f(\zeta)$ where $|f| \ll 1$. Equation (3.41) becomes

$$-C + 2f + \frac{\zeta f_\zeta}{4} = \frac{1}{96}\left(\zeta^6 f_\zeta\right)_\zeta.$$

Neglecting terms of $O(f)$ and integrating twice with respect to ζ we obtain

$$f = \frac{24C}{\zeta^4} - \frac{A_1}{5\zeta^5} + A_2,$$

where A_1, A_2 are constants, and hence

$$H = -\frac{C}{2} + \frac{24C}{\zeta^4} - \dots. \tag{3.46}$$

Therefore H tends to the constant value $-C/2$ rapidly as ζ becomes large.

We therefore want to solve (3.41) subject to the boundary conditions (3.45) as $\zeta \to 0$ and $H \to -C/2$ as $\zeta \to \infty$. We convert the second-order ODE into the two first-order ODEs

$$\begin{aligned} H_\zeta &= y, \\ y_\zeta &= \frac{96}{\zeta^6}\left(2H + y\left(\frac{\zeta}{4} - \frac{\zeta^5}{16}\right)\right), \end{aligned}$$

and use NAG routine D02PCF to integrate with respect to ζ using Runge-Kutta methods. We integrate from $\zeta = 0.8$ to $\zeta = 20$ with 1001 meshpoints and take the initial conditions to be $H = C_0 \exp(-6/\zeta^4)$, $y = (24C_0/\zeta^5)\exp(-6/\zeta^4)$. We let $C_0 = 1$, integrate, and rescale C_0 as necessary so that the boundary condition as $\zeta \to \infty$ is satisfied. From (3.36), $C = 35\pi^2/4$ for the parameters used in our simulations. Hence we find $C_0 = -0.69795$. Figure 3.8 shows the solution of (3.41). We therefore find, from (3.39), $A = 77.95802$.

Figure 3.9 shows that for $t_{final} = 1$ at short times, $\hat{F}_y \approx 77.96t^{7/4}$ as predicted.

3.2.2 Asymptotic Analysis: Long times $t \gg t_{final}$

At long times the particle is near equilibrium and we assume the motion is quasi-static, so $h_t \approx 0$. Therefore the evolution equation (3.20) reduces to

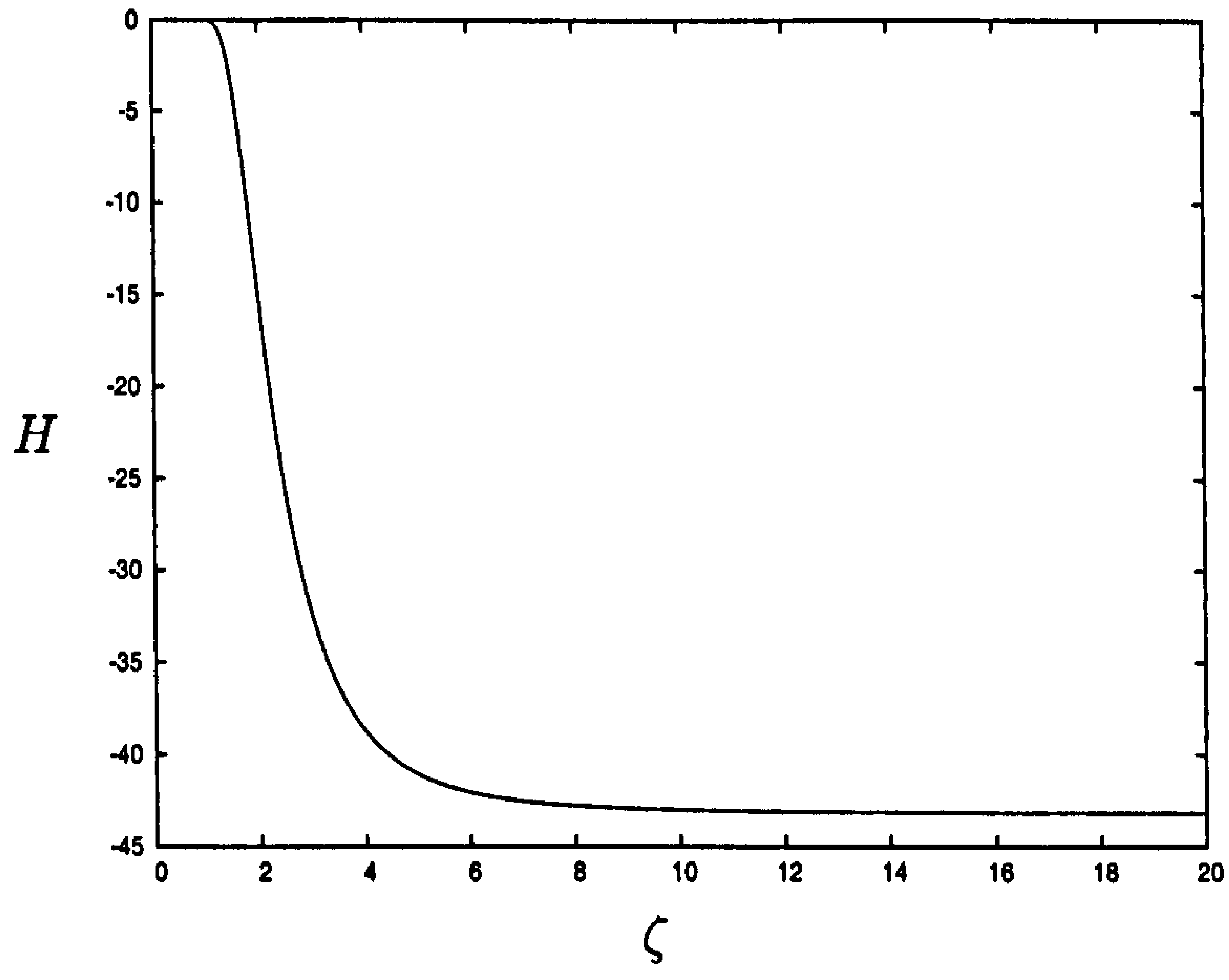

Figure 3.8: Solution $H(\zeta)$ of (3.41) against ζ.

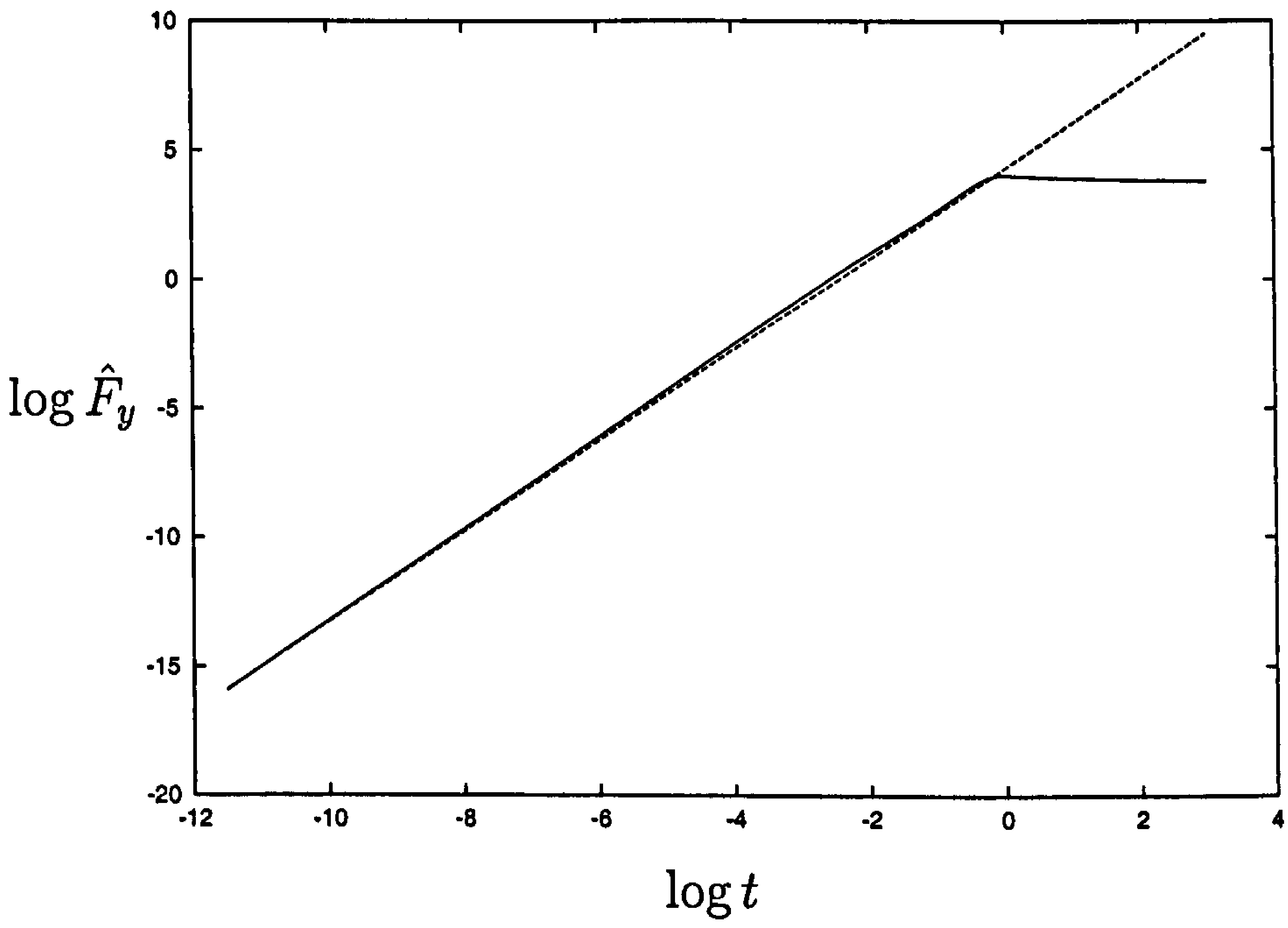

Figure 3.9: A plot of $\log \hat{F}_y$ against $\log t$ for $t_{final} = 1$ showing agreement between numerical simulation (solid line) and analytical solution (3.39) where $A = 77.96$ (dashed line) at short times.

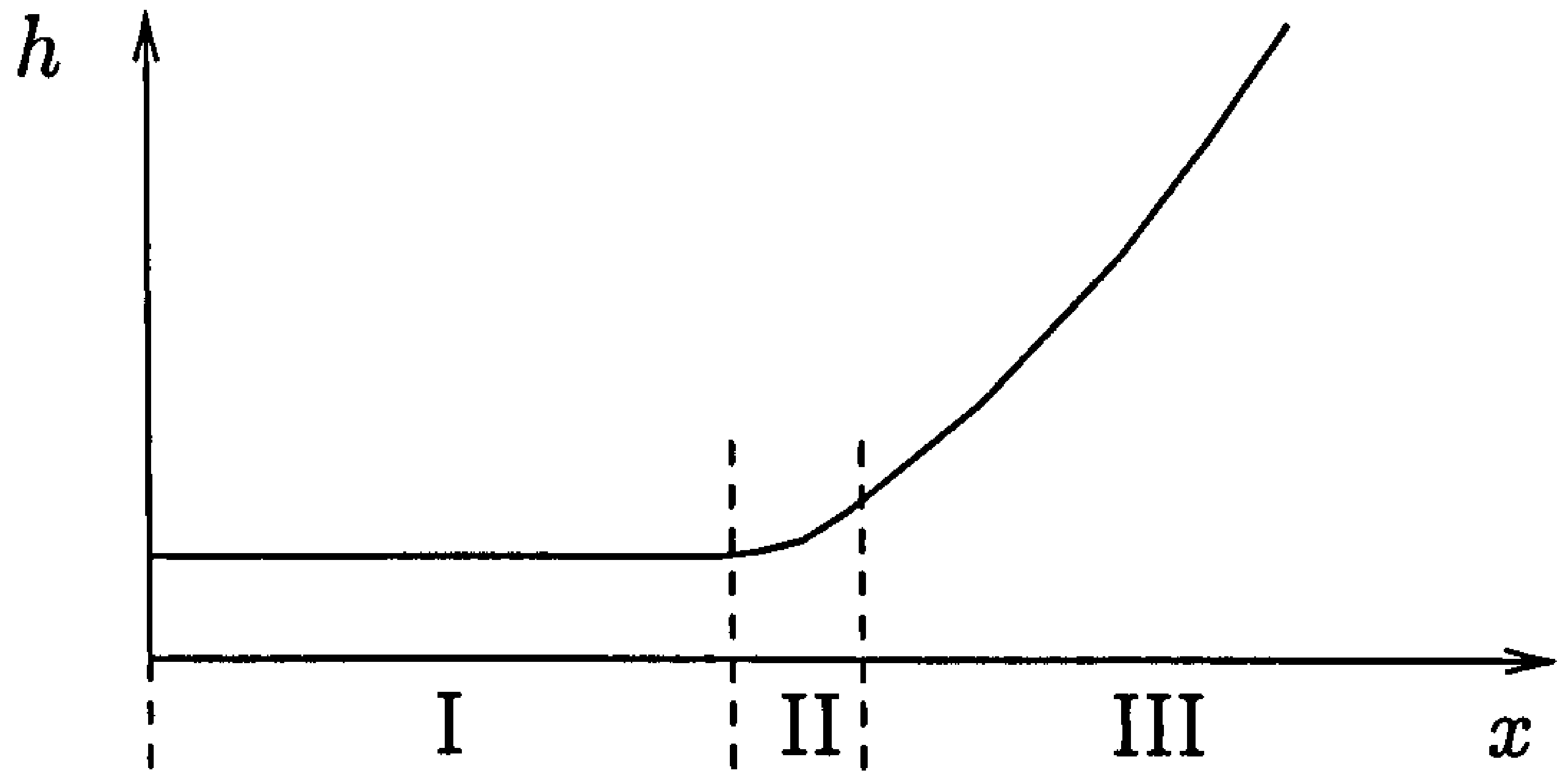

Figure 3.10: Schematic of the different regions for long-time behaviour.

$h^3x = h^3h_x$ with $h_x = 0$ at $x = 0$, and so at leading order as $t \to \infty$, $h^3 = 0$ or $x = h_x$. Since $p_x = -x + h_x$ the latter implies that $p = 0$ and hence $h = h_0 + x^2/2$, using (3.18) and (3.21). Therefore for $t \to \infty$ we obtain $h = 0$ for $0 \leq x \leq X_c$ and $h = h_0 + x^2/2$ for $X_c < x < L$.

From Figure 3.4 we see that, at long times, h may be divided into three regions: Region I, an inner region; Region II, a transition or corner region; and Region III, an outer region (see Figure 3.10). With the evolution equation (3.20) written as

$$h_t + \frac{1}{12}(h^3x)_x = \frac{1}{12}(h^3h_x)_x, \tag{3.47}$$

in region I we have a balance between the terms on the left-hand side of the equation, *i.e.* $h/t \sim h^3$, since h is nearly uniform at long times. Therefore we let $h = G(x)/t^{1/2}$ in $h_t + (h^3x)_x/12 = 0$ and obtain

$$\frac{dG}{dx} = \frac{6G - G^3}{3G^2x},$$

which has an exact solution $G = \sqrt{6}$, $G_x = 0$. Hence in the Region I we obtain

$$h \sim \frac{\sqrt{6}}{t^{1/2}}, \quad \text{as } t \longrightarrow \infty. \tag{3.48}$$

Figure 3.11 shows the consistency of this solution with a numerical simulation.

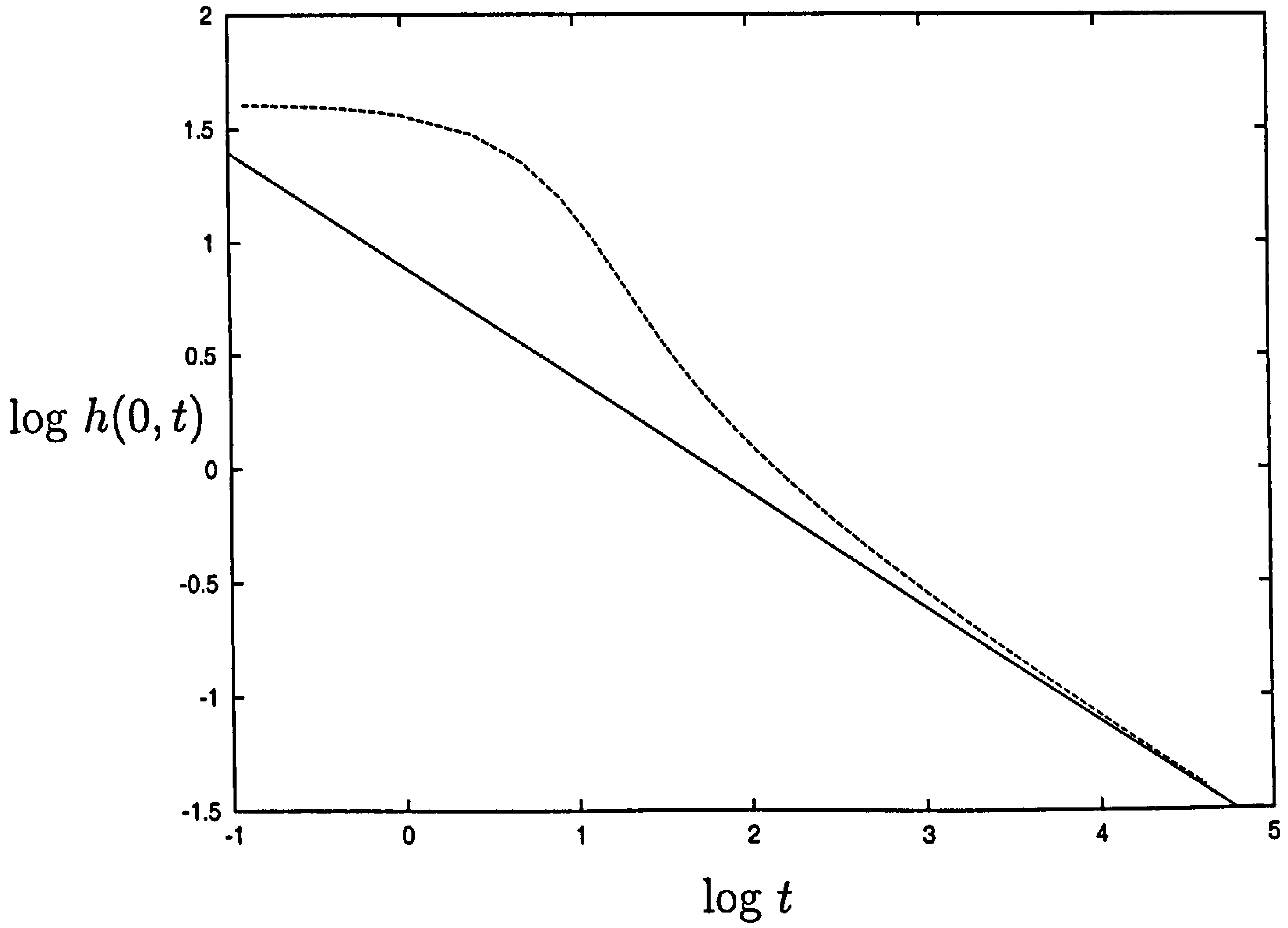

Figure 3.11: $\log h(0,t)$ (the gap thickness at $x = 0$) versus $\log t$ with $t_{final} = 10$. The numerical solution (dashed line) is consistent with the analytical solution (3.48) (solid line) for long times.

In region III ($X_c < x < L$), at long times $h \approx h_0 + x^2/2$. At $x = X_c$, $h \approx 0$ so $h_0 \rightarrow -X_c^2/2$. Therefore in the outer region we have

$$h \sim (x^2 - X_c^2)/2. \tag{3.49}$$

In region II we assume $x = X_c + \xi$ where $|\xi| \ll X_c$. In inner variables equation (3.49) becomes

$$h \sim \frac{1}{2}\left[(X_c + \xi)^2 - X_c^2\right] = X_c\xi + O(\xi^2).$$

Therefore matching conditions between Region II and Regions I & III are

$$h \sim \frac{\sqrt{6}}{t^{\frac{1}{2}}} \quad \text{as } \xi \longrightarrow -\infty, \tag{3.50}$$

$$h \sim X_c\xi \quad \text{as } \xi \longrightarrow \infty. \tag{3.51}$$

Motivated by the form of (3.50), (3.51) we rescale the variables in region II, letting $H(Z) = t^{1/2}h$, $Z = t^{1/2}\xi$, with $H, Z \sim O(1)$. Equation (3.47) becomes

$$(H^3X_c)_Z = (H^3H_Z)_Z + O\left(\frac{1}{t^{1/2}}\right),$$

neglecting smaller terms at long times. Integrating with the rescaled boundary condition $H \rightarrow \sqrt{6}$ as $Z \rightarrow -\infty$, we obtain

$$H_Z = X_c\left(1 - \frac{6^{3/2}}{H^3}\right), \tag{3.52}$$

describing the shape of the corner.

Integrating (3.52), with the boundary condition $H \rightarrow X_cZ$ as $Z \rightarrow \infty$, we can compare this asymptotic solution with the corner shape given by the numerical simulations. Figure 3.12 shows the computed corner shape (solid lines) tending towards the asymptotic corner shape (dotted line) as $t \rightarrow \infty$.

In order to calculate the force acting on the cylinder at long times we need to know the size of perturbations from the long-time limit *i.e.* from $h = 0$ for $0 \leq x \leq X_c$, $h = h_0 + x^2/2$ for $X_c < x < L$. In Region I we know $h \sim \sqrt{6}/t^{1/2}$

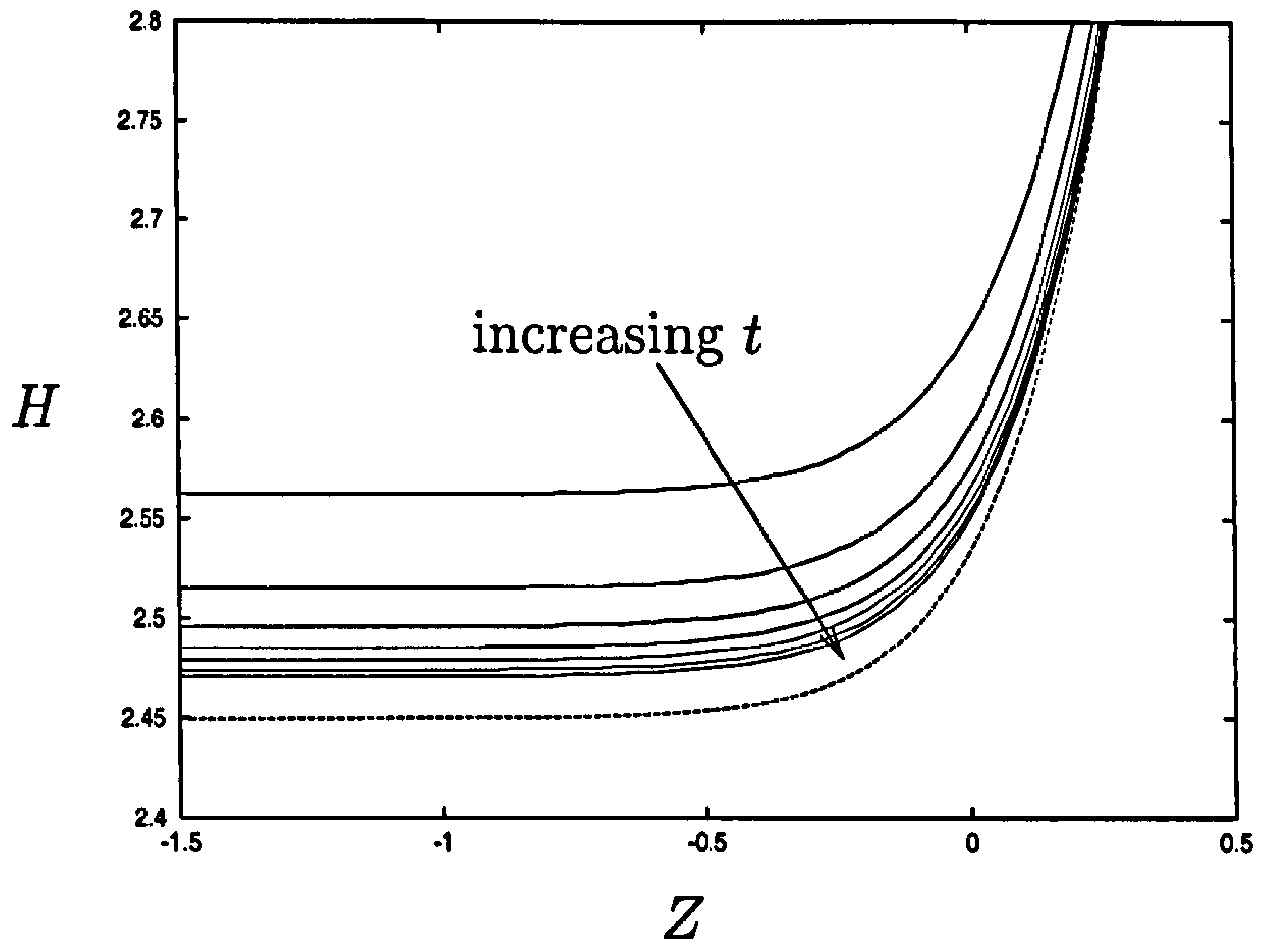

Figure 3.12: Numerical solutions of (3.20) plotted in inner variables (solid lines). The shape of the corner tends to the analytical solution (3.52) (dashed line) as t increases from $t = 10$ to $t = 150$.

from (3.48). At long times in region III, let $h = h_0 + x^2/2 + \hat{h}$ where $\hat{h}$ is a small perturbation. Linearising, (3.47) becomes

$$\hat{h}_t = \frac{1}{12}\left[\hat{h}_x\left(h_0 + \frac{x^2}{2}\right)^3\right]_x. \tag{3.53}$$

Any perturbations will be largest in the inner limit of region III, so again we let $x = X_c + \xi$, so equation (3.53) becomes

$$\hat{h}_t = \frac{1}{12}\left[\hat{h}_\xi\left(X_c\xi + \frac{\xi^2}{2}\right)^3\right]_\xi. \tag{3.54}$$

For small ξ the $X_c\xi$ term dominates so that $\hat{h}_t \approx [\hat{h}_\xi X_c^3\xi^3]_\xi/12$ and hence a lengthscale over which these perturbations decay is $\xi \sim 1/t$.

In the outer limit of region II, equation (3.52), which describes the shape of the corner, reduces to $H_Z = X_c$. Integrating and expressing in terms of h and ξ, we obtain

$$h = X_c\xi + \frac{A}{t^{1/2}},$$

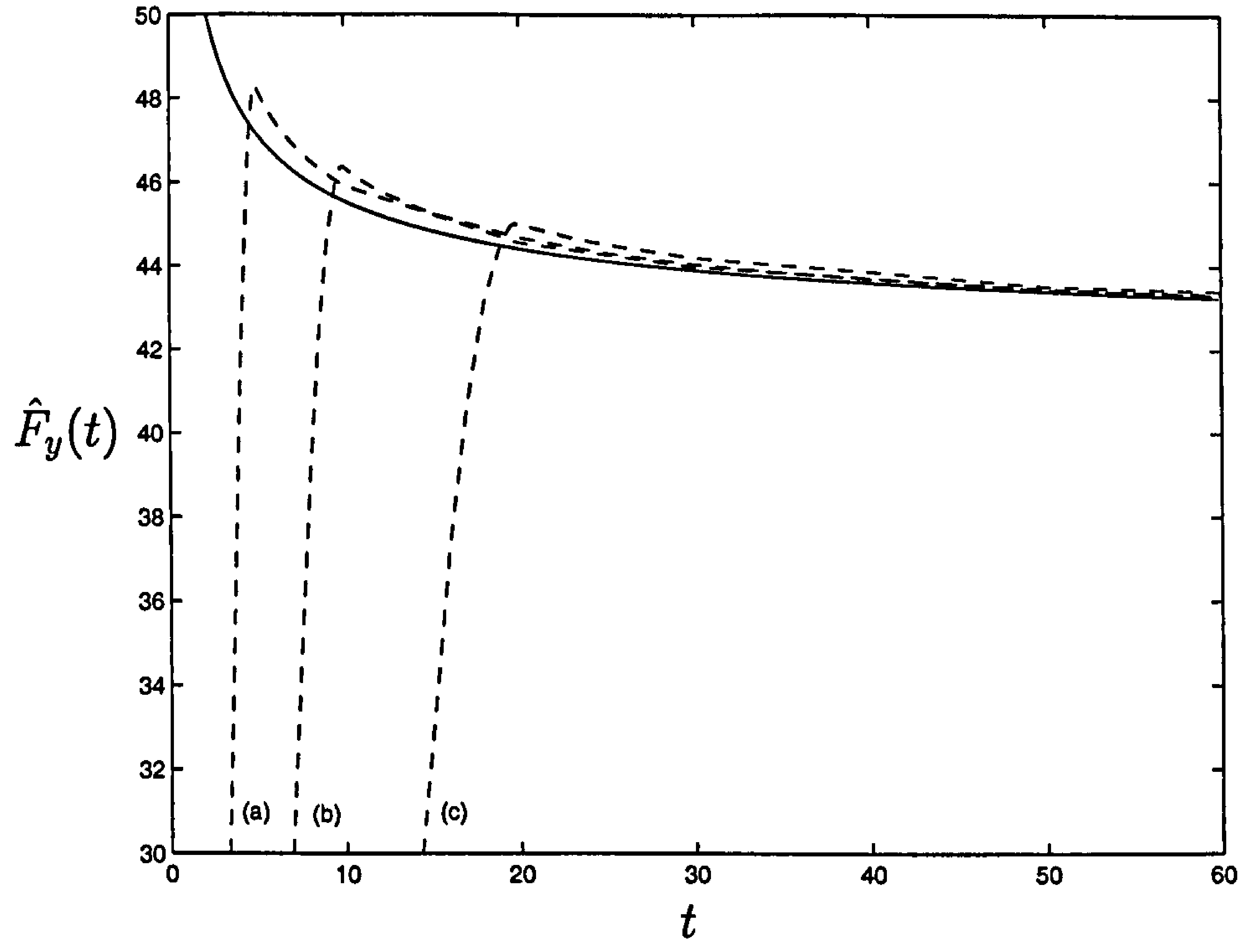

Figure 3.13: Force, $\hat{F}_y$, as t increases for t_{final} = (*a*) 5, (*b*) 10, (*c*) 20 (dashed lines). Numerical simulations are consistent with the first two terms of (3.56) for long times (solid line).

where A is a constant. Therefore from (3.51) any perturbations in Region III, $\hat{h}$, are $O(t^{-1/2})$.

We now look at the force at long time. Equation (3.32) can be expressed

$$\hat{F}_y(t) = \int_0^{X_c} h\,dx - \int_0^{X_c} \left(h_0 + \frac{x^2}{2}\right)\,dx + \int_{X_c}^{L} \left(h - h_0 - \frac{x^2}{2}\right)\,dx. \quad (3.55)$$

We know $h_0 = -X_c^2/2$ at long times and so

$$\int_0^{X_c} \left(-h_0 - \frac{x^2}{2}\right)\,dx = -\left(h_0 X_c + \frac{X_c^3}{6}\right) = \frac{X_c^3}{3}.$$

For $0 \le x \le X_c$, at long times, $h \approx \sqrt{6}/t^{1/2}$ so

$$\int_0^{X_c} h\,dx \approx \frac{\sqrt{6}X_c}{t^{1/2}}.$$

For $x > X_c$, any contribution to the force is due to perturbations, $\hat{h} = h - h_0 -$

$x^2/2$, close to the corner since $h \to h_0 + x^2/2$ as $x \to \infty$. We know $\hat{h} \sim t^{-1/2}$ and $\xi \sim t^{-1}$ so the contribution to the force is $O(t^{-3/2})$.

Equation (3.55) therefore becomes

$$\hat{F}_y(t) = \frac{X_c^3}{3} + \frac{\sqrt{6}X_c}{t^{1/2}} + O\left(\frac{1}{t^{3/2}}\right), \tag{3.56}$$

and $\hat{F}_y \longrightarrow X_c^3/3$ as $t \longrightarrow \infty$. Figure 3.13 shows this solution to be consistent with the numerical simulations at long times.

3.3 Perpendicular Motion:

Prescribed Displacement- Pulling

Numerical Method

We now look at what happens when the particle is pulled off the wall. In this case the displacement is given by

$$\begin{aligned} h_0(t) &= -\frac{X_c^2}{2} + \frac{1}{2}\left(h_0(t_f) + \frac{X_c^2}{2}\right)\left(1 - \cos\left(\frac{t\pi}{t_f}\right)\right), & 0 \leq t \leq t_f, \\ &= h_0(t_f), & t > t_f, \end{aligned}$$

where the particle is initially at $h_0 = -X_c^2/2$ with a gap thickness $\delta = \sqrt{6}/\sqrt{30}$ for $x < X_c$ and $h \approx -X_c^2/2 + x^2/2$ for $x > X_c$ (this is the state of the system at $t = 30$ for the case $t_{final} = 10$ in §3.2). The particle is pulled off the wall for $0 \leq t \leq t_f$ to a final (prescribed) position $h_0(t_f)$.

Simulations

We take $t_f = 10$, $X_c = 5$ with $h_0(t_f) = 5$. Figure 3.14 shows the gap thickness, $h(x,t)$, as t increases. Figure 3.15 illustrates correspondingly how the wall is pulled upwards in the corner region as the particle is pulled away from the wall. In comparison, Figure 3.16 shows the wall behaviour when the particle is pulled off quickly, with $t_f = 1$, where X_c, $h_0(t_f)$ are unchanged. The membrane

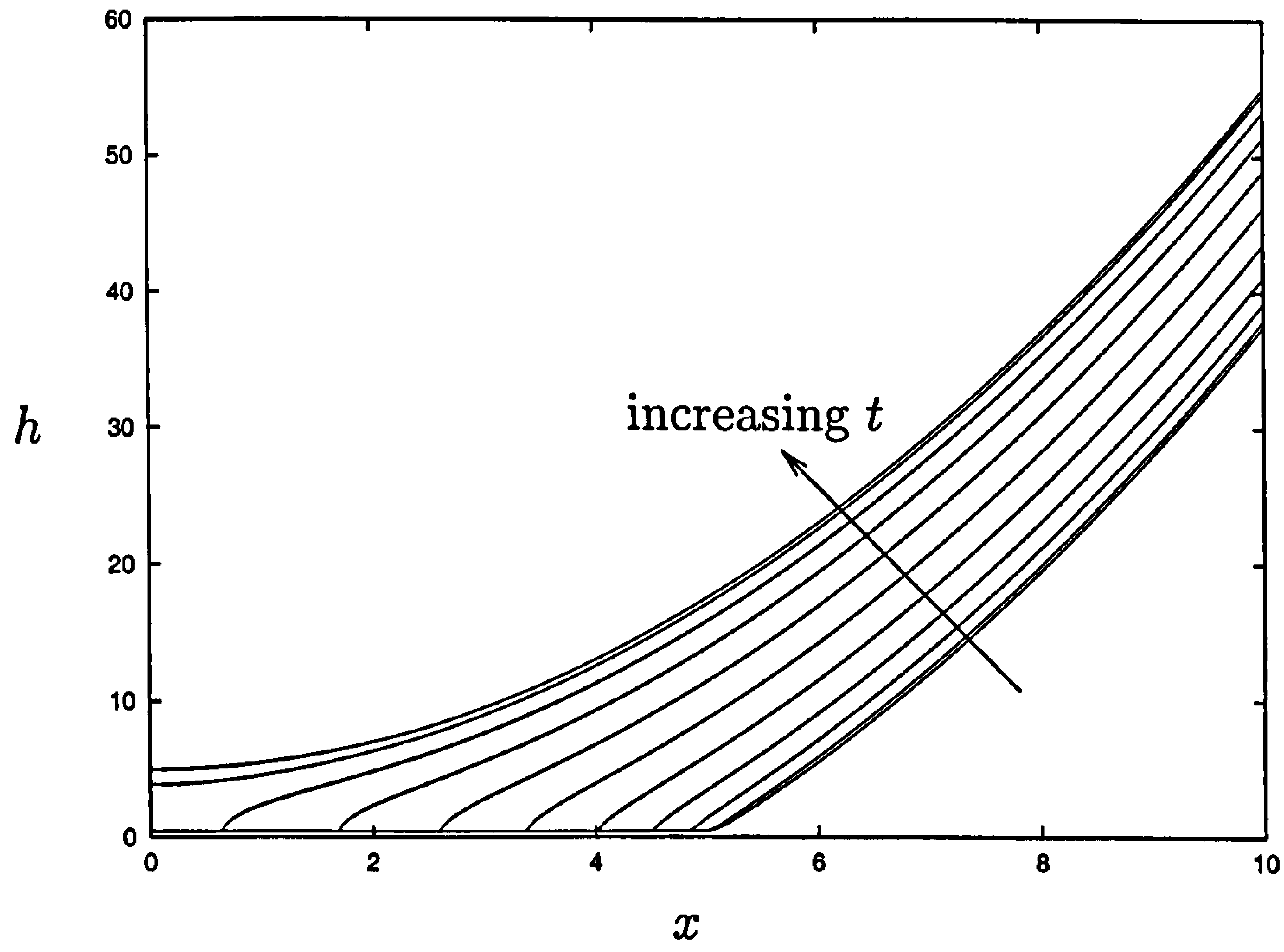

Figure 3.14: Gap thickness, $h(x,t)$, as t increases from $t=0$ to $t=42$ in unit intervals, with $t_f=10$.

is more sharply deformed in the corner region. When the particle is lifted off quickly the wall is pulled with it and continues to relax to its undeformed state after the particle has stopped moving. When the particle is pulled off slowly the effect is much less pronounced and the wall is always close to equilibrium. The position of the corner, $X_0(t)$, is defined as the maximum value of x such that $h \approx \delta$. Figure 3.17 shows how $X_0(t)$ changes with time when the particle is pulled off at different speeds. We see that as the particle begins to move there is a "waiting time" where the position of the corner remains stationary. This waiting time increases as t_f increases.

Figure 3.18 shows how the force, $\hat{F}_y$, acting on the particle depends on the speed the particle is pulled off the wall. As the particle is pulled away, the force, which is due to the compressed springs in the wall, decreases as the wall relaxes. When the wall is pulled upwards behind the particle the springs are

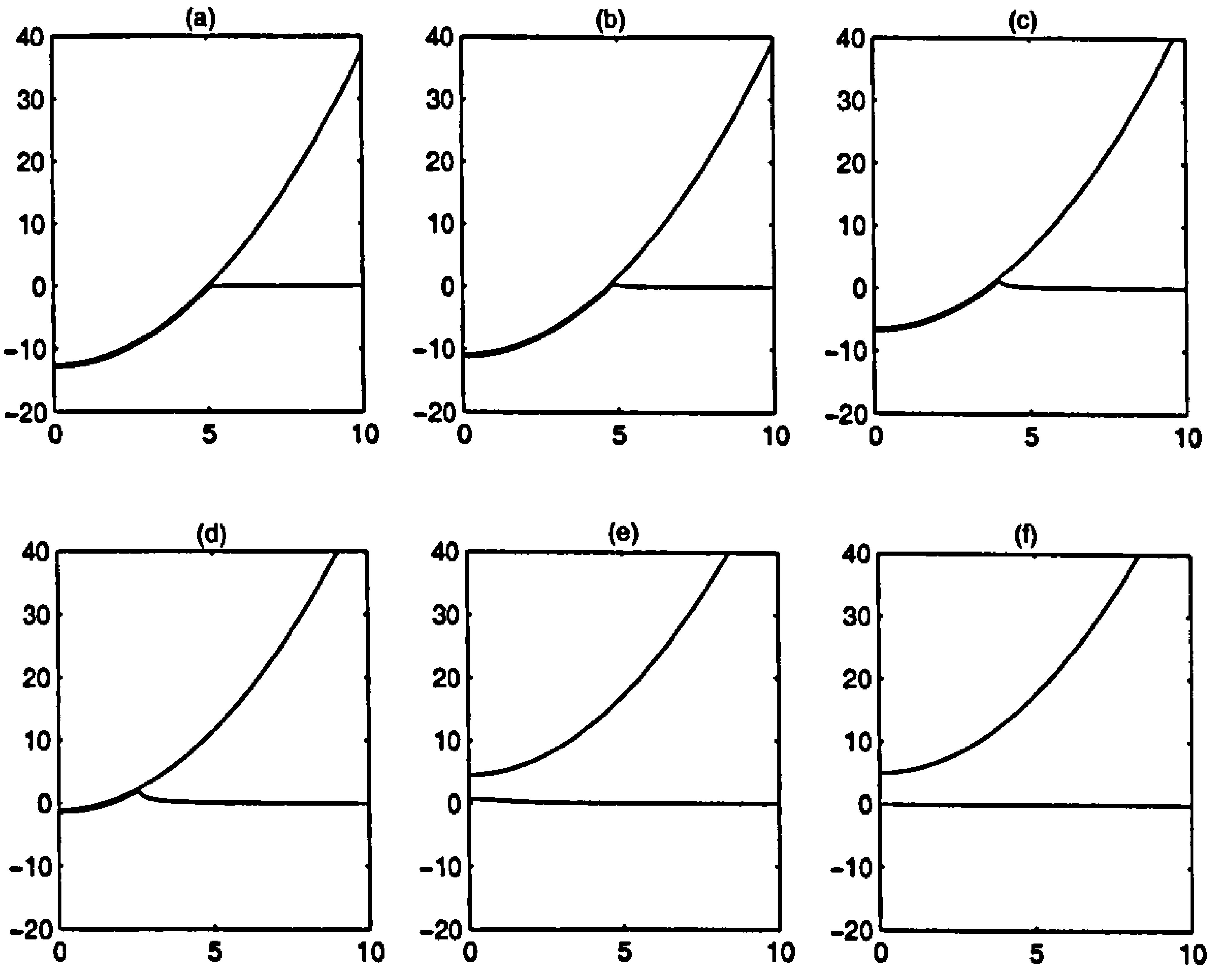

Figure 3.15: Particle lifted off with $t_f = 10$ where $t =$ (a) 0, (b) 2, (c) 4, (d) 6, (e) 9, (f) 12

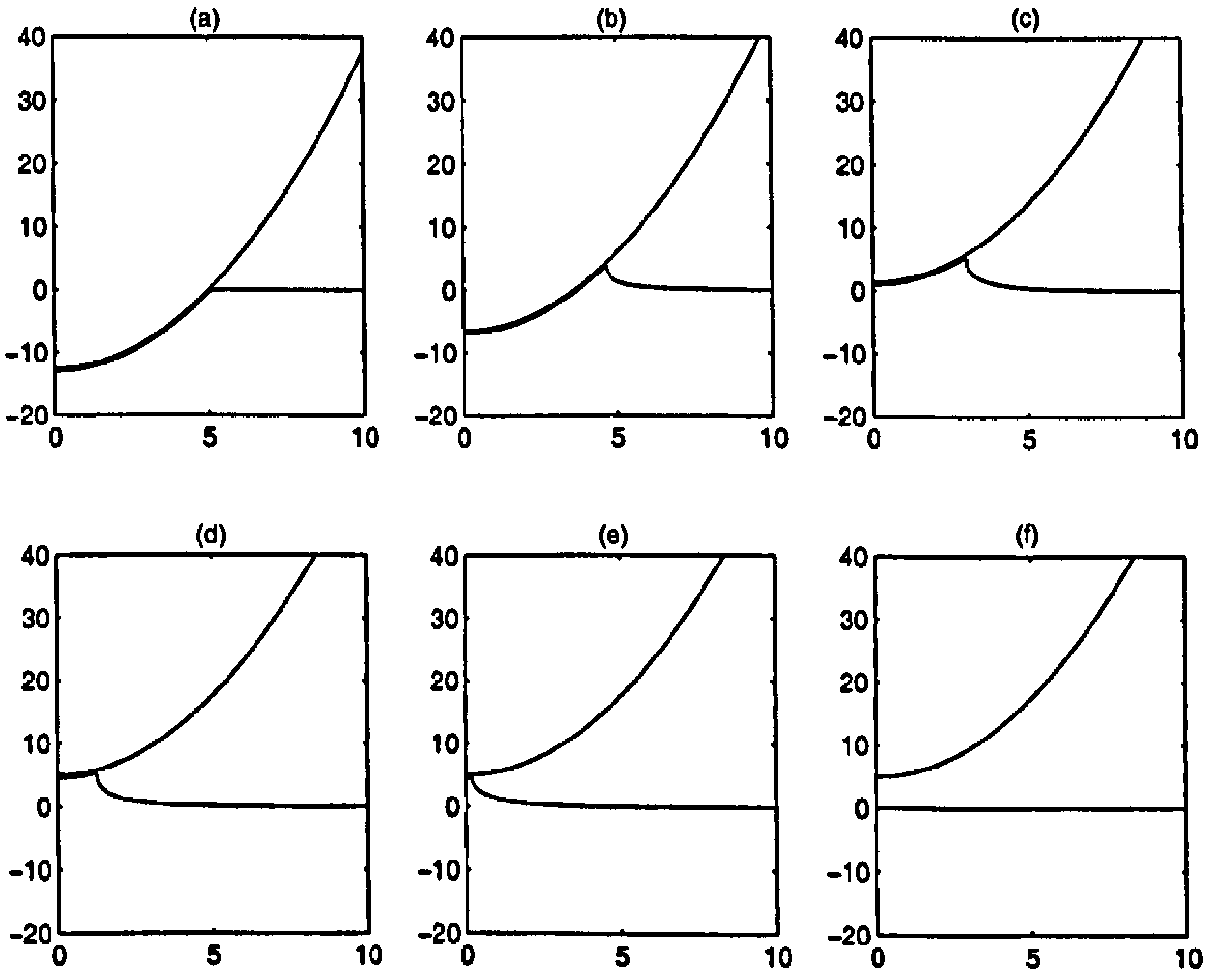

Figure 3.16: Particle lifted off with $t_f = 1$, where $t =$ (a) 0, (b) 0.4, (c) 0.7, (d) 1, (e) 1.3, (f) 2

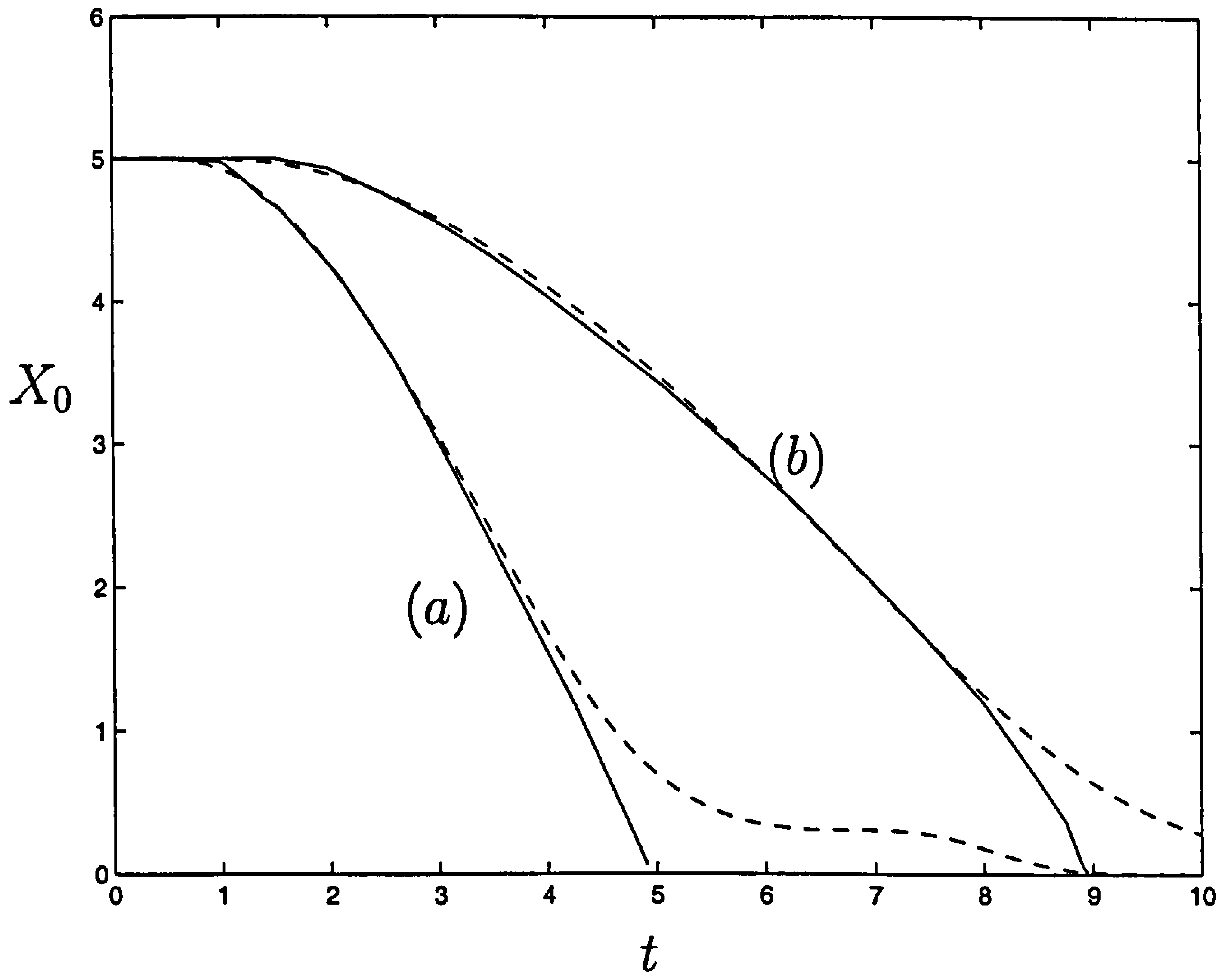

Figure 3.17: Position of corner, $X_0(t)$, as particle is pulled off the wall with $t_f =$ (a) 5, (b) 10, obtained from numerical simulations (solid lines) and showing analytical solutions (dashed lines) from (3.62).

stretched and exert a negative force on the particle, attempting to pull the particle down. As the wall returns to its undeformed state the force on the particle returns to zero. For particles pulled off quickly, *e.g.* $t_f = 1$, the suction force which acts on the particle is much greater than for particles pulled off more slowly, *e.g.* $t_f = 20$. Therefore simulations suggest that it becomes more difficult to pull a particle from the wall as t_f decreases.

3.3.1 Asymptotic analysis in the corner region

We now examine the sharp corner region that forms as the particle is pulled away from the wall. Let the corner, at $x = X_0(t)$ where $X_0(0) = X_c$, move

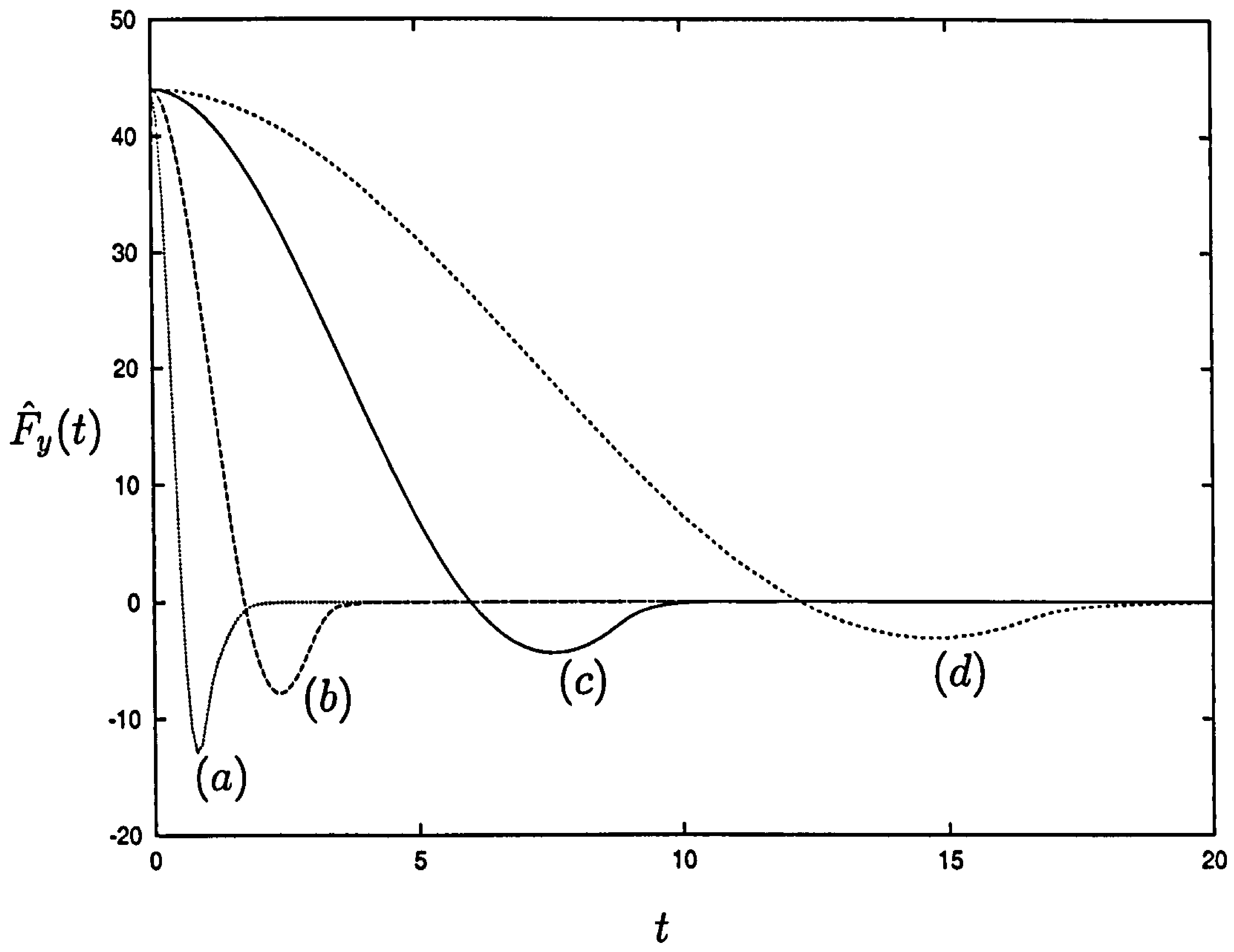

Figure 3.18: Force varying with time for (*a*) $t_f = 1$, (*b*) $t_f = 3$, (*c*) $t_f = 10$, (*d*) $t_f = 20$.

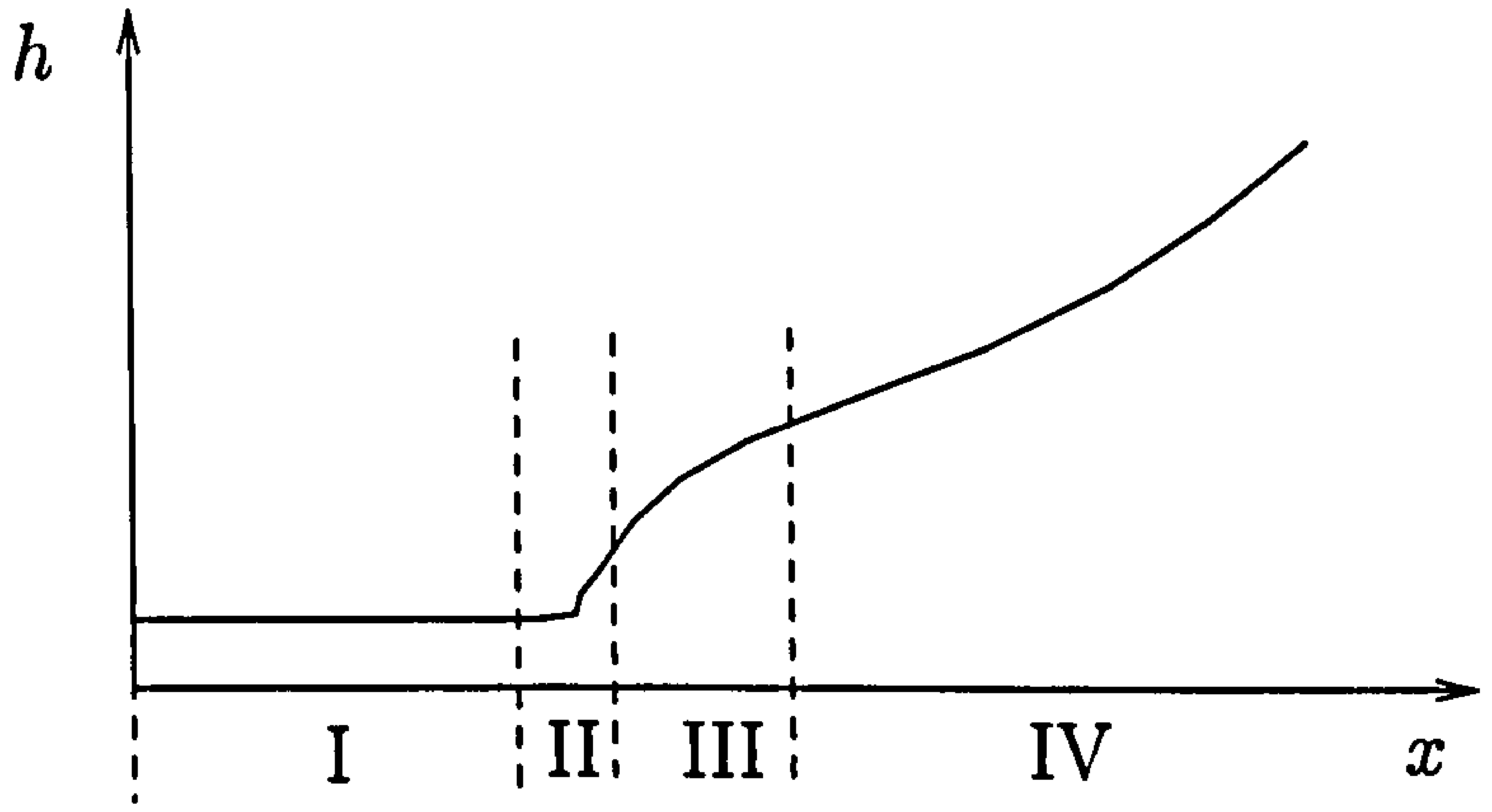

Figure 3.19: Sketch of the different regions as particle is pulled away from the wall.

towards the origin with speed $w(t)$ so that $\dot{X}_0 = -w$. We set $x = X_0(t) + \xi$ and look for quasi-steady solutions so that $\partial/\partial t = -\dot{X}_0 \partial/\partial\xi$. The evolution equation (3.47) becomes

$$wh_\xi + \frac{1}{12}\left[h^3(X_0 + \xi)\right]_\xi = \frac{1}{12}(h^3 h_\xi)_\xi. \tag{3.57}$$

In this case the domain may be divided into four regions, see Figure 3.19.

In Region I the gap thickness is almost uniform so we let $h \approx \delta$. In Regions II & III we assume that $|\xi| \ll X_0$ and so integrating (3.57), with $h \to \delta$ as $\xi \to -\infty$, gives

$$w(h - \delta) + \frac{X_0}{12}(h^3 - \delta^3) = \frac{1}{12}h^3 h_\xi. \tag{3.58}$$

In Region III, where $h \gg \delta$, (3.58) reduces to

$$h_\xi = X_0 + \frac{12w}{h^2},$$

neglecting terms of $\mathrm{O}(\delta)$. Integrating with $h \to 0$ as $\xi \to 0$ (since $\mathrm{O}(\delta)$ terms are neglected) we obtain

$$\xi = \frac{h}{X_0} - \frac{2w\sqrt{3}\tan^{-1}\left[\frac{1}{6}X_0 h\sqrt{3/wX_0}\right]}{X_0\sqrt{wX_0}}. \tag{3.59}$$

In the inner limit of Region III h is small and (3.59) reduces to

$$h \approx (36w\xi)^{1/3}.$$

In the outer limit of Region III where h is large (3.59) becomes

$$h \approx X_0\xi + \pi\sqrt{\frac{3w}{X_0}}. \tag{3.60}$$

In Region II we assume $h = \delta H$. We require this solution to match with the inner limit of Region III where $h \approx (36w\xi)^{1/3}$. Comparing these solutions for h we get $\delta \sim (w\xi)^{1/3}$ and hence a lengthscale for Region II is $\xi \sim \delta^3/w$. Letting $\xi = (\delta^3/w)\eta$, (3.58) becomes

$$H - 1 = \frac{1}{12}H^3 H_\eta, \tag{3.61}$$

which has solution

$$\eta = \frac{1}{36}H^3 + \frac{1}{24}H^2 + \frac{1}{12}H + \frac{1}{12}\ln(H-1).$$

In the inner limit of Region II we let $H = 1 + \hat{H}$ where $\hat{H} \ll 1$. Equation (3.61) reduces to $\hat{H} \approx \hat{H}_\eta/12$ and hence we find $\hat{H} \approx \hat{H}_0 e^{12\eta}$ where $\hat{H}_0$ is a constant. Therefore we obtain

$$h \approx \delta(1 + \hat{H}_0 e^{12\eta}),$$

which matches with Region I, where $h \approx \delta$, as $\eta \to -\infty$. In the outer limit of Region II (3.61) becomes $H \approx H^3 H_\eta/12$, since $H \gg 1$, and hence we have $H \approx (36\eta)^{1/3}$. In terms of h and ξ this is $h \approx (36w\xi)^{1/3}$ and therefore matches with the inner limit of Region III as required.

In Region IV, ξ is not small so (3.58) is not valid. The $O(h^3)$ terms in (3.57) dominate giving

$$h^3(X_0 + \xi) \approx h^3 h_\xi.$$

We know $h \neq 0$ and so $h_\xi \approx X_0 + \xi$. Integrating we obtain

$$h \approx X_0\xi + \frac{\xi^2}{2} + \text{const.}$$

In the outer limit of Region IV we know $h \to h_0 + x^2/2$ from the boundary condition so we can calculate the constant of integration giving

$$h \approx X_0\xi + \frac{\xi^2}{2} + h_0 + \frac{X_0^2}{2}.$$

The movement of the corner is driven by the behaviour in Region III and matching between Regions III & IV using (3.60) we obtain the following relation between the prescribed displacement, $h_0(t)$, and the position of the corner, $X_0(t)$:

$$h_0 + \frac{X_0^2}{2} = \pi\sqrt{\frac{3w}{X_0}}. \tag{3.62}$$

Taking $h_0(t_f) = 5$ and $X_c = 5$ in $h_0(t)$ we solve this equation for $X_0(t)$ numerically. Figure 3.17 shows the analytical solution compared to the previous

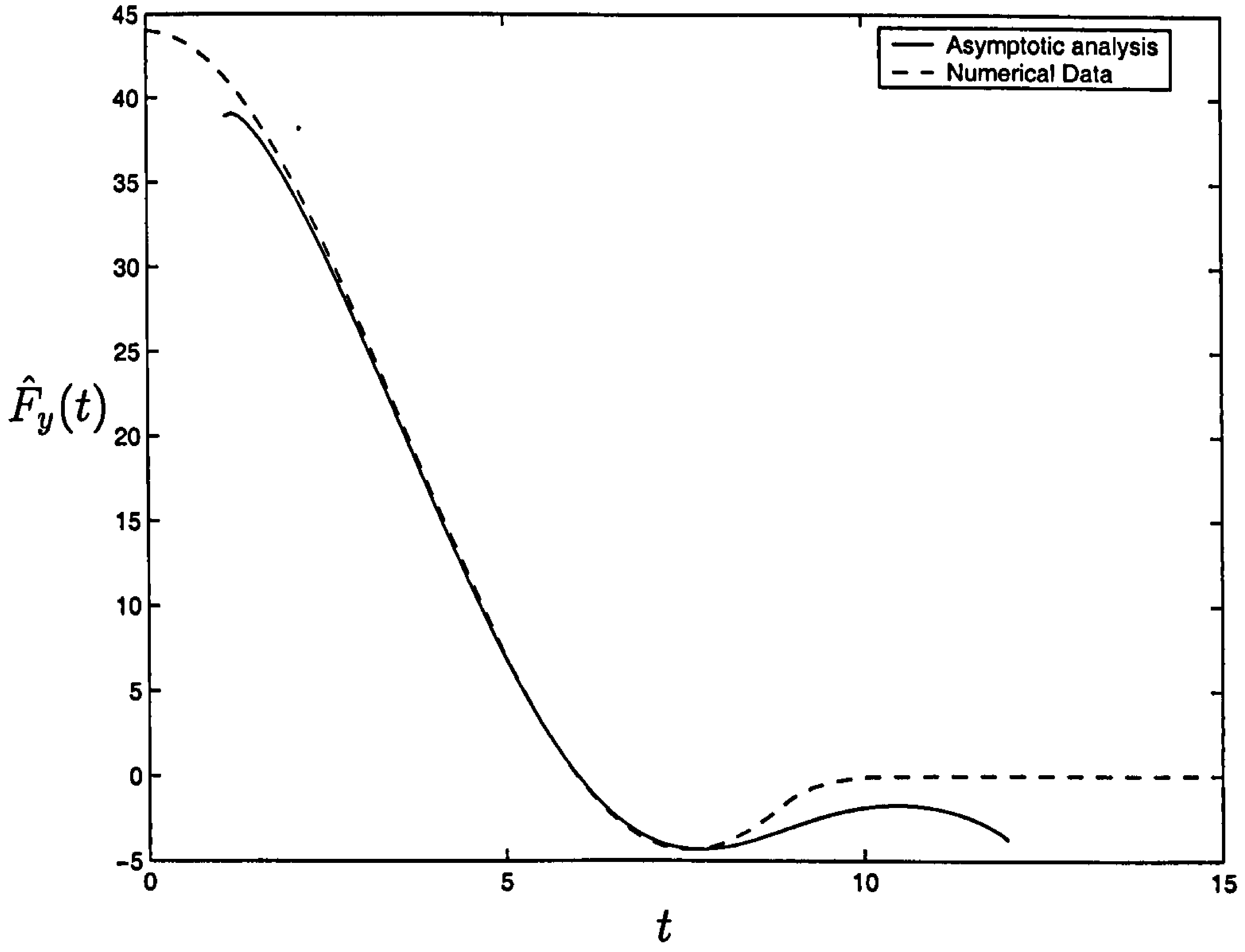

Figure 3.20: Force, $\hat{F}_y$, as the particle is pulled away from the wall with $t_f = 10$ calculated by numerical simulations (dashed line), showing agreement with the analytical approximation (solid line) for intermediate t.

numerical simulations of the PDE. The analytical solution breaks down as X_0 approaches zero and the model breaks down. This is because as X_0 approaches zero the regions are no longer distinct and separate. However the analytical solution captures the majority of the corner motion well, in particular the 'waiting time' of the corner position before it begins to move.

We can use the solution of (3.62) to calculate an approximation for the force, $\hat{F}_y(t)$, acting on the particle. The force $\hat{F}_y$ can be expressed as

$$\hat{F}_y(t) = \int_0^{X_0(t)} \left(h - h_0 - \frac{1}{2}x^2\right)\, dx + \int_{X_0(t)}^{\infty} \left(h - h_0 - \frac{1}{2}x^2\right)\, dx. \tag{3.63}$$

For $0 < x < X_0(t)$, $h \approx \delta$. For $x \gg X_0(t)$, $h \approx h_0 + x^2/2$, so in the interval $X_0(t) < x < \infty$ any contribution to the force will occur close to $X_0(t)$. We define a small region $X_0(t) < x < X_0(t) + \bar{\xi}$ where $\bar{\xi} = -\delta^3/\dot{X}_0$ (a lengthscale for Region III) and where h is given by (3.59). Using $X_0(t)$ from (3.62) and taking $h_0(t_f) = 5$ and $X_c = 5$ we can integrate (3.63) numerically to obtain an approximation for $\hat{F}_y$ valid for intermediate t. Figure 3.20 shows the agreement of the analytical approximation with the numerical simulation for intermediate t.

3.4 Perpendicular Motion: Prescribed Force

We now prescribe the force pushing the particle into the wall and determine the displacement of the particle and the deformation of the wall. There are two timescales in the problem: the timescale for the springs in the wall to push fluid along the gap, T_{sp}; and the timescale for the particle under the prescribed force to push fluid along the gap, T_{sq}, which we estimate as follows. Considering the scalings in the thin film we have a balance between pressure and viscous terms,

$$\frac{\Delta p}{(RH)^{1/2}} \sim \frac{\mu U}{H^2}, \tag{3.64}$$

and the continuity equation gives

$$\frac{U}{(RH)^{1/2}} \sim \frac{H/T}{H}. \tag{3.65}$$

For the squeezing timescale, T_{sq}, viscous forces balance the imposed force on the particle, so the pressure is given by

$$\Delta p \sim \frac{F_0}{(RH)^{1/2}},$$

where the (dimensional) force $F^*(t) = F_0 F(t)$ and $F(t) = O(1)$. Equations (3.64) & (3.65) give

$$T_{sq} \sim \frac{\mu R^{3/2}}{F_0 H^{1/2}}. \tag{3.66}$$

For the spring timescale the pressure gradient is given by

$$\Delta p \sim \kappa H,$$

which gives

$$T_{sp} \sim \frac{\mu R}{\kappa H^2}. \tag{3.67}$$

We define

$$W = \frac{T_{sp}}{T_{sq}} = \frac{F_0}{\kappa R^{1/2} H^{3/2}}, \tag{3.68}$$

to be the ratio of the two timescales so that $W \ll 1$ is the "stiff wall" case and $W \gg 1$ is the "compliant wall" case.

The dimensional vertical force is

$$F^*(t) = 2\int_0^\infty \kappa \left(h^* - h_0^* - \frac{x^{*2}}{2R}\right) dx^*,$$

so nondimensionalising and scaling as in §3.1.1 (scaling times on T_{sp}) we obtain

$$W\hat{F}(t) = \int_0^\infty \left(h - h_0 - \frac{x^2}{2}\right) dx. \tag{3.69}$$

Therefore we consider the problem

$$h_t + \frac{1}{12}\left[h^3(x - h_x)\right]_x = 0, \tag{3.70}$$

$$h \longrightarrow h_0(t) + \frac{1}{2}x^2, \text{ as } x \longrightarrow \infty \tag{3.71}$$

$$h_x = 0 \text{ at } x = 0, \tag{3.72}$$

$$W\hat{F}(t) = \int_0^\infty \left(h - h_0 - \frac{x^2}{2}\right) dx, \tag{3.73}$$

for fixed W, with $\hat{F}(t)$ prescribed. We now seek the displacement, $h_0(t)$.

3.4.1 Pushing

We assume the applied force is given by

$$\hat{F}(t) = \begin{cases} \frac{1}{2}\left[1 - \cos\left(t\pi/t_{final}\right)\right], & 0 \le t \le t_{final}, \\ 1, & t > t_{final}. \end{cases}$$

Numerical Method

Again we use NAG routine D02NBF to convert the governing PDE (3.70) into a system of ODEs and integrate using finite difference methods over the region

$[0, L]$. The following simulations used 2001 meshpoints with accuracy checked as before. At long times, equation (3.73) becomes

$$W\hat{F} = -\int_0^{X_c}\left(h_0 + \frac{x^2}{2}\right)\,dx = -\left(h_0 X_c + \frac{X_c^3}{6}\right) = \frac{X_c^3}{3},$$

since $h_0 = -X_c^2/2$ at long times, and hence we obtain $X_c = (3W)^{1/3}$. We take the domain length, L, to be the maximum of $2X_c$ and 10 to ensure the surface remains undeformed in the far field, and $h_0(0) = 5$.

We want to calculate the displacement, $h_0(t)$, for given $\hat{F}(t)$ so rearranging equation (3.73) the displacement is given by

$$h_0 = \frac{1}{L}\left[\int_0^L \left(h - \frac{x^2}{2}\right)\,dx - W\hat{F}_y(t)\right]. \qquad (3.74)$$

Simulations

Figure 3.21 shows the particle deforming the wall for the case $t_{final} = 10$, $W = 0.2$, *i.e.* stiff springs, where deformation of the wall is small. This case is similar to that of rigid walls. Figure 3.22 shows the particle and wall position for $t_{final} = 10$, $W = 10$, *i.e.* compliant wall, where the deformation of the wall in response to the particle is much greater. As in the prescribed displacement model, $h \to 0$ in the region $0 \leq x \leq X_c$ as $t \to \infty$.

Figure 3.23 shows the displacement of the particle, $h_0(t)$, as t varies for different values of W. In all cases we assume the force is imposed impulsively and let $t_{final} = 10^{-8}$. For small W the particle can be pushed only a small distance, but for large W, where the springs are compliant, the particle is displaced a significant distance into the wall. When the springs are compliant we have $T_{sp} \gg T_{sq}$ and there is a state of quasi-equilibrium.

We know that, as $t \longrightarrow \infty$,

$$h_0 \longrightarrow -\frac{X_c^2}{2} = -\frac{(3W)^{\frac{2}{3}}}{2}. \qquad (3.75)$$

so we can calculate the final displacement of the particle for a given W. We now analyse the short-time and large-time behaviour of the system.

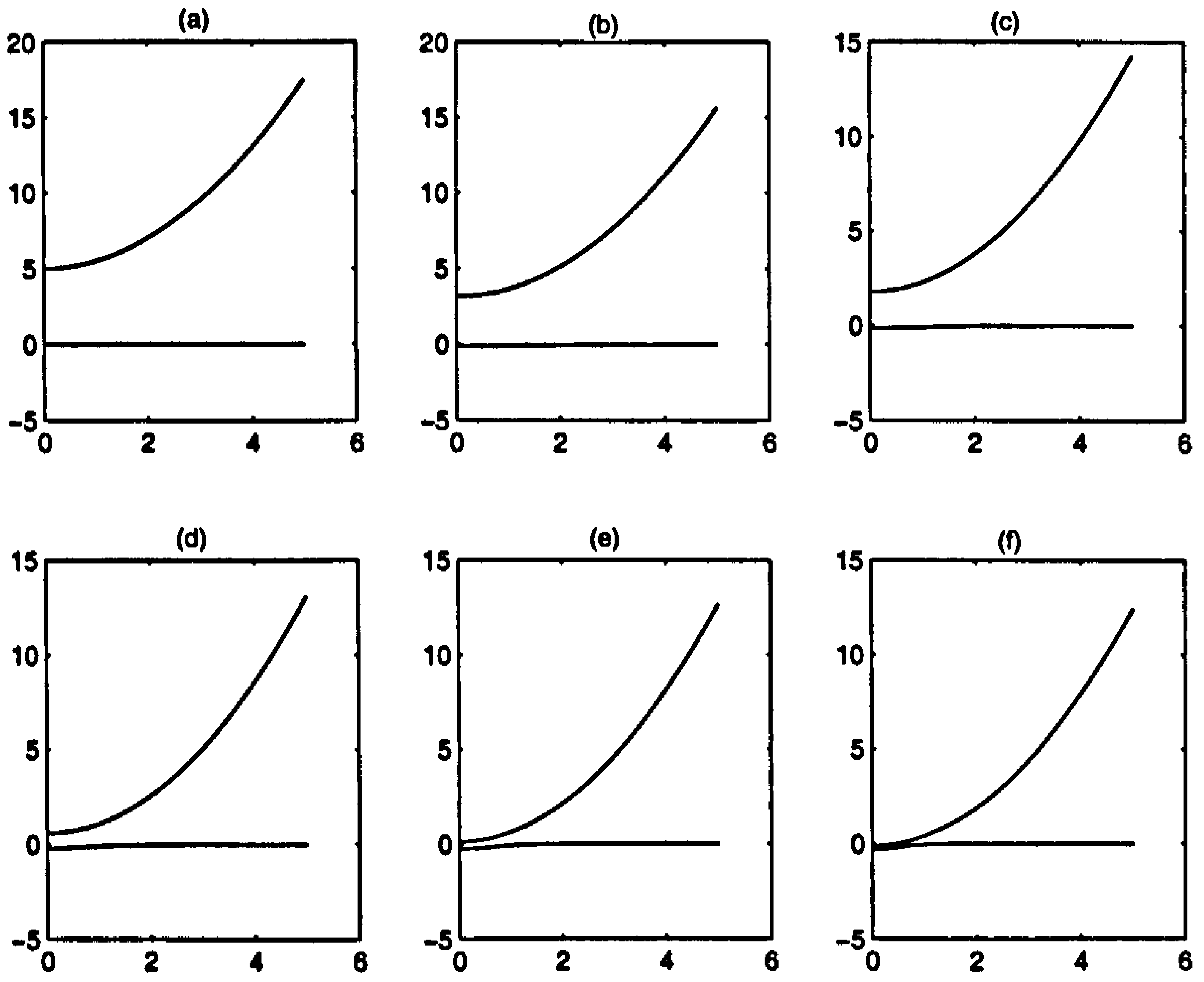

Figure 3.21: Particle position and wall deformation for the case $W = 0.2$ where $t =$ (a) 10^{-5}, (b) 10, (c) 20, (d) 50, (e) 100, (f) 200.

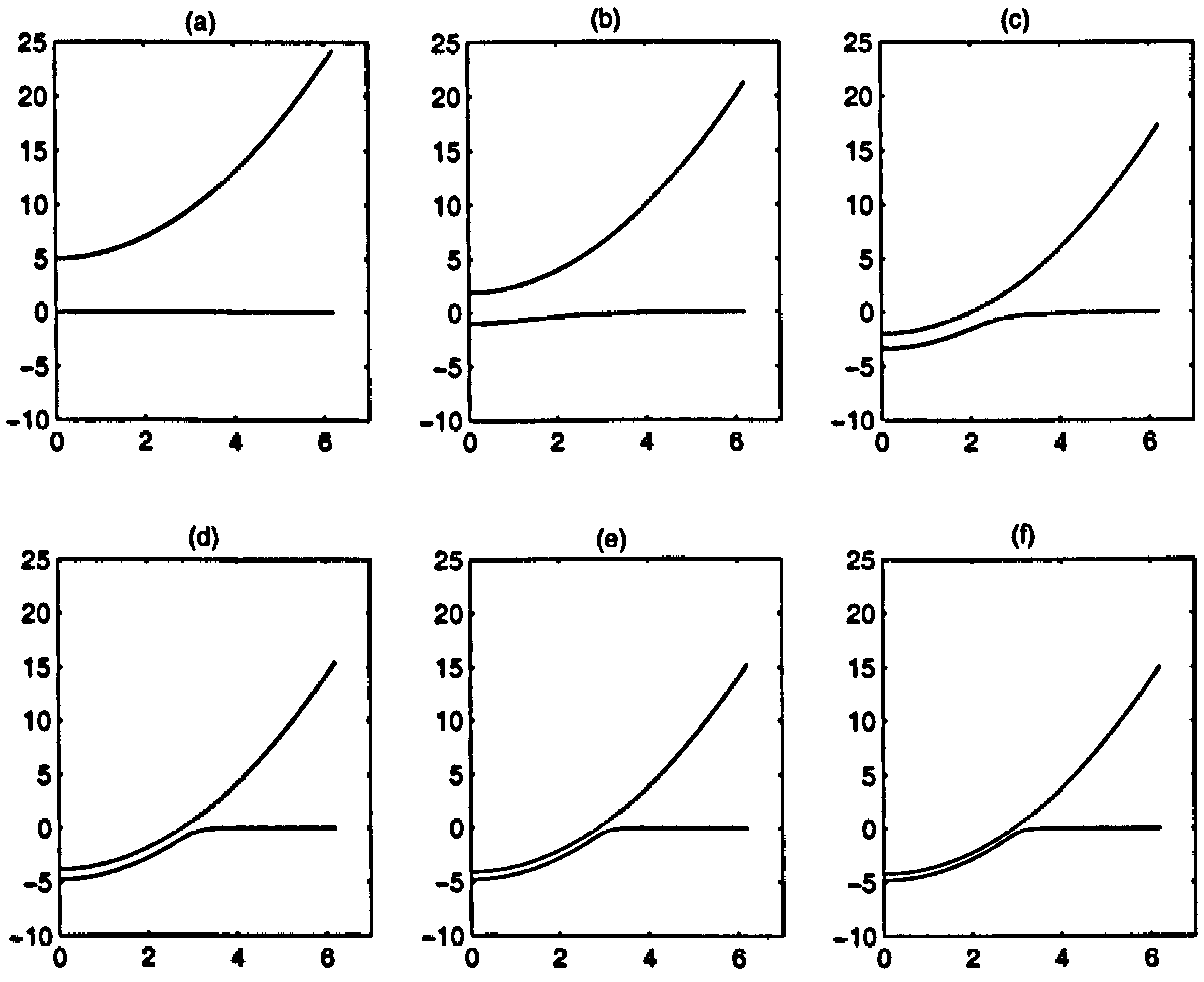

Figure 3.22: Particle position and wall deformation for the case $W = 10$ where $t =$ (a) 10^{-5}, (b) 3, (c) 6, (d) 10, (e) 15, (f) 20.

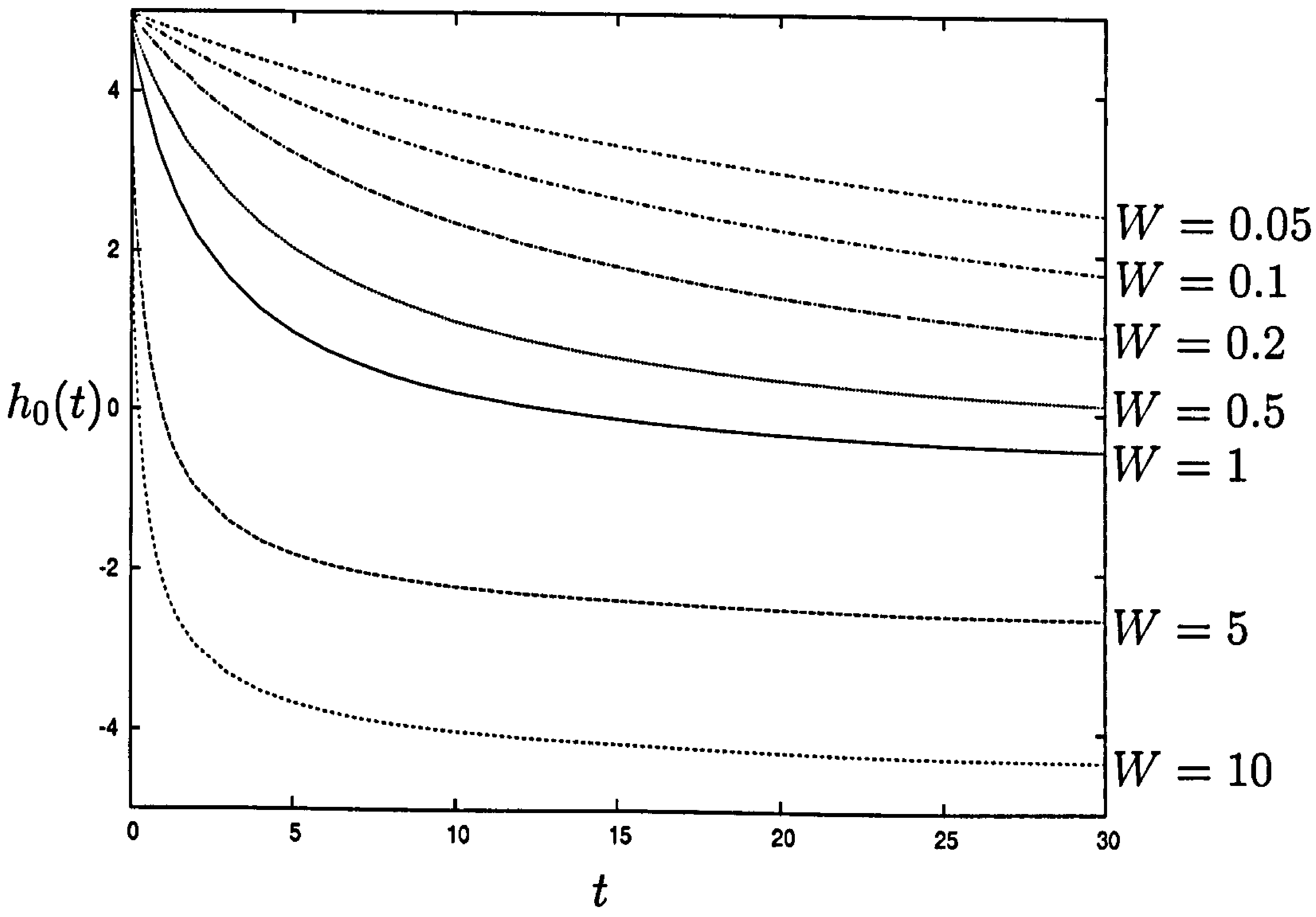

Figure 3.23: Displacement, $h_0(t)$ against time, for varying W, with $t_{final} = 10^{-8}$.

Asymptotic Analysis: Short times

As in §3.2.1, at short times we assume wall deformations to be small so we let $h = h_0(0) + x^2/2 + H(x,t)$ and $h_0 = h_0(0) + \hat{h}_0(t)$ where H, $\hat{h}_0$ are small perturbations from the initial conditions. Therefore (3.73) reduces to

$$W\hat{F} = \int_0^\infty (H - \hat{h}_0)\, dx, \tag{3.76}$$

and (3.70) becomes

$$H_t \approx \frac{1}{12}\left[\left(5 + \frac{x^2}{2}\right)^3 H_x\right]_x . \tag{3.77}$$

Balancing the terms in (3.77), we get $t^{-1} \sim x^{-2} \sim x^4$. Choosing $x = \zeta/t^{1/4}$, equation (3.76) becomes

$$W\hat{F} = \int_0^\infty (H - \hat{h}_0)\frac{d\zeta}{t^{1/4}}, \tag{3.78}$$

with the boundary condition

$$H \longrightarrow \hat{h}_0 \text{ as } \zeta \longrightarrow \infty, \tag{3.79}$$

since we prescribe the pressure to be zero in the far field. If we assume $\hat{F}(t)$ is imposed impulsively, for simplicity, *i.e.* $\hat{F} = 1$ for $t > 0$, then H and $\hat{h}_0$ increase like $t^{1/4}$. We let $H = t^{1/4}\tilde{H}$ and $\hat{h}_0 = t^{1/4}\tilde{h}_0$ so (3.78) becomes

$$W = \int_0^\infty (\tilde{H} - \tilde{h}_0)\, d\zeta, \tag{3.80}$$

and (3.77) becomes, at leading order as $t \to 0$,

$$\frac{\tilde{H}}{4} + \frac{\zeta \tilde{H}_\zeta}{4} = \frac{1}{12}\left(\frac{\zeta^6 \tilde{H}_\zeta}{8}\right)_\zeta . \tag{3.81}$$

Integrating with respect to ζ, with $\tilde{H}$ bounded as $\zeta \longrightarrow 0$, we obtain

$$\tilde{H} = \frac{1}{24}\zeta^5 \tilde{H}_\zeta. \tag{3.82}$$

We solve (3.82) to get

$$\tilde{H} = \tilde{H}_0 \exp\left[-\frac{6}{\zeta^4}\right],$$

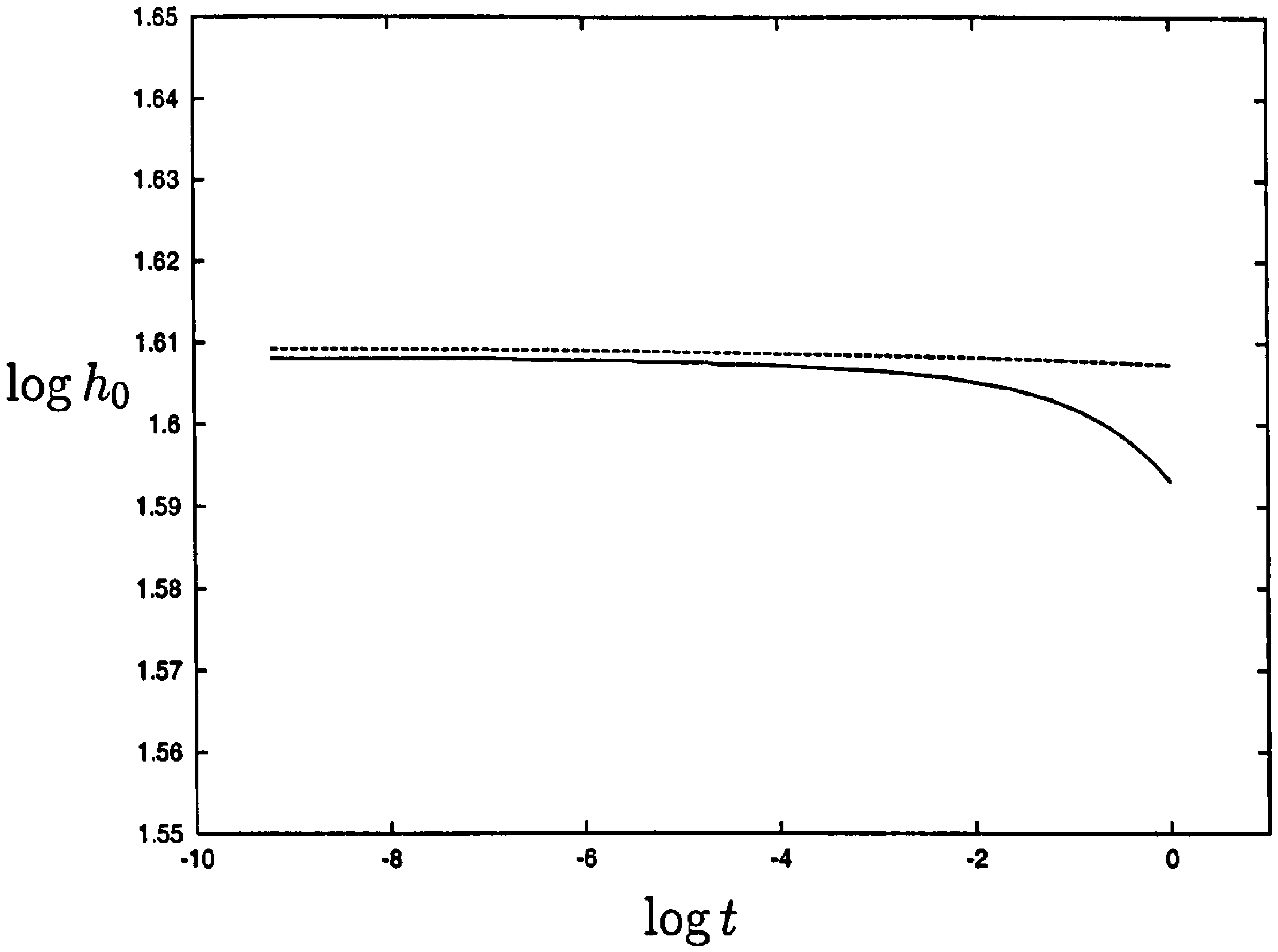

Figure 3.24: A plot of $\log h_0$ against $\log t$ showing agreement between the asymptotic solution (3.83) (dashed line) and the numerical simulation (solid) at short times for the case $W = 0.02$, $t_{final} = 10^{-8}$.

where $\tilde{H}_0$ is a constant. As $\zeta \to \infty$, $\tilde{H} \to \tilde{H}_0$ so, using (3.79), $\tilde{H}_0 = \tilde{h}_0$. Equation (3.80) becomes

$$W = \int_0^\infty \tilde{h}_0 \left[\exp\left(-\frac{6}{\zeta^4}\right) - 1\right] d\zeta.$$

We find that, at short times,

$$h_0 = 5 - \frac{W}{I} t^{1/4}, \quad \text{where } I = \int_0^\infty \left[1 - \exp\left(-\frac{6}{\zeta^4}\right)\right] d\zeta \approx 1.91788. \quad (3.83)$$

Since we assume perturbations from the initial conditions to be small this is valid provided $Wt^{1/4}$ is small. Figure 3.24 shows agreement between this asymptotic solution and the numerical solution at short times for the case $W = 0.02$, where $t_{final} = 10^{-8}$. This analysis breaks down when $Wt^{1/4}$ is not small and deformations become large.

This analysis is similar to the short-time analysis for the prescribed displacement (pushing) case, (see §3.2.1). In this case, the force is imposed impulsively, $\hat{F} \sim 1$, whereas for the prescribed displacement case $h_0 \sim t^2$. The different time dependence makes the differential equation exactly integrable in this case.

Asymptotic Analysis: Long times

At long times the particle is near equilibrium and we assume the motion is quasi-static, so $h_t = 0$. As in §3.2.2, we obtain as $t \to \infty$, $h = 0$ for $0 \leq x \leq X_c$ and $h = h_0 + x^2/2$ for $X_c < x < L$. Again we find that, at long times, the shape of h divides into an inner region, an outer region and a corner region, and the previous asymptotic matching analysis is valid in the present case, where $X_c = (3W)^{1/3}$.

We consider the displacement at long times. Equation (3.74) can be expressed

$$h_0(t) = \frac{1}{L}\int_0^{X_c}\left(h - \frac{x^2}{2}\right)\,dx + \frac{1}{L}\int_{X_c}^{L}\left(h - \frac{x^2}{2}\right)\,dx - \frac{W}{L}, \tag{3.84}$$

since $F(t) = 1$ at long times. For $X_c < x < L$, any perturbations to $h = h_0 + x^2/2$ will be close to X_c. As in §3.2.2 we can show that perturbations are $O(t^{-1/2})$ decaying over a lengthscale of $O(t^{-1})$. From (3.48) for $0 \leq x \leq X_c$ we know $h \sim \sqrt{6}/t^{1/2}$ and so (3.84) becomes

$$\begin{aligned} h_0(t) &= \frac{1}{L}\int_0^{X_c}\left(\frac{\sqrt{6}}{t^{1/2}} - \frac{x^2}{2}\right)\,dx + \frac{1}{L}\int_{X_c}^{L} h_0\,dx - \frac{W}{L} + O\left(\frac{1}{t^{3/2}}\right), \\ &= -\frac{(3W)^{2/3}}{2} + \frac{\sqrt{6}}{t^{1/2}}, \end{aligned} \tag{3.85}$$

to leading order, since $X_c = (3W)^{1/3}$. As $t \to \infty$, $h_0(t) \to -(3W)^{2/3}/2$ as required from (3.75). Figure 3.25 shows (3.85) to be consistent with the numerical simulations at long times. The analysis breaks down for small W as X_c gets close to zero and the three-region structure breaks down.

We also consider the "stiff wall" case where $W \ll 1$ and the wall is almost rigid. The asymptotic analysis for this case is not conclusive and is shown in Appendix B.

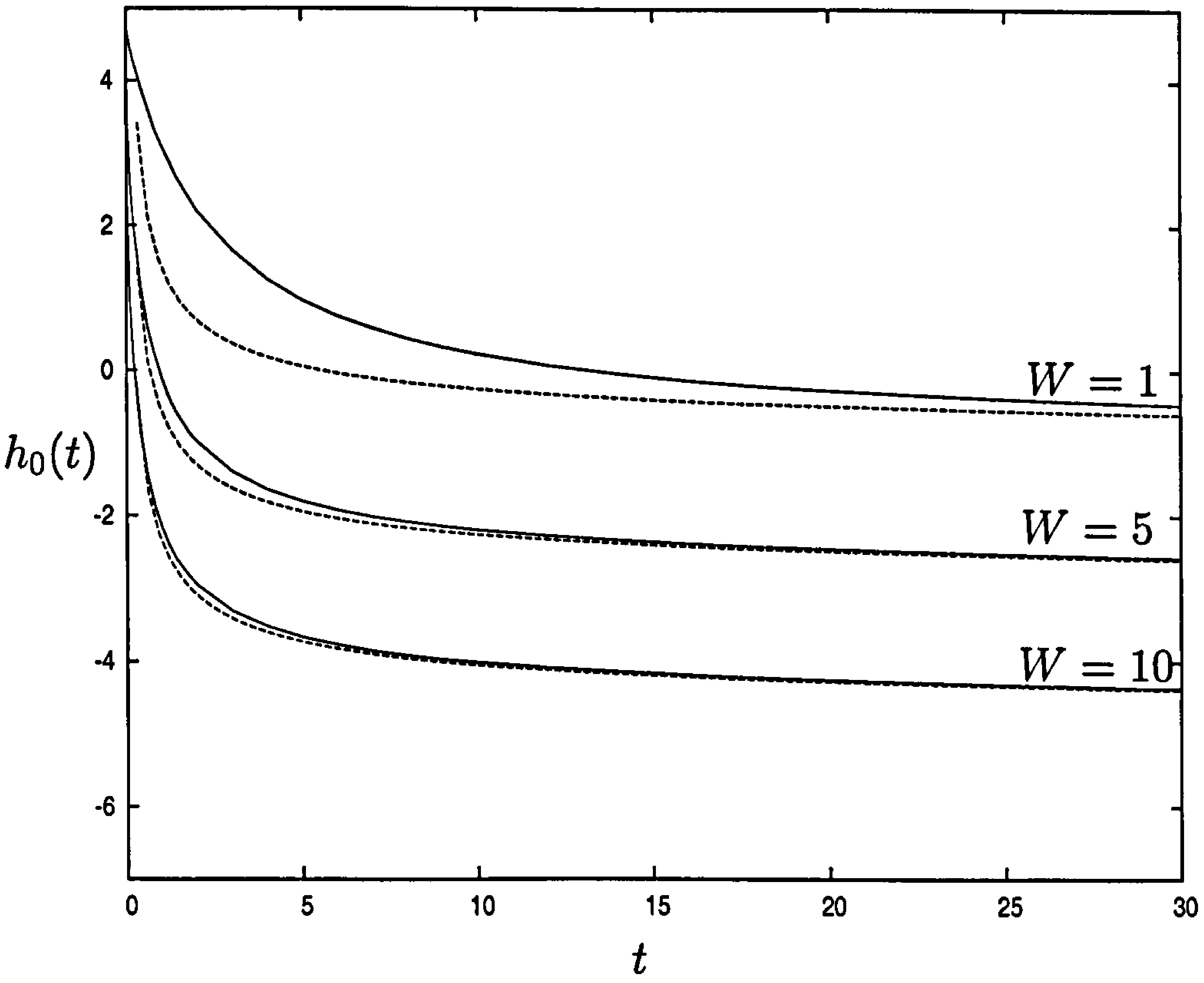

Figure 3.25: Displacement $h_0(t)$ as t increases for various W (solid lines). Numerical simulations are consistent with the analytical solutions (dashed lines) given by (3.85).

3.4.2 Pulling

Numerical Method

In the previous section the particle was subject to a force which increases for $0 \leq t \leq t_{final}$ and then remains constant. The opposing force due to the wall deformation causes the particle to reach an equilibrium position as $t \rightarrow \infty$ with a final displacement $h_0 \rightarrow -X_c^2/2$. We now look briefly at the case where a particle is removed from the wall by a force.

We run the previous simulation (§3.4.1) and take the particle and wall position at $t = 200$ as the new initial configuration. The particle is being held in position by the (dimensionless) downwards force $F(t) = 1$. We model the effect of an opposing force as a gradual reduction of the net downwards force. We use the same numerical method as in §3.4.1 with new initial conditions and the applied force now given by

$$F(t) = \begin{cases} \frac{1}{2}\left[1 + \cos\left(t\pi/t_f\right)\right], & 0 \leq t \leq t_f, \\ 0, & t > t_f. \end{cases}$$

Simulations

In all cases we take $t_f = 10$. Figure 3.26 shows the particle and wall behaviour for the case $W = 10$, where the springs are compliant. Initially the wall is significantly deformed and as the net downwards force decreases the particle moves upwards as the wall springs relax to their undeformed state. Figure 3.27 shows the case $W = 0.5$, where the springs are stiffer and the initial deformation is smaller. This exhibits similar behaviour. In both cases we notice that in the corner region the wall is pulled upwards slightly as the particle moves, as observed in §3.3. Figure 3.28 shows the displacement of the particle as t increases for different values of W. Due to our choice of initial conditions a thin film exists between the particle and wall at $t = 0$. Denoting the thickness of this film by δ we find, for all W, $h_0(t) \to \delta$ as t increases.

The asymptotic analysis in the corner region for the prescribed displacement case (§3.3.1) is also valid for the prescribed force case, and hence (3.62) describes the movement of the corner, $X_0(t)$. However, in this case $h_0(t)$ is given by (3.74) and is dependent on the gap thickness h, so integration of (3.62) to find $X_0(t)$ explicitly is no longer straightforward.

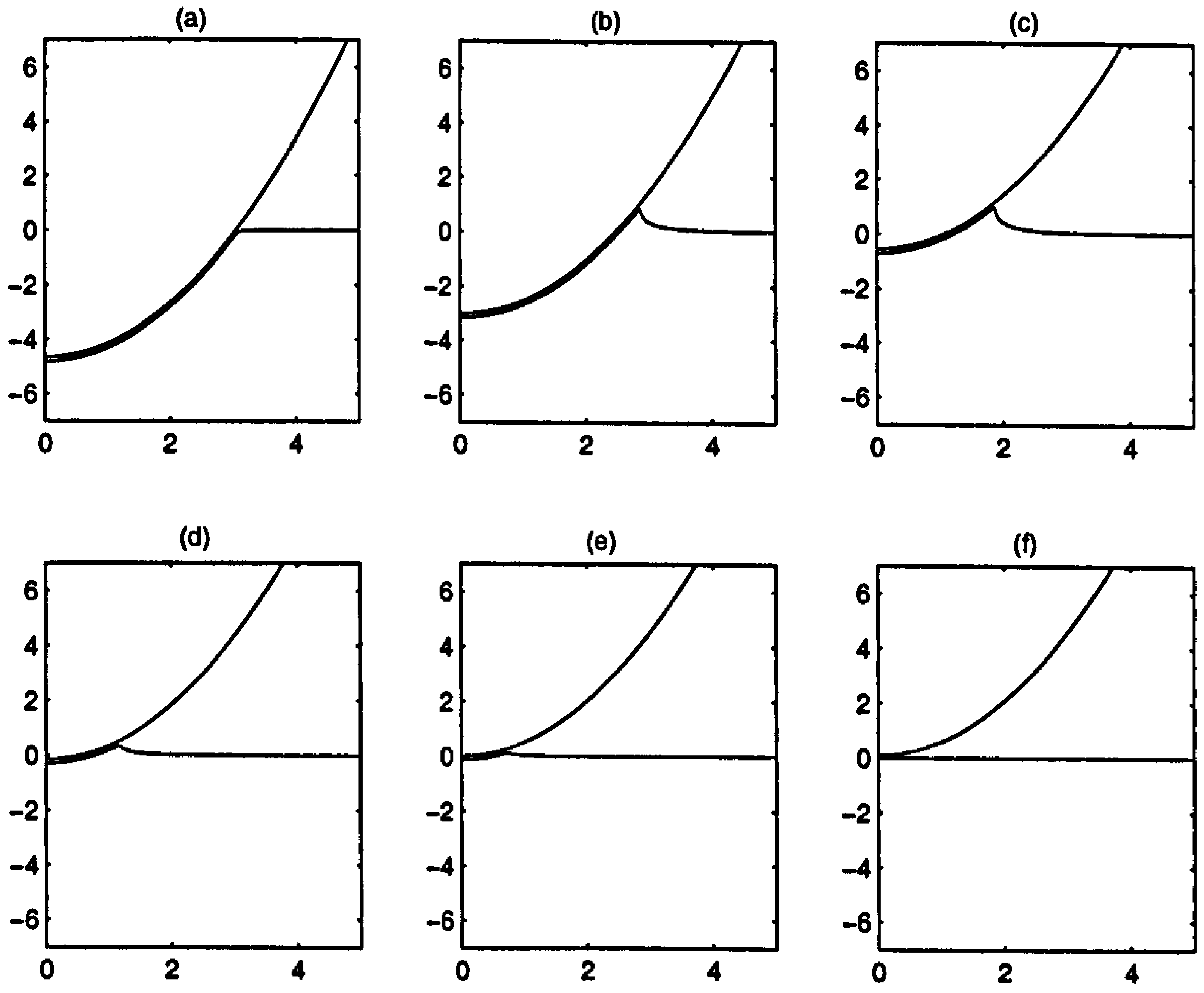

Figure 3.26: Particle position and wall deformation for the case $W = 10$ where $t =$ (a) 0, (b) 5, (c) 10, (d) 20, (e) 50, (f) 200.

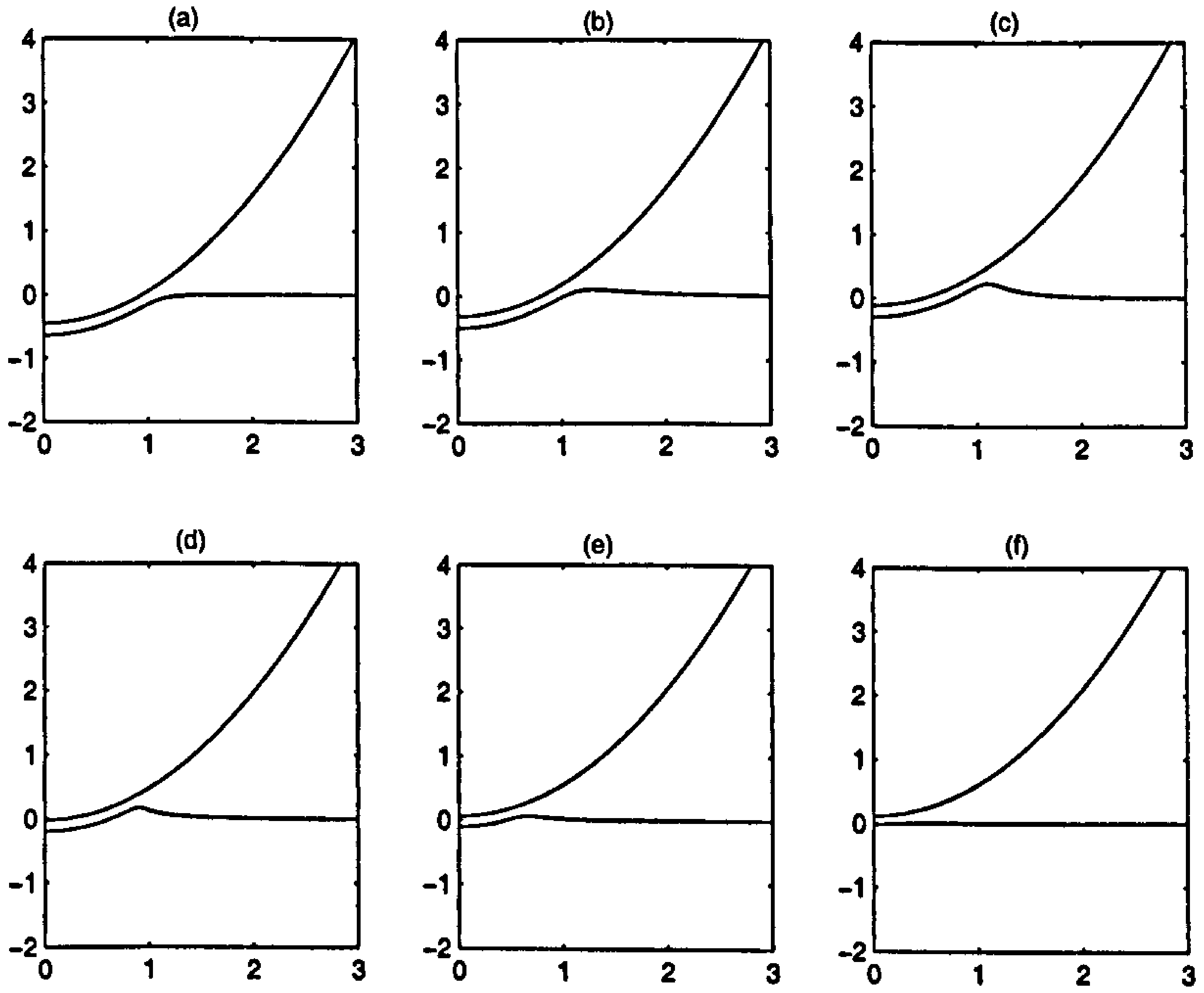

Figure 3.27: Particle position and wall deformation for the case $W = 0.5$ where $t =$ (a) 0, (b) 5, (c) 10, (d) 20, (e) 50, (f) 200.

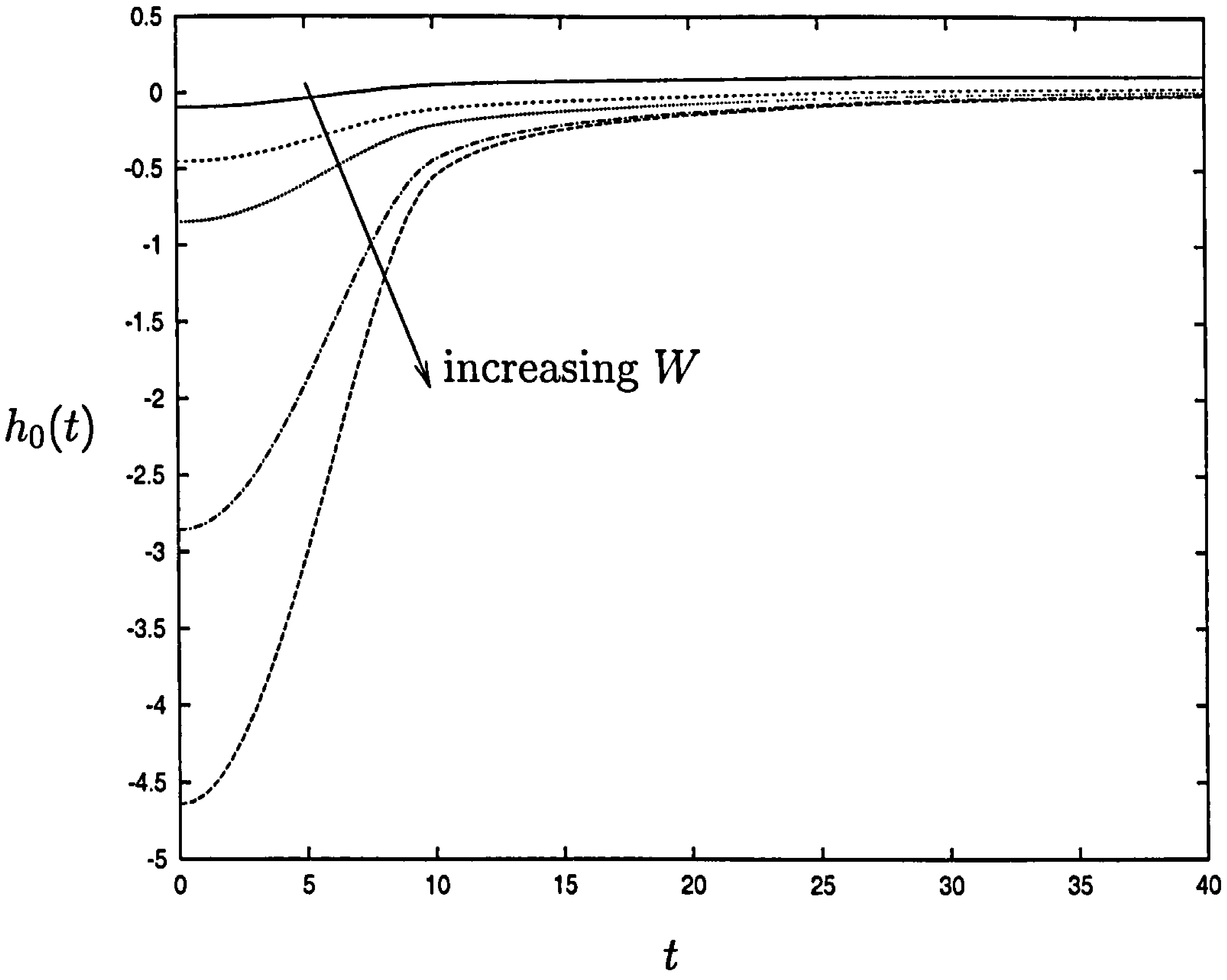

Figure 3.28: Displacement, $h_0(t)$, of the particle for $W = 0.2,\ 0.5,\ 1,\ 5,\ 10$.

3.5 Summary and Conclusions

In this chapter we consider a model for a particle immersed in the liquid lining of a lung airway, deforming the underlying epithelial cells. We look at the perpendicular motion of a 2D cylinder close to a deformable wall, modelled as a spring-backed plate. Using lubrication theory in the gap between the particle and the wall we derive an evolution equation for the gap thickness $h(x, t)$ and hence for the force acting on the particle. We solve the evolution equation numerically. We also perform asymptotic analysis of various limiting cases.

Initially we prescribe the displacement of the particle as it is pushed down to a given position, and we calculate the force acting on the particle as t increases. We compare this with the equilibrium force, *i.e.* the force in the absence of a fluid film between the particle and the wall. We find that the presence of the fluid causes an overshoot of the force (Figure 3.5). The overshoot is greater the faster the particle is pushed down but persists even at slow speeds. Asymptotic analysis in the early-time limit leads to a similarity solution for the force, showing how fluid becomes trapped under the particle, if it is pushed down sufficiently quickly, causing the observed overshoot in the force. We find that asymptotic analysis in the long-time limit requires a matching between three regions of behaviour and describes how trapped fluid drains out of the gap region.

We also prescribe the displacement of the particle as it is pulled off the wall to a given position. We find that as the particle moves the wall is pulled upwards behind it. This effect is more pronounced the faster the particle moves. Again the force curves display an overshoot from the equilibrium case (Figure 3.18). The force on the particle is due to the compressed springs in the wall and as the particle is pulled away the force decreases as the springs relax. As the particle rises further the springs become stretched and exert a suction force on the particle. This suction force is greater the faster the particle moves, suggesting that it is more difficult to remove a particle from a wall at higher speeds. We also carry out a matched asymptotic analysis of the 'peeling' region. This analysis allows us to estimate the time taken for the wall to peel off the base of the particle (Figure 3.17) and the size of the overshoot in the force (Figure 3.20).

We also look at the case where a prescribed force towards the wall is applied to the particle and we compute the resulting displacement. The opposing force due to the compressed wall springs causes the particle to reach an equilibrium position, dependent on the stiffness of the springs in the wall. The deformation is much less pronounced when the wall springs are stiff. In the prescribed force case, there appears to be no overshoot of the displacement of either the particle or the wall beyond the equilibrium position. This is true even for very compliant springs. We use large-time asymptotic analysis to determine the time taken for the wall to reach its equilibrium configuration, *i.e.* the time taken for fluid to drain out of the gap region (Figure 3.25).

If the applied force holding the particle in its equilibrium position is gradually reduced the particle moves upwards. As in the prescribed displacement case we find there is a region of the wall that is stretched upwards with the particle as it moves.

In this chapter we have suggested a model for the motion of a particle perpendicular to a deformable wall, such as an airway. In the next chapter we look at transverse motion of the particle and consider the extension of the model into three dimensions.

Chapter 4

The transverse motion of a particle relative to a deformable wall

In this chapter we consider the motion of a particle moving close to a deformable wall, as in Chapter 3. We now consider only transverse motion of the particle relative to the wall, *i.e.* the vertical displacement of the particle is fixed, $h_0(t) = h_0(0)$, and the particle moves in the x direction with speed $V > 0$. In §4.1 we use the equations derived in Chapter 3 to look at the two-dimensional problem. In §4.2 we consider the extension of the model into three dimensions.

4.1 Two Dimensional Motion

As in §3.1 we may use the evolution equation (3.20) for the gap thickness between the particle and the wall $h(x,t)$,

$$h_t + \left[\frac{h^3}{12}(x - h_x)\right]_x - \frac{V}{2}h_x = 0, \tag{4.1}$$

which is subject to

$$h \longrightarrow h_0 + \frac{x^2}{2}, \quad \text{as } x \longrightarrow \pm\infty. \tag{4.2}$$

We assume that initially the wall is undeformed *i.e.* $h(x,0) = h_0 + x^2/2$ with $h_0 > 0$. From §3.1 we also obtain expressions for the force $\mathbf{F} = (F_x, F_y)$ acting on the particle,

$$F_x = \int_{-\infty}^{\infty} \left(-\frac{hx}{2} + h_0 x + \frac{x^3}{2} - \frac{V}{h} - \frac{hh_x}{2} \right) dx, \tag{4.3}$$

$$\tilde{F}_y = \epsilon^{1/2} F_y = \int_{-\infty}^{\infty} \left(h - h_0 - \frac{x^2}{2} \right) dx, \tag{4.4}$$

(see (3.31, 3.32)), where $\epsilon = H/R \ll 1$.

4.1.1 Numerical Method

We again use finite difference methods (NAG routine D02NBF) to integrate the evolution equation (4.1) over the region $[-L, L]$, applying $h = h_0 + x^2/2$ at $x = \pm L$. The following simulations were carried out using 3001 meshpoints and taking $L = 10$. The accuracy of the results was again checked by varying the number of meshpoints and the domain length and also by performing a mass conservation check. The latter consisted of comparing the integral of $h(x,t)$ over the domain with the integral (with respect to t) of the net flux out of the region $[-L, L]$ at each time interval.

4.1.2 Simulations

The two dimensionless parameters are the speed of the particle, V, and the perpendicular distance of the particle from the undeformed wall, h_0. We consider the results of simulations for three different cases: (*i*) $V = 1$, $h_0 = 0.6$, (*ii*) $V = 1$, $h_0 = 0.2$, (*iii*) $V = 3$, $h_0 = 0.6$. Figure 4.1 shows the gap thickness $h(x,t)$ for $t \leq 8.5$ in case (*i*). Figure 4.2 illustrates the corresponding wall deformation.

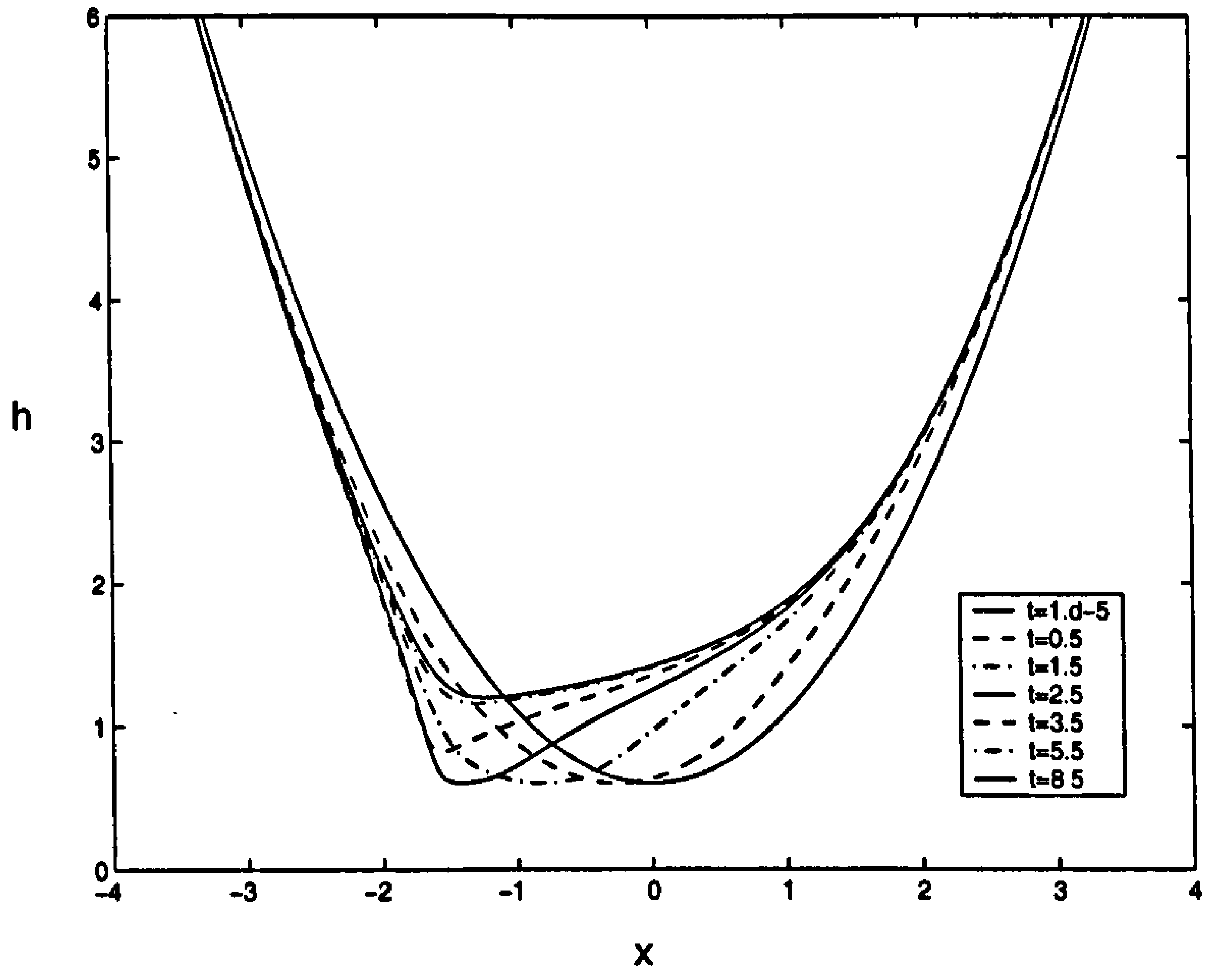

Figure 4.1: The gap thickness h against x for case (i) $V = 1$, $h_0 = 0.6$.

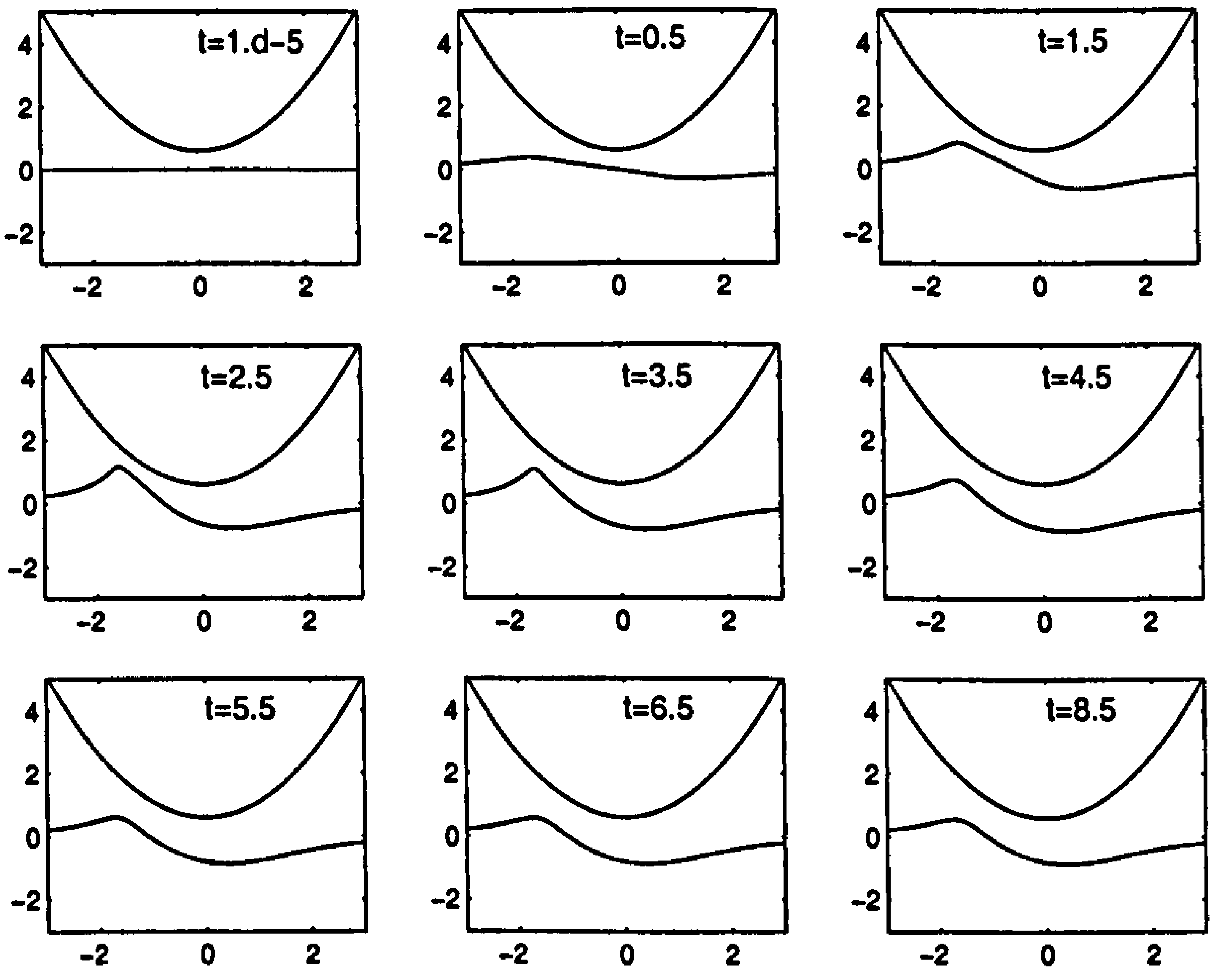

Figure 4.2: Wall deformation as t increases for case (i) $V = 1$, $h_0 = 0.6$. The wall moves from right to left relative to the particle.

We see that a region of high pressure in front of the cylinder, due to its sideways motion, causes the wall to bulge downwards. Behind the cylinder is a region of low pressure which causes the wall to be pulled upwards forming a 'corner'. As t increases a pressure gradient-driven flow through the gap increases the pressure in this region, causing the wall to relax from the sharp corner seen at early times and reach a steady state. Initially the minimum value of $h(x,t)$ occurs at $x = 0$, *i.e.* $h_{min} = h_0$; as t increases the position of h_{min} moves to the corner and remains there, but h_{min} does not decrease.

Figure 4.3 shows (*a*) the transverse stress distribution (the integrand in (4.3)) on the particle at early times, (*b*) the transverse stress distribution at long times and (*c*) the normal stress distribution on the particle (the integrand in (4.4)). Figure 4.3(*b*) shows a large spike in the transverse stress distribution associated with the transient sharp corner of the wall. Figure 4.3(*c*) shows the regions of low and high pressure behind and in front of the particle respectively.

Figures 4.4 and 4.5 show the gap thickness h and the wall deformation respectively for case (*ii*), for which $V = 1$, $h_0 = 0.2$. Figures 4.6 and 4.7 show the gap thickness h and the wall deformation respectively for case (*iii*), for which $V = 3$, $h_0 = 0.6$. We see that the wall deformation and the 'sharpness' of the transient corner are more marked as V increases or h_0 decreases. However the minimum gap thickness is never less than the value of h_0; these simulations suggest that the wall will not come into contact with the cylinder regardless of the values chosen for V, h_0.

This 'necking' effect behind the cylinder is similar to that noted by Lighthill [56] in his study of the steady pressure-forcing of elastic pellets through fluid-filled elastic tubes. Similar results have also been obtained in studies of roll coating with deformable roll covers [60, 61]. We examine this structure in more detail in §4.1.4 below.

Figures 4.8 and 4.9 show the transverse and normal components (relative

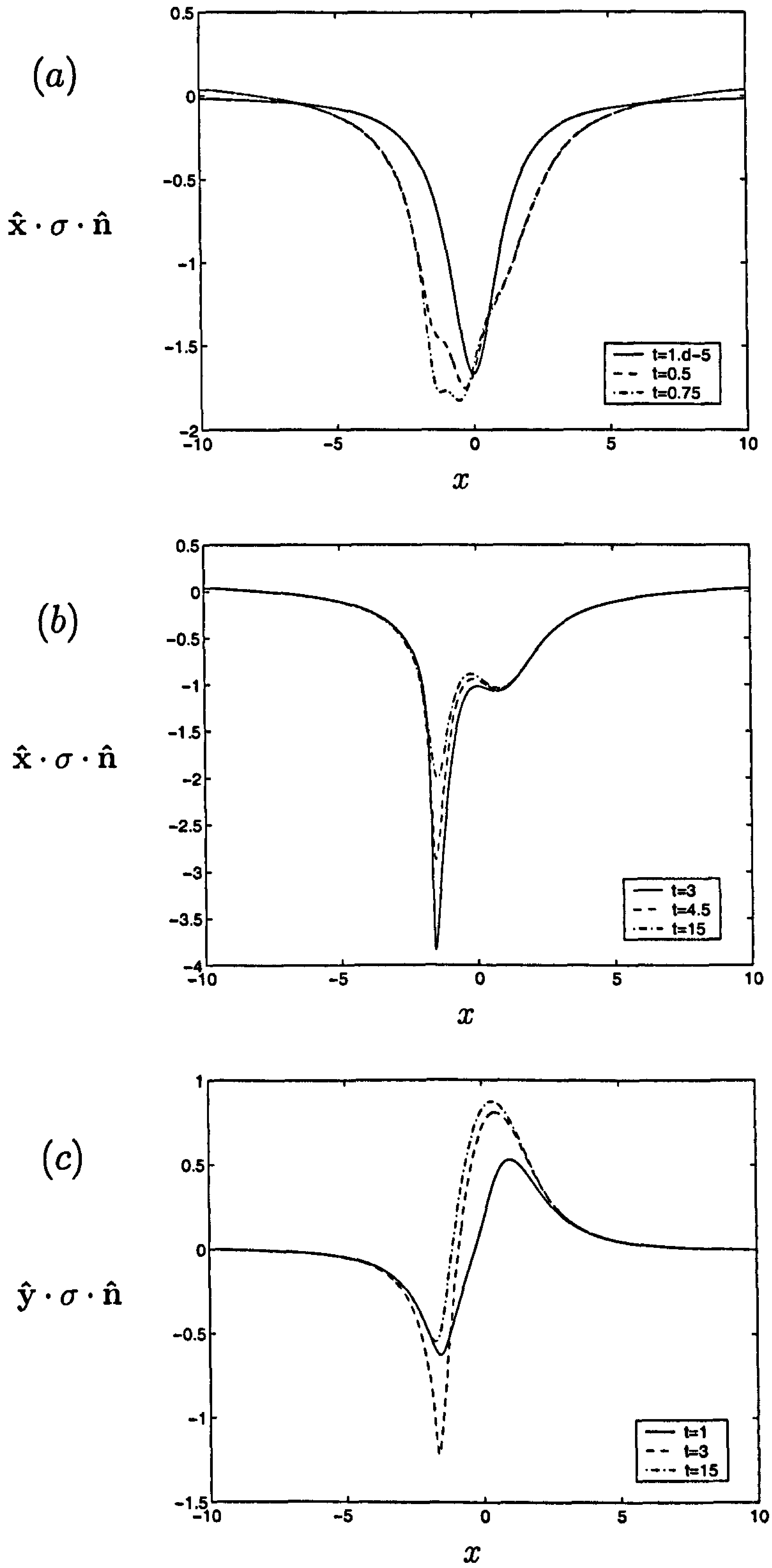

Figure 4.3: (*a*) Transverse stress distribution on the particle at early times, (*b*) Transverse stress distribution at long times, (*c*) Normal stress distribution on the particle. (Case (*i*): $V = 1$, $h_0 = 0.6$.)

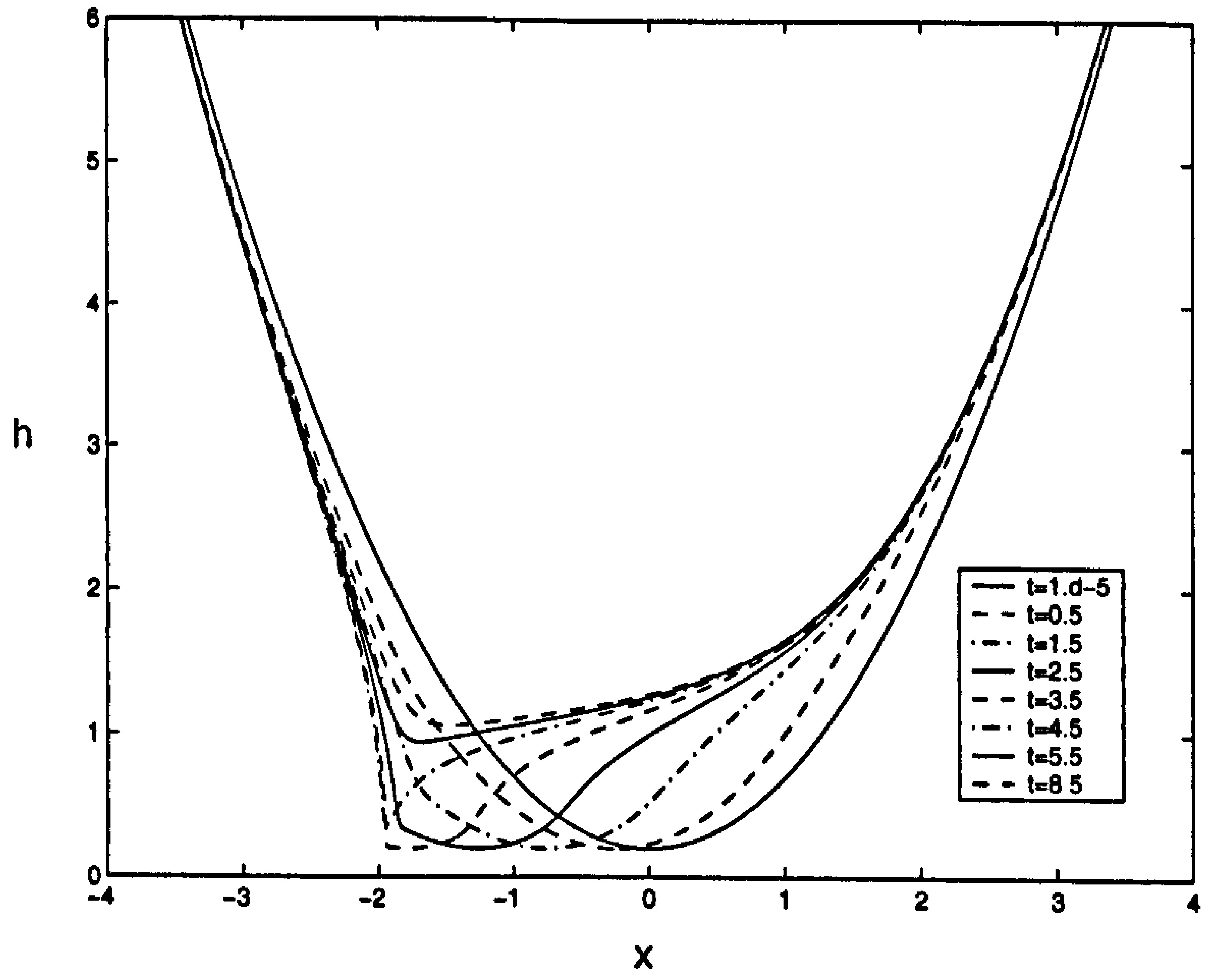

Figure 4.4: The gap thickness h against x for case (ii) $V = 1$, $h_0 = 0.2$.

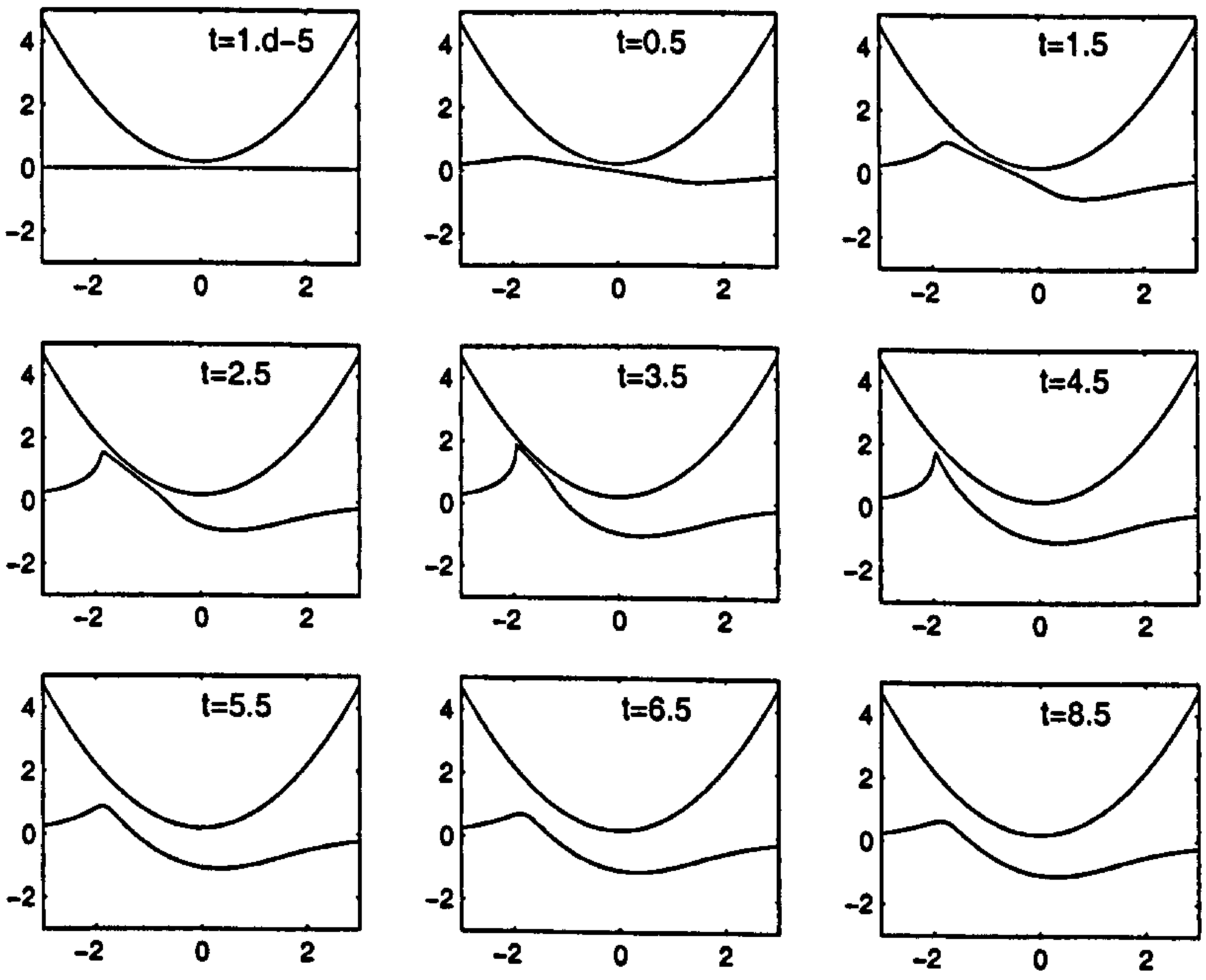

Figure 4.5: Wall deformation as t increases for case (ii) $V = 1$, $h_0 = 0.2$.

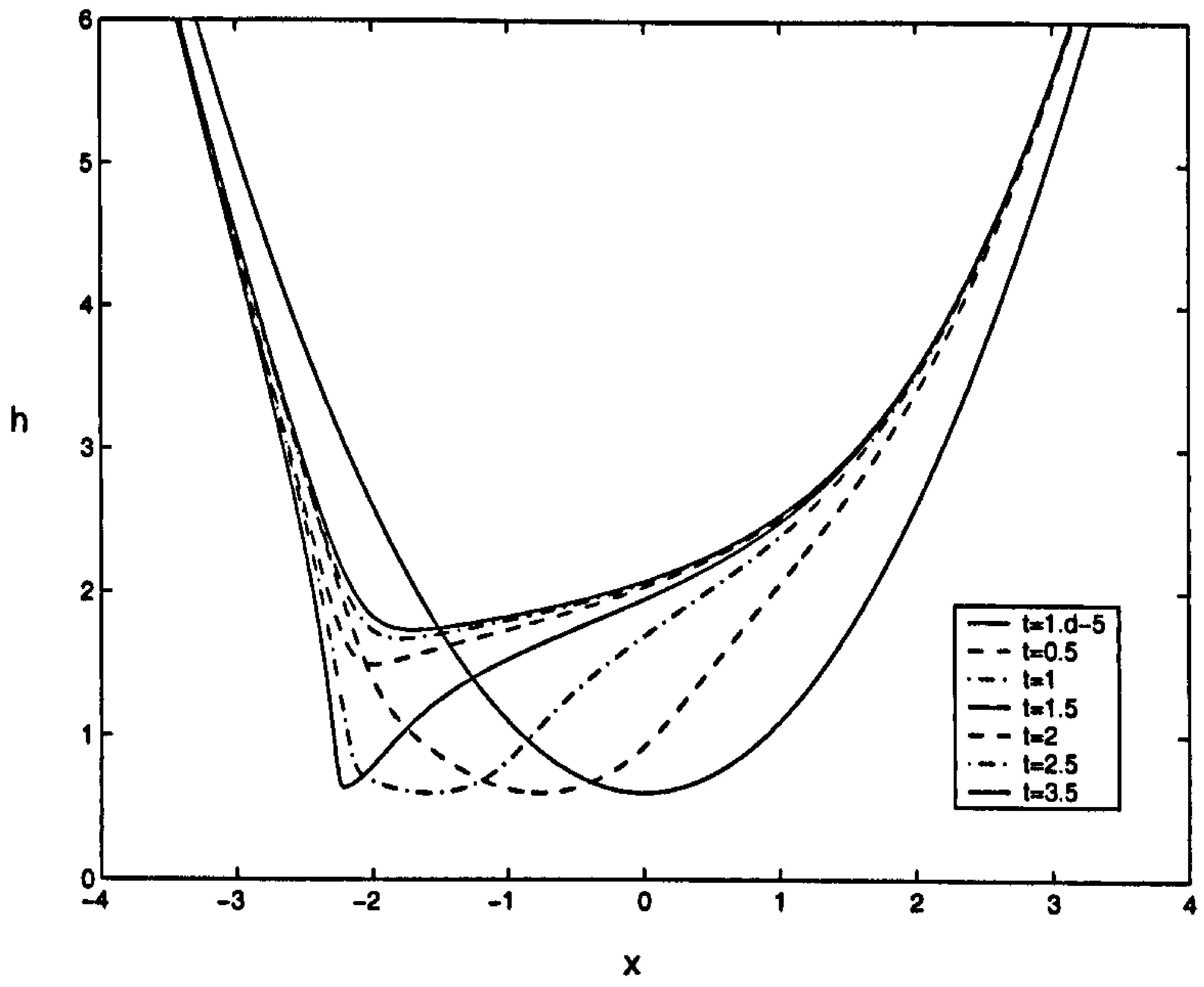

Figure 4.6: The gap thickness h against x for case (*iii*) $V = 3$, $h_0 = 0.6$.

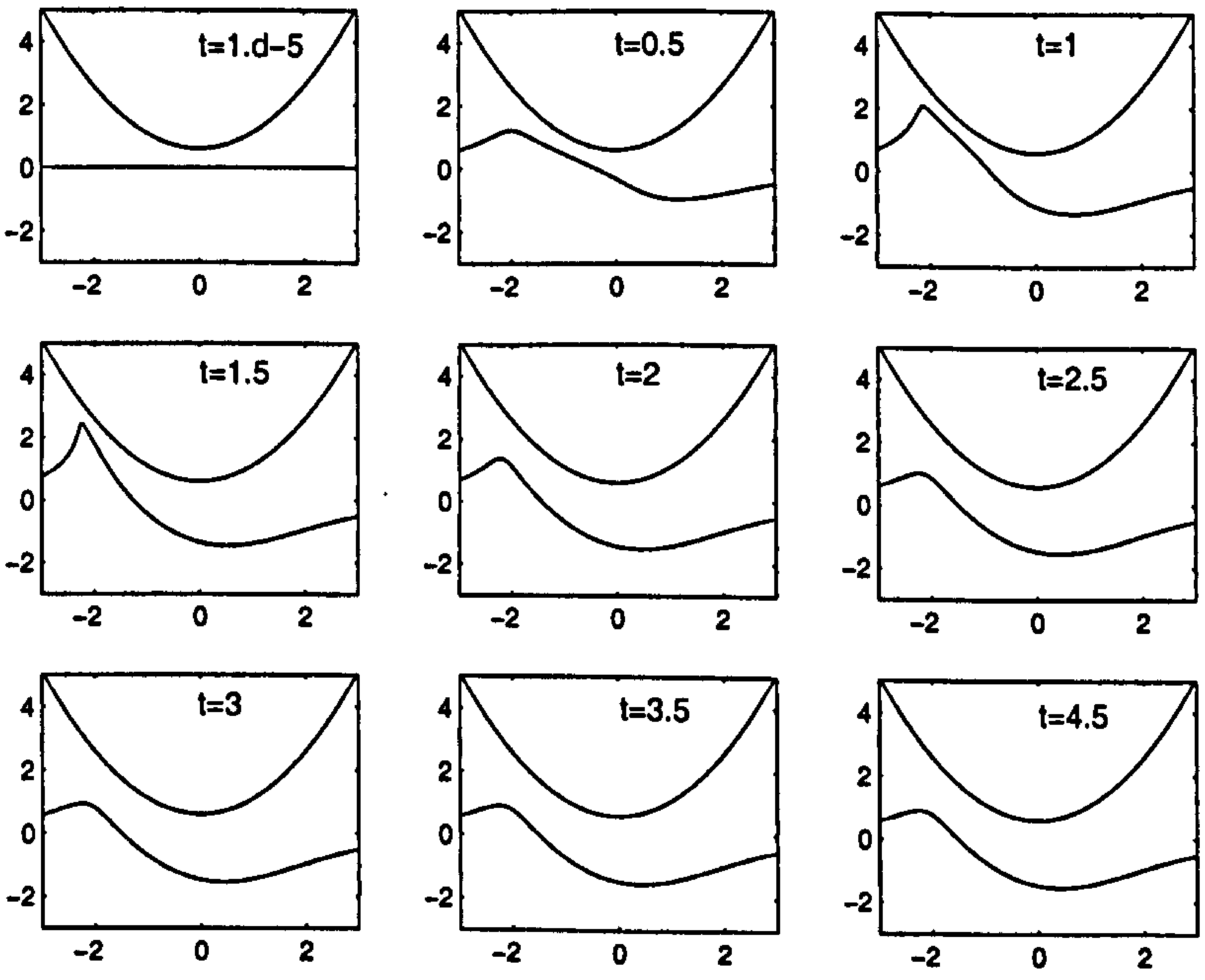

Figure 4.7: Wall deformation as t increases for case (*iii*) $V = 3$, $h_0 = 0.6$.

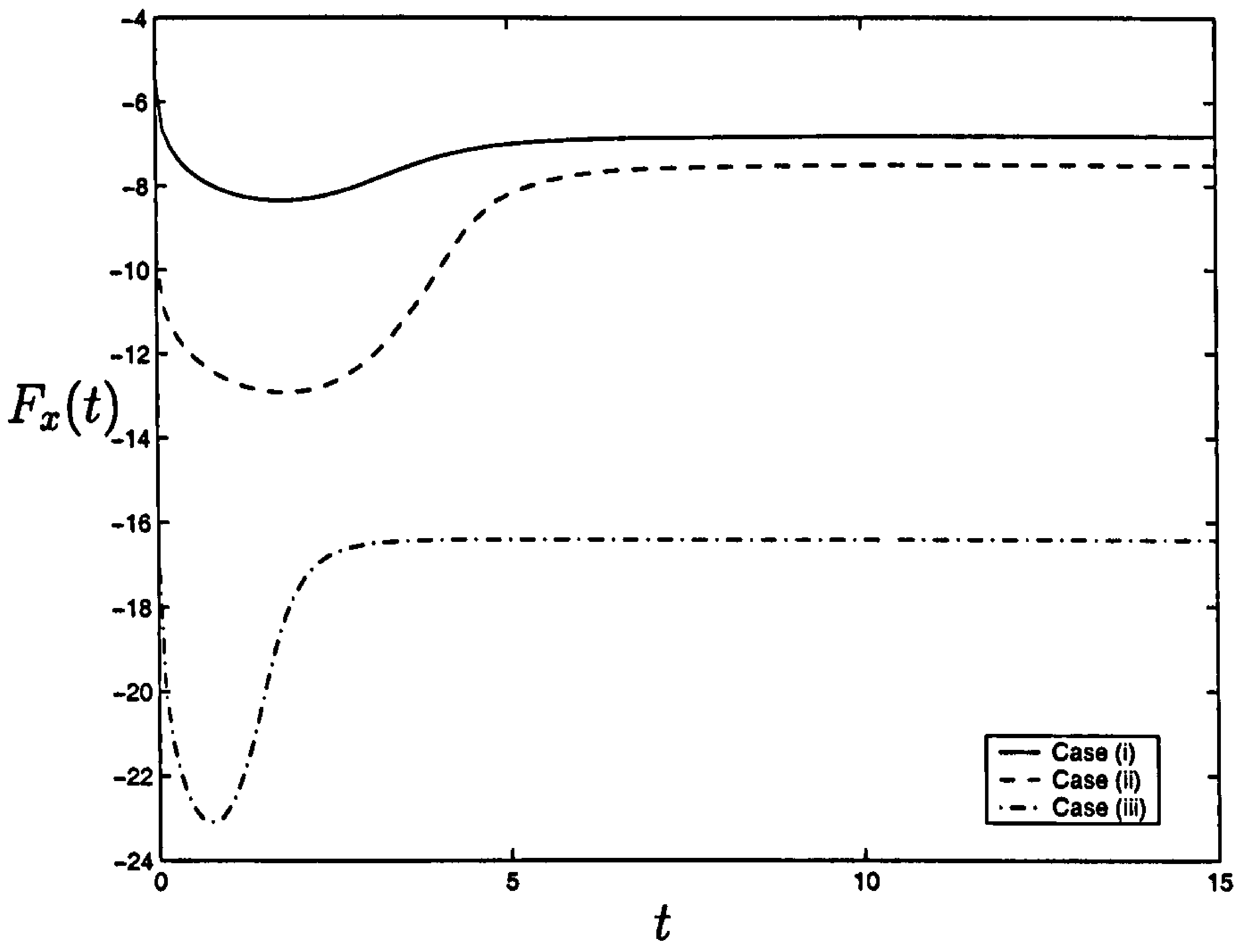

Figure 4.8: Transverse force (relative to the undeformed wall) on the particle for Case (*i*): $V = 1$, $h_0 = 0.6$, Case (*ii*): $V = 1$, $h_0 = 0.2$, Case (*iii*): $V = 3$, $h_0 = 0.6$.

to the undeformed wall) respectively, of the force acting on the cylinder as functions of time. The magnitude of the force components increases as V increases or h_0 decreases. Although there is no vertical motion of the cylinder (relative to the wall), a 'lift' force is created by the transverse motion (since we prescribe the displacement the particle does not move in response to this force).

Figure 4.10 shows the torque on the cylinder for the three cases. The initial magnitude of the torque increases as V increases or h_0 decreases. In this model we ignore rotation due to torque since we are prescribing the displacement of the cylinder.

We also consider the behaviour of the wall when the particle is initially indented into the wall and is pushed sideways. We run the simulation as in §3.2

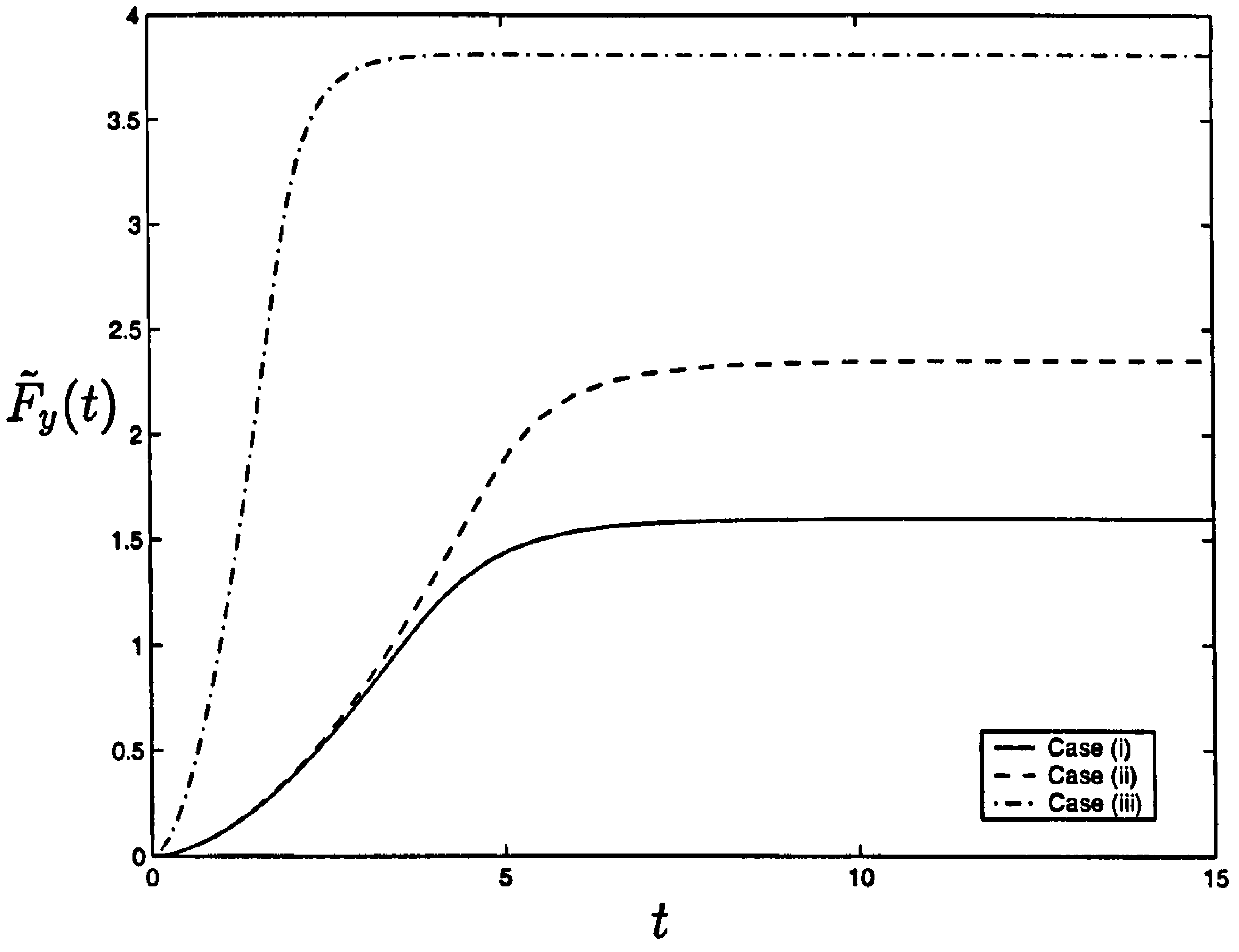

Figure 4.9: Normal force (relative to the undeformed wall) on the particle for Case (*i*): $V = 1$, $h_0 = 0.6$, Case (*ii*): $V = 1$, $h_0 = 0.2$, Case (*iii*): $V = 3$, $h_0 = 0.6$.

for long time, pushing the particle into the wall and allowing the liquid to be squeezed out leaving a thin film. We then move the particle transversely with speed V. Figures 4.11 and 4.12 show the gap thickness and wall deformation respectively for the case $V = 1$, $h_0 = -3.125$ with a nearly-uniform initial film thickness beneath the cylinder of $h \approx 0.2417$. We see that the shape of $h(x)$ for this case is similar to the results obtained for the prescribed displacement (pulling) case, see §3.3. Figure 4.12 shows the development of a peeling motion as the particle moves sideways. At large times, there is an increase in the minimum gap thickness.

We now consider some interesting aspects of these results using asymptotics. In §4.1.3 we consider the peeling behaviour observed in Figures 4.11 & 4.12. In §4.1.4 we consider the steady-state behaviour of the system.

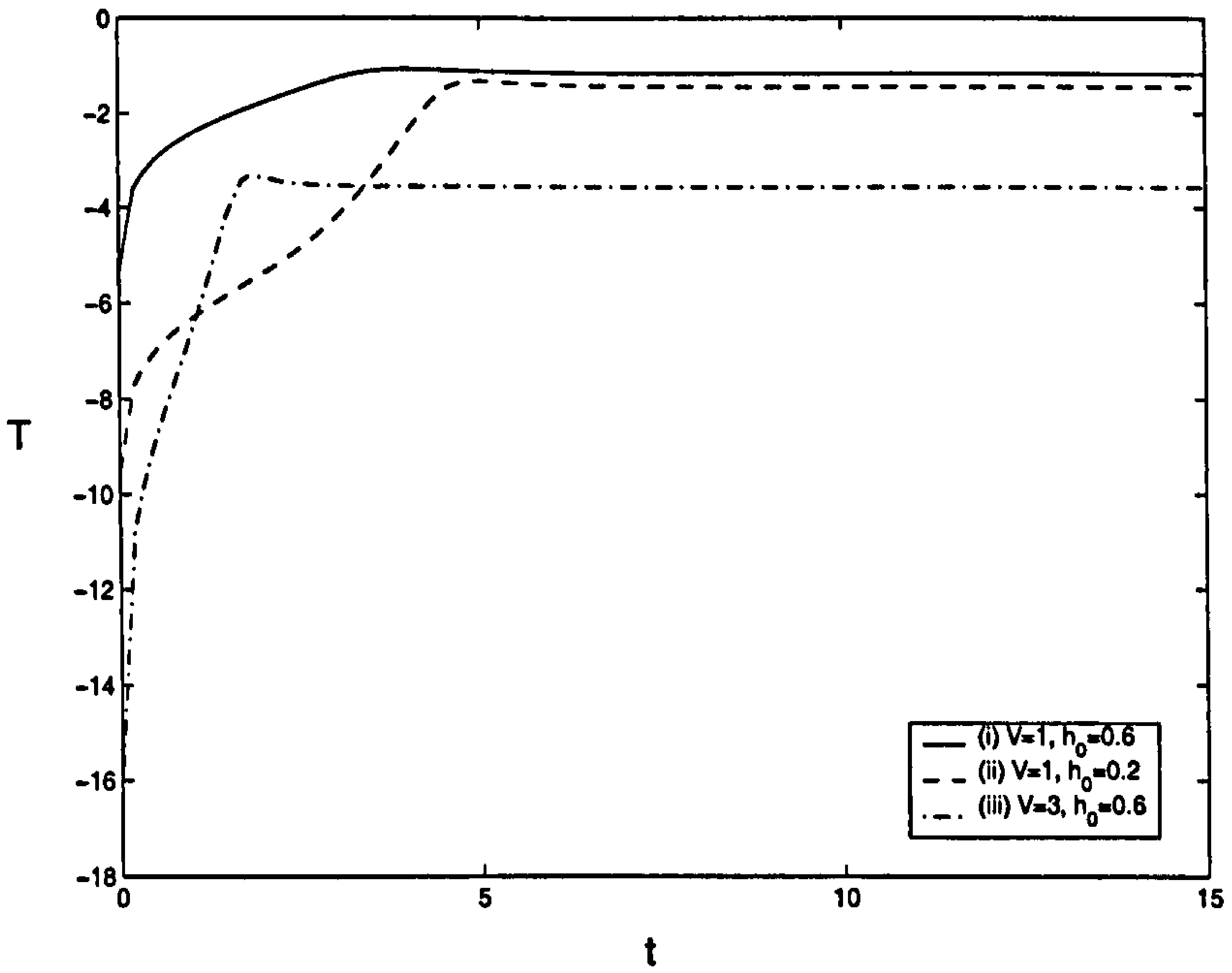

Figure 4.10: Torque on the cylinder for *(i)* $V = 1$, $h_0 = 0.6$ *(ii)* $V = 1$, $h_0 = 0.2$ *(iii)* $V = 3$, $h_0 = 0.6$.

4.1.3 Peeling Asymptotics

For a particle which is initially indented into the wall and then pushed sideways, we observe a peeling motion (Figure 4.11). The motion of the wall (in the frame of the particle) drags a small fluid flux out through the downstream (left-hand) limit of the gap region, x^-, (see Figure 4.13). A region of low pressure where the surfaces separate causes the wall to be pulled upwards forming a sharp transient corner. The wall motion also drags a much larger amount of fluid into the upstream (right-hand) limit of the gap region, peeling the wall away from the particle. We now present analysis which allows us to predict the time over which this transient behaviour persists.

We may exploit the similarity between the transverse peeling motion evident in Figure 4.11 and the perpendicular pulling behaviour (Figure 3.14). We see from Figure 4.11 that the gap thickness, h, is quasi-steady in the left-hand

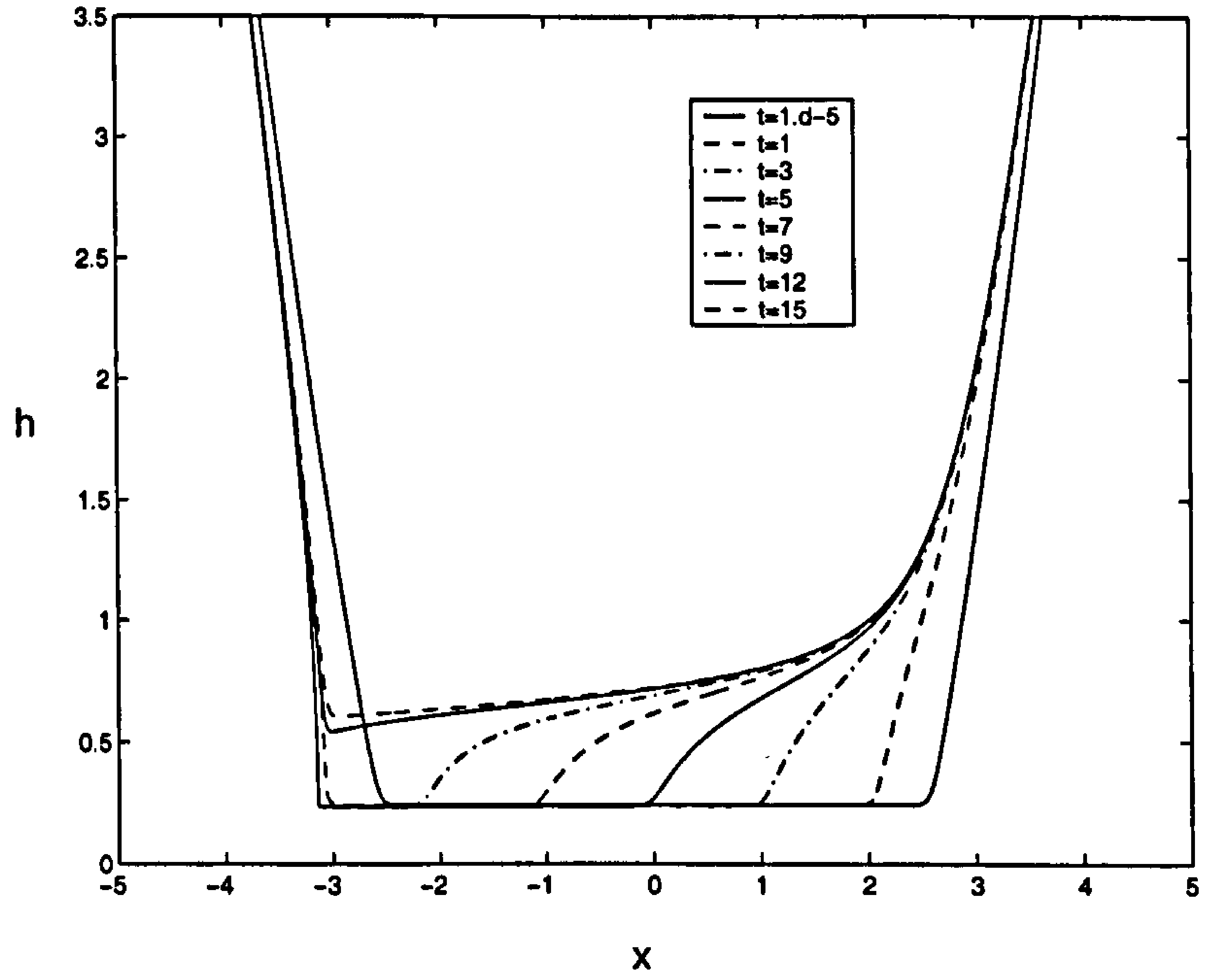

Figure 4.11: Gap thickness h against x for the case $V = 1$, $h_0 = -3.125$ with a nearly-uniform initial film thickness $h \approx 0.2417$.

side of the domain and has uniform thickness. We therefore assume $h_x \approx 0$ in this flat region. Equation (3.20) gives

$$h \sim \frac{\sqrt{6}}{t^{1/2}},$$

as in §3.2.2. In this region the fluid behaviour is unaffected by the influx of fluid upstream, caused by the transverse motion. Fluid continues to drain very slowly from this decreasing region, but by negligible amounts over the short timescales we are considering. We let $h \approx h_\delta$ in this region.

We now consider the sharp 'corner' region which is formed at the leading edge of the influx of fluid, see Figure 4.13. As in §3.3.1 we let $x = X_0(t) + \xi$ where $X_0(t)$ is the corner and obtain

$$-\dot{X}_0 h_\xi + \frac{1}{12}\left[h^3(X_0+\xi)\right]_\xi - \frac{1}{12}\left(h^3 h_\xi\right)_\xi - \frac{1}{2} V h_\xi = 0.$$

This is the same as (3.57) with the addition of a V-dependent term due to the transverse motion. The subsequent matched asymptotic analysis in §3.3.1 is

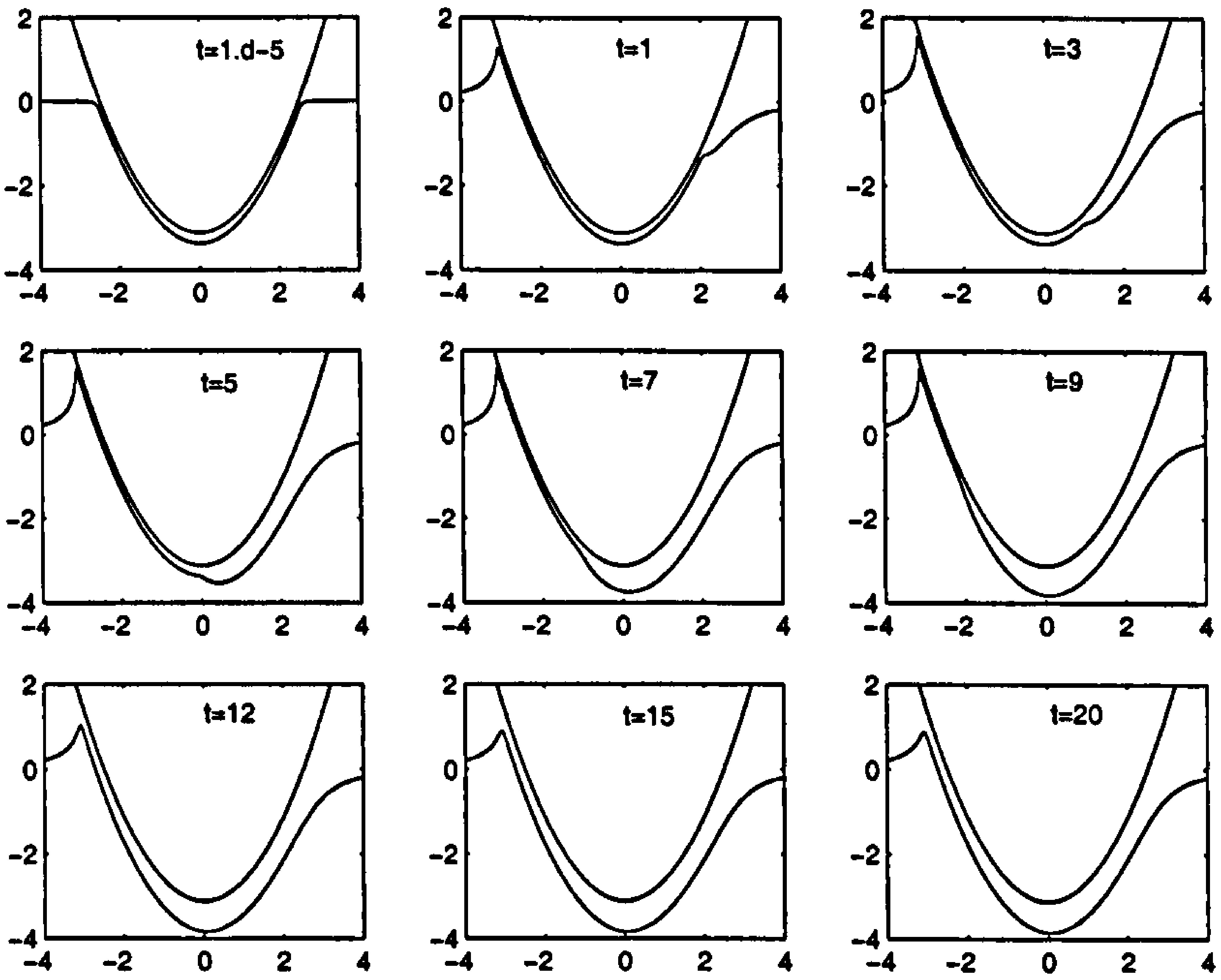

Figure 4.12: Wall deformation as t increases for the case $V = 1$, $h_0 = -3.125$ with a nearly-uniform initial film thickness $h \approx 0.2417$.

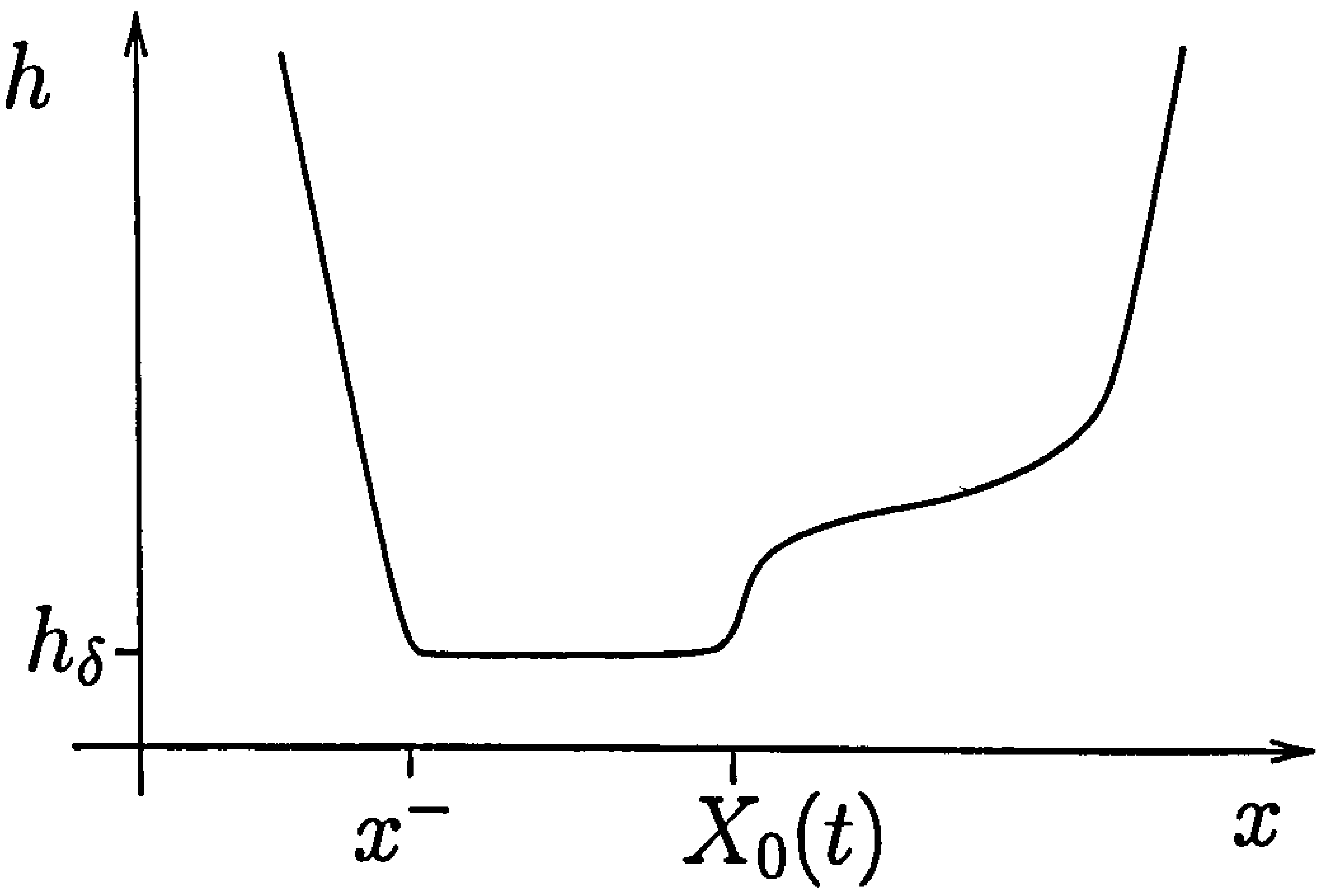

Figure 4.13: Sketch of the gap thickness h against x showing the sharp moving corner $X_0(t)$ and the quasi-steady corner at the edge of the thin-gap region x^-.

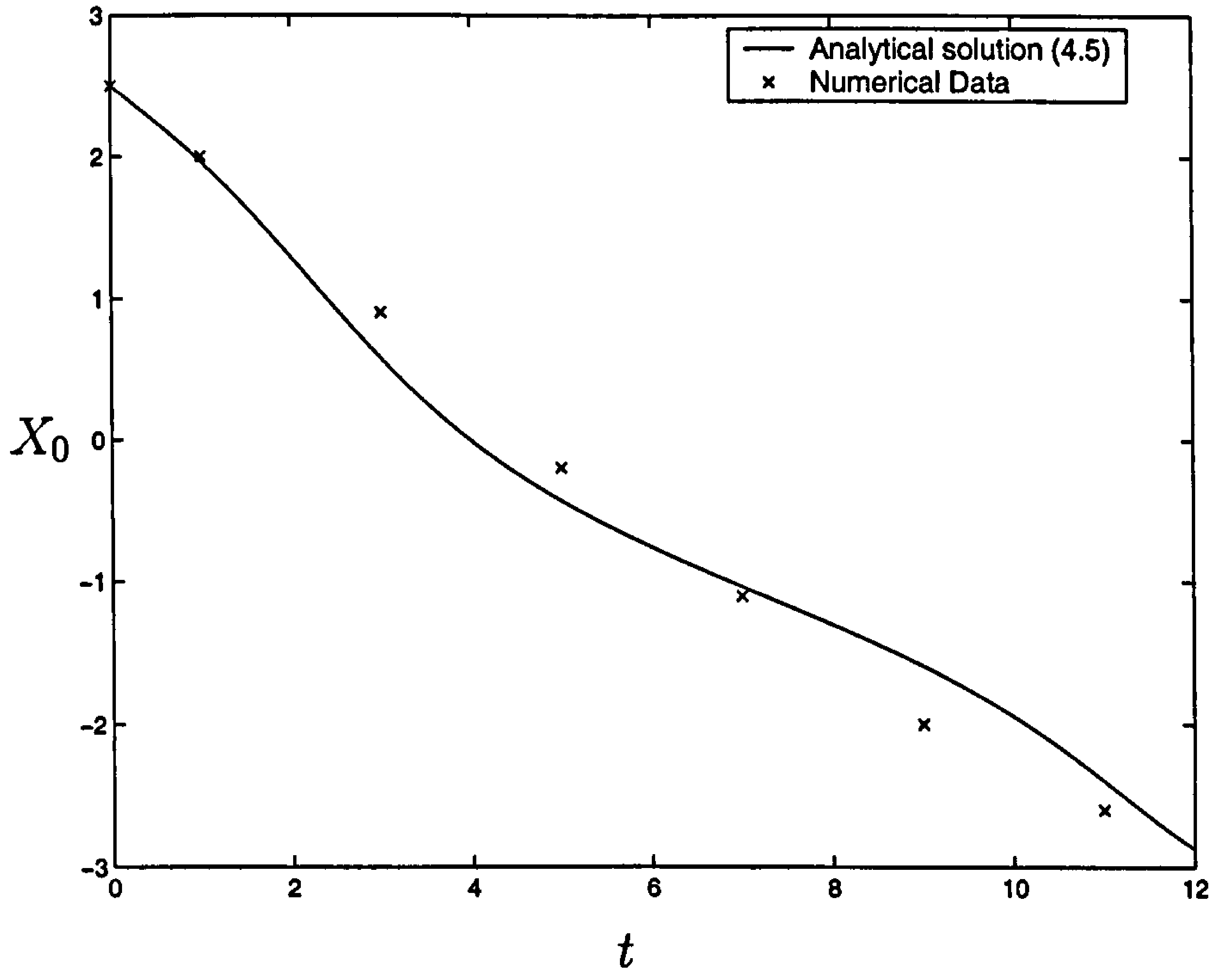

Figure 4.14: Position of the corner X_0 against t when $V = 1$, $h_0 = -3.125$ using the analytical solution (4.5). Crosses mark values of $X_0(t)$ estimated from numerical simulations.

also valid in this case and results in the following equation for $X_0(t)$:

$$h_0 + \frac{X_0^2}{2} = \pi\sqrt{\frac{3\left(-\frac{V}{2} - \dot{X}_0\right)}{X_0}}. \tag{4.5}$$

where in this case h_0 is a prescribed constant value. Equation (4.5) is the analogue of (3.62). Figure 4.14 shows agreement between the analytical solution (in which (4.5) is integrated to determine $X_0(t)$) when $V = 1$, $h_0 = -3.125$ and estimates from numerical simulations of the PDE.

We can also use this quasi-steady behaviour to find the position of x^-, the downstream (left-hand) limit of the thin-gap region, see Figure 4.13. From Figure 4.11 it appears that x^- moves from its initial position, where $x^- = \sqrt{-2h_0}$, to a quasi-steady position, where $x^- < \sqrt{-2h_0}$. We let $h_t = 0$ in the evolution equation (3.20). Integrating with respect to x and applying $h \approx h_\delta$

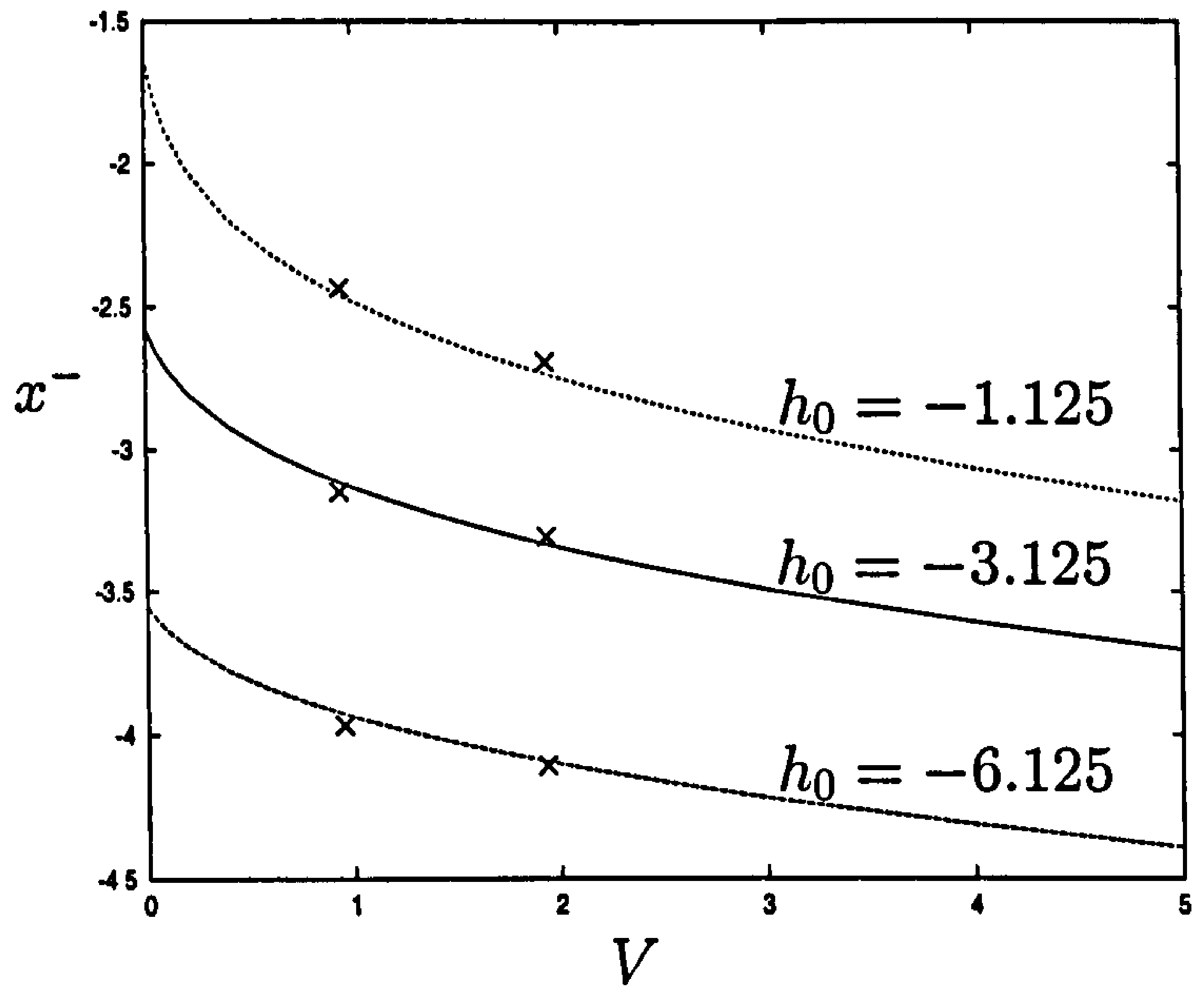

Figure 4.15: The position of the downstream thin-gap limit, x^-, against V for different values of h_0. Crosses denote the values of x^- estimated from the numerical simulations of the PDE.

at $x = x^-$ we obtain

$$\frac{h^3}{12}(h_x - x) + \frac{Vh}{2} = -\frac{h_\delta^3 x^-}{12} + \frac{Vh_\delta}{2}, \tag{4.6}$$

subject to the boundary condition

$$h \longrightarrow h_0 + \frac{1}{2}x^2, \quad \text{as } x \longrightarrow -\infty. \tag{4.7}$$

We step through values of x^- solving (4.6) numerically to find the trajectory which matches (4.7) as $x \to -\infty$. Figure 4.15 shows the position x^- against the transverse speed V for different values of h_0, the extent of the initial deformation. Crosses denote the values of x^- estimated from numerical simulations of the PDE, and we see that this analysis is consistent with the numerical simulations. The initial position of x^- is the same as the value of x^- when $V = 0$. We can see this analysis captures the observed jump of x^- to its quasi-steady position.

4.1.4 Steady State Analysis

Simulations show that the system ultimately tends to a steady state. We now consider behaviour at this steady state by letting $h_t = 0$. Therefore (3.20) becomes

$$\frac{h^3}{12}p_x + \frac{Vh}{2} = \tilde{Q}, \tag{4.8}$$

where $\tilde{Q}$ is a constant flux. For large x, $h \sim x^2/2$, so $\tilde{Q}$ here is negligible and (4.8) gives

$$p \approx \frac{8V}{x^3},$$

so we see that the pressure tends to zero in the far field, as required.

To scale V out of (4.8) we let $x = V^{1/5}\hat{x}$, $h = V^{2/5}\hat{h}$, $h_0 = V^{2/5}\hat{h}_0$, $\tilde{Q} = V^{7/5}\hat{Q}$. Equation (4.8) becomes

$$\frac{d\hat{h}}{d\hat{x}} = \frac{\hat{h}^3\hat{x} + 12\hat{Q} - 6\hat{h}}{\hat{h}^3}, \tag{4.9}$$

which must be solved subject to

$$\hat{h} \longrightarrow \hat{h}_0 + \frac{\hat{x}^2}{2}, \; \hat{x} \longrightarrow \pm\infty. \tag{4.10}$$

Numerical Simulations

We first consider the steady state numerically. Given $\hat{Q}$, L (where $2L$ is the domain length) and a starting point in the $(\hat{x}, \hat{h})$–phase plane, we integrate (4.9) forwards, thus tracing out a trajectory in the phase plane. Figure 4.16 shows trajectories in the phase plane for $\hat{Q} = 1$, taking $L = 10$ and a range of starting points.

For each $\hat{Q}$ there is a family of trajectories satisfying the equation (4.9), however only one also satisfies the boundary condition (4.10). For each trajectory in the phase plane we can calculate the quadratics onto which it matches at $\hat{x} = -L$ and $\hat{x} = L$ and compare the values of $\hat{h}_0$. For a given $\hat{Q}$ we step through the starting values of $\hat{h}$ at $\hat{x} = -L$ to find the trajectory where one

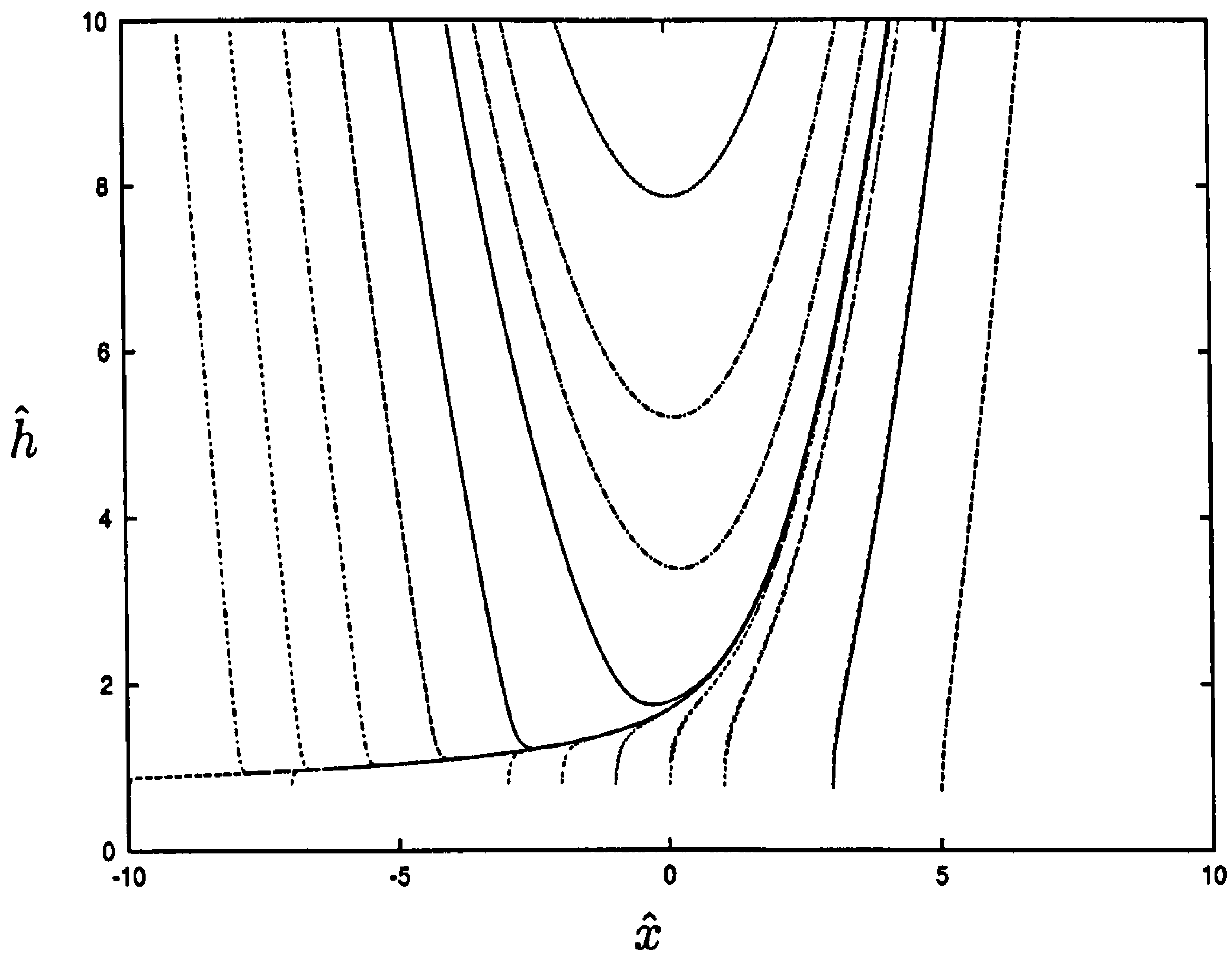

Figure 4.16: Trajectories in the phase plane for $\hat{Q} = 1$.

quadratic matches at both $\hat{x} = -L$ and $\hat{x} = L$. Figure 4.17 shows the solutions to (4.9) subject to the boundary condition for a range of $\hat{Q}$. Figure 4.18 shows typical wall deformation shape for both small and large $\hat{Q}$.

Comparing the steady state solution with the solution of the evolution equation (4.1) at long time for given V and h_0 we find they are graphically identical.

The choice of h_0 and V determines the value of the flux $\hat{Q}$. We can identify two different regimes. If $h_0 > 0$ and the wall moves slowly we obtain $\hat{Q} \gg 1$. (If the speed V is large, the wall is drawn up behind the moving particle, reducing the flux through the gap.) If $h_0 < 0$, so the particle is initially indented, and again the wall moves slowly we get $\hat{Q} \ll 1$ (see Figure 4.17). We now analyse these two different cases.

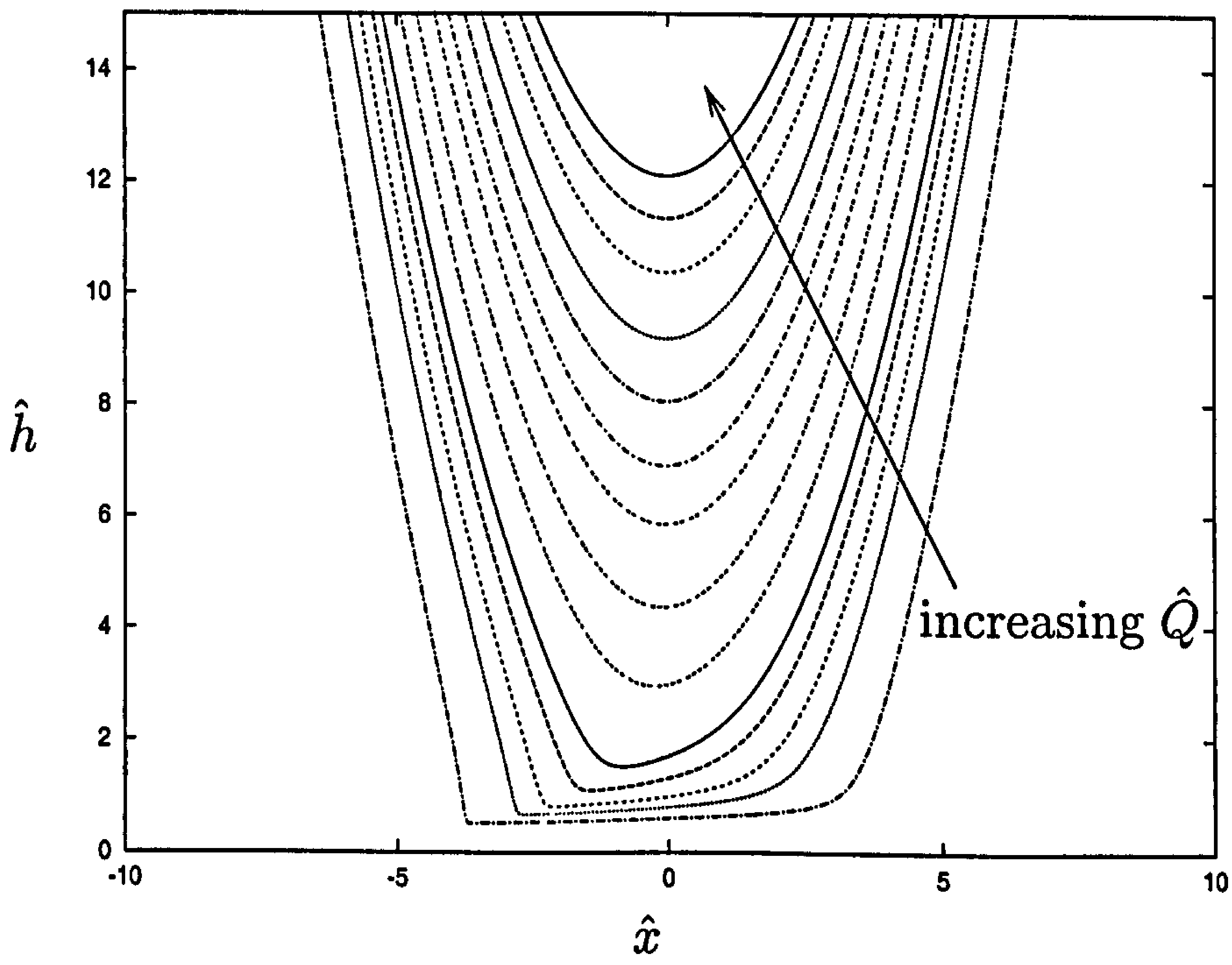

Figure 4.17: Solutions of (4.9) plotted as trajectories in the $(\hat{x}, \hat{h})$–phase plane. The boundary condition is applied at $\hat{x} = \pm L$, where $L = 10$, for $\hat{Q}$ increasing from 0.2 to 10.

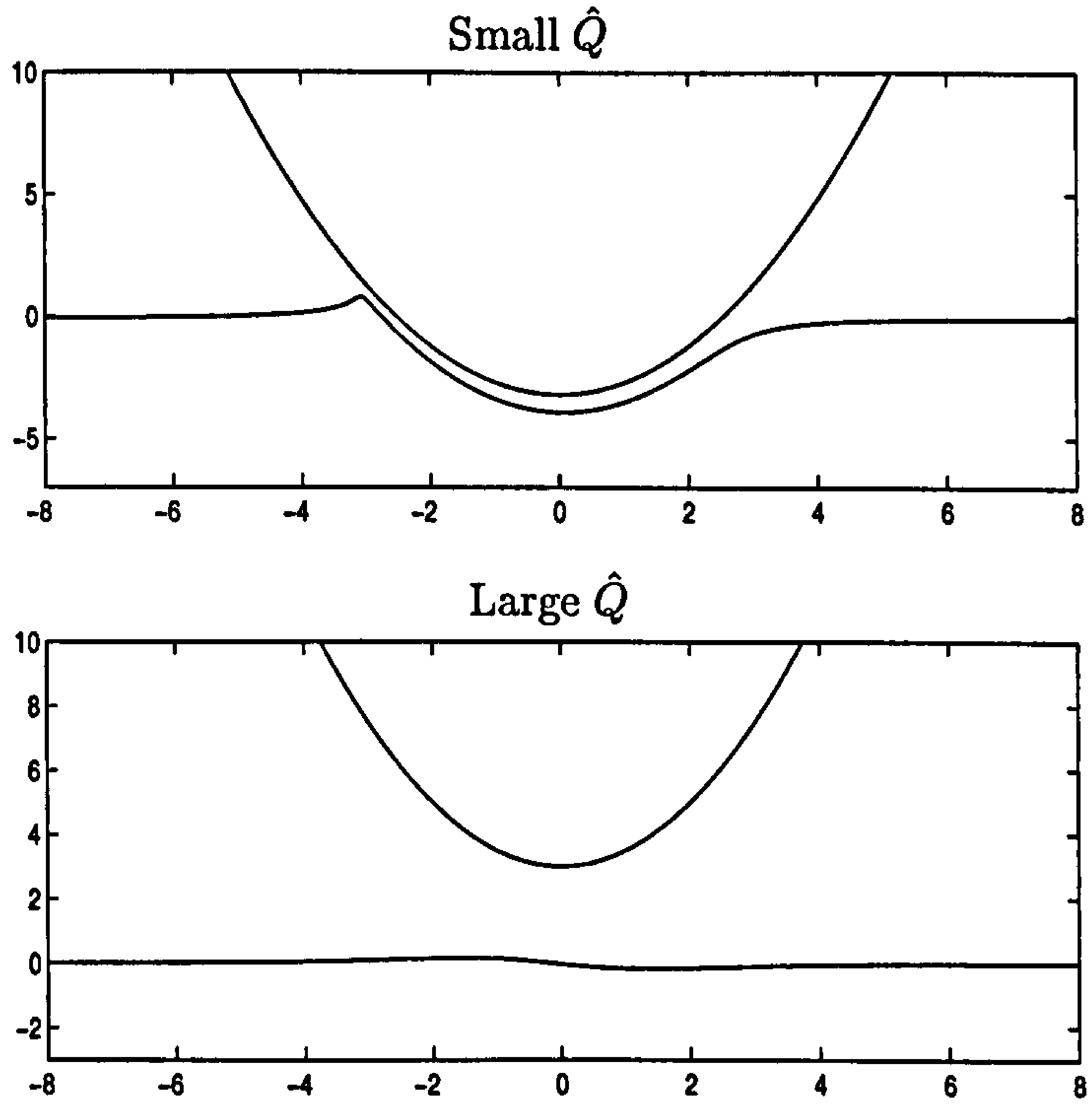

Figure 4.18: Typical wall deformation shapes for small and large $\hat{Q}$.

Large $\hat{Q}$ Analysis

For large $\hat{Q}$ from Figures 4.17 & 4.18 we assume wall deformations are small, so we let $\hat{h} = \hat{h}_0 + \hat{x}^2/2 + \tilde{h}$, where $\tilde{h}$ is small relative to $\hat{h}_0$, and linearise about $\hat{h}_0 + \hat{x}^2/2$. Equation (4.9) becomes

$$\left(\hat{h}_0 + \frac{\hat{x}^2}{2} + \tilde{h}\right)^3 (\hat{x} + \tilde{h}_{\hat{x}}) = \left(\hat{h}_0 + \frac{\hat{x}^2}{2} + \tilde{h}\right)^3 \hat{x} + 12\hat{Q} - 6\left(\hat{h}_0 + \frac{\hat{x}^2}{2} + \tilde{h}\right),$$

which reduces to

$$\tilde{h}_{\hat{x}} = \frac{12\hat{Q} - 6\left(\frac{1}{2}\hat{x}^2 + \hat{h}_0\right)}{\left(\frac{1}{2}\hat{x}^2 + \hat{h}_0\right)^3}.$$

We therefore have

$$\tilde{h} = \int_{-\infty}^{\hat{x}} \frac{12\hat{Q} - 6\left(\frac{1}{2}\hat{x}^2 + \hat{h}_0\right)}{\left(\frac{1}{2}\hat{x}^2 + \hat{h}_0\right)^3}\, d\hat{x} + C. \tag{4.11}$$

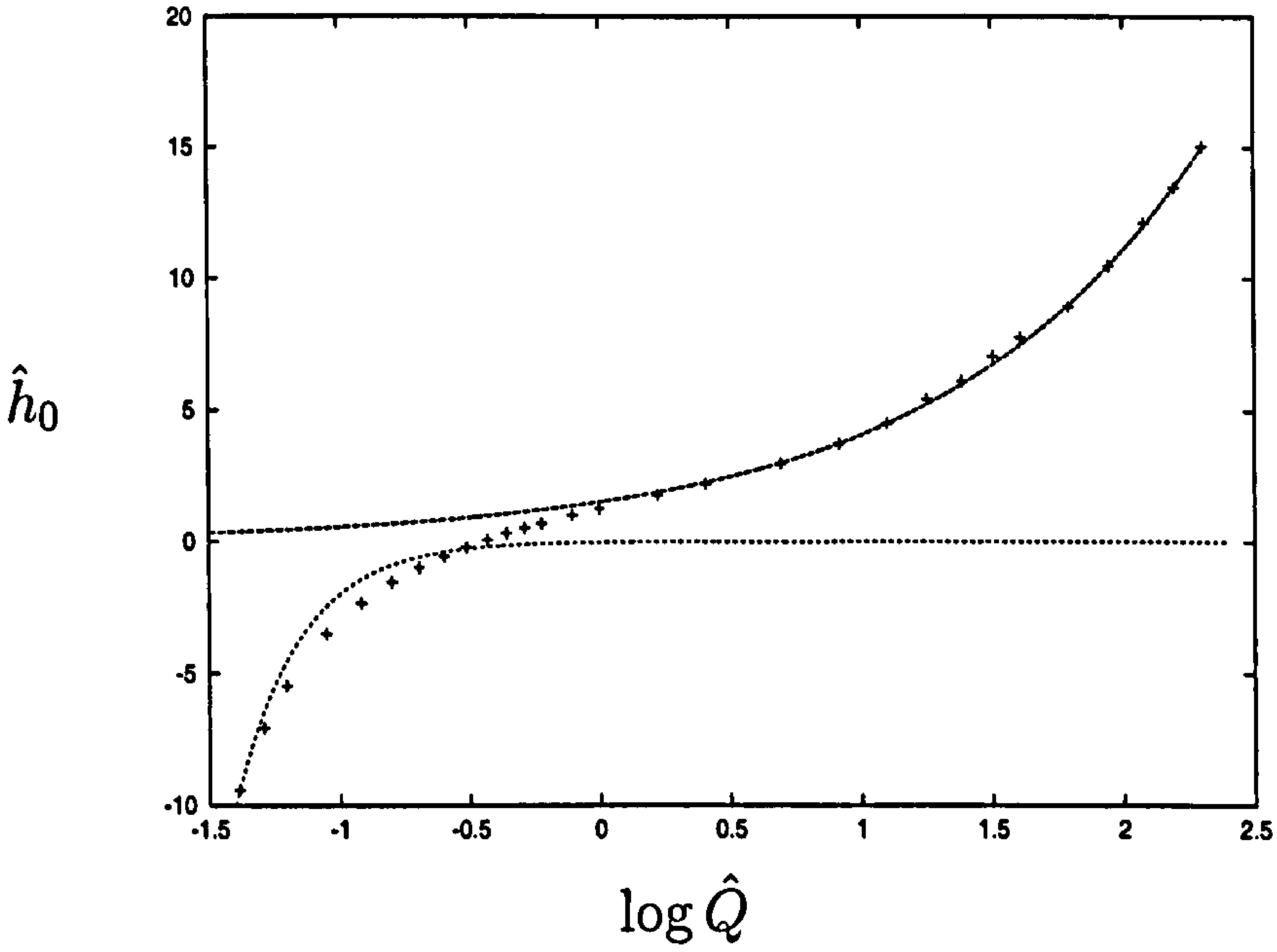

Figure 4.19: $\hat{h}_0$ against $\log \hat{Q}$ from numerical simulations (crosses) compared with analysis for small $\hat{Q}$ (4.18), (dotted curve), and large $\hat{Q}$ (4.13), (dashed curve).

for some constant C. $C = 0$ since $\tilde{h} \to 0$ as $\hat{x} \to -\infty$. Since $\tilde{h} \to 0$ as $\hat{x} \to \infty$, (4.11) gives

$$\int_{-\infty}^{\infty} \frac{12\hat{Q} - 6\left(\frac{\hat{x}^2}{2} + \hat{h}_0\right)}{\left(\frac{\hat{x}^2}{2} + \hat{h}_0\right)^3} \, d\hat{x} = 0. \tag{4.12}$$

Using the substitution $\xi = \hat{x}/\sqrt{2\hat{h}_0}$, from (4.12) we obtain

$$\hat{h}_0 = \frac{3\hat{Q}}{2}. \tag{4.13}$$

Figure 4.19 shows agreement between the numerical data (crosses) and the analysis for large $\hat{Q}$.

Small $\hat{Q}$ Analysis

From Figures 4.16 & 4.17, and noting that the isoclines in the $(\hat{x}, \hat{h})$–phase plane are $\hat{h} = 0$ and $\hat{x} = (6\hat{h} - 12\hat{Q})/\hat{h}^3$, trajectories in the phase plane have the form illustrated in Figure 4.20. We see that there are five regions of different asymptotic behaviour. (Lighthill [56] treated this problem by considering a similar six-region structure, dividing the leading 'corner' region (Region 4) into two boundary layers. However, at the level of approximation to which we are working, we claim it is sufficient to consider five regions of behaviour.)

(i) Region 3: Central region

We let $\hat{x} = X/\hat{Q}^2$, $\hat{h} = \hat{Q}H$ in (4.9) and obtain

$$\hat{Q}^5 \frac{dH}{dX} = \frac{H^3X + 12 - 6H}{H^3}.$$

Since $\hat{Q} \ll 1$, and assuming $dH/dX = O(1)$, this reduces to

$$H^3X + 12 - 6H \approx 0 \iff \hat{h}^3\hat{x} + 12\hat{Q} - 6\hat{h} \approx 0,$$

and so in region 3 the trajectory sits just beneath the isocline. At either end of the region dH/dX becomes large and this analysis breaks down.

(ii) Region 4: Corner

The isocline has a turning point at $X = 2/9$, $H = 3$. We look at the behaviour of the trajectory in this 'corner' region, close to the turning point of the isocline. We let $\hat{x} = X/\hat{Q}^2$ and set $X = 2/9 + \hat{Q}^5\xi$, where ξ is O(1), to work in the neighbourhood of the corner. Again we let $\hat{h} = QH(\xi)$ where $H = O(1)$. Equation (4.9) becomes, at leading order,

$$\frac{dH}{d\xi} = \frac{\frac{2}{9}H^3 + 12 - 6H}{H^3}, \tag{4.14}$$

which has solution

$$\frac{9}{2}H - \frac{27}{2(H-3)} + 12\ln\left|\frac{H-3}{H+6}\right| = \xi + c, \tag{4.15}$$

for some constant c. As $\xi \to -\infty$, $H \to 3$ which matches onto Region 3. As $\xi \to \infty$, $H \gg 1$ and (4.14), (4.15) reduce to

$$\frac{dH}{d\xi} \approx \frac{2}{9}, \quad H \approx \frac{2}{9}(\xi + c). \tag{4.16}$$

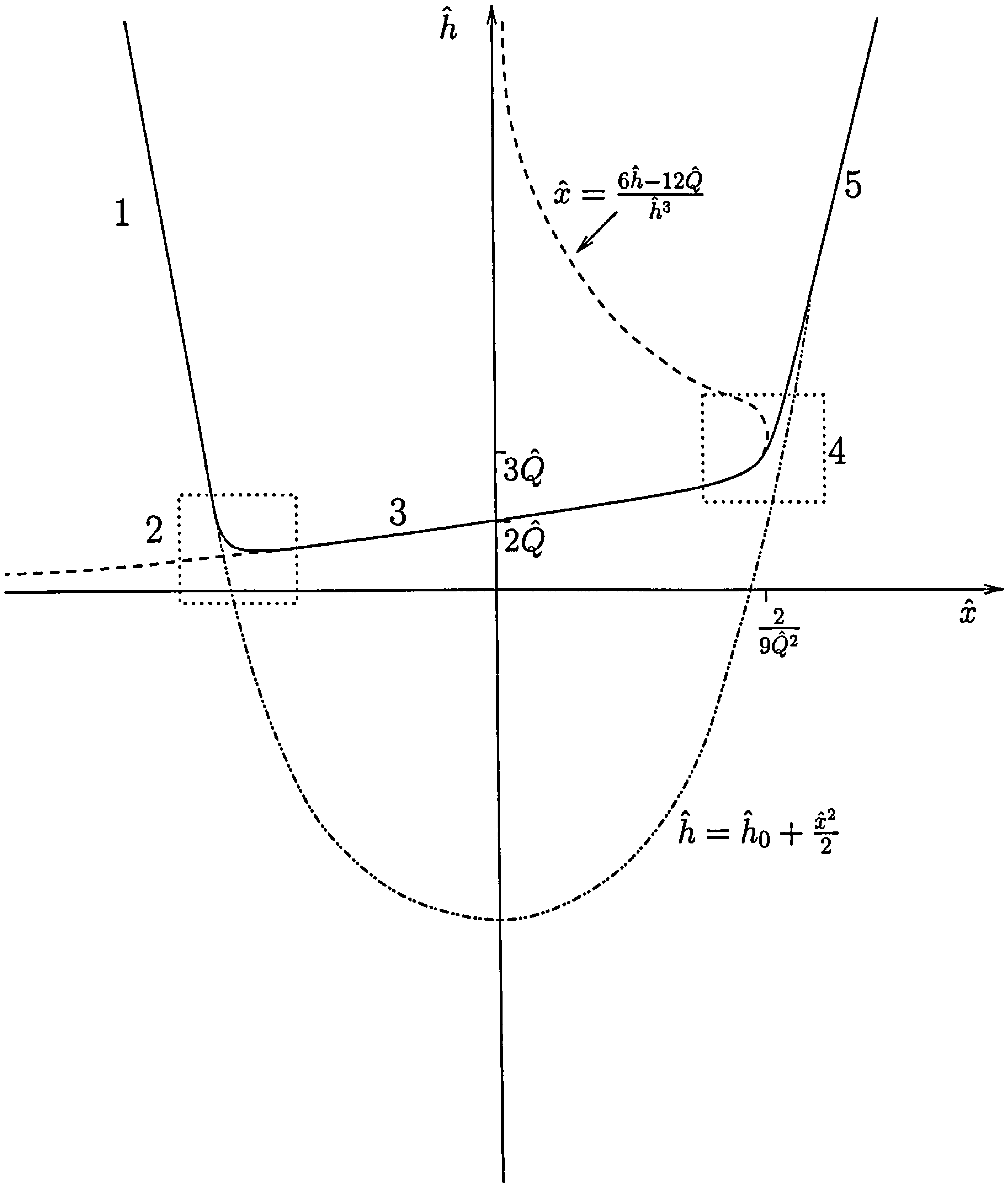

Figure 4.20: Suggested shape of trajectories in the $(\hat{x}, \hat{h})$ phase plane showing regions of different behaviour. Dashed line denotes the isocline. Dash/dot line shows the parabola which matches the required trajectory in the far field.

This becomes

$$\hat{h} \approx \frac{2}{9}\hat{Q}(\xi + c) \approx \frac{2}{9\hat{Q}^4}\left(X - \frac{2}{9}\right),$$

at leading order, and so $\hat{h}$ is linear (in ξ) with gradient $2\hat{Q}/9$ in the outer limit of the corner region.

(iii) Region 5: Outer region

Since $\hat{x} = X/\hat{Q}^2$ and $\hat{h}$ is quadratic as $\hat{X} \to \infty$ we let $\hat{h} = \hat{H}(X)/\hat{Q}^4$ and equation (4.9) becomes

$$\frac{1}{\hat{Q}^{14}}\frac{d\hat{H}}{dX} = \frac{\frac{1}{\hat{Q}^{14}}\hat{H}^3 X + 12\hat{Q} - \frac{6\hat{H}}{\hat{Q}^4}}{\hat{H}^3}.$$

Since $\hat{Q}$ is small the $O(\hat{Q}^{-14})$ terms dominate and we obtain

$$\frac{d\hat{H}}{dX} = X.$$

Integrating with respect to X and writing the solution in terms of ξ and $\hat{h}$ (so we can take the small ξ limit) we obtain

$$\hat{h} = \frac{2}{9}\hat{Q}\xi + \frac{1}{2}\hat{Q}^6\xi^2 + \frac{2}{81\hat{Q}^4} + \frac{C}{\hat{Q}^4}, \tag{4.17}$$

for some constant C. Since $\hat{Q}$ is small, matching requires $C = -2/81$. When ξ is small, $\hat{h}$ has gradient $2\hat{Q}/9$ which matches region 4, as required. In original variables,

$$\hat{h} = \frac{\hat{x}^2}{2} + \frac{C}{\hat{Q}^4},$$

and since the trajectory must satisfy the boundary condition $\hat{h} \longrightarrow \hat{h}_0 + \hat{x}^2/2$ as $\hat{x} \longrightarrow \pm\infty$, we obtain

$$\hat{h}_0 = -\frac{2}{81\hat{Q}^4}. \tag{4.18}$$

(iv) Regions 1 & 2

Region 2 is located the same distance as Region 4 from the origin, reflected in the y axis. Behaviour in Region 2 is similar to that in the other 'corner', Region 4. We take $\hat{x} = (-2/9 + \hat{Q}^5\xi)/\hat{Q}^2$ and $\hat{h} = \hat{Q}H(\xi)$ where H, $\xi = O(1)$ and ξ is small. Equation (4.9) becomes, at leading order,

$$\frac{dH}{d\xi} = \frac{-H^3\frac{2}{9} + 12 - 6H}{H^3}. \tag{4.19}$$

Looking at the limits of the solution as before we find $H \to 1.7882$ as $\xi \to \infty$ which matches onto Region 3 at $X = -2/9$ as required. As $\xi \to -\infty$, $H \gg 1$ and (4.19) reduces to

$$\frac{dH}{d\xi} = -\frac{2}{9}, \tag{4.20}$$

and so $\hat{h}$ is linear with gradient $-2\hat{Q}/9$ in the outer limit of Region 2.

Behaviour in Region 1 is the same as that in Region 5 except that (4.17) is now

$$\hat{h} = -\frac{2}{9}\hat{Q}\xi + \frac{1}{2}\hat{Q}^6\xi^2. \tag{4.21}$$

When ξ is small, $\hat{h}$ has gradient $-2\hat{Q}/9$ which matches Region 2, as required. In original variables we obtain,

$$\hat{h} = \frac{\hat{x}^2}{2} - \frac{2}{81\hat{Q}^4}.$$

Since $\hat{h} \to \hat{h}_0 + \hat{x}^2/2$ as $\hat{x} \to -\infty$, we obtain $\hat{h}_0 = -2/81\hat{Q}^4$ as before.

Figure 4.19 shows agreement between the values of $\hat{h}_0$ for given $\hat{Q}$ obtained numerically (denoted by crosses) and the asymptotic analysis (4.18) for small $\hat{Q}$.

Equations (4.18) and (4.13) relating $\hat{h}_0$ and $\hat{Q}$ for small and large $\hat{Q}$ respectively, become in dimensional variables,

$$Q^* = \frac{2}{3}V^*R\left(\frac{h_0^*}{R}\right), \quad \left(Q^* \gg \frac{\kappa H^{7/2}}{\mu R^{1/2}}\right), \tag{4.22}$$

$$Q^* = -\left(\frac{2}{81}\right)^{1/4}\left(\frac{\mu V^*}{\kappa R^2}\right)^{1/2} V^*R\left(\frac{R}{-h_0^*}\right)^{1/4}, \quad \left(Q^* \ll \frac{\kappa H^{7/2}}{\mu R^{1/2}}\right). \tag{4.23}$$

These relations agree with the predictions of Coyle [60] in his studies of roll coating with deformable roll covers. Coyle numerically integrates a first-order nonlinear ordinary differential equation and fits functions to the solutions to obtain predictions for the flow rate through the gap between two rotating deformable rolls. In the limit of small roll deformations the choice of boundary conditions downstream of the gap becomes important. One choice Coyle considers is 'submerged' boundary conditions where both rolls are surrounded by an infinite bath of fluid. Taking one roll to be stationary and of infinite radius, his model reduces to our model. Expressing in terms of our variables, Coyle's predictions are

$$Q^* = \frac{2}{3} V^* R \left(\frac{h_0^*}{R} \right),$$

for the small deformation limit (corresponding to large Q^*) and

$$Q^* = 0.4 \left(\frac{\mu V^*}{\kappa R^2} \right)^{1/2} V^* R \left(\frac{-h_0^*}{R} \right)^{-1/4},$$

for the large deformation limit (small Q^*), which agree with our solutions (4.22, 4.23), since $(2/81)^{1/4} \approx 0.396$.

4.1.5 Force at the steady state

Rescaling the variables as in §4.1.4 for the steady state, the $\hat{\mathbf{x}}$ and $\hat{\mathbf{y}}$ components of the force acting on the cylinder are given by

$$\hat{F}_x = \int_{-\infty}^{\infty} \left(-\frac{\hat{h}\hat{x}}{2} + \hat{h}_0 \hat{x} + \frac{\hat{x}^3}{2} - \frac{1}{\hat{h}} - \frac{\hat{h}\hat{h}_{\hat{x}}}{2} \right) d\hat{x} \quad \text{where} \quad \hat{F}_x = \frac{F_x}{V^{4/5}}, \tag{4.24}$$

$$\hat{F}_y = \int_{-\infty}^{\infty} \left(\hat{h} - \hat{h}_0 - \frac{\hat{x}^2}{2} \right) d\hat{x} \quad \text{where} \quad \hat{F}_y = \frac{\tilde{F}_y}{V^{3/5}}. \tag{4.25}$$

Given values for $\hat{h}_0$, V, L we can calculate the components of the force using the steady state equations or using the full equations at a given t. For $\hat{h}_0 = 0.5$, $\hat{L} = 10$, $V = 1, 3, 5$ with $t = 15$ the two methods agree to 3 decimal places.

Figure 4.21 shows how the steady force changes with the perpendicular distance of the particle from the undeformed wall, $\hat{h}_0$. We now consider the asymptotic limits of the force for large positive and negative $\hat{h}_0$.

(i) Positive $\hat{h}_0$: $\hat{F}_x$

For large positive $\hat{h}_0$ wall deformations are small and so we assume $\hat{h} \approx \hat{h}_0 + \hat{x}^2/2$. Equation (4.24) becomes

$$\hat{F}_x = \int_{-\infty}^{\infty} \frac{-1}{\hat{h}_0 + \frac{\hat{x}^2}{2}} d\hat{x} = -\frac{\pi\sqrt{(2)}}{\sqrt{\hat{h}_0}}. \qquad (4.26)$$

Figure 4.21 shows agreement between (4.26) and numerical simulations for large positive $\hat{h}_0$.

(ii) Positive $\hat{h}_0$: $\hat{F}_y$

In this case we let $\hat{h} = \hat{h}_0 + \hat{x}^2/2 + H$ where H is the small perturbation from the undeformed state. The steady state equation (4.9) becomes

$$H_{\hat{x}} = \frac{12\hat{Q}}{\left(\hat{h}_0 + \frac{1}{2}\hat{x}^2\right)^3} - \frac{6}{\left(\hat{h}_0 + \frac{1}{2}\hat{x}^2\right)^2}. \qquad (4.27)$$

Integrating (4.27) with respect to $\hat{x}$ we obtain from (4.25)

$$\hat{F}_y = \frac{4}{\hat{h}_0}. \qquad (4.28)$$

If the surfaces are rigid, for purely transverse particle motion, the lift force on the particle is zero [50]. Equation (4.28) describes the lift force on the particle arising from wall deformation. Figure 4.21 shows agreement between (4.28) and numerical simulations for large positive $\hat{h}_0$.

(iii) Negative $\hat{h}_0$: $\hat{F}_x$

For negative $\hat{h}_0$ the particle is indented in the wall and we calculate the force integral by dividing the domain into three regions (from §4.1.4, neglecting the small corner regions). For $-\infty < \hat{x} < -2/9\hat{Q}^2$ and $2/9\hat{Q}^2 < \hat{x} < \infty$, we have $\hat{h} = \hat{h}_0 + \hat{x}^2/2$ and the $O(1/\hat{h})$ term in (4.24) dominates. For $-2/9\hat{Q}^2 < \hat{x} < 2/9\hat{Q}^2$, we neglect $\hat{h}\hat{h}_{\hat{x}}/2$ in (4.24) which is $O(\hat{Q}^2)$. Therefore (4.24) becomes

$$\hat{F}_x = 2\int_{\frac{2}{9\hat{Q}^2}}^{\infty} \frac{-1}{\hat{h}_0 + \frac{1}{2}\hat{x}^2} d\hat{x} + \int_{-\frac{2}{9\hat{Q}^2}}^{\frac{2}{9\hat{Q}^2}} \left(-\frac{\hat{h}\hat{x}}{2} + \hat{h}_0\hat{x} + \frac{\hat{x}^3}{2} - \frac{1}{\hat{h}}\right) d\hat{x}. \qquad (4.29)$$

The first integral in (4.29) is undefined at its lower limit, *i.e.* at $\hat{x} = 2/9\hat{Q}^2$, $\hat{h}_0 = -\hat{x}^2/2$. We calculate this integral by integrating from within the corner region, setting the limit as $\hat{x} = (-2\hat{h}_0)^{1/2} + C\hat{Q}^5$ (where $\hat{Q}$ is small and C is an O(1) constant). We obtain

$$2\int_{\frac{2}{9\hat{Q}^2}+C\hat{Q}^5}^{\infty} \frac{-1}{\hat{h}_0 + \frac{1}{2}\hat{x}^2} d\hat{x} = \frac{1}{\sqrt{-\hat{h}_0}} \ln\left|C\hat{Q}^5\right| + \frac{1}{\sqrt{-\hat{h}_0}} \ln\left|\frac{1}{C\hat{Q}^5 + 2\sqrt{-2\hat{h}_0}}\right|. \tag{4.30}$$

Since $\hat{Q}$ is small, $\ln|C| \ll \ln\left|\hat{Q}^5\right|$ so we may drop the C from the first term in (4.30). Since $\hat{h}_0$ is large, $2\sqrt{-2\hat{h}_0} \gg C\hat{Q}^5$ and we may neglect $C\hat{Q}^5$ in the last term in (4.30). In the central region, $\hat{h}$ is given by $\hat{h}^3\hat{x} + 12\hat{Q} - 6\hat{h} = 0$ (from §4.1.4). We calculate the second integral in (4.29) numerically and, using $\hat{h}_0 = -2/81\hat{Q}^4$, (4.24) becomes

$$\hat{F}_x = -0.2243\left(\frac{81\hat{h}_0}{-2}\right)^{3/4} + \frac{1}{\sqrt{-\hat{h}_0}} \ln\left(\frac{1}{2\sqrt{2}}\left(\frac{2}{81}\right)^{5/4}\left(\frac{1}{-\hat{h}_0}\right)^{7/4}\right). \tag{4.31}$$

Figure 4.21 shows agreement between (4.31) and numerical simulations for large negative $\hat{h}_0$.

(iv) Negative $\hat{h}_0$: $\hat{F}_y$

Again we divide the domain into three regions. In the outer regions, $\hat{x} > \left|2/9\hat{Q}^2\right|$, we have $\hat{h} = \hat{h}_0 + \hat{x}^2/2$ and so (4.25) reduces to

$$\hat{F}_y = \int_{-\frac{2}{9\hat{Q}^2}}^{\frac{2}{\hat{Q}^2}} \left(\hat{h} - \hat{h}_0 - \frac{\hat{x}^2}{2}\right) d\hat{x}.$$

As before, $\hat{h}$ is given by $\hat{h}^3\hat{x} + 12\hat{Q} - 6\hat{h} = 0$ and we obtain

$$\hat{F}_y = -\frac{4\hat{h}_0}{9}\left(\frac{81\hat{h}_0}{-2}\right)^{1/2} - \frac{1}{3}\left(\frac{2}{9}\right)^3\left(\frac{81\hat{h}_0}{-2}\right)^{3/2} + 0.9185\left(\frac{81\hat{h}_0}{-2}\right)^{1/4}, \tag{4.32}$$

where the third term in (4.32) comes from numerically integrating $\hat{h}$ in the central region.

Figure 4.21 shows that the asymptotic solutions (4.26) and (4.28) for positive $\hat{h}_0$ and (4.31) and (4.32) for negative $\hat{h}_0$ compare well to the numerical simulations for $\hat{F}_x$ and $\hat{F}_y$.

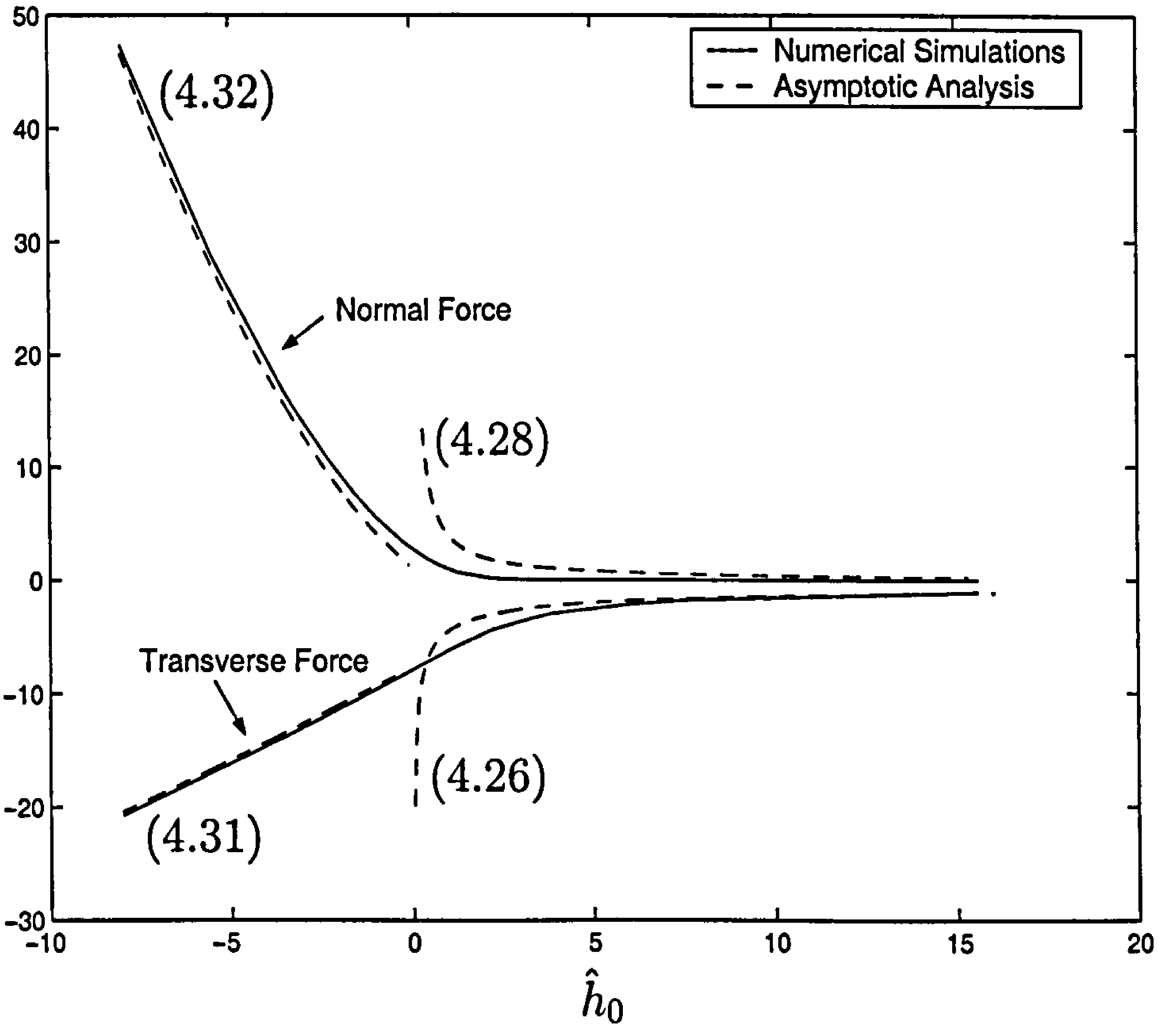

Figure 4.21: Normal force, $\hat{F}_y$, and transverse force, $\hat{F}_x$, acting on the particle against $\hat{h}_0$ for $V = 1$. Dashed lines denote the asymptotic solutions for small and large $\hat{h}_0$ (4.26, 4.28, 4.31, 4.32).

In dimensional variables the transverse force acting on the cylinder in the small deformation limit (4.26) can be expressed as

$$F_x^* = -\frac{2\pi\mu V^*}{\sqrt{2\epsilon}}, \tag{4.33}$$

where $\epsilon = h_0^*/R$, which agrees with the analysis of Jeffrey & Onishi [55] for the slow motion of a cylinder close to a rigid wall. In the large deformation limit we find (4.31) in dimensional variables becomes (to leading order)

$$F_x^* = -0.2243\left(\frac{81h_0^*}{-2}\right)^{3/4}\left(\mu\kappa V^* R^{1/2}\right)^{1/2} \tag{4.34}$$

Equations (4.32) and (4.28) relating $\hat{F}_y$ and $\hat{h}_0$ for small and large $\hat{Q}$ respectively become in dimensional variables

$$F_y^* = 1.92\kappa R^2\left(\frac{-h_0^*}{R}\right)^{3/2}, \quad \left(Q^* \ll \frac{\kappa H^{7/2}}{\mu R^{1/2}}\right), \tag{4.35}$$

$$F_y^* = 4\kappa R^2\left(\frac{\mu V^*}{\kappa R^2}\right)\left(\frac{R}{h_0^*}\right), \quad \left(Q^* \gg \frac{\kappa H^{7/2}}{\mu R^{1/2}}\right). \tag{4.36}$$

Coyle [60] also obtains predictions for the roll-separating force between two deformable rolls which we can compare with our predictions. In the large deformation limit the choice of boundary conditions is unimportant and, again assuming one roll to be stationary and of infinite radius, his numerical prediction for the force is

$$F_y^* = 1.89\kappa R^2\left(\frac{-h_0^*}{R}\right)^{3/2},$$

for the large deformation limit (corresponding to small Q^*) which agrees with (4.35). We note that, in the large-deformation limit, the lift force is independent of the sideways speed of the particle. In the small deformation limit (large Q^*) Coyle's prediction for the force using the submerged boundary condition is inconsistent with our solution (4.36). The derivation of Coyle's prediction for this limit is unclear.

From Figure 4.21 we see that a large force is needed to indent a particle into the wall and similarly a large force is needed to push it sideways once indented. In Chapter 2 we found the force on a partially-immersed cylinder in a fluid-filled rigid-walled wedge, due to capillary effects, was $O(\gamma)$, where γ is the surface tension of the fluid/air interface. We can now briefly consider this model with the addition of deformable walls by using the above analysis. We assume $F_x^* \sim \gamma$ and $F_y^* \sim \gamma$ and (4.33, 4.34, 4.35, 4.36) give $V^* \sim \gamma/\mu$, describing the transverse speed of the cylinder. This implies that the transverse motion of a cylinder is independent of κ, the stiffness of the wall, at least in leading-order scaling behaviour; a possible explanation of this is as follows. If the wall is stiff, resistance to sideways motion is likely to be strong, seeming to suggest a reduction in speed; however, when the wall is stiff, the indentation of the cylinder into the wall will be very small. If the wall is relatively floppy, the cylinder will be indented further into the wall but the resistance to sideways motion is now also reduced, so that the transverse speed of the cylinder remains largely unchanged. While κ does not appear explicitly in this scaling for V^*, it is likely to influence the coefficient.

4.1.6 Simultaneous perpendicular and transverse particle displacement

Both the perpendicular and transverse particle displacement problems suggested that 'choking' (where the wall touches the particle in finite time) does not occur, for any values of the parameters. Here we explore the possibility that a particle which is pushed downwards and sideways simultaneously may cause choking. We combine the previous models to perform numerical simulations for a range of the parameters, $h_0(t)$ and V. Figure 4.22 shows a particle that has transverse speed $V = 1$, and is pushed down from $h_0 = 0.3$ to $h_0 = -1.7$ with $t_{final} = 10$. We see that, as before, a sharp transient corner is created in the wall before the steady state is reached. As V increases the corner becomes sharper and the wall more deformed, however no values for

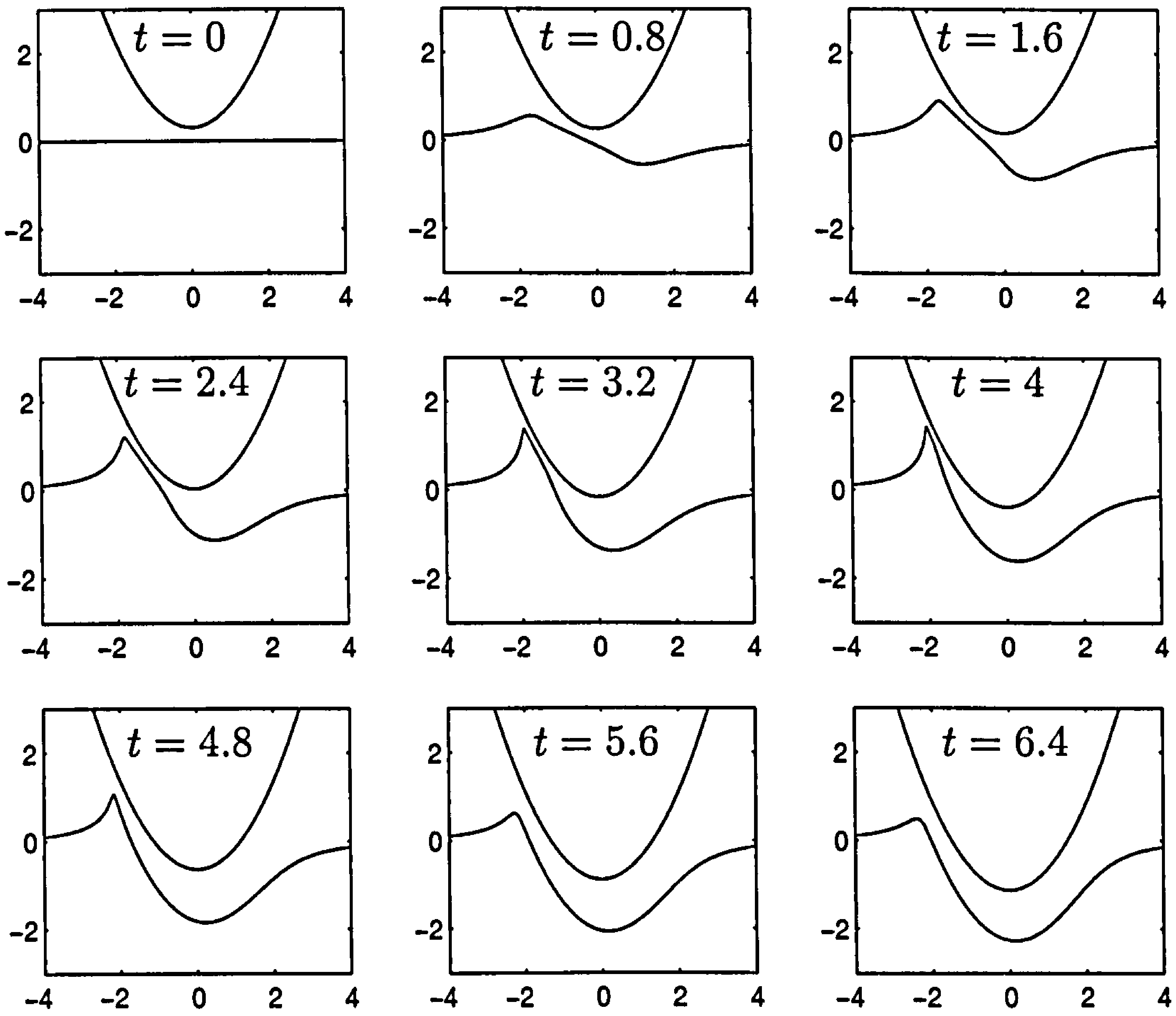

Figure 4.22: Wall deformation for the combined case where transverse speed $V = 1$ and the particle is pushed down from $h_0 = 0.3$ to $h_0 = -1.7$ with $t_{final} = 10$.

the parameters could be found for which choking occurred. Decreasing the downwards speed appears to have little effect, only marginally increasing the wall deformation.

4.2 Three Dimensional Motion

We now extend this model into three dimensions. Again we consider a small region close to the wall where we can model the rigid particle as a paraboloid (representing the base of a sphere). Initially the wall is undeformed so the gap thickness, $h(x,y,t)$, is given by $h = h_0(t) + (\mathbf{x}\cdot\mathbf{x})/2$, where $\mathbf{x} = (x,y)$. As a first case we consider motion parallel to the (x,y)–plane only so $h_0(t) = h_0$. The particle moves parallel to the x axis with speed V and as before we can derive the evolution equation for the gap thickness (the analogue of (4.1))

$$h_t + \nabla_\perp \cdot \left(\frac{h^3}{12}(\mathbf{x} - \nabla_\perp h)\right) - \frac{\mathbf{V}}{2} \cdot \nabla_\perp h = 0, \qquad (4.37)$$

(where $\mathbf{V} = V\hat{\mathbf{x}}$ and $\nabla_\perp$ denotes differentiation with respect to x, y only), subject to the boundary conditions

$$h \longrightarrow h_0 + \frac{1}{2}\mathbf{x}\cdot\mathbf{x}, \quad \text{as } |\mathbf{x}| \longrightarrow \infty. \qquad (4.38)$$

To integrate this PDE numerically we let $h = h_0 + (\mathbf{x}\cdot\mathbf{x})/2 + H$ where H is the perturbation from the undeformed state. The problem then becomes

$$H_t + \nabla_\perp \cdot \left(\frac{(h_0 + (\mathbf{x}\cdot\mathbf{x})/2 + H)^3}{12}\nabla_\perp H\right) - \frac{\mathbf{V}}{2} \cdot (\mathbf{x} + \nabla_\perp H) = 0, \qquad (4.39)$$

subject to

$$H \longrightarrow 0, \quad \text{as } x, y \longrightarrow \pm\infty, \qquad (4.40)$$

where, initially, $H = 0$ for all x,y. Equation (4.40) is more accurate to implement numerically than (4.38).

4.2.1 Force acting on the particle

The force, $\mathbf{F}^*$, on the sphere is given by

$$\mathbf{F}^* = \int_{S^*} \boldsymbol{\sigma}^* \cdot \hat{\mathbf{n}}\, dS^*,$$

where $\boldsymbol{\sigma}^*$ is the stress vector, $\hat{\mathbf{n}}$ is the outward pointing normal to the sphere and S^* is the surface of the sphere. As before we scale pressures on κH, speeds on $\kappa H^{5/2}/\mu R^{1/2}$ and lengths on $(HR)^{1/2}$ so that $F^* = \kappa H^2 R F$. The outward pointing unit normal to the sphere is

$$\hat{\mathbf{n}} = \frac{\epsilon^{1/2} r\hat{\mathbf{r}} - \hat{\mathbf{z}}}{(1+\epsilon r^2)^{1/2}},$$

and $dS^* = HRrdrd\theta$, in cylindrical polar coordinates (r, θ, z). Taking the $\hat{\mathbf{x}}$ component of the stress vector we obtain

$$F_x = \int_0^{2\pi} \int_0^{\infty} \Big[\cos\theta \left(-p\epsilon^{1/2} r + 2\epsilon^{3/2} r u_r - \epsilon^{3/2} w_r - \epsilon^{1/2} u_z\right) \\ - \sin\theta \left(\epsilon^{3/2} r \left(r \left(\frac{v}{r}\right)_r + \frac{1}{r}\epsilon^{1/2} v_\theta\right) - v_z - \frac{\epsilon^{3/2}}{r} w_\theta\right)\Big] r\Big|_{z=h_0+\frac{r^2}{2}} drd\theta, \tag{4.41}$$

where F_x is the transverse force acting on the particle. Taking the $\hat{\mathbf{z}}$ component of the stress vector we obtain

$$F_z = \int_0^{2\pi} \int_0^{\infty} \left(p + \epsilon^2 r w_r + \epsilon r u_z - 2\epsilon w_z\right) r\Big|_{z=h_0+\frac{r^2}{2}} drd\theta, \tag{4.42}$$

where F_z is the force acting on the particle normal to the undeformed surface.

At leading order we obtain, from (4.41) and (4.42)

$$\frac{F_x}{\epsilon^{1/2}} = -\int_0^{2\pi} \int_0^{\infty} \left[\cos\theta \left(pr + u_z\right) - \sin\theta \left(v_z\right)\right] r\Big|_{z=h_0+\frac{r^2}{2}} drd\theta, \tag{4.43}$$

$$F_z = \int_0^{2\pi} \int_0^{\infty} pr\, drd\theta. \tag{4.44}$$

Standard lubrication theory in three dimensions gives

$$\nabla_\perp p = \mathbf{u}_{zz}, \tag{4.45}$$

subject to

$$\mathbf{u} = 0 \text{ on } z = h_0 + \frac{r^2}{2}, \tag{4.46}$$

$$\mathbf{u} = -V_p \hat{\mathbf{x}} \text{ on } z = h_0 + \frac{r^2}{2} - h, \tag{4.47}$$

where $\nabla_\perp$ denotes differentiation with respect to r, θ only. Solving (4.45) using (4.46, 4.47) we calculate u_z, v_z on the sphere's surface. Since $p = -h_0 - r^2/2 + h$ we obtain

$$\frac{F_x}{\epsilon^{1/2}} = -\int_0^{2\pi} \int_0^{L} \cos\theta \left(\frac{Hr + H_r\left(h_0 + \frac{r^2}{2} + H\right)}{2} + \frac{V\cos\theta}{h_0 + \frac{r^2}{2} + H}\right) \\ - \sin\theta \left(\frac{H_\theta\left(h_0 + \frac{r^2}{2} + H\right)}{2r} - \frac{V\sin\theta}{h_0 + \frac{r^2}{2} + H}\right) rdrd\theta, \tag{4.48}$$

$$F_z = \int_0^{2\pi} \int_0^{L} Hr\, drd\theta, \tag{4.49}$$

where H is the perturbation from the undeformed state as before and $2L$ is the region of integration.

4.2.2 Numerical Method

We solve the PDE (4.39) using an alternating-direction-implicit (ADI) method to integrate forward in time. We use centred difference formulae with nonlinear coefficients and products of derivatives are treated explicitly. We integrate over a rectangular domain, $-10 \le x \le 10$, $-10 \le y \le 10$, with a grid of 200 by 200 meshpoints. We integrate from $t = 0$ to $t = 20$ with 10^6 timesteps. The accuracy was checked by varying the number of meshpoints and timesteps as well as validating using asymptotics (see below).

4.2.3 Simulations

Figure 4.23 shows the wall deformation for the case $V = 1$, $h_0 = 0.5$ at $t = 1$. We can clearly see that, as in the 2D case, high pressures in front of the particle cause the wall to bulge downwards and low pressures behind cause the formation of an extended 'corner' below the particle. Figure 4.24(a) further illustrates this case, showing a contour plot of the wall deformation. Figure 4.24(b) shows the wall displacement varying with x along the line $y = 0$, showing similarity with the 2D case.

Figure 4.25 shows how the wall displacement varies as time increases for $V = 1$, $h_0 = 0.5$. As in the 2D model we see that the corner formation appears to be transient before the deformation relaxes to a steady state.

Figure 4.26 shows (a) cross-sectional views and (b) contour plots for a range of V at the steady state configuration, when $h_0 = 0.5$. The wall deformation and 'sharpness' of the corner formation are more pronounced as V increases, as in the 2D model.

We can also consider the behaviour of the wall when the particle is initially

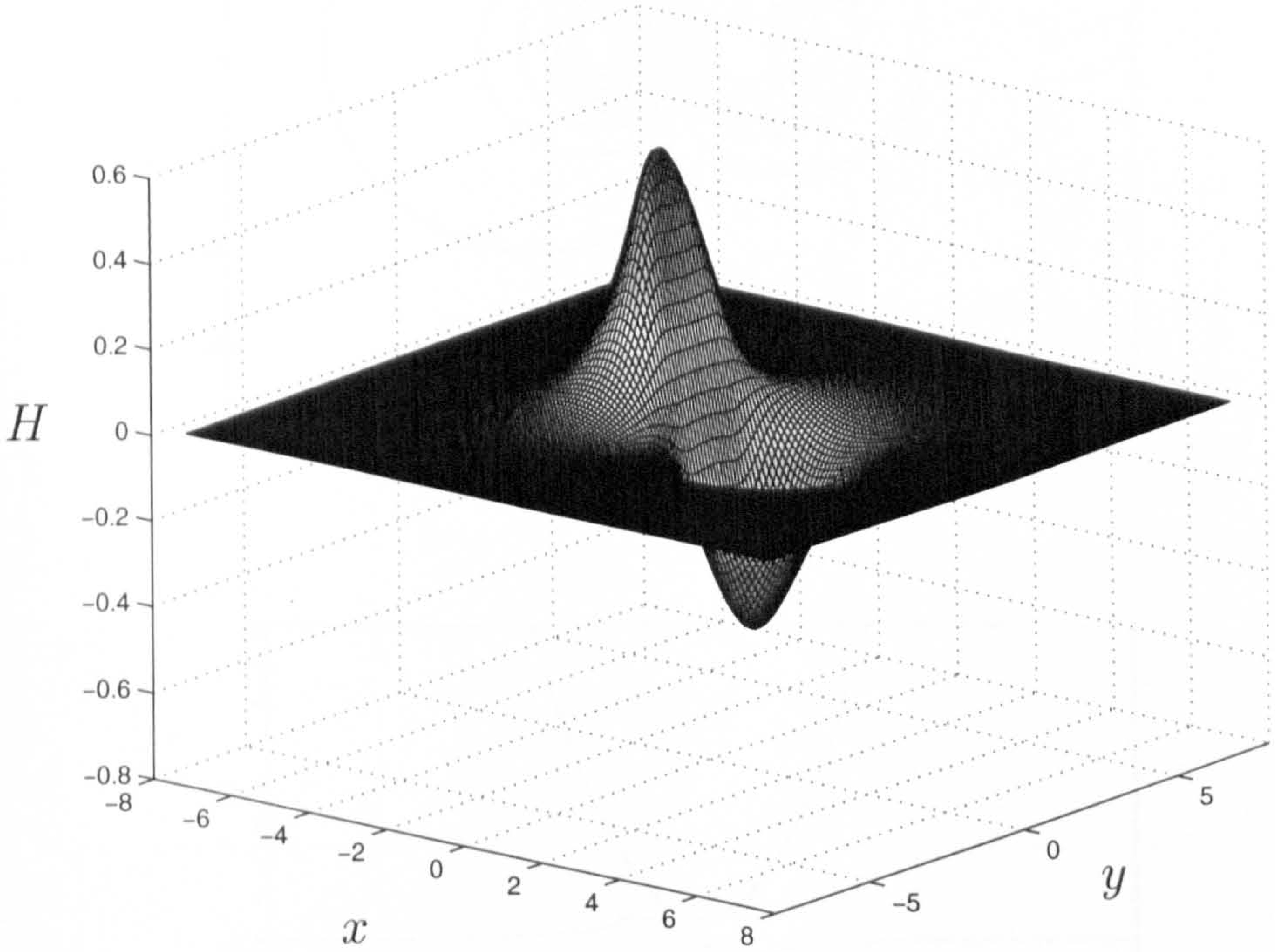

Figure 4.23: Wall displacement for the case $V = 1$, $h_0 = 0.5$ at $t = 1$.

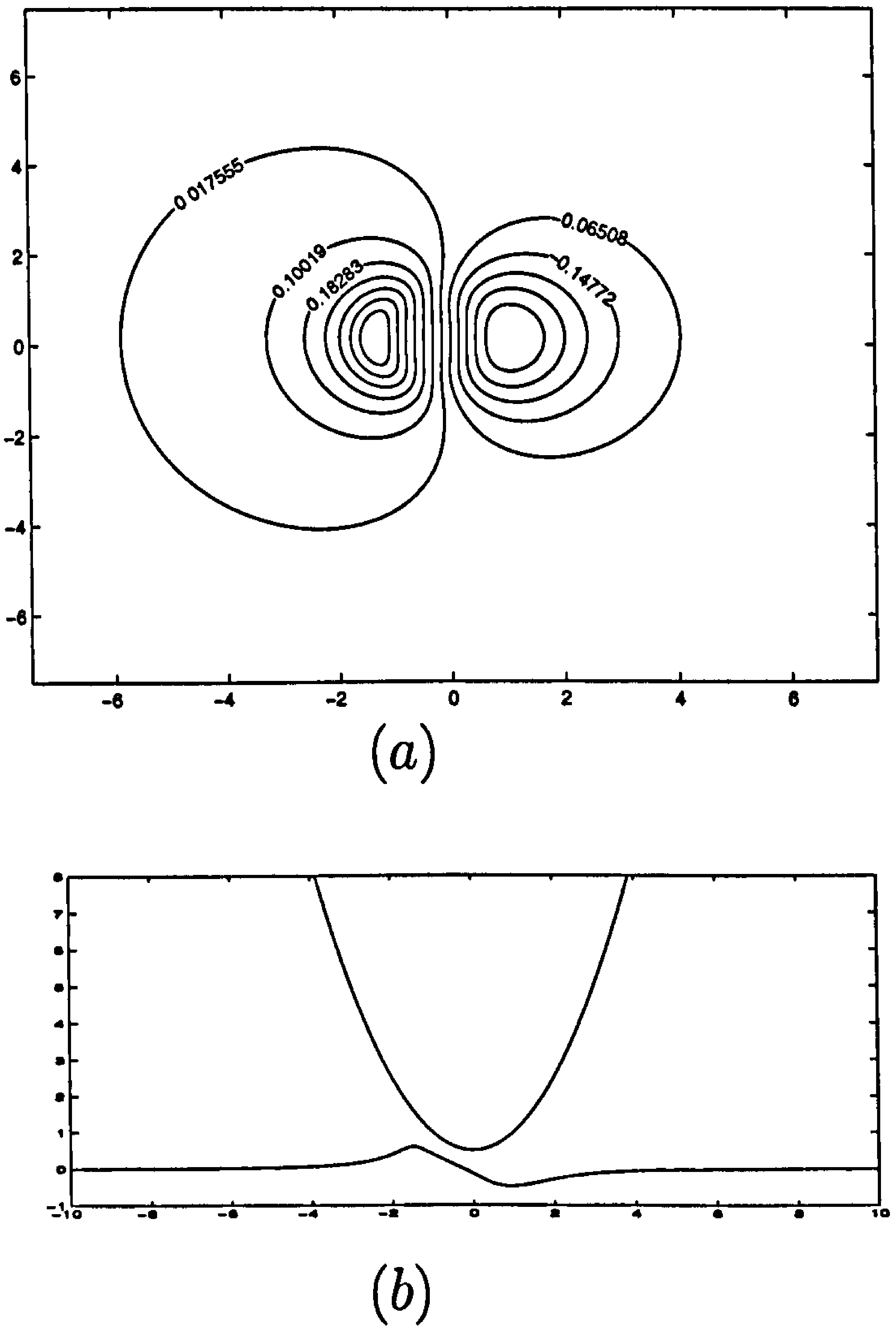

Figure 4.24: (a) Contour plot of the wall displacement for the case $V = 1$, $h_0 = 0.5$ at $t = 1$, (b) cross-sectional view (on the line $y = 0$) of the same case, showing the deformation of the wall and the position of the particle.

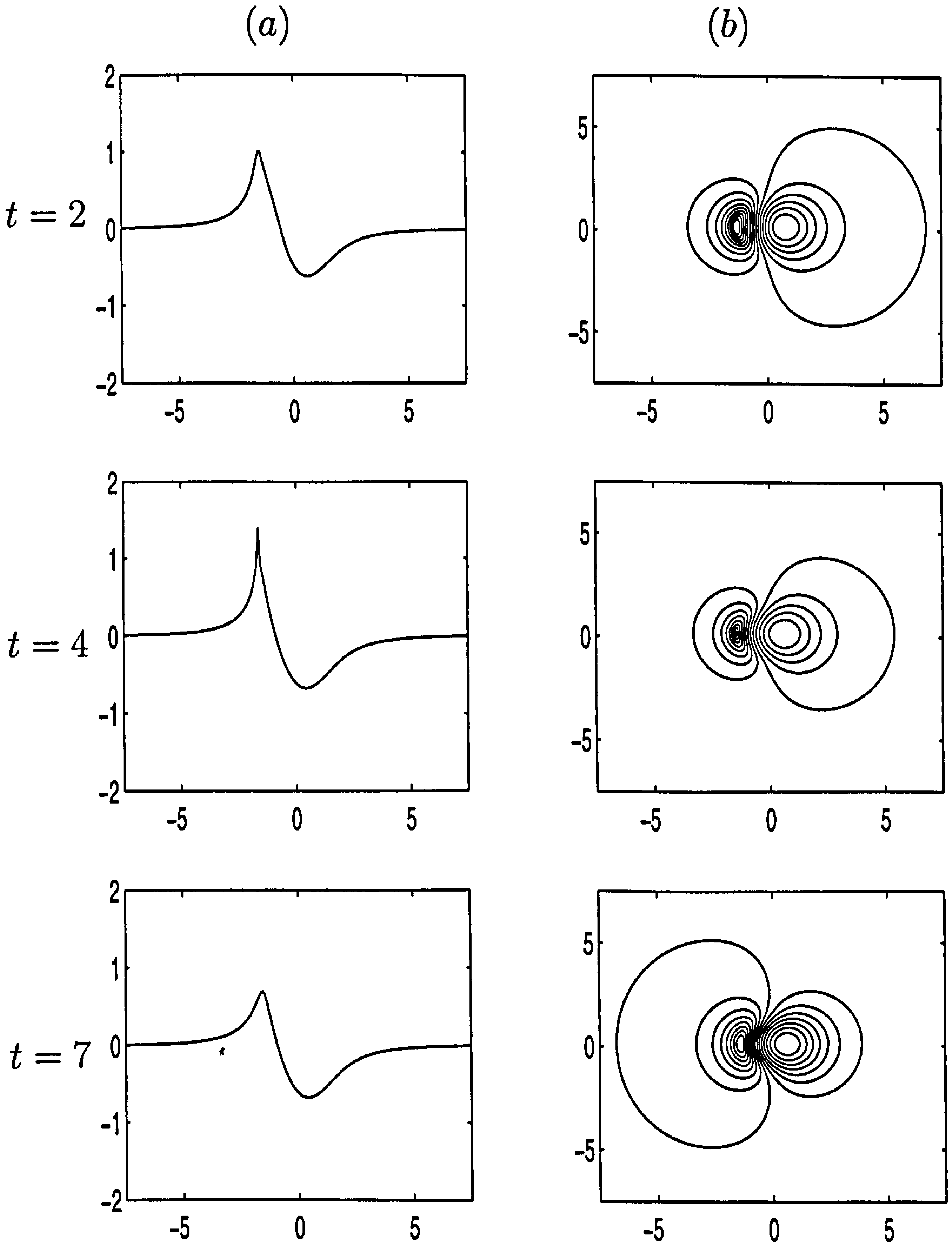

Figure 4.25: Cross-sectional view (a) and contour plots (b) for the case $V = 1$, $h_0 = 0.5$ as time increases. (Contour values are arbitrary.)

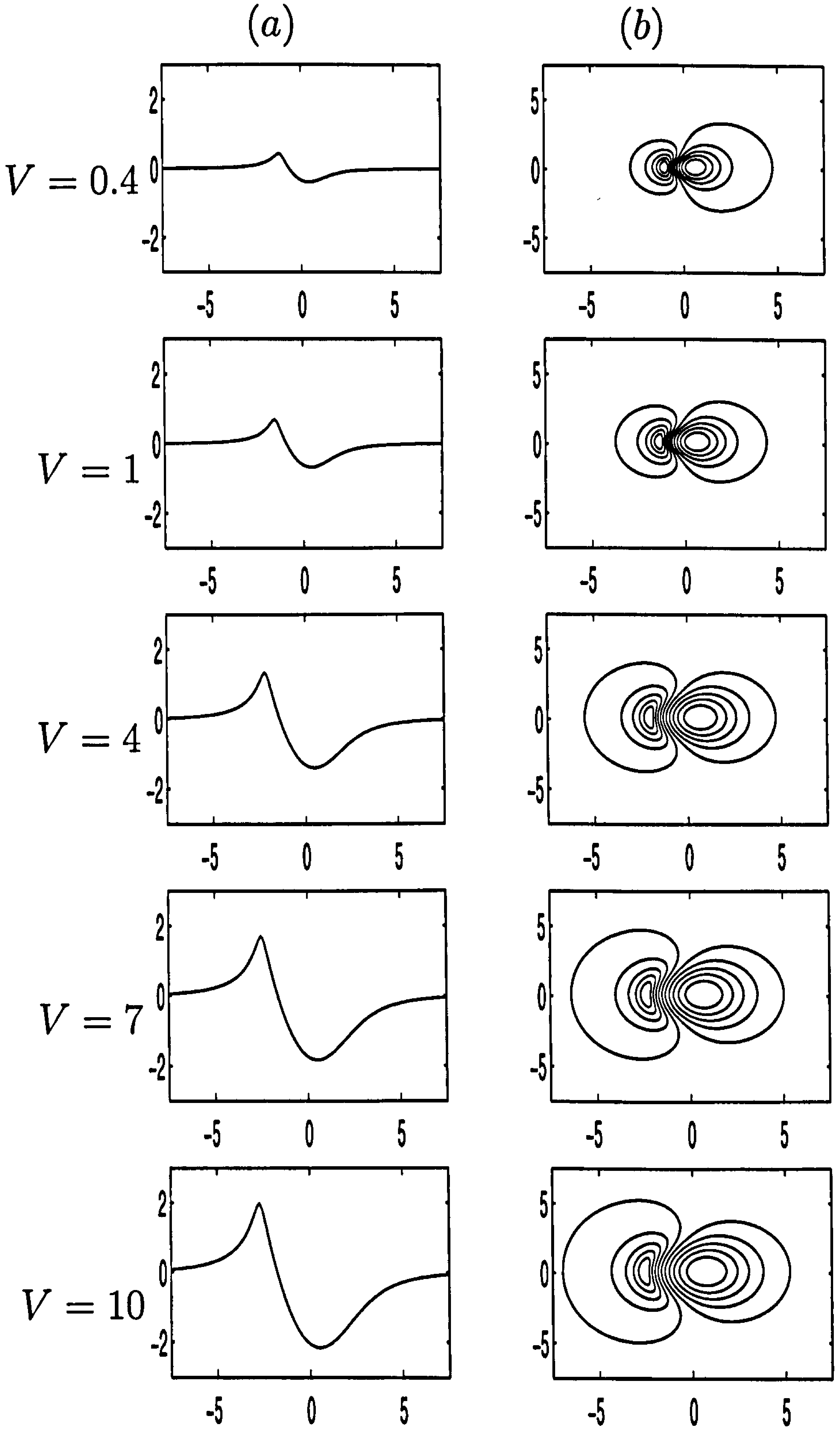

Figure 4.26: Cross-sectional views (a) and contour plots (b) for a range of V, when $h_0 = 0.5$, at the steady state.

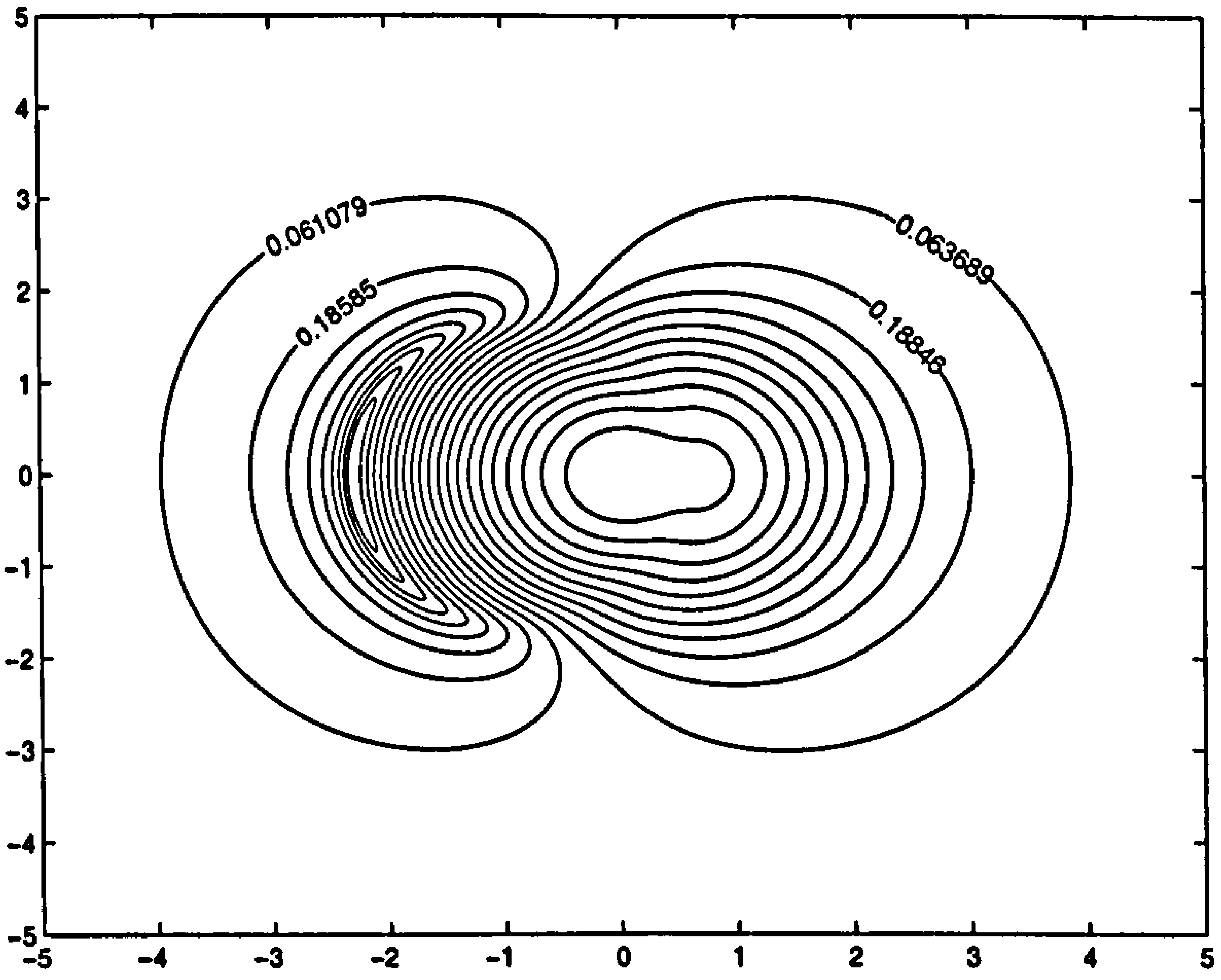

Figure 4.27: Contour plot showing wall deformation for the case $V = 1$, $h_0 = -1$ at $t = 2$.

indented into the wall and is then pushed sideways. We displace the particle perpendicularly to the plane as in Chapter 3, allowing fluid to be squeezed out creating a uniform thin film between the sphere and the wall. We then move the particle transversely relative to the wall with speed V. Figure 4.27 shows a contour plot for the case $V = 1$, $h_0 = -1$ with a nearly-uniform initial film thickness of 0.2, at $t = 2$. We see that the deformation becomes more pronounced, with the low pressures behind the sphere creating a thin ridge-like corner formation and high pressures in advance of the sphere creating a large bulge into the wall. (The ridge does not lie on a circle, r =constant.)

We also use these numerical simulations to obtain approximations for $F_x(t)$ and $F_z(t)$ given h_0, V, from (4.48) and (4.49). Figure 4.28 shows the transverse force on the sphere $F_x/\epsilon^{1/2}$, for a range of h_0, where $V = 1$. We see that, as in the two-dimensional model, the transverse force on the particle is greater as h_0 decreases and there is a peak in the magnitude of the force after initial

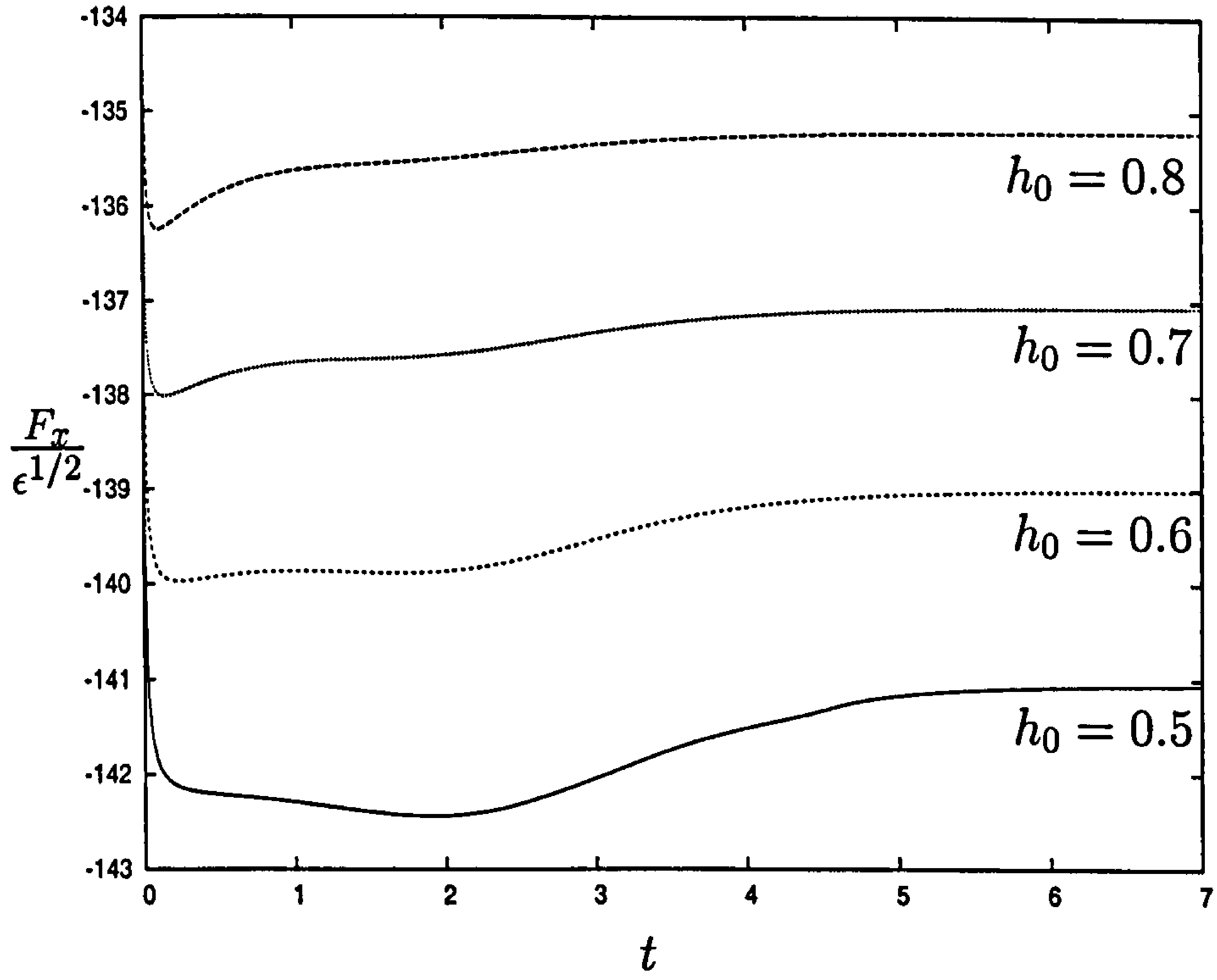

Figure 4.28: Force acting on the sphere, $F_x/\epsilon^{1/2}$, as time increases, when $V = 1$, for a range of h_0.

displacement, when the wall deformation is most pronounced. Calculating the force on the sphere for a range of V we find that as V increases, F_x increases roughly linearly.

Figure 4.29 shows the transverse force, F_x, and the normal force, F_z, acting on the particle at the steady state against h_0 when $V = 1$ and $\epsilon = 0.00125$. Dotted lines show the values of the force in the stiff wall limit, from (4.57), (4.58) below. When the wall is stiff and there is no deformation there is zero normal force acting on the particle. However, when the wall is allowed to deform a 'lift' force is created on the particle by this deformation. This lift force increases as the extent of the wall deformation increases. Similarly, the magnitude of the transverse force increases as wall deformation increases.

We now describe the stiff-wall limit in more detail.

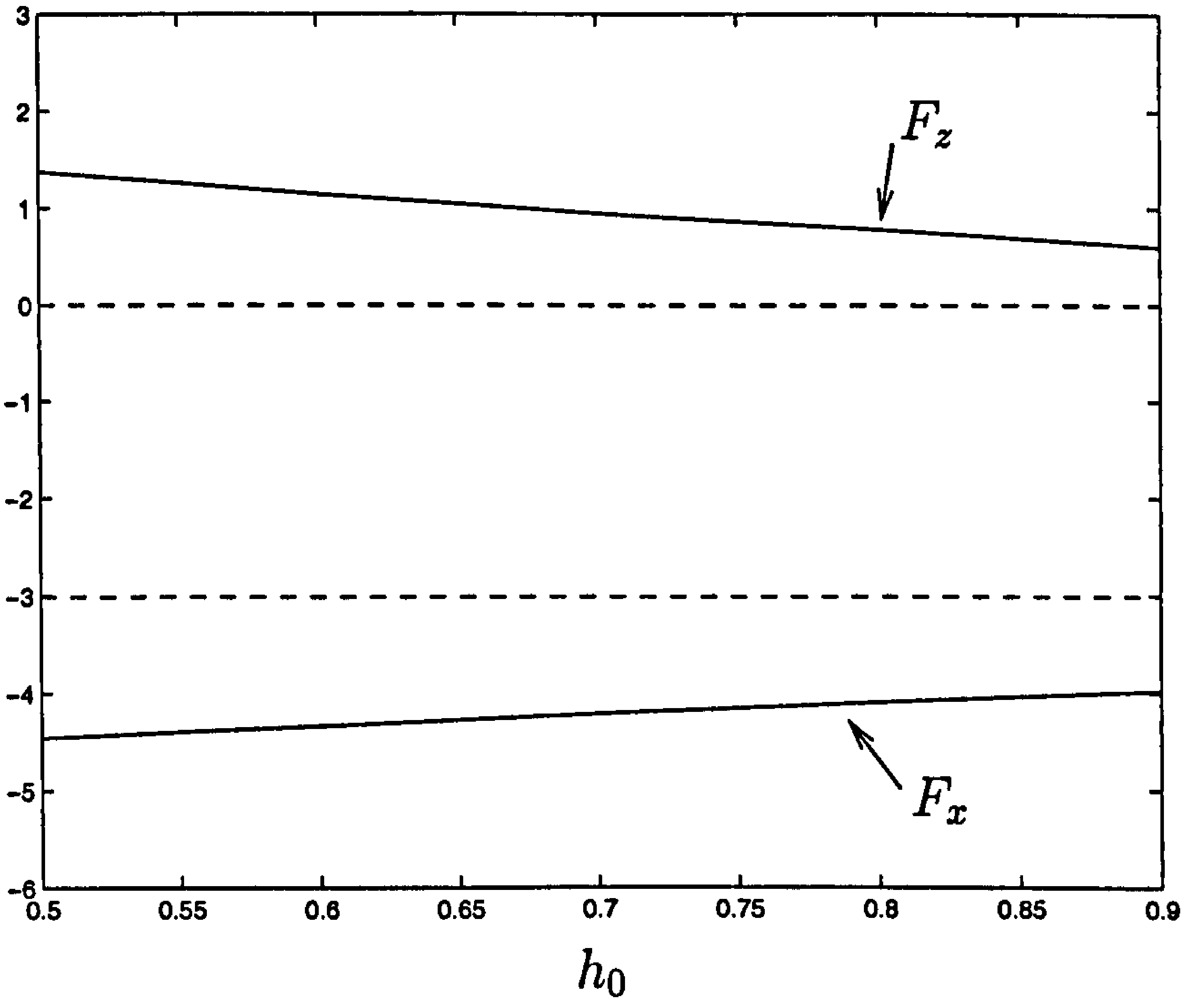

Figure 4.29: Transverse force, F_x, and normal force, F_z, acting on the particle at the steady state against h_0 when $V = 1$ and $\epsilon = 0.00125$. Dashed lines show the values of the force in the stiff wall limit, (4.57, 4.58).

4.2.4 Steady state analysis in the small deformation limit

We let $h_t = 0$ and consider the steady problem when $h_0 > 0$. We consider the small deformation limit so we let $h = \hat{h}_0 + V\hat{h}_1 + \ldots$ where $V \ll 1$. To leading order (4.37, 4.38) become

$$\nabla_\perp \cdot \left[\frac{\hat{h}_0^3}{12}(\mathbf{x} - \nabla_\perp \hat{h}_0)\right] = 0, \tag{4.50}$$

$$\hat{h}_0 \longrightarrow h_0 + \frac{1}{2}\mathbf{x}\cdot\mathbf{x}, \quad \text{as } \mathbf{x} \longrightarrow \pm\infty. \tag{4.51}$$

Therefore we obtain

$$\hat{h}_0 = h_0 + \frac{1}{2}\mathbf{x}\cdot\mathbf{x}.$$

Considering the first-order terms in V, (4.37) gives

$$\nabla \cdot \left[\frac{\hat{h}_0^3}{12}(-\nabla \hat{h}_1)\right] - \frac{\hat{\mathbf{x}}}{2} \cdot \nabla \hat{h}_0 = 0. \tag{4.52}$$

Converting into cylindrical polar coordinates this becomes

$$-\frac{1}{r}\left(\frac{r\hat{h}_{1r}\hat{h}_0^3}{12}\right)_r - \frac{1}{r^2}\left(\frac{\hat{h}_0^3\hat{h}_{1\theta}}{12}\right)_\theta - \frac{\hat{h}_{0r}}{2}\cos(\theta) + \frac{\hat{h}_{0\theta}}{2r}\sin\theta = 0. \tag{4.53}$$

Let $\hat{h}_1 = G(r)\cos(\theta)$. Since $\hat{h}_0 = h_0 + r^2/2$, we obtain

$$-\frac{1}{r}\left(\frac{rG_r(h_0 + r^2/2)^3}{12}\right)_r + \frac{1}{r^2}\left(\frac{(h_0 + r^2/2)^3 G}{12}\right) - \frac{r}{2} = 0.$$

Substituting $G(r) = Ar/(h_0 + r^2/2)^2$ into this equation we obtain $A = 6/5$ (following O'Neill & Stewartson [50]) and hence

$$h = h_0 + \frac{r^2}{2} + \frac{6Vr}{5(h_0 + r^2/2)^2}\cos(\theta). \tag{4.54}$$

Figure 4.30 shows agreement between numerical simulations and analysis (for the perturbation H) for the case $V = 0.01$, $h_0 = 0.5$.

For this analysis to be valid we require $\hat{h}_0 \gg V\hat{h}_1$. Since $r \sim h_0^{1/2}$ this condition becomes

$$\frac{V}{h_0^{5/2}} \ll 1.$$

When the wall is stiff, deformations are small and we use this analysis to calculate the force acting on the particle in this limit. Substituting

$$H = \frac{6Vr}{5\left(h_0 + \frac{r^2}{2}\right)^2}\cos\theta,$$

into (4.48, 4.49) and evaluating, we obtain

$$\frac{F_x}{\epsilon^{1/2}} = -\frac{16}{5}V\pi\log\left(1 + \frac{1}{2}L^2\right), \tag{4.55}$$

$$F_z = 0. \tag{4.56}$$

The dimensional length of the integration region is given by $L^* = \epsilon^\alpha R$ where $0 < \alpha < 1/2$; it extends into the overlap region between the inner (lubrication

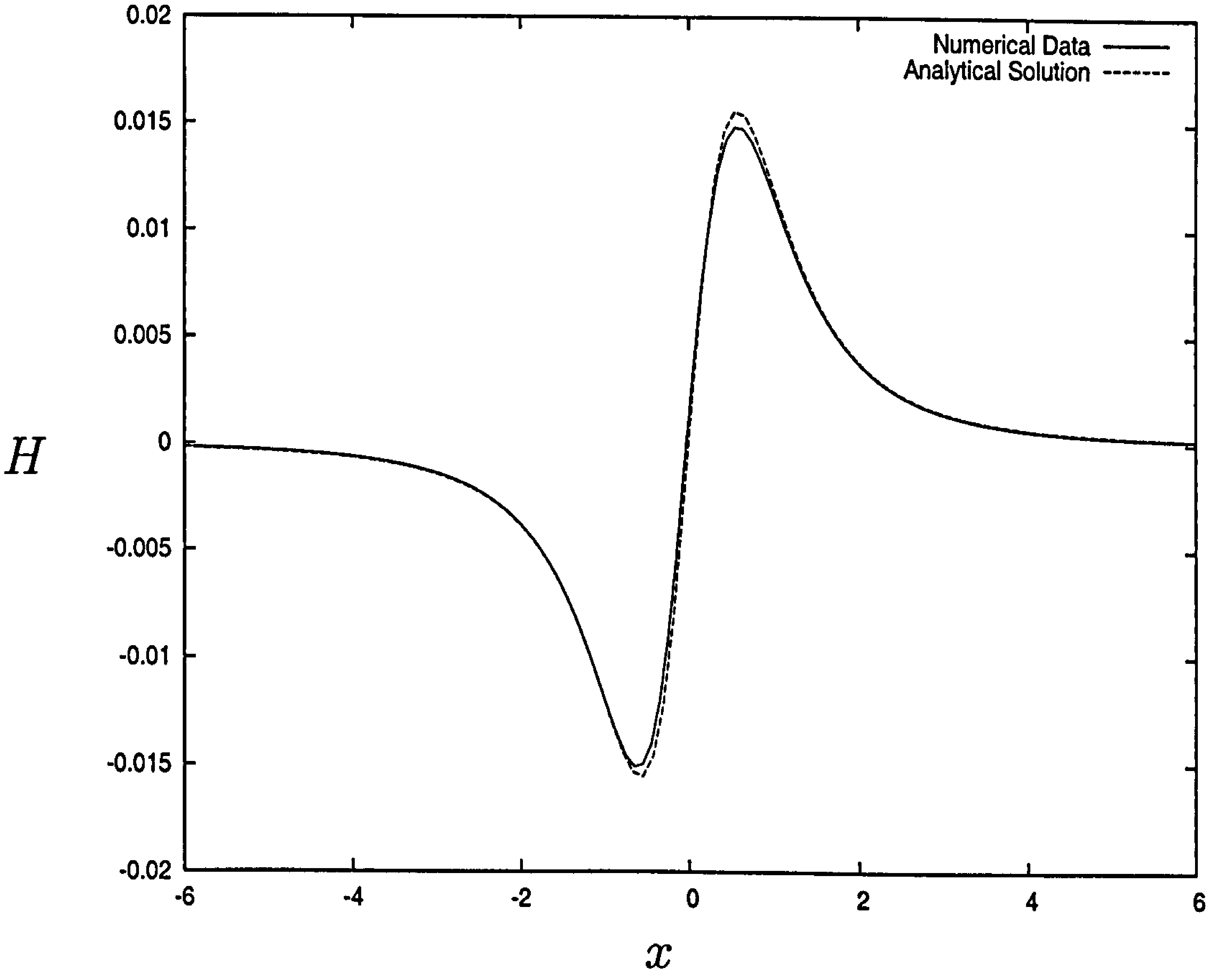

Figure 4.30: Comparison between numerical data and analytic solution for H for $V = 0.01$, $h_0 = 0.5$.

theory) region and the outer region (on the lengthscale of the particle radius). The integrand in (4.48) is $O(1/r^*)$ in this overlap region, giving a $\log(r^*)$ contribution to the force, as calculated in (4.55).. The integral (4.48) in the inner region is dominated by its upper limit L^*, in this region scaled on $\epsilon^{1/2}R$, *i.e.* $L = L^*/\epsilon^{1/2}R$. The integral (4.48) in the outer region is dominated by its lower limit L^*, in this region scaled on R, *i.e.* $L = L^*/R$. Therefore, over the whole region of integration, the log term in (4.55) can be approximated by $\log((L^*/\epsilon^{1/2}R)^2) - \log((L^*/R)^2) = \log(1/\epsilon)$. In dimensional variables, (4.55) and (4.56) are therefore

$$F_x^* = -6V^*\mu\pi R\frac{8}{15}\log\left(\frac{1}{\epsilon}\right), \tag{4.57}$$

$$F_z^* = 0, \tag{4.58}$$

which agrees with the analysis of O'Neill & Stewartson [50] which calculates the force acting on a sphere moving parallel to a nearby rigid plane wall. Figure 4.29 shows these values for F_x and F_z in the stiff wall limit, taking $V = 1$ and $\epsilon = 0.00125$, in comparison with results from the numerical simulations.

4.3 Summary and Conclusions

In Chapter 4 we extend the results of the previous chapter by considering the transverse motion of a particle relative to a deformable surface. As before we begin by modelling this as a two-dimensional cylinder moving at speed V close to an elastic wall modelled as a spring-backed plate. Using lubrication theory in the thin gap between the particle and the wall we derive an evolution equation for the gap thickness $h(x,t)$ and the force acting on the particle.

High pressures created in front of the moving particle cause the deformable surface to bulge downwards. Simultaneously low pressures behind the particle pull the wall up forming a corner. This corner formation is 'sharpest' following initial displacement. This 'necking' effect is similar to that noted by Lighthill

[56] in studies of pellets in tubes, as well as in industrial roll coating applications [60]. Particles which are initially indented into the wall before moving transversely produce gap thickness profiles resembling those observed in Chapter 3 when pulling a particle perpendicularly away from the wall. Asymptotic analysis for both particle motions is very similar.

Analysis of the steady state configuration, both numerical and analytical, reveals two regimes of behaviour: large flow rate $\hat{Q}$ where h_0 is positive and the deformation is small, and small $\hat{Q}$ where h_0 is negative and the wall deformation is large. For small $\hat{Q}$ we perform a matched asymptotic analysis similar to (but we believe more transparent than) that of Lighthill [56]. Asymptotic analysis in both regimes obtains expressions for the flow rate and force on the particle consistent with those found numerically in roll coating studies [60].

We briefly consider a particle undergoing simultaneous perpendicular and transverse displacement by combining the previous models. Simulations suggest that 'choking', where the particle makes contact with the wall, will not occur.

In the latter part of Chapter 4 we consider an extension of the model into three dimensions and look at the transverse motion of a sphere close to a deformable plane. Using lubrication theory we obtain an evolution equation for $H(\mathrm{x}, t)$, the perturbation from the undeformed state, and use an ADI method to integrate this numerically forward in time. As in the 2D model we observe a bulge of the wall in advance of the particle and the formation of a crescent-shaped corner behind it. We consider the force acting on the particle at the steady state. The deformation of the wall creates a 'lift' force on the particle which increases as the deformation increases. Similarly, the transverse force on the particle is increased in comparison to the stiff wall limit as the wall deformation increases. We show in the limit of rigid walls and negligible deformation our analysis is consistent with O'Neill & Stewartson [50].

Here we have extended existing work on a rigid sphere moving in proximity to a rigid planar surface to consider the effect of wall deformability on the hydrodynamic force acting on the sphere. With regards to particle motion in lungs we have shown that the deformability of the cellular airway wall will have a significant effect on the motion of a deposited particle and hence plays a key role in lung clearance. Other effects such as particle rotation and surface tension acting on the upper surface of the sphere would need to be considered before any therapeutic recommendations could be made. However these results provide an interesting extension to existing elastohydrodynamical models and may be directly applicable to non-biological problems, for example in industrial roll coating problems with deformable roll covers.

As mentioned above, a very interesting extension to the model would be to consider the effect of particle rotation. Due to flow in the gap the particle will be subject to a non-zero torque. In Chapters 3 and 4 we assumed no rotation due to this force. However it would be interesting to allow the particle, in both the 2D and 3D models, to rotate as it moves perpendicular and transverse to the surface and calculate any effects this may have on our existing calculations. In this model we have assumed a perfectly smooth particle; it would also be interesting to study the effect of particle roughness, and even different particle shapes, on the gap thickness and force calculations. Also at these very small lengthscales, we may have to consider the effect of interparticle (van der Waals and electrostatic) forces. We used a simple linear springs model to represent the airway deformable wall; a further extension to the model would be to represent more accurately the mechanical properties of the cellular wall. We have assumed the wall is compressible; an incompressible elastic layer could be modelled in a first approximation by taking the fluid pressure to be a function of h_{xx} instead of h, for example.

Finally, many epithelial cells in the lungs are ciliated, mainly in the upper respiratory airways. In the next chapter we consider the effect of ciliary propulsion on the clearance of a deposited particle.

Chapter 5

Motion of a particle trapped in a mucus sheet

In previous chapters we have modelled a particle that is deposited in a non-ciliated airway with no mucus layer. We now consider motion of a deposited particle trapped in a layer of mucus overlaying a periciliary fluid layer, accounting for the effects of propulsive cilia (see [2] and references therein). The particle may interfere with local ciliary function, and may be subject to a large drag. We want to assess how these factors reduce the speed of the particle relative to the speed of the surrounding mucus layer. Stone & Ajdari [73] computed the drag on a flat-bottomed disk trapped in a thin viscous surface film overlying a fluid of finite depth. They retrieved the earlier work of Evans & Sackmann [76] who considered the limit of thin sublayers. These models do not deal with serous-layer flow explicitly. We extend the existing work to consider flow in the serous layer and include the effects of cilia and variation in disk shape. Our asymptotic analysis below follows a standard approach for thin free films, *e.g.* Matar *et al.* [72].

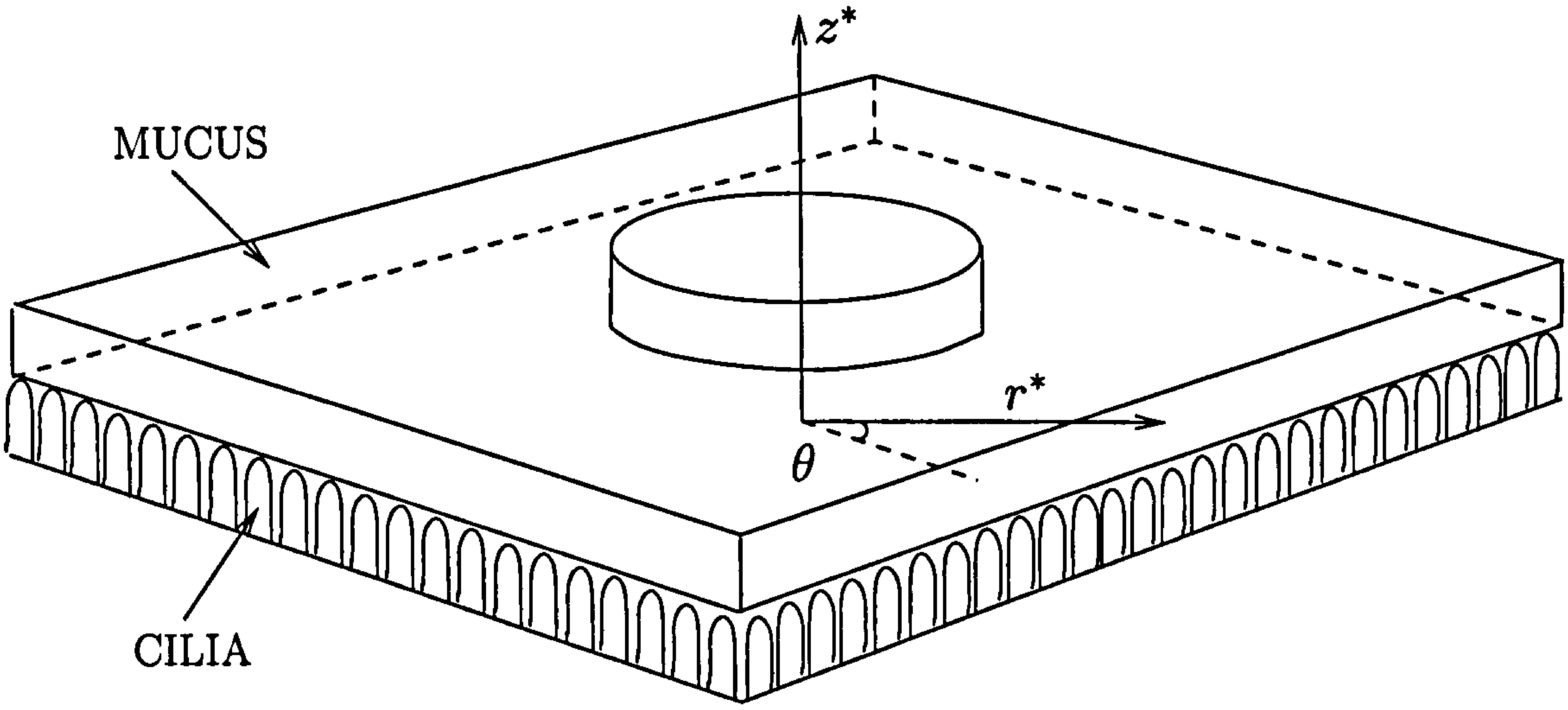

Figure 5.1: Schematic of cylindrical disk within a mucus layer, overlying the periciliary fluid (serous) layer.

5.1 Model Formulation

We model the particle as a cylindrical disk, radius R, moving within a viscous sheet which is propelled by an underlying serous layer. We use a cylindrical polar coordinate system (r^*, θ, z^*), taking the origin to lie on the epithelium/serous interface directly below the centre of the disk (see Figure 5.1). We assume the epithelium/serous interface is flat, *i.e.* $z^* = 0$. We prescribe the mucus/air interface to be flat, at $z^* = h_1^* + \bar{h}^*$ (Figure 5.2). The mucus/serous interface (or, under the disk, the disk/serous interface) is given by $z^* = h_1^*(r^*)$. Outside the disk, h_1^* is assumed constant; if the bottom of the disk is flat $h_1^*(r^*) =$ constant everywhere. These flat-interface assumptions are justifiable provided we assume high surface tension acting at the interfaces. The fluid velocity in the serous layer is denoted $\mathbf{u}^{u*}(r^*, \theta, z^*) = (u^{u*}, v^{u*}, w^{u*})$ under the disk and $\mathbf{u}^{e*}(r^*, \theta, z^*) = (u^{e*}, v^{e*}, w^{e*})$ elsewhere. The pressure in the serous fluid is p^{u*}, p^{e*} respectively and the serous fluid viscosity is $\lambda\mu$, where $\lambda < 1$. In the mucus layer, the fluid velocity is $\mathbf{U}^*(r^*, \theta, z^*) = (U^*, V^*, W^*)$,

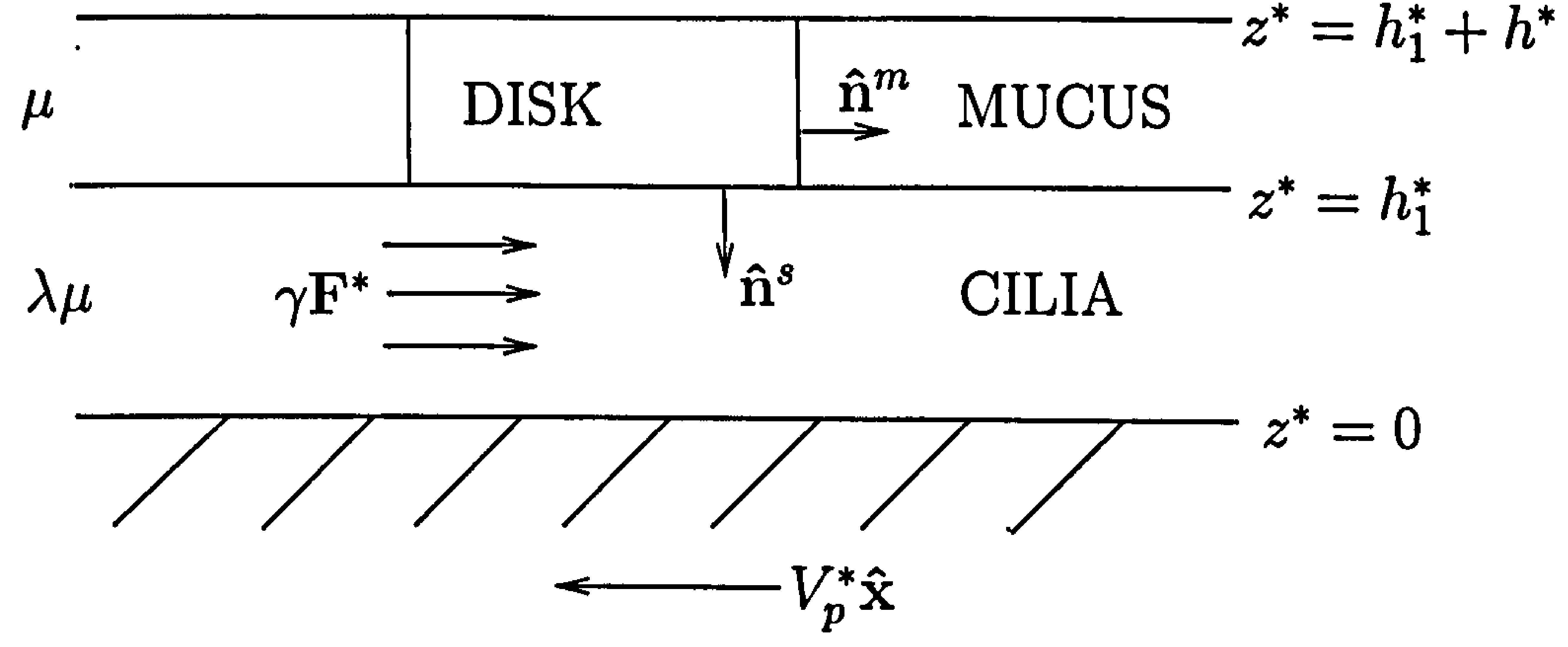

Figure 5.2: Cross-sectional sketch of the disk in a mucus sheet, in the frame of the disk.

the pressure is P^* and the viscosity is μ.

In reality the force on the serous layer fluid due to the cilia is both space- and time-dependent. Cilia move in a regular beat cycle, one phase of which is the 'propulsive' or 'effective' stroke (see §1.2). There is some debate as to the effect of the cilia on the periciliary fluid. It has been suggested that the net movement of the fluid is small and the propulsive force is transmitted to the mucus largely via the upper section of the cilia [13]. However experiments by Knowles & Boucher [16] and Matsui *et al.* [19] have suggested that the velocities in the two layers are similar and there is an important coupling between the layers.

In this model we choose to represent the effect of the cilia as a uniform steady body force γF^* acting on the serous layer fluid (where $\mathbf{F}^* = F^*\hat{\mathbf{x}}$). The parameter γ is a measure of the effect of the particle on the ciliary action, *i.e.* for $r^*/R > 1$, $\gamma = 1$, and $r^*/R \leq 1$, $0 \leq \gamma \leq 1$. The disk moves with unknown velocity $\mathbf{V}_p^* = V_p^*\hat{\mathbf{x}}$ parallel to the wall. We neglect the effects of gravity, curvature of the airway wall and inertial effects.

We assume the mucus and serous fluid behave as Newtonian fluid and so the governing equations are (in the frame of the particle)

$$0 = -\nabla^* P^* + \mu \nabla^{*2} \mathbf{U}^*, \tag{5.1a}$$

$$\nabla^* \cdot \mathbf{U}^* = 0, \tag{5.1b}$$

$$0 = -\nabla^* p^{u*} + \lambda \mu \nabla^{*2} \mathbf{u}^{u*} + \gamma \mathbf{F}^*, \tag{5.1c}$$

$$\nabla^* \cdot \mathbf{u}^{u*} = 0, \tag{5.1d}$$

$$0 = -\nabla^* p^{e*} + \lambda \mu \nabla^{*2} \mathbf{u}^{e*} + \mathbf{F}^*, \tag{5.1e}$$

$$\nabla^* \cdot \mathbf{u}^{e*} = 0, \tag{5.1f}$$

subject to boundary conditions

$$\mathbf{u}^{u*} = \mathbf{u}^{e*} = -\mathbf{V}_p^* \quad \text{on } z^* = 0, \tag{5.2a}$$

$$\mathbf{u}^{u*} = 0 \quad \text{on } z^* = h_1^*,\ r^*/R < 1 \tag{5.2b}$$

$$\mathbf{u}^{e*} = \mathbf{U}^*, \ \ \lambda \mathbf{u}^{e*}_{z^*} = \mathbf{U}^*_{z^*} \quad \text{on } z^* = h_1^*,\ r^*/R > 1 \tag{5.2c}$$

$$\mathbf{U}^*_{z^*} = 0 \quad \text{on } z^* = h_1^* + \bar{h}^*. \tag{5.2d}$$

Normal stress conditions are neglected as we assume flat interfaces. In the absence of the particle the mucus moves at a constant velocity due to the effect of the ciliary body force on the serous layer. We therefore assume the mucus velocity is constant in the far field, *i.e.*

$$\mathbf{U}^* \longrightarrow \tilde{U}\hat{\mathbf{x}} - \mathbf{V}_p^*, \quad \text{as } r^* \longrightarrow \infty, \tag{5.3}$$

where $\tilde{U}\hat{\mathbf{x}}$ is the constant velocity of the undisturbed mucus relative to the epithelium. We also assume

$$\mathbf{U}^* = 0 \quad \text{on } r^*/R = 1. \tag{5.4}$$

We assume zero net force on the particle. Balancing the forces acting on the particle we obtain

$$\int_{A^*} \hat{\mathbf{x}} \cdot (\sigma^{m*} \cdot \hat{\mathbf{n}}^m)\, dA^* = -\int_{S^*} \hat{\mathbf{x}} \cdot (\sigma^{s*} \cdot \hat{\mathbf{n}}^s)\, dS^*, \tag{5.5}$$

where A^* is the surface over which the mucus is in contact with the particle, with outward pointing normal $\hat{\mathbf{n}}^m$, $\boldsymbol{\sigma}^{m*}$ is the stress tensor in the mucus layer, S^* is the surface of the bottom of the disk with outward pointing normal $\hat{\mathbf{n}}^s$, and $\boldsymbol{\sigma}^{s*}$ is the stress tensor in the serous layer (Figure 5.2).

Therefore we have the following known parameters: the sizes of the layers and the particle, R, h_1^*, $\bar{h}^*$; the viscosity ratio, λ; and the body force, $\gamma \mathbf{F}^*$. We seek the resultant velocity of the particle $\mathbf{V}_p^*$.

Nondimensionalisation

From (5.1a) we obtain

$$\frac{P^*}{R} \sim \frac{\mu \tilde{U}}{R^2},$$

where R is a typical particle radius, and so we nondimensionalise pressures on $\mu\tilde{U}/R$, speeds on $\tilde{U}$, lengths on R and stresses on $\mu\tilde{U}/R$. We let $F^* = \mu\tilde{U}F/R^2$.

Therefore we obtain

$$0 = -\nabla P + \nabla^2 \mathbf{U}, \tag{5.6a}$$

$$\nabla \cdot \mathbf{U} = 0, \tag{5.6b}$$

$$0 = -\nabla p^u + \lambda \nabla^2 \mathbf{u}^u + \gamma \mathbf{F}, \tag{5.6c}$$

$$\nabla \cdot \mathbf{u}^u = 0, \tag{5.6d}$$

$$0 = -\nabla p^e + \lambda \nabla^2 \mathbf{u}^e + \mathbf{F}, \tag{5.6e}$$

$$\nabla \cdot \mathbf{u}^e = 0, \tag{5.6f}$$

subject to boundary conditions

$$\mathbf{u}^u = \mathbf{u}^e = -\mathbf{V}_p \quad \text{on } z = 0, \tag{5.7a}$$

$$\mathbf{u}^u = 0 \quad \text{on } z = h_1, \tag{5.7b}$$

$$\mathbf{u}^e = \mathbf{U}, \quad \lambda \mathbf{u}^e_z = \mathbf{U}_z \quad \text{on } z = h_1, \tag{5.7c}$$

$$\mathbf{U}_z = 0 \quad \text{on } z = h_1 + \bar{h}. \tag{5.7d}$$

$$\mathbf{U} \longrightarrow \hat{\mathbf{x}} - \mathbf{V}_p \quad \text{as } r \longrightarrow \infty, \tag{5.7e}$$

$$\mathbf{U} = 0 \quad \text{on } r = 1. \tag{5.7f}$$

and

$$\int_A \hat{\mathbf{x}} \cdot (\sigma^m \cdot \hat{\mathbf{n}}^m)\, dA = -\int_S \hat{\mathbf{x}} \cdot (\sigma^s \cdot \hat{\mathbf{n}}^s)\, dS. \tag{5.8}$$

Scaling

We assume $\epsilon = h_1^*/R \ll 1$ (implying the serous layer is thin compared to the particle radius), and then rescale by letting $z = \epsilon Z$, $h_1 = \epsilon H_1$, $\bar{h} = \epsilon \bar{H}$ and $w^u = \epsilon W^u$, $w^e = \epsilon W^e$, $W = \epsilon \hat{W}$. We also let $\lambda = \hat{\lambda}\epsilon^2$ (implying the mucus is much more viscous than the serous layer). Equations (5.6a–5.6f) become

$$\mathbf{0} = -\nabla_\perp P + \left(\nabla_\perp^2 + \frac{1}{\epsilon^2}\frac{\partial^2}{\partial Z^2}\right)\mathbf{U}_\perp, \tag{5.9a}$$

$$0 = -\frac{P_Z}{\epsilon} + \epsilon\left(\nabla_\perp^2 + \frac{1}{\epsilon^2}\frac{\partial^2}{\partial Z^2}\right)\hat{W}, \tag{5.9b}$$

$$\nabla_\perp \cdot \mathbf{U}_\perp + \hat{W}_Z = 0, \tag{5.9c}$$

$$\mathbf{0} = -\nabla_\perp p^u + \hat{\lambda}\epsilon^2\left(\nabla_\perp^2 + \frac{1}{\epsilon^2}\frac{\partial^2}{\partial Z^2}\right)\mathbf{u}_\perp{}^u + \gamma\mathbf{F}, \tag{5.9d}$$

$$0 = -\frac{p_Z^u}{\epsilon} + \epsilon^3\hat{\lambda}\left(\nabla_\perp^2 + \frac{1}{\epsilon^2}\frac{\partial^2}{\partial Z^2}\right)W^u, \tag{5.9e}$$

$$\nabla_\perp \cdot \mathbf{u}_\perp^u + W_Z^u = 0, \tag{5.9f}$$

$$\mathbf{0} = -\nabla_\perp p^e + \hat{\lambda}\epsilon^2\left(\nabla_\perp^2 + \frac{1}{\epsilon^2}\frac{\partial^2}{\partial Z^2}\right)\mathbf{u}_\perp{}^e + \mathbf{F}, \tag{5.9g}$$

$$0 = -\frac{p_Z^e}{\epsilon} + \epsilon^3\hat{\lambda}\left(\nabla_\perp^2 + \frac{1}{\epsilon^2}\frac{\partial^2}{\partial Z^2}\right)W^e, \tag{5.9h}$$

$$\nabla_\perp \cdot \mathbf{u}_\perp^e + W_Z^e = 0, \tag{5.9i}$$

where '⊥' denotes 'in the (x, y)−plane', with

$$\mathbf{u}^u = \mathbf{u}^e = -\mathbf{V}_\mathrm{p} \quad \text{on } Z = 0, \tag{5.10a}$$

$$\mathbf{u}^u = 0 \quad \text{on } Z = H_1, \tag{5.10b}$$

$$\mathbf{u}^e = \mathbf{U},\ \epsilon^2\hat{\lambda}\mathbf{u}^e_Z = \mathbf{U}_Z \quad \text{on } Z = 1, \tag{5.10c}$$

$$\mathbf{U}_Z = 0 \quad \text{on } Z = 1 + \bar{H}, \tag{5.10d}$$

$$\mathbf{U} \longrightarrow (1 - V_p)\hat{\mathbf{x}} \quad \text{as } r \longrightarrow \infty, \tag{5.10e}$$

$$\mathbf{U} = 0 \quad \text{on } r = 1, \tag{5.10f}$$

assuming $\mathbf{V}_p = V_p\hat{\mathbf{x}}$. We have assumed H_1 is uniform in $r > 1$ and, from scaling arguments, we obtain $H_1 = 1$. We allow H_1 to vary under the disk with $H_1(r = 1) = 1$. Since $\hat{\mathbf{n}}^m = \hat{\mathbf{r}}$ and $\hat{\mathbf{n}}^s = (\epsilon H_{1r}, 0, -1)$ we obtain

$$\sigma^m \cdot \hat{\mathbf{n}}^m = \begin{pmatrix} -P + 2U_r \\ r\left(V/r\right)_r + U_\theta/r \\ U_Z/\epsilon \end{pmatrix}, \tag{5.11}$$

and

$$\sigma^s \cdot \hat{\mathbf{n}}^s = \begin{pmatrix} -p^u\epsilon H_{1r} + \epsilon^2\hat{\lambda}\left(2u^u_r\epsilon H_{1r} - u^u_Z/\epsilon\right) \\ \epsilon^2\hat{\lambda}\left(\epsilon H_{1r}\left(r\left(v^u/r\right)_r + v_\theta/r\right) - v^u_Z/\epsilon\right) \\ p^u + \epsilon^2\hat{\lambda}\left(\epsilon H_{1r}u^u_Z/\epsilon\right) \end{pmatrix}. \tag{5.12}$$

We know $dA^* = r^*d\theta dz^* = \epsilon R^2 r d\theta dZ$ and $dS^* = r^*dr^*d\theta = R^2 r dr d\theta$, so (5.5) becomes

$$\begin{aligned} &\int_1^{1+\bar{H}}\int_0^{2\pi} \epsilon\left[\cos\theta\left(-P + 2U_r\right) - \sin\theta\left(r\left(\frac{V}{r}\right)_r + \frac{U_\theta}{r}\right)\right] r\Big|_{r=1} \, d\theta dZ = \\ &-\int_0^{2\pi}\int_0^1 \left[\cos\theta\left(-p^u\epsilon H_{1r} + \epsilon^2\hat{\lambda}\left(2u^u_r\epsilon H_{1r} - \frac{u^u_Z}{\epsilon}\right)\right) - \right. \\ &\qquad \left. \sin\theta\left(\epsilon^2\hat{\lambda}\left(\epsilon H_{1r}\left(r\left(\frac{v^u}{r}\right)_r + \frac{v_\theta}{r}\right) - \frac{v^u_Z}{\epsilon}\right)\right)\right] r\Big|_{Z=H_1} \, dr d\theta. \end{aligned} \tag{5.13}$$

Expansion

We expand the variables in powers of ϵ^2, letting

$$\mathbf{U}_\perp = \mathbf{U}_{\perp 0} + \epsilon^2 \mathbf{U}_{\perp 1} + \ldots, \quad \mathbf{u}_\perp{}^u = \mathbf{u}_{\perp 0}^u + \epsilon^2 \mathbf{u}_{\perp 1}^u + \ldots, \quad \mathbf{u}_\perp{}^e = \mathbf{u}_{\perp 0}^e + \epsilon^2 \mathbf{u}_{\perp 1}^e + \ldots,$$

$$\hat{W} = \hat{W}_0 + \epsilon^2 \hat{W}_1 + \ldots, \quad W^u = W_0^u + \epsilon^2 W_1^u + \ldots, \quad W^e = W_0^e + \epsilon^2 W_1^e + \ldots,$$

$$P = P_0 + \epsilon^2 P_1 + \ldots, \quad p^u = p_0^u + \epsilon^2 p_1^u + \ldots, \quad p^e = p_0^e + \epsilon^2 p_1^e + \ldots,$$

and now consider each problem in turn.

5.1.1 Leading Order in ϵ^2

At leading order the governing equations are (dropping the '$\perp$' notation for convenience),

$$\mathbf{U}_{0ZZ} = 0, \tag{5.14a}$$

$$0 = -P_{0Z} + \hat{W}_{0ZZ}, \tag{5.14b}$$

$$\nabla \cdot \mathbf{U}_0 + \hat{W}_{0Z} = 0, \tag{5.14c}$$

$$0 = -\nabla p_0^u + \hat{\lambda} \mathbf{u}_{0ZZ}^u + \gamma \mathbf{F}, \tag{5.14d}$$

$$0 = -p_{0Z}^u, \tag{5.14e}$$

$$\nabla \cdot \mathbf{u}_0^u + W_{0Z}^u = 0, \tag{5.14f}$$

$$0 = -\nabla p_0^e + \hat{\lambda} \mathbf{u}_{0ZZ}^e + \mathbf{F}, \tag{5.14g}$$

$$0 = -p_{0Z}^e, \tag{5.14h}$$

$$\nabla \cdot \mathbf{u}_0^e + W_{0Z}^e = 0, \tag{5.14i}$$

subject to

$$\mathbf{u}_0^u = \mathbf{u}_0^e = -\mathbf{V_p} \quad \text{on } Z = 0, \tag{5.15a}$$

$$\mathbf{u}_0^u = \mathbf{0} \quad \text{on } Z = H_1, \tag{5.15b}$$

$$\mathbf{u}_0^e = \mathbf{U}_0 \quad \text{on } Z = 1, \tag{5.15c}$$

$$\mathbf{U}_{0Z} = \mathbf{0} \quad \text{on } Z = 1, \tag{5.15d}$$

$$\mathbf{U}_{0Z} = \mathbf{0} \quad \text{on } Z = 1 + \bar{H}, \tag{5.15e}$$

$$\mathbf{U}_0 = \mathbf{0} \quad \text{on } r = 1, \tag{5.15f}$$

$$\mathbf{U}_0 \longrightarrow (1 - V_p)\hat{\mathbf{x}} \quad \text{as } r \longrightarrow \infty. \tag{5.15g}$$

Integrating (5.14a) twice with respect to Z with (5.15d) we obtain

$$\mathbf{U}_0 = \mathbf{U}_0(x, y), \tag{5.16}$$

for the flow in the mucus layer. Differentiating (5.14c) with respect to Z therefore gives $\hat{W}_{0ZZ} = 0$. Hence from (5.14b) we obtain

$$P_0 = P_0(x, y). \tag{5.17}$$

Integrating $\hat{W}_{0ZZ} = 0$ using $\hat{W}_0 = 0$ on $Z = H_1$ and on $Z = H_1 + \bar{H}$ (since we assume flat interfaces) we also obtain

$$\nabla \cdot \mathbf{U}_0 = 0.$$

Now we consider the leading–order flow in the serous layer. From (5.14e) and (5.14h) we know $p_0 = p_0(x, y)$ everywhere. Using the boundary conditions (5.15a—5.15c) we solve (5.14d) and (5.14g) to obtain

$$\mathbf{u}_0^u = \frac{1}{\hat{\lambda}} \left(\nabla p_0^u - \gamma \mathbf{F}\right) \left(\frac{Z^2}{2} - \frac{Z H_1}{2}\right) - \mathbf{V_p} \left(1 - \frac{Z}{H_1}\right) \tag{5.18}$$

for flow under the disk and

$$\mathbf{u}_0^e = \frac{1}{\hat{\lambda}} \left(\nabla p_0^e - \mathbf{F}\right) \left(\frac{Z^2}{2} - \frac{Z}{2}\right) + Z\mathbf{U}_0 - \mathbf{V_p} \left(1 - Z\right) \tag{5.19}$$

for flow outside the disk. Integrating (5.18) & (5.19) we obtain for the leading order flux

$$\mathbf{Q}_0^u = -\frac{1}{\hat{\lambda}} \left(\nabla p_0^u - \gamma \mathbf{F}\right) \frac{H_1^3}{12} - \frac{\mathbf{V_p} H_1}{2}, \tag{5.20}$$

$$\mathbf{Q}_0^e = -\frac{1}{\hat{\lambda}} \left(\nabla p_0^e - \mathbf{F}\right) \frac{1}{12} + \frac{\mathbf{U}_0}{2} - \frac{\mathbf{V_p}}{2}. \tag{5.21}$$

Imposing continuity of flux across $r = 1$, *i.e.* $\mathbf{Q}_0^u \cdot \hat{\mathbf{r}} = \mathbf{Q}_0^e \cdot \hat{\mathbf{r}}$, we obtain

$$\hat{\mathbf{r}} \cdot \nabla p_0^u - \hat{\mathbf{r}} \cdot \nabla p_0^e = (\gamma - 1) F \cos\theta, \quad \text{on } r = 1, \tag{5.22}$$

since $\hat{\mathbf{n}} = \hat{\mathbf{r}}$ and $\mathbf{U}_0 = 0$ on the disk. The continuity equation $H_{1t} + \nabla \cdot \mathbf{Q}_0 = 0$, since $Z = H_1$ is steady, gives

$$\nabla \cdot \left[-\frac{H_1^3}{12\hat{\lambda}} (\nabla p_0^u - \gamma \mathbf{F}) - \mathbf{V}_\mathrm{p} \frac{H_1}{2} \right] = 0, \tag{5.23}$$

$$\nabla \cdot \left[-\frac{1}{12\hat{\lambda}} (\nabla p_0^e - \mathbf{F}) + \frac{(\mathbf{U}_0 - \mathbf{V}_\mathrm{p})}{2} \right] = 0. \tag{5.24}$$

Since $\nabla \cdot \mathbf{U}_0 = 0$ and $\mathbf{V}_p$, $\mathbf{F}$ are (assumed) uniform, we can solve these equations for p_0 dependent on the form of H_1, *i.e.* the shape of the bottom of the disk. From (5.24) we obtain $\nabla^2 p_0^e = 0$ outside the disk. The shape of the disk and the nonuniformity of the ciliary beating (if $0 \leq \gamma < 1$) can create a pressure field in the serous layer which will in turn affect the mucus layer.

To find $\mathbf{U}_0$ we need to consider the equations in the mucus layer at the next order.

5.1.2 Next Order in the Mucus Layer

At next order in the mucus layer, (5.9a) yields

$$0 = -\nabla P_0 + \nabla^2 \mathbf{U}_0 + \mathbf{U}_{1ZZ}, \tag{5.25}$$

subject to boundary conditions (5.10c), (5.10d)

$$\mathbf{U}_{1Z} = \hat{\lambda} \mathbf{u}_{0Z}^e \quad \text{on } Z = 1, \tag{5.26}$$

$$\mathbf{U}_{1Z} = 0 \quad \text{on } Z = 1 + \bar{H}. \tag{5.27}$$

We integrate (5.25) with these boundary conditions. From (5.19) we know

$$\mathbf{u}_{0Z}^e \,|_{Z=1} = \frac{1}{2\hat{\lambda}} (\nabla p_0^e - \mathbf{F}) + \mathbf{U}_0 + \mathbf{V}_p, \tag{5.28}$$

and since P_0, $\mathbf{U}_0$ are uniform in Z, we obtain

$$-\nabla P_0 + \nabla^2 \mathbf{U}_0 = \frac{\hat{\lambda}}{\bar{H}} \left[\frac{1}{2\hat{\lambda}} (\nabla p_0^e - \mathbf{F}) + \mathbf{U}_0 + \mathbf{V}_p \right]. \tag{5.29}$$

We solve (5.29) and (5.14c) for $\mathbf{U}_0$ by letting

$$\mathbf{U}_0 = \frac{1}{r}\psi_\theta \hat{\mathbf{r}} - \psi_r \hat{\boldsymbol{\theta}}, \tag{5.30}$$

where ψ is a streamfunction, and so

$$\nabla^2 \mathbf{U}_0 = \nabla^2(\nabla\psi \times \hat{\mathbf{Z}}) = (\nabla_\perp \nabla_\perp^2 \psi) \times \hat{\mathbf{Z}},$$

$$\nabla \wedge \mathbf{U}_0 = -\nabla^2 \psi \hat{\mathbf{Z}}.$$

Taking the curl of (5.29) we obtain

$$\left(\nabla^2 - \alpha^2\right) \nabla^2 \psi = 0, \tag{5.31}$$

where $\alpha^2 = \hat{\lambda}/\bar{H}$. Equation (5.31) is satisfied by $\psi = \psi_1 + \psi_2$ where

$$\nabla^2 \psi_1 = 0, \quad (\nabla^2 - \alpha^2)\psi_2 = 0. \tag{5.32a,b}$$

The boundary conditions are

$$\psi = 0, \;\; \psi_r = 0, \quad \text{on } r = 1, \tag{5.33}$$

from (5.15f), and

$$\psi \longrightarrow (1 - V_p) r \sin\theta \;\; \text{as } r \longrightarrow \infty, \tag{5.34}$$

from (5.15g). From (5.34) we let $\psi_1 = F_1(r)\sin\theta$ and $\psi_2 = F_2(r)\sin\theta$, substitute into (5.32a,b) and solve to find F_1, F_2, and hence $\psi = f(r)\sin\theta$. We obtain

$$\psi = \left(\frac{a_1}{r} + a_2 r + a_3 \mathcal{I}_1(\alpha r) + a_4 \mathcal{K}_1(\alpha r)\right) \sin\theta, \tag{5.35}$$

where a_1, a_2, a_3, a_4 are constants to be determined and $\mathcal{I}_1$, $\mathcal{K}_1$ are Modified Bessel functions of order 1. From (5.34) we know that $a_2 = 1 - V_p$ and $a_3 = 0$ since $\mathcal{I}_1(\alpha r)$ is unbounded as $r \to \infty$. Using (5.33) we obtain

$$a_1 = -(1 - V_p)\left(\frac{2\mathcal{K}_1(\alpha)}{\alpha \mathcal{K}_0(\alpha)} + 1\right), \quad a_4 = \frac{2(1 - V_p)}{\alpha \mathcal{K}_0(\alpha)}. \tag{5.36}$$

Figure 5.3 shows the streamlines about the particle surface at $r = 1$. This result agrees with the analysis by Evans & Sackmann [76] of a disk moving in a liquid membrane adjacent to a rigid substrate.

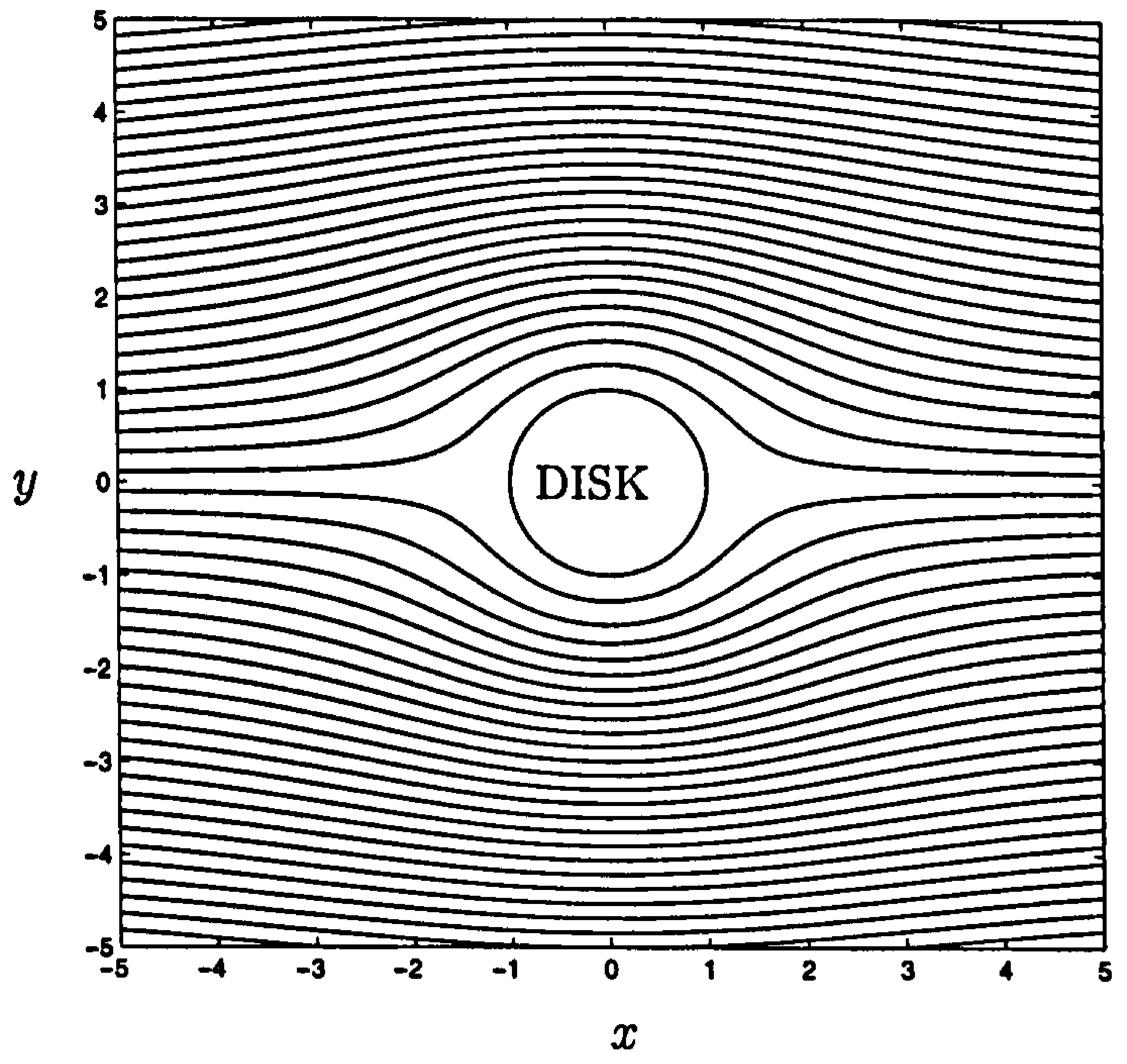

Figure 5.3: Streamlines in the mucus layer. The particle surface is at $r = 1$.

We want to find the speed of the particle $\mathbf{V}_p$. Given $H_1(r)$, the shape of the bottom of the particle, we can solve (5.23) and (5.24), subject to (5.22) and the condition that $p_0 \to 0$ as $r \to \infty$, to find the pressure field in the serous layer at leading order. Then, using the solution for $\mathbf{U}_0$ (from 5.35), we can solve (5.29) to find P_0, the pressure in the mucus layer. At leading order, the force balance integral (5.13) is

$$\int_1^{1+\bar{H}} \int_0^{2\pi} \left[\cos\theta\left(-P_0 + 2U_{0r}\right) - \sin\theta\left(r\left(\frac{V_0}{r}\right)_r + \frac{U_{0\theta}}{r}\right)\right] r\Big|_{r=1} d\theta dZ = \\ -\int_0^{2\pi} \int_0^1 \left[\cos\theta\left(-p_0^u H_{1r} - \hat{\lambda} u_{0Z}^u\right) + \sin\theta\left(\hat{\lambda} v_{0Z}^u\right)\right] r\Big|_{Z=H_1} drd\theta. \quad (5.37)$$

Substituting the calculated values into (5.37) will yield an equation for $\mathbf{V}_p$. In the next section we carry out this calculation, assuming that the base of the disk is almost flat.

5.2 Non-flat disk

In the previous section we set up the model for a particle with a base defined by the arbitrary function $H_1(r)$. We now consider the simplest case of a small perturbation to a flat-bottomed disk. We let $H_1 = 1 + \delta H_{11}(r)$ for $r \leq 1$ where $\delta \ll 1$ and $H_{11}(1) = 0$. For $r > 1$ $H_{11}(r) = 0$ (and so $H_{11}(r)$ describes the shape of the bottom of the particle). We expand the variables of the leading-order problem in powers of δ letting

$$\begin{aligned}
p_0^u &= p_{00}^u + \delta p_{01}^u + \cdots, & \mathbf{u}_0^u &= \mathbf{u}_{00}^u + \delta \mathbf{u}_{01}^u + \cdots, \\
p_0^e &= p_{00}^e + \delta p_{01}^e + \cdots, & \mathbf{u}_0^e &= \mathbf{u}_{00}^e + \delta \mathbf{u}_{01}^e + \cdots, \\
P_0 &= P_{00} + \delta P_{01} + \cdots, & \mathbf{U}_0 &= \mathbf{U}_{00} + \delta \mathbf{U}_{01} + \cdots, \\
\mathbf{V}_p &= \mathbf{V}_{p0} + \delta \mathbf{V}_{p1} + \cdots .
\end{aligned}$$

At leading order in δ the problem describes the case of a flat-based disk. At next order in δ the effects due to the disk protruding slightly into the serous layer are captured.

5.2.1 Serous Layer: Leading Order in δ

Since $\mathbf{F}$, $\mathbf{V}_p$ are uniform and $\nabla \cdot \mathbf{U}_0 = 0$, we obtain from (5.23) and (5.24),

$$\nabla^2 p_{00}^u = 0, \quad \nabla^2 p_{00}^e = 0. \tag{5.38a,b}$$

Letting $p_{00}^u = \tilde{p}^u \cos\theta$ and $p_{00}^e = \tilde{p}^e \cos\theta$ we obtain

$$\tilde{p}_{rr}^u + \frac{\tilde{p}_r^u}{r} - \frac{\tilde{p}^u}{r^2} = 0, \quad \tilde{p}_{rr}^e + \frac{\tilde{p}_r^e}{r} - \frac{\tilde{p}^e}{r^2} = 0. \tag{5.39a,b}$$

Using the boundary condition that $\tilde{p}^u$ must be well-behaved at $r = 0$, we integrate (5.39a) to get

$$\tilde{p}^u = b_1 r,$$

and using the boundary condition $\tilde{p}^e \to 0$ as $r \to \infty$, we integrate (5.39b) to obtain

$$\tilde{p}^e = \frac{b_2}{r}.$$

Imposing continuity of pressure at $r = 1$ and using the boundary condition (5.22) we obtain

$$p^u_{00} = \frac{(\gamma - 1)Fr}{2}\cos\theta, \quad 0 \le r < 1, \tag{5.40}$$

$$p^e_{00} = \frac{(\gamma - 1)F}{2r}\cos\theta, \quad r \ge 1. \tag{5.41}$$

If the cilia beneath the disk act uniformly ($\gamma = 1$) the pressure p_{00} is trivially zero. If ciliary function beneath the disk is impaired ($0 \le \gamma < 1$), an imbalance in ciliary fluxes demands a pressure gradient be generated to ensure incompressibility. The pressure gradient acts over long lengthscales outside the edge of the disk.

5.2.2 Mucus Layer: Leading Order in δ

From (5.29) we obtain

$$-\nabla P_{00} + \nabla^2 \mathbf{U}_{00} = \frac{\hat{\lambda}}{\bar{H}}\left[\frac{1}{2\hat{\lambda}}\left(\nabla p^e_{00} - \mathbf{F}\right) + \mathbf{U}_{00} + \mathbf{V}_{p0}\right]. \tag{5.42}$$

As before, we let

$$\mathbf{U}_{00} = \frac{1}{r}\psi_{0\theta}\hat{\mathbf{r}} - \psi_{0r}\hat{\boldsymbol{\theta}},$$

and solving (5.42) as in §5.1.2 we obtain $\psi_0 = f(r)\sin\theta$ where

$$f(r) = (1 - V_{p0})\left(-\frac{1}{r}\left(\frac{2\mathcal{K}_1(\alpha)}{\alpha\mathcal{K}_0(\alpha)} + 1\right) + r + \frac{2}{\alpha\mathcal{K}_0(\alpha)}\mathcal{K}_1(\alpha r)\right), \tag{5.43}$$

and $\alpha^2 = \hat{\lambda}/\bar{H}$. The two components of (5.42) are

$$\left(\frac{\nabla^2\psi_0}{r}\right)_\theta - P_{00r} = \alpha^2\left(\frac{1}{r}\psi_{0\theta} + V_{p0}\cos\theta\right) + \frac{1}{2\bar{H}}\left(p^e_{00r} - F\cos\theta\right), \tag{5.44}$$

$$-\left(\nabla^2\psi_0\right)_r - \frac{1}{r}P_{00\theta} = \alpha^2\left(-\psi_{0r} - V_{p0}\sin\theta\right) + \frac{1}{2\bar{H}}\left(\frac{1}{r}p^e_{00\theta} + F\sin\theta\right). \tag{5.45}$$

Integrating (5.45) with respect to θ, then differentiating with respect to r and comparing with (5.44) we obtain

$$P_{00} = \left(rf''' + f'' - \frac{2f'}{r} + \frac{2f}{r^2}\right)\cos\theta - \alpha^2(rf' + rV_{p0})\cos\theta - \frac{1}{2\bar{H}}(p^e_{00} - rF\cos\theta). \tag{5.46}$$

From (5.37) the force balance integral at leading order in δ is

$$\int_1^{1+\bar{H}} \int_0^{2\pi} \left[\cos\theta\,(-P_{00} + 2U_{00r}) - \sin\theta \left(r \left(\frac{V_{00}}{r} \right)_r + \frac{U_{00\theta}}{r} \right) \right] r \Big|_{r=1} \, d\theta dZ =$$
$$- \int_0^{2\pi} \int_0^1 \left[\cos\theta \left(-\hat{\lambda} u^u_{00Z} \right) + \sin\theta \left(\hat{\lambda} v^u_{00Z} \right) \right] r \Big|_{Z=1} \, dr d\theta. \qquad (5.47)$$

From (5.18) we know

$$\mathbf{u}^u_{00Z} = \frac{1}{\hat{\lambda}} (\nabla p^u_{00} - \gamma \mathbf{F}) \left(Z - \frac{1}{2} \right) + \mathbf{V}_{p0}. \qquad (5.48)$$

Using (5.40), (5.41) and (5.48), (5.47) becomes

$$-\bar{H}\pi \left(\alpha^2 V_{p0} - 4(1 - V_{p0})\alpha \frac{\mathcal{K}_1(\alpha)}{\mathcal{K}_0(\alpha)} - 2\alpha^2 + \frac{F}{2\bar{H}} - \frac{1}{4\bar{H}}(\gamma - 1)F \right) =$$
$$\frac{\pi}{2} \left(\frac{(\gamma - 1)F}{2} - \gamma F + 2V_{p0}\hat{\lambda} \right). \qquad (5.49)$$

Rearranging (5.49) we obtain

$$V_{p0} = 1 + \frac{(\gamma - 1)F}{4\bar{H}\alpha^2} \left(1 + \frac{2\mathcal{K}_1(\alpha)}{\alpha \mathcal{K}_0(\alpha)} \right)^{-1}. \qquad (5.50)$$

Therefore, if $\gamma = 1$, the disk moves at the same speed as the mucus, as a uniformly translating slab of material. The disk slows relative to mucus if the cilia beneath the disk do not beat efficiently ($0 \leq \gamma < 1$).

In this model we have assumed that the net force on the particle (D, say) is zero. From (5.49) we know that, in the absence of ciliary effects,

$$D = -\bar{H}\pi \left(2\alpha^2 V_{p0} + 4V_{p0}\alpha \frac{\mathcal{K}_1(\alpha)}{\mathcal{K}_0(\alpha)} \right), \qquad (5.51)$$

i.e. $F = 0$ and $\mathbf{U} = -\mathbf{V}_{p0}$ in the far field. In dimensional variables this can be written

$$D^* = -4\mu\pi V^*_{p0}\bar{h}^* \left(\frac{1}{2}\alpha^2 + \frac{\alpha \mathcal{K}_1(\alpha)}{\mathcal{K}_0(\alpha)} \right),$$

where $D^* = \mu\tilde{U}RD\epsilon$ (using (5.13)). This dimensional force on a disk moving across the serous layer agrees with the analysis of Stone & Ajdari [73] and

Evans & Sackmann [76] for the force on a membrane-trapped particle above a thin sublayer.

We now see how the leading-order speed of the particle changes if the base of the particle is assumed not to be flat.

5.2.3 Serous Layer: $O(\delta)$

Since $\mathbf{F}$, $\mathbf{V}_p$ are uniform and $\nabla \cdot \mathbf{U}_0 = 0$, at $O(\delta)$ (5.23) & (5.24) become

$$\frac{1}{12\hat{\lambda}}\nabla^2 p^u_{01} = -\frac{1}{4\hat{\lambda}}\left(\nabla H_{11} \cdot \nabla p^u_{00} - \gamma \mathbf{F} \cdot \nabla H_{11}\right) - \frac{\mathbf{V}_{p0}}{2} \cdot \nabla H_{11}, \qquad (5.52)$$

$$\frac{1}{12\hat{\lambda}}\nabla^2 p^e_{01} = 0, \qquad (5.53)$$

since $H_{11} = 0$ outside the disk. Letting $p_{01} = \tilde{p}(r)\cos\theta$ we obtain

$$\tilde{p}_{rr} + \frac{\tilde{p}_r}{r} - \frac{\tilde{p}}{r^2} = C_1 H_{11r}, \quad 0 \le r < 1, \qquad (5.54)$$

$$\tilde{p}_{rr} + \frac{\tilde{p}_r}{r} - \frac{\tilde{p}}{r^2} = 0, \quad r \ge 1, \qquad (5.55)$$

where $C_1 = (5\gamma + 1)F/2 - 6V_{p0}\hat{\lambda}$. Using the boundary condition that $\tilde{p}$ must be well-behaved at $r = 0$, we integrate (5.54) to get

$$\tilde{p} = \frac{C_1}{r}\int_0^r H_{11}(r')r'\,dr' + \frac{b_3 r}{2}, \quad 0 \le r < 1, \qquad (5.56)$$

and using the boundary condition $\tilde{p} \to 0$ as $r \to \infty$, we integrate (5.55) to obtain

$$\tilde{p} = \frac{b_4}{r}, \quad r \ge 1, \qquad (5.57)$$

where b_3, b_4 are constants. Imposing continuity of pressure and pressure gradient (from (5.22) at $O(\delta)$) at $r = 1$ gives

$$b_3 = 0, \qquad b_4 = C_1 \int_0^1 H_{11}(r) r\,dr. \qquad (5.58)$$

Physically, the nonuniform disk sliding over the serous layer generates a pressure gradient beneath the disk, that again extends out beyond the disk into the serous layer beneath the mucus.

5.2.4 Mucus Layer: $\mathrm{O}(\delta)$

From (5.29) at $\mathrm{O}(\delta)$ we obtain

$$-\nabla P_{01}+\nabla^2\mathbf{U}_{01}=\frac{\hat{\lambda}}{\bar{H}}\left[\frac{1}{2\hat{\lambda}}\nabla p^e_{01}+\mathbf{U}_{01}+\mathbf{V}_{p1}\right]. \tag{5.59}$$

As before, we let $\mathbf{U}_{01}=\frac{1}{r}\psi_{1\theta}\hat{\mathbf{r}}-\psi_{1r}\hat{\boldsymbol{\theta}}$, where ψ_1 is a streamfunction. Solving (5.59) as in §5.1.2 with

$$\mathbf{U}_{01}=0 \quad \text{on } r=1, \tag{5.60}$$

$$\mathbf{U}_{01}\longrightarrow -V_{p1}\hat{\mathbf{x}}, \quad \text{as } r\longrightarrow\infty, \tag{5.61}$$

we obtain

$$\psi_1=\left(\frac{V_{p1}}{r}\left(\frac{2\mathcal{K}_1(\alpha)}{\alpha\mathcal{K}_0(\alpha)}+1\right)-V_{p1}r-\frac{2V_{p1}}{\alpha\mathcal{K}_0(\alpha)}\mathcal{K}_1(\alpha r)\right)\sin\theta. \tag{5.62}$$

The two components of (5.59) are therefore

$$\left(\frac{\nabla^2\psi_1}{r}\right)_\theta-P_{01r}=\alpha^2\left(\frac{1}{r}\psi_{1\theta}+V_{p1}\cos\theta\right)+\frac{1}{2\bar{H}}\left(p^e_{01r}\right) \tag{5.63}$$

$$-\left(\nabla^2\psi_1\right)_r-\frac{1}{r}P_{01\theta}=\alpha^2\left(-\psi_{1r}-V_{p1}\sin\theta\right)+\frac{1}{2\bar{H}}\left(\frac{1}{r}p^e_{01\theta}\right) \tag{5.64}$$

Integrating (5.64) with respect to θ, then differentiating with respect to r and comparing with (5.63), we obtain

$$P_{01}=\left(rf'''+f''-\frac{2f'}{r}+\frac{2f}{r^2}\right)\cos\theta-\alpha^2\left(rf'+rV_{p1}\right)\cos\theta-\frac{1}{2\bar{H}}p^e_{01}. \tag{5.65}$$

From (5.37) the force balance integral at $\mathrm{O}(\delta)$ is

$$\begin{aligned}\int_1^{1+\bar{H}}\int_0^{2\pi}\left[\cos\theta\left(-P_{01}+2U_{01r}\right)-\sin\theta\left(r\left(\frac{V_{01}}{r}\right)_r+\frac{U_{01\theta}}{r}\right)\right]r\Big|_{r=1}\,d\theta dZ=\\ -\int_0^{2\pi}\int_0^1\left(\left[\cos\theta\left(-p^u_{00}H_{11r}-\hat{\lambda}u^u_{01Z}\right)+\sin\theta\left(\hat{\lambda}v^u_{01Z}\right)\right]r\Big|_{Z=1}+\right.\\ \left.H_{11}(r)\left[\cos\theta\left(-\hat{\lambda}u^u_{00ZZ}\right)+\sin\theta\left(\hat{\lambda}v^u_{00ZZ}\right)\right]r\Big|_{Z=1}\right)\,drd\theta.\end{aligned} \tag{5.66}$$

From (5.18) at $\mathrm{O}(\delta)$ we obtain

$$\mathbf{u}^u_{01Z}=\frac{1}{\hat{\lambda}}\left(\nabla p^u_{01}\left(Z-\frac{1}{2}\right)+\frac{H_{11}}{2}\left(\gamma\mathrm{F}-\nabla p^u_{00}\right)\right)+\mathbf{V}_{p1}, \tag{5.67}$$

and from (5.48) we obtain

$$\mathbf{u}^u_{00ZZ} = \frac{1}{\hat{\lambda}} \left(\nabla p^u_{00} - \gamma \mathbf{F}\right). \tag{5.68}$$

We know from the O(δ) problem in the serous layer that

$$p^u_{01} = \left(\frac{C_1}{r} \int_0^r H_{11}(r')r'\,dr'\right)\cos\theta, \quad p^e_{01} = \left(\frac{C_1}{r} \int_0^1 H_{11}(r)r\,dr\right)\cos\theta, \tag{5.69}$$

where $C_1 = (5\gamma + 1)F/2 - 6\hat{\lambda}V_{p0}$, and we determined p^u_{00} and p^e_{00} from (5.40) & (5.41) respectively. Substituting into (5.66) and integrating we obtain

$$\begin{aligned}
-\bar{H}\pi\left(4\alpha V_{p1}\frac{\mathcal{K}_1(\alpha)}{\mathcal{K}_0(\alpha)} + \alpha^2 V_{p1} - \frac{C_1}{2\bar{H}}\int_0^1 H_{11}(r)r\,dr\right) &= \\
\frac{\pi C_1}{2}\int_0^1 H_{11}(r)r\,dr - \gamma F\pi \int_0^1 H_{11}(r)r\,dr + \hat{\lambda}V_{p1}\pi & \\
+\frac{(\gamma-1)F\pi}{2}\left(\int_0^1 r^2 H_{11r}(r)\,dr + \int_0^1 H_{11}(r)r\,dr\right), &
\end{aligned} \tag{5.70}$$

which can be rearranged to give

$$V_{p1} = \frac{(3\gamma - 1)F}{4\bar{H}\alpha^2}\left(1 + \frac{2\mathcal{K}_1(\alpha)}{\alpha\mathcal{K}_0(\alpha)}\right)^{-1} \int_0^1 H_{11}(r)r\,dr \tag{5.71}$$

Combining (5.50) and (5.71) we obtain

$$\begin{aligned}
V_p = 1 + \frac{(\gamma-1)F}{4\bar{H}\alpha^2}&\left(1 + \frac{2\mathcal{K}_1(\alpha)}{\alpha\mathcal{K}_0(\alpha)}\right)^{-1} \\
&+\frac{\delta(3\gamma-1)F}{4\bar{H}\alpha^2}\left(1 + \frac{2\mathcal{K}_1(\alpha)}{\alpha\mathcal{K}_0(\alpha)}\right)^{-1}\int_0^1 H_{11}(r)r\,dr.
\end{aligned} \tag{5.72}$$

From (5.42) in the far field we know $F = 2\hat{\lambda}$ (since $U_{00} \to 1 - V_{p0}$ as $r \to \infty$). Therefore, in dimensional variables, $\tilde{U} = F^* h^{*2}_{10}/2\mu\lambda$ and so, (5.72) becomes (in dimensional variables),

$$\begin{aligned}
V_p^* = \tilde{U}\Bigg[1 + \frac{(\gamma-1)}{2}&\left(1 + \frac{2\mathcal{K}_1(\alpha)}{\alpha\mathcal{K}_0(\alpha)}\right)^{-1} \\
&+\frac{\delta(3\gamma-1)}{2}\left(1 + \frac{2\mathcal{K}_1(\alpha)}{\alpha\mathcal{K}_0(\alpha)}\right)^{-1}\int_0^1 H_{11}(r)r\,dr\Bigg],
\end{aligned} \tag{5.73}$$

where the dimensionless ratio $\alpha^2 = \lambda R^2/h^*_{10}\bar{h}^*$ (expressed in dimensional variables).

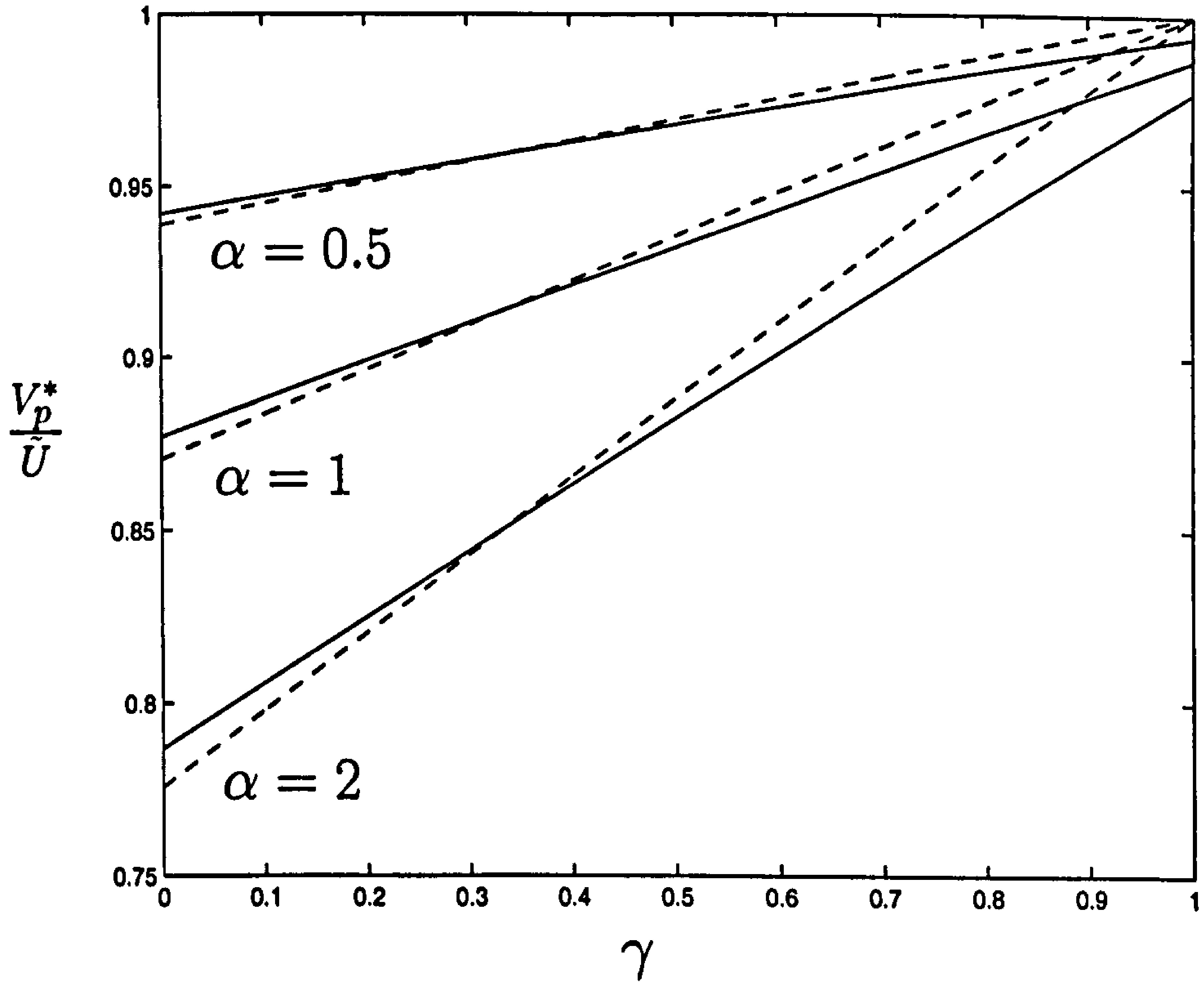

Figure 5.4: Speed of the disk against γ, the cilia activity, for various α, where $\delta = 0$ (dotted lines) and $\delta = 0.2$ (solid lines).

5.2.5 Discussion

Figure 5.4 shows the dependence of the disk speed on γ, the cilia reactivity, for various values of α. We let $H_{11}(r) = -1 + r^2$ so that the integral in (5.73) is equal to $-1/4$. In the simplest case when the disk is flat ($\delta = 0$), and the cilia function is unaffected ($\gamma = 1$), we see $V_p^* = \tilde{U}$, and the particle moves at the same speed as the mucus, as expected. If the particle protrudes into the serous layer, *i.e.* $\delta \neq 0$, (when $\gamma = 1$) then the integral in (5.73) is negative and the speed of the particle is reduced due to the increased drag of the disk moving over the serous layer.

Now consider the case $\gamma = 0$, where ciliary function beneath the disk is totally inhibited (see Figure 5.5). When the disk is flat the particle moves

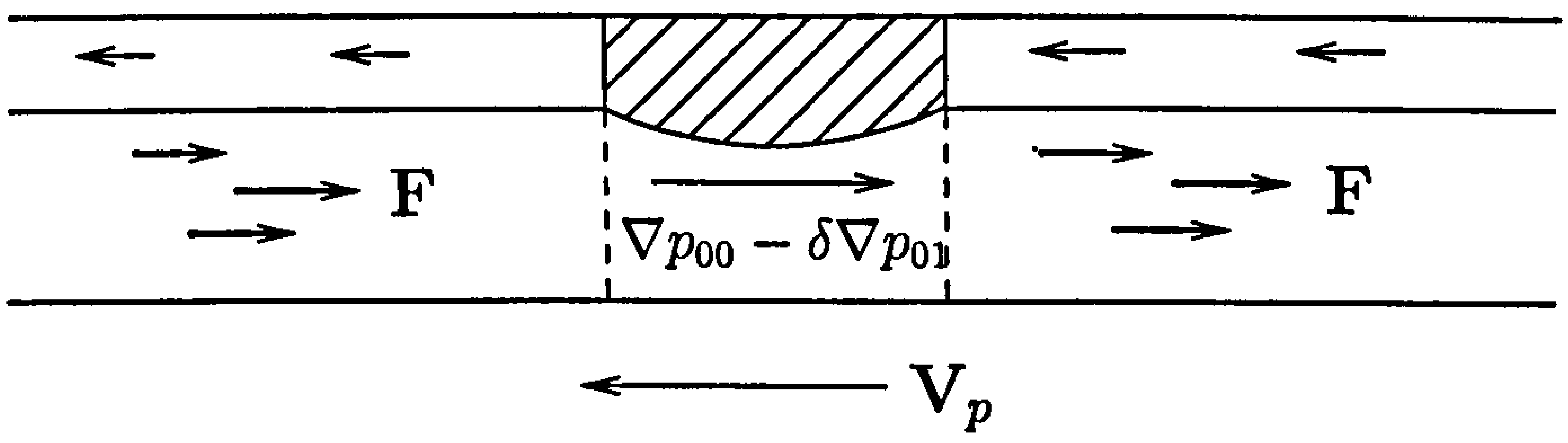

Figure 5.5: Sketch of the flow in the two layers when $\gamma = 0$.

slower than the speed of the undisturbed mucus. When $\delta \neq 0$, the presence of a non-flat disk appears to increase the particle speed relative to the flat-disk case. The reason for this is as follows. Continuity of flux under the particle requires a pressure-gradient-driven flow to be induced in the direction of ciliary motion, to balance the ciliary-driven flux outside the disk. When $\delta \neq 0$ and the particle protrudes into the sublayer, this leading-order pressure gradient must increase in magnitude to maintain the same flux, due to the narrowing of the gap beneath the particle. There is an increase of the shear stress on the particle and hence V_p^* increases. A $O(\delta)$ pressure gradient in the opposing direction is generated, due to an increase in drag from the protrusion moving over the serous layer; however this is small relative to the leading-order pressure gradient.

Figure 5.6 shows the speed of the disk against α for various values of γ, comparing the flat-disk case, $\delta = 0$, and the non-flat case, $\delta = 0.2$. As before we let $H_{11}(r) = -1 + r^2$. The relative speed of the disk falls as α increases. For $\gamma > 1/3$, the perturbation of the disk base slows the disk (relative to the flat-disk case); for $\gamma < 1/3$, the perturbation of the base increases the disk speed. However velocity reductions when $\delta \neq 0$ are relatively small. The parameter α can be written $\alpha = R/(\sqrt{h_{10}^* h^*}/\sqrt{\lambda}) = R/L$, say. Motion of the mucus layer creates a two-layer structure around the disk (see Figure 5.7). For $\alpha \gg 1$, a boundary layer of thickness $L \ll R$ forms around the disk; for

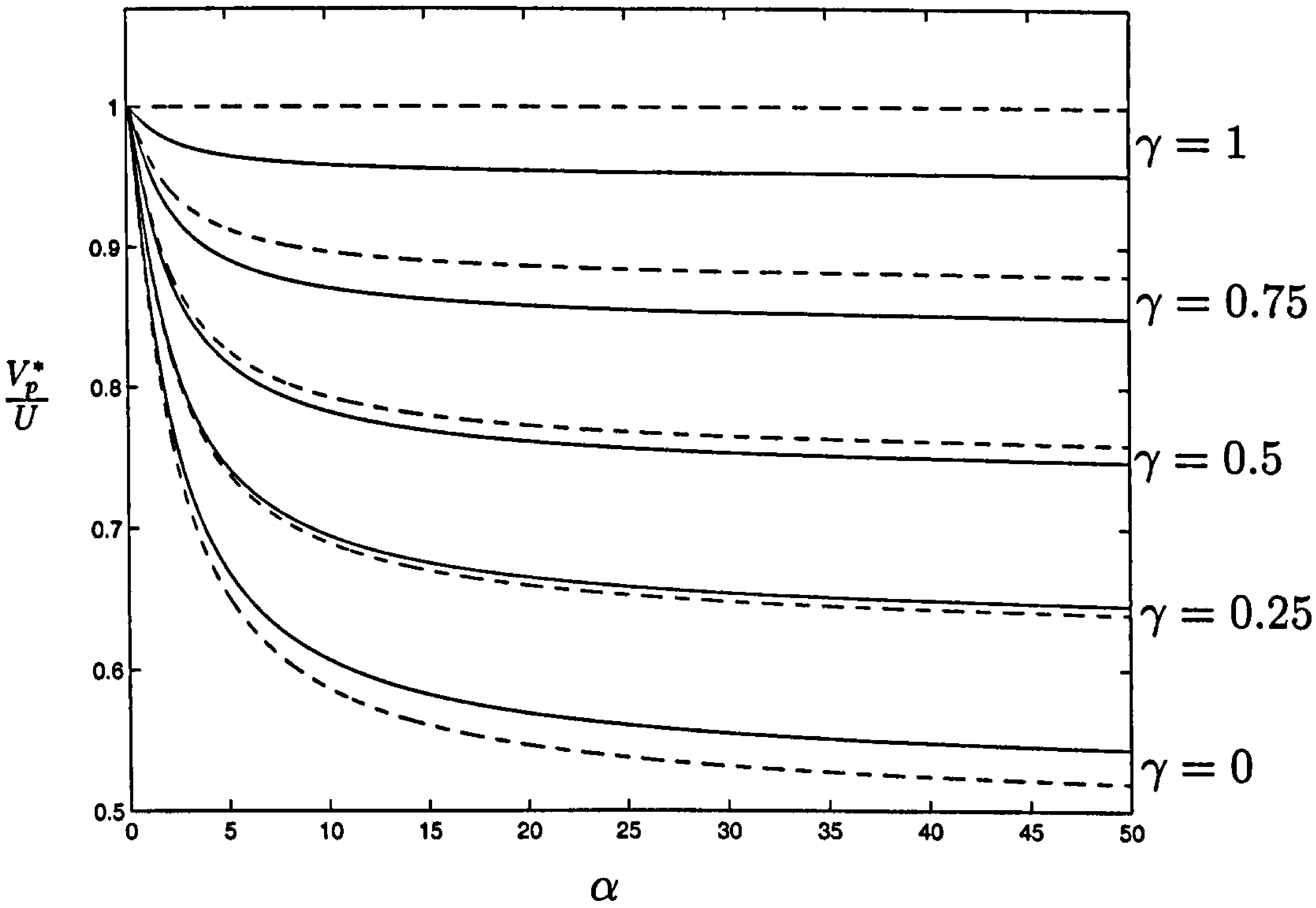

Figure 5.6: Speed of the disk for varying γ, the effect of the particle on cilia function. Dotted lines correspond to $\delta = 0$ flat-bottomed disk, solid lines correspond to $\delta = 0.2$ the disk protrudes slightly into the serous layer.

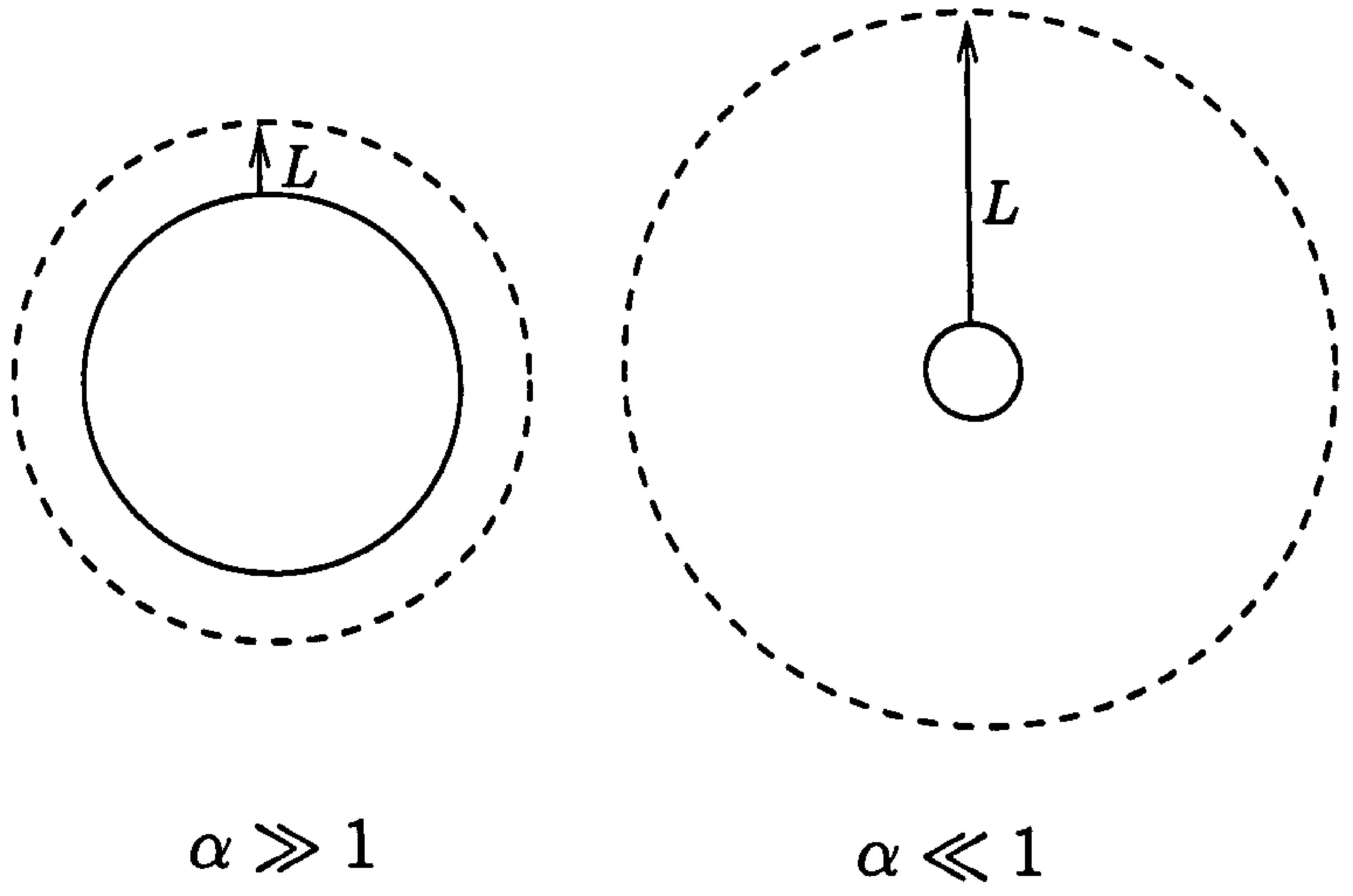

Figure 5.7: Sketch of the two-layer structure around the disk for small and large α.

$\alpha \ll 1$, the disk drives mucus motion over a long lengthscale $L \gg R$. In the layer adjacent to the disk the dominant resistance to motion comes from in-plane shearing of mucus, whereas outside the layer the dominant resistance comes from shear of the serous layer as the mucus moves over it. For large α, which corresponds to a large particle or large λ (more viscous sublayer), the motion of the particle is dominated by the serous layer resistance. For small α, which corresponds to small particles or small λ (less viscous sublayer), the motion of the particle is dominated by the mucus resistance to in-plane shear.

If α is small then

$$\mathcal{K}_0(\alpha) \sim -\ln\alpha, \quad \mathcal{K}_1(\alpha) \sim \frac{1}{\alpha},$$

and so the denominator in (5.73) grows like $1/(\alpha^2 \ln\alpha)$. Therefore, for small α, the disk speed is equal to the mucus speed $V_p^* = \tilde{U}$ regardless of the shape of the disk or the effect of the disk on the cilia, as expected.

For large α we know

$$\mathcal{K}_0(\alpha) \sim \mathcal{K}_1(\alpha) \sim \sqrt{\frac{\pi}{2\alpha}}e^{-\alpha},$$

and so we obtain

$$V_p^* \approx \tilde{U}\left[1 + \frac{(\gamma-1)}{2} + \frac{\delta(3\gamma-1)}{2}\int_0^1 H_{11}(r)r\,dr\right].$$

Taking parameter values $h_{10}^* = \bar{h}^* \approx 5\mu m$ and $\lambda \approx 0.01$ from Table 1.1, we obtain $L = \sqrt{(h_{10}^*\bar{h}^*/\lambda)} \approx 50\mu m$. For $R \ll 50\mu m$ (as would be the case for most inhaled particles) we therefore have $\alpha = R/L \ll 1$. The motion of the particle trapped in a mucus sheet is dominated by the stresses existing within the mucus layer rather than by the drag created as the particle moves over the serous layer. From Figures 5.4 & 5.6 we see that for small α the disk is transported at close to the speed of the undisturbed mucus, *i.e.* $V_p^*/\tilde{U} \approx 1$. This is true even for $\gamma = 0$, when the cilia under the disk are inoperative, and when $\delta \neq 0$ and the disk is not perfectly flat. We obviously have a constraint on the parameters such that $R \gg h_{10}^*$ for the lubrication theory assumptions to be valid. Also if $L \gg R$ we cannot ignore finite-size effects such as the curvature of the airway wall.

In this model we have assumed that the net (dimensionless) force, D, on the particle is zero. From (5.49) we have

$$-\bar{H}\pi\left(2\alpha^2 V_{p0} - 4(1-V_{p0})\alpha\frac{\mathcal{K}_1(\alpha)}{\mathcal{K}_0(\alpha)} - 2\alpha^2 - \frac{(\gamma-1)F}{2\bar{H}}\right) = D. \tag{5.74}$$

Here we briefly consider the motion of a particle trapped in the mucus layer, when the particle comes into close proximity with the epithelium, so that the drag, D, will rise dramatically. We take $\gamma = 1$, so cilia beneath the particle are unaffected and for simplicity we neglect induced pressure gradients in the serous layer. Equation (5.74) becomes

$$V_{p0} = 1 - \frac{D}{2\bar{H}\pi\alpha^2}\left(1 + \frac{2\mathcal{K}_1(\alpha)}{\alpha\mathcal{K}_0(\alpha)}\right)^{-1}. \tag{5.75}$$

In the large α limit, (5.75) becomes, in dimensional variables,

$$V_{p0}^* = \tilde{U} - \frac{D^* h_{10}^*}{2\mu\lambda\pi R^2}. \tag{5.76}$$

For the drag on the particle to appreciably stop the particle's motion we require $D^* \sim \mu\pi\lambda R^2/h_{10}^*$. From (4.57) we know that the force on a sphere translating close to a plane wall is $O(\mu\pi\lambda R)$. Therefore we need $R \gg h_{10}$ for good mobility of the particle, which is satisfied by the assumptions of lubrication theory.

5.3 Summary and Conclusions

In this chapter we consider the motion of a particle trapped in a mucus layer which is propelled by cilia acting in the underlying serous layer. We model this as a disk moving within a viscous sheet where a less viscous underlying layer is subject to a uniform body force representing the cilia. We prescribe the shape of the disk base and assume all other horizontal interfaces are flat. We include a parameter representing the effect of the particle on the movement of the cilia beneath it. We neglect gravitational and inertial effects and the curvature of the airway wall.

Using lubrication theory we find the flow and pressure fields in the serous layer and then find the resultant coupled flow in the mucus. We assume zero net force acting on the particle, which requires a balance between the resistance from the in-plane shear stress in the mucus and the drag from the disk moving over the serous layer. We perform the calculations, initially for a flat-based disk and then for a small perturbation to a flat disk where the base protrudes slightly into the serous layer. Using the force balance we find the speed of the particle as a function of the size and shape of the particle, the thickness and viscosity of the layers and the body force acting on the serous layer. The model assumptions are chosen to allow a fully rational theory, amenable to analysis. To treat particles of arbitrary shape properly would require further numerical studies.

We consider the particle speed for various values of the parameters. For a flat disk, when $\gamma = 1$, and the cilia are unaffected by the particle, the disk travels at the undisturbed speed of the mucus. As γ decreases to zero and the cilia become inoperative the disk speed is reduced. For $\gamma > 1/3$, the disk protruding into the serous layer will further reduce the disk speed; however when $\gamma < 1/3$ and the disk protrudes into the serous layer the disk speed is increased slightly compared to the flat-disk case.

For large particles or very viscous sublayers the dominant resistance to motion is from the disk moving over the sublayer. For small particles or less viscous sublayers the dominant resistance is from in-plane shear in the mucus. In the airways we expect the latter case to apply where serous layer drag is less important, although biological parameters may vary widely, particularly in disease, so that a wide spectrum of behaviour may occur at various times. We see that the disk moves at speeds close to that of the mucus regardless of disk shape or cilia reactivity. Our model predicts that the mucus will transport a trapped particle regardless of its shape or effect on cilia making it an extremely effective clearance mechanism.

This problem extends existing models of disks trapped in viscous sheets to consider perturbations to the disk shape and the effect of the disk on local ciliary function. We show that these effects can create a pressure field in the serous layer which acts over long lengthscales, which in turn will affect the mucus layer behaviour. However many simplifying assumptions have been made to allow the problem to be considered analytically. For example, the model assumes the disk is almost flat but transport may be very different if the particle gets close to the epithelium. In order to make more accurate predictions of particle transport via the mucociliary escalator we would need to relax some of our model assumptions. Some possible improvements that could be made are discussed below.

An important extension is to consider a more accurate representation of cilia which takes into account the non-uniformity of their propulsive force and the unsteadiness of the beat cycle. We need to know how much the spatiotemporal distribution of the forcing matters compared to a net forcing. Previous models of cilia-propelled mucus transport have treated cilia explicitly [20, 22]. We need to determine how spatial and temporal averaging of individual cilia relates to our assumed uniform body force. In many cases it is also likely that the cilia tips penetrate the mucus, which may have a large impact on the flow structure.

We have assumed interfaces to be flat which, despite high surface tension in the lungs, is unlikely to occur. It would be interesting to allow the serous/mucus interface and in particular, the mucus/air interface to move normally as well as transversely and to consider what happens to the mucus around the disk.

We have used a disk with small perturbations as a model for a trapped particle. It would be informative to consider other shapes, such as spheres or long fibres. Another improvement would be to consider the visco-elastic properties of mucus, rather than modelling it as a viscous Newtonian fluid. As previously mentioned, in airways the motion of the disk is affected by a large area of the surrounding mucus and therefore wall curvature effects may become important, especially in the smaller airways.

An interesting extension to this model would be to look at two or more particles trapped in a mucus sheet and determine under what conditions such particles may affect each other's behaviour. In particular, we would like to determine if trapped particles will be subject to an attractive force and aggregate to form clusters.

Chapter 6

Summary and Conclusions

Many particles become trapped in the liquid-lining of the lung airways during breathing. Understanding the subsequent fate of these particles is very important not only in relation to their role in the pathogenesis of lung disease but increasingly in the development of effective drug delivery by aerosol. In order to understand a particle's potential effect on health we need to consider the speed and direction of deposited particles' motion relative to the airway wall surface as a result of various forces, and to understand physical mechanisms underlying routes of clearance from the lungs.

In this thesis we have used theoretical fluid dynamics to consider three model problems motivated by existing studies of particle deposition in lungs. First we investigated the idea that, in the alveoli, deposited particles may be transported, not only by surface tension-driven flows, but also by capillary action and pressure gradients in the substrate towards areas with greater amounts of subphase materials such as alveolar corners. This may facilitate clearance, as it is known that macrophages preferentially inhabit these areas [45]. In Chapter 2 we considered a model of a deposited particle moving within a fluid-filled alveolar corner. It has been shown that surface forces can displace particles into the fluid layer with sufficient force to indent underlying epithelial cells [45]. In Chapters 3 and 4 we considered a model of a particle moving near to a deformable wall, in both perpendicular and transverse directions relative to the surface. The quickest method of particle clearance from the lungs is via the mucociliary escalator. Trapped particles in the mucus layer are transported towards the pharynx as the cilia in the underlying serous layer propel the mucus [18]. Several models have been suggested for the ciliary propulsion of mucus sheets [15, 17, 20, 23], and in Chapter 5 we considered a model of a particle trapped within a cilia-propelled mucus sheet.

In Chapter 2 we considered the problem of a two-dimensional cylinder partially immersed in a liquid pool in the corner of a rigid-walled wedge. We found that the problem requires a matching between capillary statics in the bulk fluid and viscous forces, modelled using lubrication theory, in the thin gap between the particle and the wall. The direction of motion of the particle subject to these forces is non-intuitive and depends on the particle radius a, the volume of fluid V, the wedge angle α and the site of initial particle deposition within the wedge. Given values for the parameters a, V, α, the problem falls into one of four different categories of particle behaviour where we can predict, for any initial position, whether a particle will move to the corner, become submerged, move to the contact line or move to a stable equilibrium point. Therefore we can calculate under what conditions a particle will have an increased likelihood of coming into contact with macrophages in the alveolar corner pool and being removed from the lungs, in particular we can determine the effect of particle size. In the case of inhaled drug therapies there may be potential for developing aerosols with particle size such that the retention time before clearance is optimised.

In Chapters 3 and 4 we considered the problem of a two-dimensional cylinder moving perpendicularly and transversely to a nearby deformable surface through a viscous fluid, where the surface is modelled using a simple linear springs model. Using elastohydrodynamics and lubrication theory in the thin gap between the particle and the wall we derived an evolution equation for the gap thickness and hence calculated the force acting on the particle.

When the particle is subject to a perpendicular displacement into the wall, the presence of the fluid film between the particle and the wall causes a transient overshoot in the force acting on the particle. A similar overshoot (in magnitude) occurs when the particle is pulled away from the wall; when the particle moves, the wall is pulled upwards behind it creating a transient negative or 'suction' force on the particle. When the particle is pushed sideways parallel to the wall a region of high pressure is created in front of the particle which causes the wall to bulge downwards. Behind the particle a region of low pressure causes the wall to be 'sucked up' creating a corner. This corner formation is sharpest immediately following initial displacement. This 'necking' effect behind the particle is similar to that found by Lighthill [56] in studies of pellets in elastic tubes and in industrial roll coating applications [60].

In Chapter 4 we also extended the model into three dimensions, considering the motion of a spherical particle parallel to a deformable plane. As in the 2D model we observed a bulge of the wall in front of the particle and the formation of a corner behind it. The wall deformation creates a lift force on the particle which increases as the deformation increases. Similarly the transverse force on the particle increases as the deformation increases, in comparison to the rigid-wall limit calculated by O'Neill & Stewartson [50].

For both perpendicular and transverse particle motion the resulting wall deformation has a significant effect on the force acting on the particle and hence on its subsequent fate. This analysis may have applications to many areas of study in addition to our model problem of a particle in the lung.

In Chapter 5 we considered the motion of a particle trapped in a mucus layer which is propelled by cilia within an underlying serous layer. We modelled this as a cylindrical disk moving within a viscous sheet with a uniform body force in the serous layer representing the action of cilia. Using lubrication theory we derived equations for the flow and pressure field in the serous layer and the resulting flow in the mucus layer. The problem required a balance between the drag on the disk as it moves over the serous layer and the resistance from the in-plane shear stress in the mucus. We found the speed of the particle as a function of the size of the disk, the thickness and viscosity of the layers, the body force representing the cilia, the shape of the disk base and the effect of the particle on the directly underlying cilia. For typical sizes and viscosities found in airways, the dominant resistance is from in-plane mucus shear; the drag due to moving over the serous layer is less important. The model suggests that a disk will be transported at speeds close to that of the undisturbed mucus, regardless of the shape of the base of the disk or the effect of the particle on the underlying cilia, thus making it a very effective clearance mechanism.

Many physical effects have been neglected in these models. In order to make the models more realistic, and any predictions more accurate, it would be interesting to extend this work to incorporate some of these effects.

In the mucus layer model we represented the mucus as a viscous sheet. A change to the model would be to consider the mucus as a viscoelastic gel layer with a yield stress. Similarly we have used a simplified representation for the cilia. An extension to the model would be to include the effect of the time-dependent ciliary beat cycle. In addition the ciliary propulsive force is likely to vary significantly along the length of the cilia. Mucus-propelling cilia have previously been modelled as an impermeable wall undergoing a travelling-wave motion [17], and as an infinite array of long slender bodies moving with a prescribed beat pattern [20]. It would be interesting to combine some of these ideas with the presence of a deposited particle. We also assumed flat interfaces in the mucus layer model. An important extension to the model would be to allow the serous/mucus interface and, in particular, the mucus/air interface to vary. There is likely to be significant variation in mucus thickness surrounding the moving particle which may alter our existing model predictions.

In all of the models we have assumed the particles to be perfectly smooth. In particular for a particle in a wedge or close to a wall, the effect of particle roughness could have a significant effect on its subsequent motion. It would also be interesting to consider different particle shapes. In the mucus layer model we allowed the disk base to vary slightly but we could consider a spherical particle in the mucus or even needle-like shapes such as fibres. For a particle in a wedge, the wetting properties of the particle are also very important. Different types of particles are inhaled into the lungs and the wetting properties of particles may vary considerably. Including this variation in the model may have a significant effect. Interparticle forces between deposited particles and epithelial cells may also have to be considered when particles come into sufficiently close contact with the airway wall.

In our models we have also neglected the effect of breathing. During the respiratory cycle, not only the air pressure but also many lung properties (*e.g.* surface tension, surface area and lung volume) will change considerably. These effects would be particularly important to a particle in a wedge.

We have so far modelled a particle in an alveolar corner only in two dimensions. Further work would be to extend this model into the three dimensional problem of a spherical particle within a fluid-filled shallow cone shape representing the alveolar corner. This problem is likely to be significantly different from the two-dimensional model as the fluid is no longer divided into separate regions by the particle. The particle in the wedge is subject to forces pushing it perpendicularly and parallel to the wall. It would be very interesting to combine this model with the model for particle motion near a deformable wall, in both the two and three dimensional case. We could therefore consider the effect of a deformable alveolar wall would have on the motion of a partially immersed particle and hence predict the particle's fate after deposition in an alveolar corner.

A relatively simple and important addition to the deformable wall model would be the inclusion of particle rotation. As fluid flows through the narrow gap between the particle and the wall, the particle is subject to a non-zero torque. We have previously imposed no rotation of the particle due to this force. It would be interesting to allow the particle to rotate and consider the effect of this on the model.

Another possible area of further work would be to consider two or more deposited particles trapped in the airway liquid lining in close proximity. Existing models show that, under certain conditions, particles floating at an interface or trapped in a fluid film are subject to an attractive force and will cluster together. It would be particularly interesting to study these particle interactions in relation to our mucus layer model. Bussell *et al.* [80] considered the interaction of two equal-sized cylinders moving in a thin viscous sheet surrounded by a lower viscosity fluid, and show that significant hydrodynamic interactions exist between the cylinders. We could extend our model to consider whether two particles trapped in the mucus will attract or repel each other and what effect this has on the transport of the particles and the effectiveness of the clearance mechanism.

We have assumed the airway wall to be impermeable. In reality, fluid will be drawn through the cellular wall in response to nearby particle motion and may influence particle behaviour. Inclusion of porosity effects would be a useful and interesting extension to these models, in particular to the deformable wall model.

A final idea for further investigation is the inclusion of surfactant effects. Surfactant is found throughout the lung particularly in the smaller airways and alveoli. The presence of surfactant causes surface tension gradients in the airway liquid lining and hence surface tension-driven flows. Including these effects in our models may cause significant changes in the model predictions.

In this thesis we have considered three model problems relevant to the dynamics of particles deposited in the liquid-lining of the lung. Using numerical and analytical techniques we have obtained predictions for particle behaviour that can be used to inform physiological investigations and that provide a basis for further study.

Appendix A

Volume condition for the inner gap region

In Chapter 2 we consider the motion of a particle partially immersed in a fluid-filled wedge. There is no fluid flux through the contact lines and so any change in the fluid volumes, V_1 and V_2, is due to flux through the gap between the particle and the wall. Using this, we derive conditions on V_1 and V_2.

Let $G_1(x,t)$ be the single-valued function of x describing the fluid/air interface between $x = X + a$ and $X = X_1$ and let $G_3(x,t)$ describe it between $x = X_2$ and $x = X - a$. $G_2(x,t)$ describes the bottom of the particle between $X - a$ and $X + a$. The distance of the fluid/wall interface from $y = 0$ is given by $B(x)$ (see figure A.1(a)). Figure A.1(b) shows a close-up of the top of the particle. Let $S(x,t)$ denote the fluid surface and $P(x,t)$ the top of the particle, between $X - a$ and $X + a$, so that between the contact lines $S(x,t) = P(x,t)$.

The fluid volume V_1 is given by

$$V_1 = \int_X^{X+a} G_2(x,t)\, dx + \int_{X+a}^{X_1} G_1(x,t)\, dx + \int_X^{X+a} S(x,t) - P(x,t)\, dx, \quad \text{(A-1)}$$

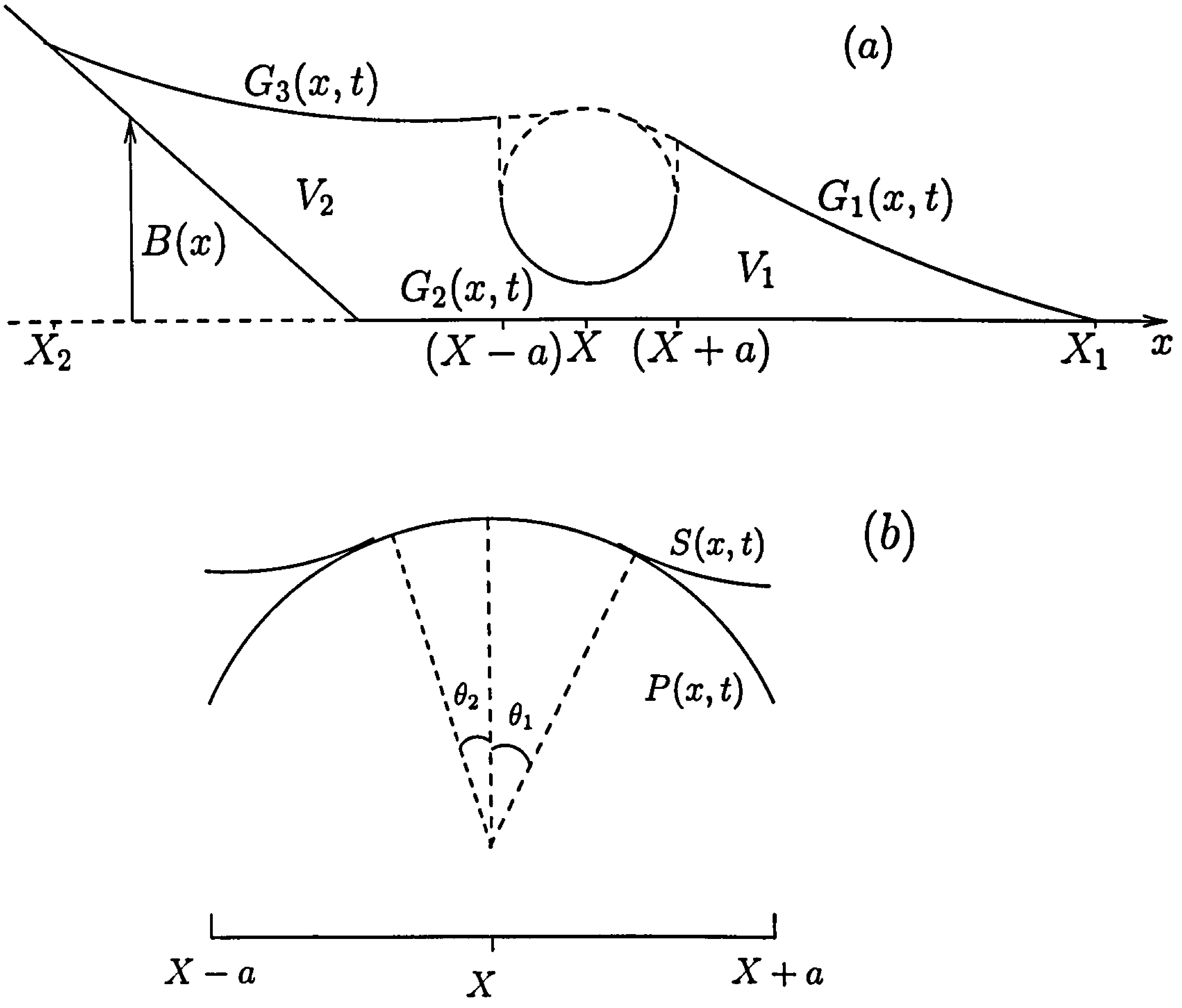

Figure A.1: Sketch of the particle in the fluid-filled wedge showing (*a*) the fluid volumes and interfaces and (*b*) the contact lines on the particle.

and differentiating with respect to t we obtain

$$\dot{V}_1 = \int_X^{X+a} \dot{G}_2 \, dx + G_2|_{X+a}\dot{X} - G_2|_X \dot{X} + \int_{X+a}^{X_1} \dot{G}_1 \, dx + G_1|_{X_1}\dot{X}_1$$
$$-G_1|_{X+a}\dot{X} + \int_X^{X+a} (\dot{S} - \dot{P}) \, dx + (S-P)|_{X+a}\dot{X} - (S-P)|_X \dot{X}. \quad \text{(A-2)}$$

We know from the kinematic boundary condition that $(S-P)_t + \hat{Q}_x = 0$, $G_{1t} + Q_{1x} = 0$ and $G_{2t} + Q_{2x} = 0$, where $\hat{Q}$, Q_1, Q_2 are the fluid fluxes associated with each region of V. There is no flux through the contact points and $G_1|_{X_1} = (S-P)|_X = 0$. Equation (A-2) therefore becomes

$$\dot{V}_1 = -Q_2|_{X+a} + Q_2|_x + G_2|_{X+a}\dot{X} - G_2|_X\dot{X} + Q_1|_{X+a}$$
$$-G_1|_{X+a}\dot{X} - \hat{Q}|_{X+a} + (S-P)|_{X+a}\dot{X}. \quad \text{(A-3)}$$

At $x = X + a$, the regions must match, *i.e.* $G_1 - G_2 = (S-P)$ and $Q_1 - Q_2 = \hat{Q}$, and so we obtain

$$\dot{V}_1 = Q_2|_X - G_2|_X\dot{X}. \quad \text{(A-4)}$$

The fluid volume V_2 can be written

$$V_2 = \int_{X_2}^{X-a} G_3(x,t) - B(x) \, dx + \int_{X-a}^{X} G_2(x,t) \, dx + \int_{X-a}^{X} S(x,t) - P(x,t) \, dx, \quad \text{(A-5)}$$

and in a similar method to above we obtain

$$\dot{V}_2 = -Q_2|_X + G_2|_X\dot{X}. \quad \text{(A-6)}$$

As expected, the change in volume depends on the behaviour of the fluid in the gap region. At $x = X$, $Q_2 = Q$ and $G_2 = h$ and therefore the volume condition for the dynamic problem is

$$\dot{V}_1 = Q|_X - \dot{X}h|_X, \quad \text{(A-7)}$$

$$\dot{V}_2 = -Q|_X + \dot{X}h|_X. \quad \text{(A-8)}$$

Appendix B

Stiff wall asymptotics

In Chapter 3 we consider the motion of a particle moving perpendicular to a deformable wall. Here we consider the prescribed force (pushing) case where $W \ll 1$. This is the "stiff case", so wall deformations are again small. We linearise about the undeformed state by letting

$$h = h_0(t) + \frac{1}{2}x^2 + h_1,$$

where h_1 is small. Linearising, (3.70) is then

$$h_{0t} + \frac{1}{12}\left[\left(h_0 + \frac{1}{2}x^2\right)^3 (-h_{1_x})\right]_x = 0, \tag{B-1}$$

with

$$h_{1x} = 0, \quad \text{at } x = 0, \tag{B-2}$$

$$h_1 \longrightarrow 0 \quad \text{as } x \longrightarrow \infty. \tag{B-3}$$

Equation (3.73) becomes

$$WF(t) = \int_0^\infty h_1 \, dx, \tag{B-4}$$

and therefore we have $W \sim h_1 x$, since $F(t) = O(1)$.

Looking at the magnitudes of the terms in equation (B-1) we obtain

$$\frac{h_0}{t} \sim \frac{h_0^3 W}{x^3} \sim W x^3.$$

Balancing the first two terms we get $x \sim (h_0^2 Wt)^{1/3}$ with $Wt \ll h_0^{-1/2}$. Balancing terms two and three we get $h_0 \sim x^2$ with $h_0^{-1/2} \ll Wt$. Therefore a balance of all three requires

$$Wt \sim h_0^{-\frac{1}{2}}.$$

Assuming $h_0 \sim 1$, we let $t = T/W$ and $h_1 = W\hat{h}_1$, and consider the evolution over long timescales. Equations (B-1) & (B-4) become

$$\begin{aligned} h_{0_T} &= \frac{1}{12}\left[\left(h_0 + \frac{1}{2}x^2\right)^3 \hat{h}_{1_x}\right]_x, &\text{(B-5)}\\ F(t) &= \int_0^\infty \hat{h}_1 \, dx. &\text{(B-6)} \end{aligned}$$

Integrating equation (B-5) twice with respect to x gives

$$\hat{h}_1 = \int_{-\infty}^{x} \frac{12 h_{0_T} x}{\left(h_0 + \frac{1}{2}x^2\right)^3} \, dx = \frac{-6h_{0_T}}{\left(h_0 + \frac{1}{2}x^2\right)^2}, \qquad \text{(B-7)}$$

Using the substitution $\zeta = x/(2h_0)^{1/2}$ to integrate (B-7), we then obtain, from (B-6),

$$h_{0_T} = -\frac{\sqrt{2}F(t)}{3\pi} h_0^{3/2}. \qquad \text{(B-8)}$$

This agrees with (2.38) for the vertical speed of a particle close to a rigid wedge wall. Equation (B-8) can be rewritten as

$$(h_0^{-1/2})_T = \frac{1}{2}\frac{\sqrt{2}F(t)}{3\pi}, \qquad \text{(B-9)}$$

and integrating we obtain

$$h_0^{-1/2} = h_0(0)^{-1/2} + \int_0^T \frac{F(t)}{3\sqrt{2}\pi} \, dt. \qquad \text{(B-10)}$$

Since we are looking over long timescales we assume $F(t)$ is imposed impulsively, *i.e.* $F = 1$, ignoring initial changes in the force. Equation (B-10) therefore becomes

$$h_0^{-1/2} = h_0(0)^{-1/2} + \frac{T}{3\sqrt{2}\pi}. \qquad \text{(B-11)}$$

Figure B.1 compares the analytical solution (B-11) with numerical simulations for $W = 0.002$ and we see there is little close agreement.

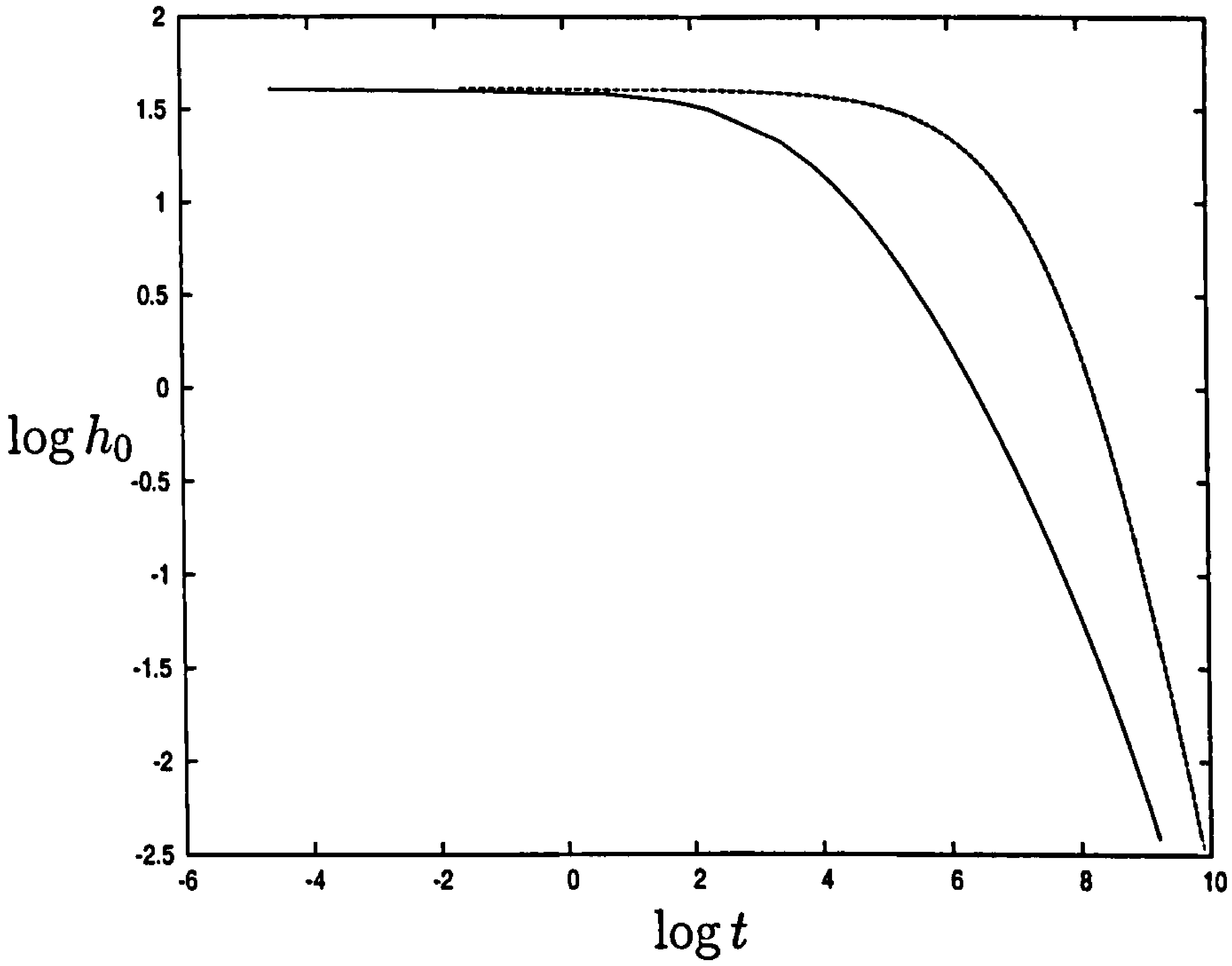

Figure B.1: $\log h_0(t)$ against $\log t$ for the case $W = 0.002$, comparing numerical simulations (solid line) with the analytical solution (B-11) (dashed line).

Combining (B-4) and (B-7) we obtain

$$6h_{0T} = -1 \Big/ \int \frac{dx}{\left(h_0 + \frac{1}{2}x^2 + h_1\right)^2},$$

replacing the neglected 'h_1' term in the denominator of the integrand. The neglection of this term will cause the analytic solution (B-11) to underestimate the speed of the displacement calculated by numerical simulation. This may cause the discrepancy observed in Figure B.1.

References

[1] M. P. Hlastala and A. J. Berger. *Physiology of Respiration.* Oxford University Press, 1996.

[2] S. Schürch, M. Geiser, M. Lee, and P. Gehr. Particles at the airway interfaces of the lung. *Colloids & Surfaces B: Biointerfaces*, 15:339–353, 1999.

[3] P. Gehr, M. Geiser, V. Im Hof, S. Schürch, U. Waber, and M. Baumann. Surfactant and inhaled particles in the conducting airways: Structural, stereological, and biophysical aspects. *Microscop. Res. Tech.*, 26:423–436, 1993.

[4] J. Bastacky, C. Y. C. Lee, J. Goerke, H. Koushafar, D. Yager, L. Kenaga, T. P. Speed, Y. Chen, and J. A. Clements. Alveolar lining layer is thin and continuous: low-temperature scanning electron microscopy of rat lung. *J. Appl. Physiol.*, 79(5):1615–1628, 1995.

[5] J. T. Sharp and M. D. Hammond. Pressure-volume relationships. In R. G. Crystal, J. B. West, et al., editors, *The Lung: Scientific Foundations*, Chapter 5.1.1.4. Raven Press Ltd., 1991.

[6] P. Gehr, S. Schürch, M. Geiser, and V. Im Hof. Retention and clearance mechanisms of inhaled particles. *J. Aerosol Sci.*, 21 (Suppl. 1):S491–S496, 1990.

[7] P. Gehr, F. H. Y. Green, M. Geiser, V. Im Hof, M. M. Lee, and S. Schürch. Airway surfactant, a primary defense barrier: Mechanical and immunological aspects. *J. Aerosol Med.*, 9:163–181, 1996.

[8] D. E. Carney, C. E. Bredenberg, H. J. Schiller, A. L. Picone, U. G. McCann II, L. A. Gatto, G. Bailey, M. Fillinger, and G. F. Nieman. The mechanism of lung volume change during mechanical ventilation. *Am. J. Respir. Crit. Care Med.*, 160:1697–1702, 1999.

[9] D. B. Yeates. Mucus rheology. In R. G. Crystal, J. B. West, et al., editors, *The Lung: Scientific Foundations*, Chapter 3.1.5. Raven Press Ltd., 1991.

[10] J. B. Grotberg. Pulmonary flow and transport phenomena. *Annu. Rev. Fluid Mech.*, 26:529–571, 1994.

[11] W. G. Kreyling and G. Scheuch. Clearance of particles deposited in the lungs. In P.Gehr and J. Heyder, editors, *Particle-Lung Interactions*, Chapter 7. Marcel Dekker Inc., 2000.

[12] M. A. Sleigh, J. R. Blake, and N. Liron. The propulsion of mucus by cilia. *Am. Rev. Respir. Dis.*, 137:726–741, 1988.

[13] M. A. Sleigh. Mucus propulsion. In R. G. Crystal, J. B. West, et al., editors, *The Lung: Scientific Foundations*, Chapter 3.1.4. Raven Press Ltd., 1991.

[14] M. King. Effect of particles on mucus and mucociliary clearance. In P.Gehr and J. Heyder, editors, *Particle-Lung Interactions*, Chapter 13. Marcel Dekker Inc., 2000.

[15] J. R. Blake. On the movement of mucus in the lung. *J. Biomechanics*, 8:179–190, 1975.

[16] M. R. Knowles and R. C. Boucher. Mucus clearance as a primary innate defense mechanism for mammalian airways. *J. Clin. Invest.*, 109(5):571–577, 2002.

[17] S. M. Ross and S. Corrsin. Results of an analytical model of mucociliary pumping. *J. Appl. Physiol.*, 37:333–340, 1974.

[18] S. W. Clarke and D. Pavia. Mucociliary clearance. In R. G. Crystal, J. B. West, et al., editors, *The Lung: Scientific Foundations*, Chapter 7.3.2. Raven Press Ltd., 1991.

[19] H. Matsui, S. H. Randell, S. W. Peretti, C. W. Davis, and R. C. Boucher. Coordinated clearance of periciliary liquid and mucus from airway surfaces. *J. Clin. Invest.*, 102(6):1125–1131, 1998.

[20] J. R. Blake. Mechanics of muco-ciliary transport. *IMA J. Appl. Math.*, 32:69–87, 1984.

[21] P. J. Basser, T. A. McMahon, and P. Griffith. The mechanism of mucus clearance in cough. *J. Biomech. Eng.*, 111:288–297, 1989.

[22] M. King, M. Agarwal, and J. B. Shukla. A planar model for mucociliary transport: effect of mucus viscoelasticity. *Biorheology*, 30:49–61, 1993.

[23] N. Liron and S. Mochon. The discrete-cilia approach to propulsion of ciliated micro-organisms. *J. Fluid Mech.*, 75:593–607, 1976.

[24] G. K. Batchelor. *An Introduction to Fluid Dynamics.* Cambridge University Press, 1967.

[25] R. F. Probstein. *Physicochemical hydrodynamics: an introduction.* John Wiley & Sons, 1994.

[26] P. S. Hammond. Nonlinear adjustment of a thin annular film of viscous fluid surrounding a thread of another within a circular cylindrical pipe. *J. Fluid Mech.*, 137:363–384, 1983.

[27] P. A. Gauglitz and C. J. Radke. An extended evolution equation for liquid film breakup in cylindrical capillaries. *Chem. Eng. Sci.*, 43:1457–1465, 1988.

[28] O. E. Jensen. Self-similar, surfactant-driven flows. *Phys. Fluids*, 6(3):1084–1094, 1993.

[29] O. E. Jensen and J. B. Grotberg. The spreading of heat or soluble surfactant along a thin liquid film. *Phys. Fluids A*, 5(1):58–68, 1992.

[30] J. B. Grotberg, D. Halpern, and O. E. Jensen. Interaction of exogenous and endogenous surfactant: spreading-rate effects. *J. Appl. Physiol.*, 78(2):750–756, 1995.

[31] M. J. Rosen. *Surfactants and Interfacial Phenomena.* John Wiley & Sons, 2nd edition, 1989.

[32] K. J. Stebe and C. Maldarelli. Remobilizing surfactant retarded fluid particle interfaces. ii: Controlling the surface mobility at interfaces of solutions containing surface active components. *J. Colloid Interface Sci.*, 163:177–189, 1994.

[33] J. B. West. *Respiratory Physiology- the essentials.* Williams & Wilkins, 5th edition, 1995.

[34] D. Halpern and J. B. Grotberg. Fluid-elastic instabilities of liquid-lined flexible tubes. *J. Fluid Mech.*, 244:615–632, 1992.

[35] J. B. Grotberg. Respiratory fluid mechanics and transport processes. *Annu. Biomed. Eng.*, 3:421–457, 2001.

[36] D. P. Gaver, D. Halpern, O. E. Jensen, and J. B. Grotberg. The steady motion of a semi-infinite bubble through a flexible-walled channel. *J. Fluid Mech.*, 319:25–65, 1996.

[37] O. E. Jensen, M. K. Horsburgh, D. Halpern, and D. P. Gaver III. The steady propagation of a bubble in a flexible-walled channel: Asymptotic and computational models. *Phys. Fluids*, 14:443–457, 2002.

[38] D. R. Otis, M. Johnson, T. J. Pedley, and R. D. Kamm. Role of pulmonary surfactant in airway closure: a computational study. *J. Appl. Physiol.*, 75(3):1323–1533, 1993.

[39] D. Halpern and J. B. Grotberg. Surfactant effects on fluid-elastic instabilities of liquid-lined flexible tubes: A model of airway closure. *J. Biomech. Eng.*, 115:271–277, 1993.

[40] D. C. F. Muir. Particle deposition. In R. G. Crystal, J. B. West, et al., editors, *The Lung: Scientific Foundations*, Chapter 7.3.1. Raven Press Ltd., 1991.

[41] P. J. Thompson. Drug delivery to the small airways. *Am. J. Respir. Crit. Care Med.*, 157:S199–S202, 1998.

[42] T. B. Martonen. Mathematical model for the selective deposition of inhaled pharmaceuticals. *J. Pharm. Sci.*, 82:1191–1199, 1993.

[43] P. Gehr, M. Geiser, V. Im Hof, and S. Schürch. Surfactant-ultrafine particle interactions: what we can learn from PM10 studies. *Phil. Trans. R. Soc. Lond. A*, 358:2707–2718, 2000.

[44] R. G. Crystal. Alveolar macrophages. In R. G. Crystal, J. B. West, et al., editors, *The Lung: Scientific Foundations*, Chapter 3.4.5. Raven Press Ltd., 1991.

[45] S. Schürch, P. Gehr, V. Im Hof, M. Geiser, and F. Green. Surfactant displaces particles toward the epithelium in airways and alveoli. *Resp. Physiol.*, 80:17–32, 1990.

[46] H. M. Princen. The equilibrium shape of interfaces, drops, and bubbles. rigid and deformable particles at interfaces. In E. Matijevic, editor, *Surface and Colloid Science*, volume 2, pages 1–84. Wiley Interscience, 1969.

[47] A. V. Rapacchietta, A. W. Neumann, and S. N. Omenyi. Force and free-energy analyses of small particles at fluid interfaces: 1. cylinders & 2. spheres. *J. Colloid Interface Sci.*, 59(3):541–567, 1977.

[48] C. Allain and M. Cloitre. Interaction between particles trapped at fluid interfaces: 1. exact and asymptotic solutions for the force between two horizontal cylinders. *J. Colloid Interface Sci.*, 157:261–268, 1993.

[49] P. A. Kralchevsky and K. Nagayama. Capillary interactions between particles bound to interfaces, liquid films and biomembranes. *Adv. Colloid Interface Sci.*, 85:145–192, 2000.

[50] M. E. O'Neill and K. Stewartson. On the slow motion of a sphere parallel to a nearby plane wall. *J. Fluid Mech.*, 27(4):705–724, 1967.

[51] A. J. Goldman, R. G. Cox, and H. Brenner. Slow viscous motion of a sphere parallel to a plane wall- I: Motion through a quiescent fluid. *Chem. Eng. Sci.*, 22:637–651, 1967.

[52] A. J. Goldman, R. G. Cox, and H. Brenner. Slow viscous motion of a sphere parallel to a plane wall- II: Couette flow. *Chem. Eng. Sci.*, 22:653–660, 1967.

[53] H. Brenner. The slow motion of a sphere through a viscous fluid towards a plane surface. *Chem. Eng. Sci.*, 16:242–251, 1961.

[54] R. G. Cox and H. Brenner. The slow motion of a sphere through a viscous fluid towards a plane surface- II: Small gap widths, including inertial effects. *Chem. Eng. Sci.*, 22:1753–1777, 1967.

[55] D. J. Jeffrey and Y. Onishi. The slow motion of a cylinder next to a plane wall. *Q. J. Mech. Appl. Math.*, 34:129–137, 1981.

[56] M. J. Lighthill. Pressure-forcing of tightly fitting pellets along fluid-filled elastic tubes. *J. Fluid Mech.*, 34:113–143, 1968.

[57] M. S. Carvalho and L. E. Scriven. Effect of deformable roll cover on roll coating. *TAPPI J.*, 77:201–208, 1993.

[58] F. R. Pranckh and D. J. Coyle. Elastohydrodynamic coating systems. In S. F. Kistler and P. M. Schweizer, editors, *Liquid Film Coating*, Chapter 12c. Chapman & Hall, 1997.

[59] M. S. Carvalho and L. E. Scriven. Deformable roll coating flows: steady state and linear perturbation analysis. *J. Fluid Mech.*, 339:143–172, 1997.

[60] D. J. Coyle. Forward roll coating with deformable rolls: a simple one-dimensional elastohydrodynamic model. *Chem. Eng. Sci.*, 43(10):2673–2684, 1988.

[61] M. J. Gostling, M. D. Savage, A. E. Young, and P. H. Gaskell. A model for deformable roll coating with negative gaps and incompressible compliant layers. *J. Fluid Mech.*, 489:155–184, 2003.

[62] R. H. Davis, J.-M. Serayssol, and E. J. Hinch. The elastohydrodynamic collision of two spheres. *J. Fluid Mech.*, 163:479–497, 1986.

[63] J.-M. Serayssol and R. H. Davis. The influence of surface interactions on the elastohydrodynamic collision of two spheres. *J. Colloid Interface Sci.*, 114(1):54–66, 1986.

[64] Y. Zhao, K. P. Galvin, and R. H. Davis. Motion of a sphere down a rough plane in a viscous fluid. *Int. J. Multiphas. Flow*, 28:1787–1800, 2002.

[65] S. R. Hodges and O. E. Jensen. Spreading and peeling dynamics in a model of cell adhesion. *J. Fluid Mech.*, 460:381–409, 2002.

[66] S. R. Hodges, O. E. Jensen, and J. M. Rallison. Sliding, slipping and rolling: the sedimentation of a viscous drop down a gently inclined plane. *Under consideration for publication in J. Fluid Mech.*, 2004.

[67] C. C. Mei, R. W. Yeung, and K.-F. Liu. Lifting of a large object from a porous seabed. *J. Fluid Mech.*, 152:203–215, 1985.

[68] B. W. Van de Fliert, P. D. Howell, and J. R. Ockenden. Pressure-driven flow of a thin viscous sheet. *J. Fluid Mech.*, 292:359–376, 1995.

[69] P. D. Howell. Models for thin viscous sheets. *Euro. Jnl Appl. Maths*, 7:321–343, 1996.

[70] N. M. Ribe. A general theory for the dynamics of thin viscous sheets. *J. Fluid Mech.*, 457:255–283, 2002.

[71] N. D. Di Pietro and R. G. Cox. The spreading of a very viscous liquid on a quiescent water surface. *QJ Mech. Appl. Math.*, 32(4):355–381, 1979.

[72] O. K. Matar, R. V. Craster, and M. R. E. Warner. Surfactant transport on highly viscous surface films. *J. Fluid Mech.*, 466:85–111, 2002.

[73] H. A. Stone and A. Ajdari. Hydrodynamics of particles embedded in a flat surfactant layer overlying a subphase of finite depth. *J. Fluid Mech.*, 369:151–173, 1998.

[74] P. G. Saffman. Brownian motion in thin sheets of viscous fluid. *J. Fluid Mech.*, 73:593–602, 1976.

[75] B. D. Hughes, B. A. Pailthorpe, and L. R. White. The translational and rotational drag on a cylinder moving in a membrane. *J. Fluid Mech.*, 110:349–372, 1981.

[76] E. Evans and E. Sackmann. Translational and rotational drag coefficients for a disk moving in a liquid membrane associated with a rigid substrate. *J. Fluid Mech.*, 194:553–561, 1988.

[77] T. M. Fischer. The drag on needles moving in a Langmuir monolayer. *J. Fluid Mech.*, 498:123–137, 2004.

[78] E. Denny and R. C. Schroter. Relationships between alveolar size and fibre distribution in a mammalian lung alveolar duct model. *J. Biomech. Eng.*, 119:289–297, 1997.

[79] H-H. Wei, S. W. Benintendi, D. Halpern, and J. B. Grotberg. Cycle-induced flow and transport in a model of alveolar liquid lining. *J. Fluid Mech.*, 483:1–36, 2003.

[80] S. J. Bussell, D. L. Koch, and D. A. Hammer. The resistivity and mobility functions for a model system of two equal-sized proteins in a lipid bilayer. *J. Fluid Mech.*, 243:679–697, 1992.